UNIVERSITY OF SOUTHAMPTON

GAS DISSOLUTION PHENOMENA IN CRUDE OIL PRODUCTION

LISA MARIE HUNT

SUBMITTED FOR THE DEGREE OF
DOCTOR OF PHILOSOPHY

DEPARTMENTS OF MECHANICAL ENGINEERING AND CHEMISTRY

MARCH 1995

UNIVERSITY OF SOUTHAMPTON

ABSTRACT

FACULTY OF SCIENCE

MECHANICAL ENGINEERING AND CHEMISTRY

Doctor of Philosophy

GAS DISSOLUTION PHENOMENA IN CRUDE OIL PRODUCTION

Lisa Marie Hunt

Reducing the size of offshore separator vessels can result in large economic and safety advantages, in terms of space saving, mobility and installation costs. Yet the lack of knowledge and understanding regarding the rapid evolution of gas following a sudden reduction in pressure, has so far hampered any significant size reductions in surface separating facilities. Following a review into the needs of the offshore oil and gas industry, and a review of the literature concerning the behaviour of gases in liquids, a fully instrumented thermodynamically enclosed rig facility was designed to study the non steady-state conditions created during, and immediately after, the rapid depressurization of a gas-saturated liquid. The mechanisms of gas evolution and the processes controlling the rate of gas evolution were investigated using techniques predominantly experimental in nature. The test conditions, in what is essentially a pressure vessel, included initial saturation pressures up to 30 bara, liquid temperatures up to 60°C and salinities up to full saturation. The range of gases, CO_2, N_2, O_2, Ar and CH_4, were investigated in water, brine (NaCl) solutions, two distillate oils, kerosene and gas oil and Statfjord crude, under controlled conditions. Owing to their industrial significance, exploratory tests were carried out using mixed gas compositions of N_2 and CO_2, and oil/water mixes.

Video evidence of events during depressurization and subsequent recovery was recorded and correlated with the pVT data. Gas evolution and hence pressure recovery to equilibrium occurred predominantly by bubbling, although pressure recovery by molecular diffusion was apparent over the latter stages of the approach to equilibrium for all gases. Owing to the dissociation reaction of CO_2 in water, a more complex gas evolution pattern and a slower rate of approach to equilibrium, by ~ 2 orders of magnitude, was observed with CO_2 in water compared to the other gases in water. In addition, the extent of dissociation of CO_2 in brine, compared with that in tap water, was found to significantly influence the rate of gas evolution. In kerosene, the behaviour of CO_2 was found to be similar to that of the other gases tested, where equilibrium was generally reached within seconds of depressurization. The main factors which were found to significantly increase the rate of gas evolution included the initial liquid temperature, fluid agitation and the addition of solid nuclei, in the form of $5\mu m$ uni-sized silica flour particles. The implications of these results to the oil industry have been highlighted. The rate of gas evolution was not found to be significantly influenced by the purity of the water.

LIST OF CONTENTS

APPENDICES

LIST OF FIGURES

LIST OF TABLES

LIST OF PLATES

ACKNOWLEDGEMENTS

The author would like to thank Professor Martin T. Thew of the Mechanical Engineering department, and Dr. Anthony J. Rest of the Chemistry department, who jointly supervised the project. Coming from a chemistry background, several people contributed enormously in some way to the learning process of the author, and thanks must go particularly to Mike E. Cox, of the Central Design Service, for the vessel design drawings, and to Paul Bickmore, of Electronic Services, who helped in setting up the data logging software and who wrote the data reduction programme. Thanks must also go Paul Dean, from the Mechanical Engineering workshop, who played a large part in the construction of the rig in the laboratory. The author shall always be grateful to Derek Leadbetter, then of Conoco UK Ltd, who arranged a two month work placement at Conoco Specialty Products' Research and Development Centre in Ponca City, Oklahoma, USA, and to Elwyn Shimoda, the perfect host in Ponca City, who organized the finer details and the home comforts. A visit to the offshore oil platform, Hutton TLP, was also arranged, courtesy of Conoco UK Ltd. Thanks must finally go to BP Exploration, who showed an interest in the research and who continued the sponsorship over the final few months of the project.

NOMENCLATURE

a,b	constants in equations of state
A	surface area of gas-liquid interface of a bubble, mm^2
B	pre exponential constant in nucleation rate equation
C	molar concentration
D	kinetic coefficient
g_{cav}	energy required to form a cavity in the solvent
g_{int}	energy of interaction between the gas and solvent molecules
G	Gibbs free energy
G_b	Gibbs number
J	rate of bubble nucleation, bubbles cm^{-3} $secs^{-1}$
H	Henry's law constant
k	Boltzmann's constant, J/K
k	rate constant in CO_2 equilibria
K	equilibrium constant
L	Ostwald coefficient
m	constant in equations of state
m	mass of a molecule, g
M	molecular weight
n	number of moles
N	number of molecules in unit volume
p	pressure, barg or bara
p_{eqm}	equilibrium pressure, bara
p_f	final pressure, bara
p_g	pressure of gas in the bubble (where $p_g = p_v + p_s$), bara
p_i	initial pressure, barg or bara
p_l	ambient liquid pressure, bara
p_{min}	minimum pressure, bara
p_s	partial pressure of solute, bara
p_v	vapour pressure, bara
r	radius, μm
r_c	critical radius of bubble, μm
r_o	radius of bubble, μm
r_p	pressure reduction ratio

R	universal gas constant
Ra	surface roughness measurement, μm
S	supersaturation ratio
t	time, secs
T	temperature, K
U	rise velocity of bubble, cm sec^{-1}
V	volume, cm^3
V	intermolecular potential
V_g	volume of gas reduced to 0°C and 1 bara
V_m	molar volume
V_s	volume of solvent reduced to 0°C and 1 bara
W	work required to create a bubble capable of further growth in homogeneous nucleation
W'	work required to create a bubble capable of further growth in heterogeneous nucleation
x_g	mole fraction solubility

α	Bunsen coefficient
α, δ, ∞	factors and coefficients in equations of state
π_x	supersaturation function
σ	surface tension of the liquid-gas interface of a bubble, mN/m
μ	dynamic liquid viscosity, cP
μ	kinematic liquid viscosity, cS
μ	chemical potential
μ^*	excess chemical potential
ρ	liquid density, kg/m^3
γ	ratio of specific heat at constant pressure to that at constant volume
ϕ	heterogeneous nucleation factor
ϕ	volume fraction of solvent occupied by solute
ϵ, σ	Lennard Jones parameters
υ	wavenumber, cm^{-1}
ω	acentric factor, used in equations of state

BPD	barrels per day
BWPD	barrels of water per day
ppm	parts per million
PWRI	produced water re-injection
UKCS	UK continental shelf

1.0 INTRODUCTION

1.1 Introduction

Areas like the North Sea, covering some 600,000 km^2, are becoming mature in oil field terms. Future development therefore lies in fields which are smaller, more remote, and more difficult to exploit economically. Cost effective exploration and recovery of oil and gas will be a key factor in determining the long term economic viability of the North Sea industry. New or improved technologies are required to keep down the costs of running existing, and often ageing platforms, and to overcome the difficulties associated with finding and developing new fields further afield, in deeper and more hostile waters, whilst keeping to a minimum the costs of recovering and transporting oil and gas.

Large economic and safety advantages can be gained by reducing the size of the offshore separation equipment. Smaller separating vessels can be readily transported, installed without the need for heavy installation equipment and maintained (removing solids and checking for corrosion) more easily. By reducing the topside size and weight, offshore production platforms can be made smaller and therefore lighter, whilst still maintaining the optimum efficiency of the separating facilities.

In addition, the handling of produced water, which was once a small consideration in the offshore production facilities is now costly and, in some fields, the major factor limiting oil production. As oil fields mature, the volumes of produced water requiring disposal tend to increase, often exceeding the oil production by a large margin. The size, weight and cost of offshore production equipment is often directly related to the installation and operation of the produced water treating facilities, which are required to process the fluid to a specified level of free oil-in-water, prior to discharge overboard.

At the same time, concern for the environment has resulted in increasingly stringent standards for the quality of the discharged water. Whilst existing units provide adequate oil removal performances to meet current offshore oily water discharge standards, pollution regulations could well become more demanding over the next few years. It therefore becomes increasingly important to adopt efficient, environmentally sound disposal systems.

The requirement for the future, therefore, is for the separation systems to be effective in handling the increasing volumes of produced water from mature oil fields, protecting the environment against pollution, whilst driving to reduce capital and operating expenditure. The alternatives to consider, are to improve the performance of existing facilities, which may also require a significant improvement in the quality of the discharged water, or to develop new methods for treating oily water.

1.2 Scope and objectives of work

Despite the initial three phase separation of the bulk well head fluid into gas, water-based liquids and oil, significant amounts of gas still remain in the liquid stream. Throughout the successive stages of oil production, dissolved gas is continually evolved as the liquid stream, flowing through control valves, pipes, venturis and separating equipment, is exposed to large and sudden pressure drops. In order to cope with the unsteady and turbulent flow, experienced due to the breakout of gas, a significant residence time, reflected in the size of the separator units, is required. Ideally, the retention time of the liquid in the separator should be kept to a minimum. Too long a residence time, and the process becomes time consuming and unnecessarily expensive. Too short a residence time, however, and optimum efficiency is not achieved. Allowances also have to be made to cope with the possibility of sudden slugs and surges which would otherwise cause an increase in the amount of liquid carried over in the gas stream, as well as an increase in the amount of gas being carried out of the separator in the liquid stream.

The phenomena of gas dissolution in relation to offshore platform separating facilities is a key area which has received little attention in the oil industry. The main reason being that in the past, the size of the separator vessels tended to be influenced by factors such as the space available on the platform, and as such, were oversized, particularly since the extra capacity required to accommodate a liquid surge is difficult to calculate. The vessel volume for the more recent separators is largely dependent on estimated flows and well head conditions. Now that there is the necessity to reduce the size of the separating equipment, particularly for floating platforms and small fields, the ways in which this can be achieved must be addressed. Reducing the size of the separation systems increases the likelihood of foaming, carryover of liquid in the gas stream and carryunder of gas in the liquid stream when the system in the separator vessel does not reach equilibrium. The potentially hazardous problems centred on sensing and control of foam and dissolved gas in the stream must be overcome before the residence time of the liquid, and therefore the size of the separators, can be reduced. As a result, the knowledge and understanding regarding the role of dissolved and free gases must be strengthened.

This investigation is the first stage towards addressing the problems associated with gas breakout. The present three year PhD programme was set up by the Departments of Mechanical Engineering and Chemistry. Drawing on certain thermodynamic aspects of physical chemistry, the study was aimed at finding out more about the mechanisms of gas evolution from hydrocarbons and water-based liquids during rapid depressurization, and the processes controlling the rate of gas evolution. The main objectives were to design and construct a fully instrumented thermodynamically enclosed rig facility in which to study the response of a saturated or partly saturated liquid when exposed to a sudden reduction in pressure. A selection of gases and liquids were tested, under a wide range of controlled, experimental conditions. Focusing on the rapid depressurization of the pressure vessel, the effects of saturation pressure, initial liquid temperature, the rate of pressure reduction, salinity and the liquid and gas properties, on the gas evolution process were studied, together with an investigation into those parameters which could be used to control the rate of gas evolution, such as fluid agitation or the addition of inert solids.

It is relatively easy and straightforward to provide quantitative information for systems in steady state conditions. The solubilities of gases in liquids under all conditions of temperature, pressure and salinity have been determined using various adaptations of equations of state and Henry's law for systems at equilibrium. It is, however, more difficult to obtain quantitative and reliable data for non equilibrium conditions, where, as a result of the rapidly changing conditions and the increasing deviation from steady state conditions, the steady state equations may no longer be applied. The key area of interest in the present study lay in the non steady state conditions set up in the vessel during and immediately after the rapid depressurization of a saturated liquid, as a new equilibrium state is established.

1.3 Structure of thesis

The following chapter provides a background into the production of crude oil, focusing on the stages of processing the fluid from the well heads, to the re-injection or overboard discharge of the produced water, and the transportation of the marketable crude. The existing offshore separation processes, particularly for the treatment of oily water, are discussed, together with their suitability for meeting future environmental oily water discharge standards, whilst handling potentially large volumes of produced water. The presence and role of free gas and dissolved gas is also discussed.

A review of the literature and assessment of contemporary work of relevance to the present study is given in chapter 3. The review focuses on three areas. The first area focuses on the thermodynamics of the gas dissolution process, in terms of how and why gases dissolve in liquids, on a molecular scale, enabling accurate predictions of the solubility of simple gases in water to be made. The second area focuses on systems at equilibrium, and how equations of state are used to describe the relationships between the pressure, temperature and volume of gas in a steady state system. Two equations of state, which are widely accepted in the petroleum industry for modelling the behaviour of CO_2 in water, brine and oil, are identified and discussed. Attention has then been focused on the non equilibrium situation created during depressurization of a liquid saturated with gas. The mechanisms of gas evolution are discussed, in terms of bubble dynamics, nucleation and growth, together with how the overall rate of depressurization influences the evolution process. The rapid depressurization studies which have been carried out to date, stemming mainly from the recognition of potential hazards in nuclear reactors, have been described.

Chapter 4 describes in detail, the design and construction of the instrumented facility in which the phenomena of gas dissolution and evolution was studied. The instrumentation selected to look at the rates at which gas is released from water-based liquids and hydrocarbons under finely controlled conditions is described, together with an account of the developments and the modifications of the experimental apparatus which occurred during the initial stages of design, and during the commissioning the rig.

The experimental programme designed to study and explore the variables controlling the rate of gas evolution from the initially saturated and partly saturated liquids is documented in chapter 5. The physical characteristics of the gases and liquids used in the experimental programme are given, which is followed by a brief introduction into the data analysis, in terms of how the data collected was analysed and presented. The main source of information was obtained from the pVT data, and is displayed in the form of pressure-time histories, free gas volume-time and piston velocity-time plots.

Being predominantly experimental in nature, a vast amount of experimental data was collected during the investigation. A selection of the experimental results are documented in chapter 6, together with an account of the visual and photographic observations of the events captured during the depressurization of the vessel. The discussion and interpretation of the results reported in chapter 6 is given in chapter 7. Drawing on the results of the experimental data, and drawing on the visual and photographic observations, an overall picture of the depressurization process is presented. The factors which were shown to influence both the rapid depressurization process and the rate of approach to the new equilibrium state are highlighted and discussed, particularly in the context of offshore field operations and conditions. In addition, suggestions have been put forward to describe the more unusual observations and behaviour recorded, particularly for the complex evolution pattern and the slow rate of approach to equilibrium associated with CO_2 in water, compared to the other gases in water, which was considered to be due to the dissociation reaction which takes place between CO_2 and water.

Chapter 8 outlines a programme for further work. The results of the experimental study are used to establish an overall framework, which enables predictions to be made regarding the nature and behaviour of other gases. By carrying out a few additional experiments, the theories and predictions made, during the interpretation and discussion of results, can be validated. An extended programme for a long term study is also included, outlining three areas of research which are considered to have significant industrial applications. The final section in chapter 8 focuses on the application to industry, in which consideration is given to scaled up systems and to thermodynamically open systems, which are more commonly found in the industrial environment.

The key results obtained from the experimental programme are summarized in the concluding comments in chapter 9.

2.0 CRUDE OIL PRODUCTION OFFSHORE

2.1 Introduction

Physical separation of the well head fluids into marketable products is the basic operation in the production, processing, and treatment of oil and gas on offshore oil facilities. Produced well head fluids are a complex mixture of hydrocarbons and water-based liquids, saturated or part saturated with gas. The fluids also contain a wide range of solids, such as reservoir solids, deposited scale, heavy metals and corrosion products. A series of separators, operating at sequentially reduced pressures, enables maximum recovery of hydrocarbons from the well fluid. The primary production facility separates the well head fluid into the three bulk oil, water and gas phases. Gas is flashed from the liquid, and the free water separated from the oil. After the initial bulk separation into gaseous and liquid components, additional processing equipment is required to treat and clean the oily water stream before it can be either discharged overboard, without violating environmental laws, or re-injected into the well. The crude oil product must also be further treated to remove water, basic sediment and salt content to meet transport specifications. It is then put into tankers or piped to shore.

Whilst multiphase pipelining may become viable in the future, as a means of getting the unseparated mixture of oil, gas and water to shore, before treatment, at present it is not practical. The main problems are associated with predicting temperature and pressure losses along the miles of pipework, and establishing enough pressure at the well head to actually pump the fluids to shore. The more practical method currently practised is to separate the phases on the platform.

Economic sources of oil and gas on land are limited. The basic separation techniques used for onshore recovery, but with consideration given to the size, weight and safety limitations imposed by the confined environment, have been developed to allow offshore drilling and production to take place, but now exploration is necessary in harsher environments, further offshore. As a result, more difficult enhanced recovery techniques are being developed, and major barriers such as deeper water, greater well depths and ice environments must be overcome. Problems therefore arise in relation to the size of the massive steel and concrete structures which must be transported from their onshore fabrication sites to the offshore fields, as well as transportation of the raw material from the fields to shore. Installing equipment is ~ 3 times the cost on land [1], which is further increased through operation and maintenance costs. For each tonne of equipment on the platform, an estimated 3 tonnes of sub and super structure is required to support it [2]. The process equipment and associated steel works account for 20% of the topside weight. A reduction in the size of the offshore separating facilities, particularly for sub-sea plants and tie-ins to existing platforms, using lighter and stronger materials, in terms of improved mobility, easier installation and cheaper maintenance costs will enable the efficient and economic exploration and production of oil and gas to continue.

2.2 Role of free and dissolved gases in the production of crude oil

Crude oil in the reservoir is liquid existing in the porous rock at a natural pressure of ~350 bara, and a temperature of ~100°C. Under these conditions the gases are dissolved in the oil. The controlled release of natural reservoir pressure frees some of the gas from solution and permits the mixture of oil and gas to flow through the wells to the platform, cooling and losing pressure as it rises. At the wellheads, the pressure can range from 10, to hundreds of bara, and the temperature from 20 to 120°C. The crude oil/water mixture at the top of the production well is still saturated or supersaturated with gas. Gases typically constitute a significant fraction of the well head fluid [3], and even after degassing, 5-20% by volume of the fluid flow is gas, although clearly this value depends on the nature of the field, and will change as the fluid progresses through the treatment train.

The physical and chemical characteristics of the oil and water determine the dissolved gas content, which is a direct function of the initial pressure, temperature and dissolved solids concentration. At any given temperature and pressure, the components in each phase will be in equilibrium, until exposed to a sudden drop in pressure or temperature [4]. The fluid produced from the wells, is a mixture of many hydrocarbons ranging from methane (the lightest) to very heavy and complex hydrocarbons. Each time there is a drop in pressure, gas is liberated. Pressure drops arise as a result of acceleration, flow through control valves, friction losses and elevation changes. Generally the pressure loss due to acceleration is small, whilst elevation changes are the most significant. As the stream flows from the high pressure and temperature reservoir, large and rapid reductions in temperature and pressure are experienced, and indeed, they occur at various stages through the separation process. The heavier gases are stripped out at the higher pressures, whilst the light end fractions go with the flow and are stripped out further down the production process. The rate at which gas is liberated from a given oil is a function of the change in pressure and temperature, both in terms of timescale and the magnitude of depressurization.

Problems can also be caused by large scale foaming, which generally occurs as a result of impurities, other than water, in the crude oil. The extent of foaming is dependent on the characteristics of the fluid, the magnitude and rate of pressure drop, and more often than not, the temperature. For certain types of crude oil, as a result of the reduction in pressure, the bubbles of gas coming out of solution are encased in a liquid film of oil. Foaming occurs when drainage of the liquid surrounding the liquid film is retarded, commonly caused by surface active compounds or colloidal solids in the crude oil stabilizing the liquid film [3]. Foaming in a separator can result in carryover of the free liquid with gas, and carryunder of free gas with the liquid phase. Control also becomes more difficult as there are effectively three liquid phases present rather than two. Not only will the capacity of the separator be affected, since the foam can occupy a significant volume of the vessel space, but the residence time necessary for foams to break can be increased by a factor of four [5], reducing the separation efficiency. In addition, many of the control valves are density based. Any changes in density and indeed, to the flow pattern, caused by frothy mixtures, can affect the operation of the valves, making control and sensitivity more difficult. Whilst the volumes of gas in solution cannot be easily controlled, certain factors can be controlled to help reduce foam formation and reduce their stability. In cases where foaming is anticipated, anti foaming agents, usually based on silicones, can be added which modify the surface tension of the oil, making the foam collapse more readily.

Even after the gas has left the platform, pressure reductions in the pipelines can cause problems. More than three quarters of natural gas is normally methane, containing some nitrogen, some carbon dioxide and a small percentage of heavy hydrocarbons. It is the latter group of compounds which cause a phenomena known as retrograde condensation [7]. When the gas pressure drops, the gas solubility decreases, but whereas methane may be unaffected, the other compounds become visible in the form of liquid droplets resembling gasoline. The liquid can attack the gas pipelines and cause damage to the pumps transporting the gas.

In summary, the presence of free and dissolved gas is significant in a number of oil and gas operations, placing significant demands upon the performance, durability and compactness of the separation equipment. This is evident not only at the well heads, where large amounts of gas are present, but also further down the separation process, where gas evolution can cause instability with respect to sensing and control, unsteady flow and potential large scale foaming.

2.3 Oil-water separation systems

Offshore platform facilities generally use combinations of separator systems to separate and clean the oil and water. The most suitable separator systems are often specific to each particular platform location, as separation is dependent on a number of factors such as flow rate, pressure, temperature and physical characteristics of the oil/water mixture. The physical and chemical properties of North Sea crudes differ markedly from field to field, ranging from the very light volatile crudes from the Piper field to the waxy crude from the Beatrice field [8]. It is desirable for the separators to be unaffected by motion, and be able to handle sudden and sometimes large changes in oil, water and gas flow rates. Other factors to consider include the capability of handling solids, foaming, high viscosity fluids, cold temperature and low pressure fluids, in addition to the economics, installation, maintenance and manoeuvrability of the separator unit.

The initial bulk separation of the three phases at the well head is the first stage of processing. The primary separators must be large enough to handle the potentially large volumes of gas produced, and must be capable of handling up to 100,000 bpd from the well heads. By removing the free water in the early stages, the size of the additional separators can be reduced. Large residence times are also generally required for the fluid in the separator, to ensure that equilibrium, or a condition approaching equilibrium, is reached, thus ensuring optimum separation efficiency. Ideally, the separators will have a large throughput and low residence time.

Gravity settling tanks are the simplest of primary water separators. Long residence times enable coalescence and gravity separation to occur and allow chemical treatment, such as demulsifiers and foam inhibitors to act. The function of these water treating systems is to cause the oil droplets in the water continuous phase to float to the surface where they are skimmed off. Whilst small amounts of gas in the system may be advantageous in aiding the recovery of oil, particularly in conventional separators where the buoyancy effects of bubbles attached to the oil droplets can influence the rate of migration of oil through the water, large amounts of gas do become a problem. Bubble-drop attachment also requires substantial amounts of surfactant chemicals.

Removing water from crude oil generally requires more than just gravity separation. Emulsions take anything from a few minutes to weeks or months to separate if left alone in a tank with no treating. The high and intermediate pressure separators are normally three phase, separating the gas from the liquid and the liquid stream into oil and water components, whilst the low pressure separators are generally two phase, further separating the gas from the liquid stream. The produced water from a three phase separator contains oil at levels of anything between a few hundred and a few thousand mg/l. The additional separating equipment must be capable of cleaning the fluid to free oil-in-water concentrations of between 15 and 40 mg/l.

The current main secondary oil-water separation systems for produced water are tilted plate separators, gas flotation units, and hydrocyclones. The older platforms generally used tilted plate separators and gas flotation units, whereas the more modern developments favour hydrocyclone technology. Indeed, many of the older facilities have been retrofitted, where possible, with hydrocyclones. A typical stage separation processing layout can be seen in figure 2.1.

Any gas still left in the produced water from the water outlet of the three phase separator is entrained within the liquid, and as a result the flow entering the next separation stage is usually a mixture of gas and turbulent liquid flowing at high velocities. Approximately a few percent by weight of the bulk water phase is oil, in the form of finely dispersed droplets [5]. The temperature of produced water varies from 20°C and 105°C and its pressure from 2 barg to 20 barg. In addition to the sand, deposited scale, and heavy metals such as Cd and Hg, chemical residues from substances often injected during the production process to control corrosion, foaming, bacterial growth and emulsion formation may also be present in the stream. The composition of produced water changes from field to field, and also changes with time, during the progressive changes from connate water to produced injected sea water through the life of a field.

2.3.1 Horizontal and vertical separators

Typical designs for a three phase horizontal and vertical separator can be seen in figure 2.2. In each case the fluid from the well head, downstream from the choke valve, enters the separator and hits an inlet diverter. The sudden change in momentum results in the initial bulk separation of the liquid droplets which fall to the bottom of the vessel, and the gas which flows over the diverter and through the gravity settling section above the liquid. The liquid is retained in the vessel for a short time to allow the evolution of the entrained gas, and is then transported to the next stage. The gas is passed through a coalescing section or mist extractor as it leaves the separator. The very small liquid droplets carried in the gas phase collect and coalesce on the wire meshes. The mist extractors also help to reduce turbulence in the gas flow. The pressure is maintained in the vessel using a control valve, which is opened and closed as a pressure controller senses pressure changes in the separator.

Horizontal separators, figure 2.2a, are more common than vertical separators and are generally more efficient at handling large gas volumes, since the surface area of the liquid-gas interface is larger, and the distance travelled by the bubbles to reach the vapour space, as the liquid reaches equilibrium, is minimized. Gas-liquid separation occurs at a much faster rate if the liquid is flowing in a horizontal rather than a vertical direction. Horizontal vessels are considered more economical for normal oil-gas separation, particularly if emulsions, high gas-oil ratios, and foaming are experienced [5]. They are also more effective for removal of liquid droplets larger than 200-400μm. Vertical separators, figure 2.2b, are more practical in terms of floor space required, and are better at handling solids and coping with liquid slugs following, for example, well shut down.

The physical characteristics of the fluids and the operating conditions strongly influence the efficiency of the separators. The larger the oil droplets, the greater the vertical velocity through the bulk fluid, the less time taken to reach the surface. The lighter the crude, the larger the differential density between the oil and water, the easier it is to treat. The higher the temperature, the lower the viscosity of the water, the greater the vertical velocity, the easier it is to treat.

Although reliable (except on floating facilities), simple and inexpensive to operate, gravity separators require time and quiescence to ensure that most of the free oil droplets rise to the surface. Gravity separators generally dispel droplets with diameters less than 30μm and have residual concentrations around 40-50 mg/l [6], although drop sizes can easily be up to 80μm and concentrations up to ~ 100 mg/l if the residence time falls to around 5 mins. Secondary separators are generally required to remove the remaining emulsified and dissolved oils prior to disposal.

2.3.2 Tilted plate interceptors

The two common forms of tilted plate coalescers are the parallel plate interceptors and the corrugated plate interceptors. The principle, in each case, relies on gravity separation to allow the oil droplets present in the water to rise to the plate surface where coalescence occurs. As shown in figure 2.3, flow is split between a number of parallel plates spaced a short distance apart. To capture the oil droplets, the plates are inclined to the horizontal. The parallel plates form a V when viewed along the axis of flow such that the oil sheet migrates up the underside of the plate and to the sides. The sediments migrate towards the middle and down to the bottom of the separator where they are removed. The main problem in using parallel plate interceptors is the potential for sand and wax sticking to, and clogging the plates. It is desirable for most of the sand

and solid matter to be removed before the fluid enters the interceptor. The plates are commonly corrugated to increase the surface area, which also has the added benefit of making sediment handling easier. The axis of the corrugations are installed parallel to the direction of flow and the plates are inclined at an angle of 45°. The bulk water flow is forced downwards, whilst the oil sheet rises upwards, counter to the water flow, and is concentrated in the top of each corrugation. When the oil reaches the end of the plate pack, it is collected in a channel and brought to the oil-water interface. Offshore, parallel separators have a residence time of around 50 mins, which produces an average effluent concentration of 25-70 mg/l.

2.3.3 Gas flotation units

Unlike most other oil-water separation units, flotation units do not rely solely on gravity separation. Instead, the success of the flotation units, figure 2.4, relies on the principle that gas bubbles generated in the oily water attach to the suspended oil droplets and small solids. These bubbles then rise to the surface due to the differential density difference between the water and the bubbles. Two method are used to generate the bubbles. In dissolved gas units, figure 2.4a, which are not used as much offshore, gas is dissolved under pressure to form a saturated solution, which is injected into the flotation unit. The gas, air, CH_4, N_2 or CO_2, dissolved in the water becomes supersaturated upon reduction of pressure, generally from ~ 5 bara to atmospheric, thus forming gas bubbles. Following depressurization the gas bubbles, oil and suspended solids rise to the surface. In induced air flotation units, figure 2.4b, high speed impellers are used to mix the gas and liquid. This agitation generates the bubbles. The amount of gas dissolved and the amount of gas released are functions of the initial pressure, the degree of saturation and the degree of mixing. The solubility of the gas is a function of the temperature and the dissolved solids concentration.

Air flotation units usually follow a primary separator as the units work better with feed streams having oil concentrations up to 300 mg/l. The residence time in air flotation units is dependent on the rate of rise of air bubbles in the liquid, but is generally in the region of 5-10 mins. The bubbles move at different velocities depending on their respective diameters. For example, bubble sizes are ~ 5 times larger for CO_2 than air, and would therefore be expected to rise faster, creating turbulent conditions. Bubbles with diameters of around 10 mm have a vertical rise velocity ~ 25 times that of a bubble only 0.2 mm in diameter [6].

Operating costs of air flotation units are considerably more than gravity settling systems and there is the likelihood of mechanical breakdown since the air must be pressurized or dispersed into the flow. The space required, however, is significantly reduced. Despite their well established technology, gas flotation units respond poorly to upsets. Departures from steady state operations affect the separation efficiency. Their performance tends to decline over time, with newer installations performing better than older ones. As a result, for realistic operating conditions, whilst some platforms comfortably meet the 40 mg/l target, others struggle to do so, often requiring significant quantities of chemicals, sometimes in quantities greater than 100 ppm, and often requiring continual attention to operation and maintenance. Flotation units can also be affected by motion, and in some cases the stream containing the oil can rise to >10% of the feed stream [6].

2.3.4 Hydrocyclones

Development of deoiling hydrocyclones for oily water clean up led to their introduction into the North Sea in 1984. Since then, hydrocyclone technology has long been established as the preferred method for the treatment of produced oily waters offshore due to the significant advantages over the more traditional systems of a reduction in weight, space required, simplicity of operation and low maintenance costs, as well as being insensitive to motion and orientation. To date, deoiling hydrocyclone systems capable of treating over 8 million BWPD have been sold worldwide [8]. Hydrocyclone systems are currently operational on over 20 North Sea platforms, treating over 2.5 million BWPD, whilst others are under construction or on new platforms awaiting start up.

The produced oily water from the water outlet of the three phase production separator enters the hydrocyclone for further separation. The two phase mixture is subjected to a large centrifugal force causing the dense phase to migrate to the wall, where it is removed, and the lighter phase to form a central core, which flows up and out the separator, as shown in figure 2.5. Flow reversal of the vortex core means that the residence time for the oil enriched stream is roughly twice that for the cleaned stream, giving more time for the droplets to migrate to the centre core. The flow reversal is achieved by the correct unit geometry and the correct balance of pressures at the two outlets. Any gas dissolved in the inlet feed entering the hydrocyclone, which breaks out due to the pressure drop experienced in the hydrocyclone, migrates along with the lighter oil phase towards the central oil core, which is itself the lowest pressure region.

Due to its geometry and the potentially high turbulence levels, the hydrocyclone cannot be scaled up to handle the throughput directly from the well heads. In addition, at the well heads, except for very wet (old) fields, flow will be oil continuous. Instead, hydrocyclones are used in conjunction with primary separators. Where installed, hydrocyclones are capable of separating bulk water with oil feed concentrations in the range 0-3000 ppm to give water with concentrations well within the 40 mg/l limit when the plant is in steady operation.

The residence time in the hydrocyclone itself, is only a second or two, and allowing for manifolding ~ 10 seconds for the installation. Due to the low residence time in the hydrocyclone, gas-liquid equilibrium is not achieved. There is very little time for gas to evolve from solution and hence there are indications that gas does not normally cause any major problems in deoiling systems. Photographic studies of a transparent hydrocyclone operating with a gas saturated feed, carried out at Southampton University, have indicated that under the conditions experienced in the hydrocyclone even though a gas core was evident, there were no gas bubbles visible anywhere within the separator [10]. The results suggested that a considerable fraction of the flow in the hydrocyclone could exist in a supersaturated state, at least until the fluid leaves the hydrocyclone. Some degassing vessel may therefore be required downstream of the hydrocyclone to cope with, and control the potentially large volumes of gas evolution. This stage may be particularly necessary before overboard disposal, owing to the large pressure drops experienced as the saturated fluid is discharged overboard.

With dewatering hydrocyclones, problems may be caused by the presence of dissolved and free gas in the stream, since the inlet flow is oil continuous. Although the technology has not yet been fully developed, larger quantities of gas are involved, the effects of dissolved gas are likely to be more significant and hence the demands are likely to be more stringent. The presence of gas not only takes up some of the system volume, but the throughput of oil through a hydrocyclone separator can be restricted by the gas, resulting in unsteady flow and instability regarding sensing and control.

One of the significant advantages of hydrocyclones is that as water production increases, additional units may be added without extensive piping modifications. Multiple units inside a single vessel increase the capacity over a single liner, whilst maintaining identical separation performance and amassing savings in terms of installation costs and space. In addition, many units in parallel can handle very large flows, of around 20 m^3/min. Mechanical problems are fairly rare, centering on corrosion of unlined carbon steel pressure vessels and wear on the liners caused by excessive solids in the water. Improved designs and the use of pressure vessel linings or better materials can and have improved reliability even further.

In terms of future technology for the oil industry, the application for hydrocyclones is widening to include treatment of highly emulsified water mixtures, treatment of low temperature produced waters, treatment of waters containing heavy oil and treatment of oily waters where only limited pressure is available to drive the units. Systems are also being developed to provide bulk oil/water separation [11,12].

2.4 Discharges from offshore operations

The application of legislation to discharges from offshore activities stems mainly from the concern for the marine environment [13]. In 1976 it was estimated that 85×10^6 tonnes p.a. of produced water in the North Sea had to be cleaned [14]. By 1986, the figure had risen to 94×10^6 tonnes p.a. for the UK sector alone [15]. For the North Sea, the figure is probably approaching 200×10^6 tonnes p.a. In 1991, 2.2 million BPD of treated produced water were discharged to the North Sea, which is estimated to rise to around 4 million BPD in 1998, although this may be reduced by re-injection as described in section 2.5.

The current legislation for UKCS sets a target standard for all oil production platforms of 40 milligrams of free oil per litre of discharged water (40 ppm). At specific locations, the level has been reduced to 15 mg/l. As the environmental regulations increasingly limit the maximum allowable free oil discharged, the oil and gas industries must look at the existing systems for oil-water separation in terms of maintaining and even improving discharge levels to meet current and future laws.

Putting things into perspective however, offshore operations are considered to contribute just over 1% of the total oil entering rivers and seas [16]. The benefits of reducing oil discharges must be weighed up against the increase in chemical discharges, because whilst striving to maintain lower water-in-oil discharge levels, the water treatment chemical dosages may have to be increased to improve the separation performance. Consequently, the reduction in oil-water is matched by the increase in chemical discharges. The implications of reducing the monthly dispersed oil content in produced water discharged from offshore facilities from 40 to 30 mg/l has recently been under review. It was concluded that a reduction in the oil-in-water limit would only produce a small reduction in terms of the total oil discharged to the North Sea [16], and thus the environmental benefit due to reduced levels of hydrocarbon pollutants would be negligible. More likely, the increased levels of chemical dosages required to meet the lower standard may well increase the impact on the environment. So for the near future, at least, the limit has been maintained at 40 mg/l.

2.5 Produced water treatment

One alternative for overboard disposal which should briefly be mentioned is the re-injection of produced water [17,18], being both economically sound and environmentally attractive, particularly for older installations where upgrading facilities are required to handle the increasing volumes of produced water from mature fields. The costs of re-injecting produced water can be comparable to those of the cheapest methods for treating water to current oil-in-water discharge limits prior to overboard disposal, as the environmental restrictions become ever more demanding.

The most serious concern for produced water re-injection schemes is likely to be how much water can be re-injected into a particular well (50,000-250,000 bpd are required). Sea water injection facilities have been installed in most offshore platforms to boost the productivity of the oil well, and have proved effective, but the differences in water quality, in terms of temperature and solids content, between sea water and produced water must be considered. The warmer temperatures of produced water are likely to encourage the growth of bacteria, and the increased quantities of solids and deposited scale increases the potential of blockages in the pipes. The injection rate is also likely to be significantly lower than for sea water and the rate will tend to decline with time. Recent field trials in the North Sea [19], have showed mixed responses in performance for different reservoirs, depending on the differing reservoir characteristics, and thus the water quality, in terms of the oil droplet and suspended solids size distribution in the injected produced water.

Produced water re-injection could be a key to the financial success of offshore developments, even challenging the success of hydrocyclone technology, particularly in high production cost areas such as the North Sea, for water re-injection systems can as much as double the amount of oil recovered. In conclusion, the future could tend towards produced water re-injection, as a cost effective and simple method for treatment of large volumes of produced water, although the long term effects of PWRI, particularly at high oil and solids loading, on reservoir performance are not known for North Sea formations. However, there will always be situations when treatment costs are too high, or re-injection not possible, in which case other technologies must be employed, making the continued development of new and improved water treatment facilities essential.

3.0 GAS DISSOLUTION AND EVOLUTION: A REVIEW OF PREVIOUS WORK

3.1 Introduction

There are many facets to the study of the behaviour of gases in liquids. The review in this chapter has attempted to explore the relevant areas, to give an overview of gas-liquid systems, correlating ideas, in an attempt to provide an informative picture of the various processes involved with gas dissolution and evolution. The next two sections, 3.2 and 3.3, discuss the gas dissolution process, in terms of the thermodynamics of how and why a gas dissolves in a liquid on a molecular scale, and how the solubility can be affected by parameters such as pressure and temperature. Sections 3.4 and 3.5 discuss the thermodynamics of a saturated state at equilibrium, which can be described using equations of state. The final few sections, 3.6-3.11, and indeed the most significant part of the review, concentrate on the non equilibrium situation created when a saturated liquid, at equilibrium, is exposed to a sudden change in conditions. Attention is focused firstly on the mechanism of bubble formation and how equilibrium is re-established, in terms of bubble nucleation and growth, and then on the overall rate of depressurization and rate of desorption of gases from supersaturated liquids.

3.2 Solubility of gases in liquids

The solubility of gases in liquids has been the subject of considerable experimental and theoretical interest in many branches of science for a number of years. At modest pressures, nearly all gases are at least sparingly soluble in all liquids. The very early work, dating back to the beginning of the nineteenth century was, on the whole, qualitative. Since then, techniques and theories have been improved and developed over the years, providing a vast volume of experimental data for the solubility of gases in liquids, over an extensive range of pressures and temperatures. Detailed and comprehensive surveys have been carried out on the quality of the substantial volume of published data [20-22], and compilations of actual solubility data can be found in later publications [23-25], which focus on the general trends and behaviour of gas-solvent systems. The most recent and indeed extensive compilations of data for the solubility of gases in liquids are being produced as volumes in the Solubility Data Series, by the International Union of Pure and Applied Chemistry.

Of particular interest in this study was the solubility data for the gases, CO_2, Ar, O_2 CH_4 and N_2 in water, brine and hydrocarbons over a pressure range of 1-30 bara, a temperature range of 15-70°C and a salt concentration over the whole range of 0-100% saturation. The data was compiled from several sources in the literature for the various conditions for CO_2 in water [25-29], CO_2 in salt solutions [30-34], CO_2 in kerosene and crude [35] and Ar [36-39], N_2 [25,40-43], O_2 [25,44-46] and CH_4 [25,47,48] in water, salt solutions and hydrocarbons.

The large volume of published data on the solubility of gases in liquids was generally determined either by saturating a previously degassed liquid with gas or by removing the dissolved gas from a previously saturated liquid. The solubility of a gas in a liquid is determined by temperature and the partial pressure of the gas. Finely controlled conditions are therefore required, in which the temperature, pressure and volume can be readily measured or calculated. Detailed reviews, establishing the reliability of the experimental techniques employed to determine the quantities of the components in the liquid and gas phases, such as volumetric analysis, chromatography and measurement of vapour pressure, giving the limitations and uses of the data obtained by each method, can be found in many texts [22-25].

In order to determine the solubility, in all cases, the gas and liquid phases of the system must be in a state of thermodynamic equilibrium. More often than not, the reasons for the discrepancies of certain data could be explained by the experimental technique, and were generally a result of failure to completely degas the solution, failure to correctly determine the amount of dissolved gas in solution initially, and more importantly, failure to reach equilibrium. Indeed, it has only recently come to light just how difficult it is to completely degas a solution. In addition, very little data, if any, actually exists in the literature which allows the time taken to reach equilibrium to be predicted. The most recent indication suggests that in order to ensure complete saturation of soluble gases such as CO_2 in water, a time of 16-48 hours is required during which the solvent should be continually swirled, shaken or pumped in contact with the gas [49]. Other inaccuracies included the presence of gas impurities, affecting the partial pressure of the gas under test, and making allowances, where necessary for the partial pressure of the solvent.

The solubility data of gases in aqueous solutions are generally presented in one of four ways, as Bunsen coefficients (α), Ostwald coefficients (L), mole fraction solubilities (x_g) and Henry's law constants (H). The Bunsen coefficient is defined as the volume of gas reduced to 0°C and 1 bara, dissolved per unit volume of solvent at the same temperature and pressure

$$\alpha = \frac{V_g}{V_s}\frac{273}{T} \qquad \textbf{(3.1)}$$

Equations of state are required for real gases for the correction to standard conditions, since the correction assumes ideal gas behaviour.

The Ostwald coefficient is defined as the ratio of the volume of gas absorbed to the volume of the absorbing liquid, measured at the same temperature

$$L=\frac{V_g}{V_s} \tag{3.2}$$

The Ostwald coefficient is independent of the partial pressure of the gas, as long as ideality may be assumed, and the volume is assumed to be independent of pressure, which can lead to errors at higher pressures. It therefore becomes a more reliable measure of the solubility when pressure and temperature are specified. If the gas phase is ideal, and the gas solubility small, hence no change in the volume of the liquid phase during gas dissolution, the Ostwald coefficient can also be defined as the concentration of gas molecules dissolved in equilibrium in the liquid solvent to their concentration in the gas phase. Obviously for very soluble gases under certain pressure and temperatures, an appreciable change in volume may occur, in which case equation 3.1 should be used.

The mole fraction solubility, x_g, of a gas dissolved in a solvent is given by

$$x_g=\frac{n_g}{n_g+n_l} \tag{3.3}$$

where n_g and n_l are the number of moles of gas and liquid respectively. The mole fraction solubility ranges from 0 to 1. In future chapters, where solubility data has been used by the author to predict equilibrium pressures and solubilities, the mole fraction was found to be the most suitable to work with, particularly when determining the mass of gas in each phase at the initial and final equilibrium states. The mole fraction solubilities for the gases used in the experimental study over a range of temperatures and pressures can be found in appendix I.

Henry's law constant is expressed as the ratio of gas pressure to the mole fraction of gas in solution, and is a function of temperature. For dilute solutions at low pressure, the mole fraction solubility, x_g, is adequately described by Henry's Law

$$p_g=x_gH \tag{3.4}$$

where p_g is the partial pressure of the solute gas and H is a constant of proportionality. Henry's law constants and mole fraction solubilities are the most commonly used method in more recent times of displaying solubilities.

3.3 Thermodynamics of gas dissolution in water

When the surface of a liquid is exposed to a solute gas, the gas molecules enter the liquid at microcavities and then diffuse, or are stirred into the bulk liquid until equilibrium is reached, at which point the temperature and pressure of each phase is the same. The driving force for chemical systems to reach equilibrium is provided by the chemical potential, which may be expressed as

$$\mu_i = \frac{dG}{dn_i} \tag{3.5}$$

Also known as the partial molar Gibbs free energy, the chemical potential represents the increase in free energy of a system when one mole of component, i, is added to an infinitely large quantity of the mixture so it does not significantly change the overall composition.

The Gibbs free energy is at a minimum when a system is in equilibrium. The drive to equilibrium is to minimize the energy and maximise the entropy. In an isolated system, a spontaneous change tends to produce states of higher entropy, as the temperature and concentration gradients are eliminated, thus approaching equilibrium, until a maximum value for the entropy is reached, at which point the system is in equilibrium and the entropy is constant at that maximum value. Consider a chemical, i, distributed between two phases, α and ß. In transferring dn_i moles of i, from α to ß,

$$dG = [\mu_{i\beta} - \mu_{i\alpha}]dn_i \tag{3.6}$$

$$dG = 0 \quad \text{at eqm} \tag{3.7}$$

$$\therefore \mu_{i\alpha} = \mu_{i\beta} \tag{3.8}$$

Therefore, for a system at constant pressure and temperature, the chemical potential of each component must be equal in all parts of the system. In a system containing more than one gas, equilibrium is reached when the chemical potential of each component in the liquid equals the chemical potential of that component in the gas. The chemical potential varies with pressure according to the Gibbs-Duhem equation [50]

$$\frac{d\mu}{dp} = V_m \tag{3.9}$$

The mechanism most frequently used to describe the solubility process is the cavity model, proposed by Uhlig, in 1937 [51]. The solubility of a gas in a liquid is considered to be a process occurring in two steps. Firstly, the creation of a cavity in the solvent which is large enough to accommodate a solute molecule, and secondly the introduction of the solute molecule into the cavity which then interacts with the neighbouring solvent molecules. The model was used and developed by later workers [52-54] to calculate the separate contributions to the energy and entropy changes involved in each step.

The solubility of a gas in a liquid depends on the equilibrium of Gibbs free energies. In the first step, work is done on the solvent to create a cavity, g_{cav}. The second step involves the energy of interaction between the gas and solvent molecules, g_{int}. In terms of the excess chemical potential, μ^*, which is influenced by the molecular arrangement of the solvent and depends on the potential energy of solute-solvent and solvent-solvent interactions,

$$\mu^*_{(T)} = -RT\ln L = g_{cav} + g_{int} \tag{3.10}$$

In general $g_{cav} > 0$ and $g_{int} < 0$, and the energy required to form a cavity is larger in water than in non polar liquids. A property of the dissolution of gases in liquids is that non polar gases, such as Ar and CH_4, tend to concentrate more in non polar liquids, such as hydrocarbons, compared to water and aqueous solutions. The smaller the excess chemical potential, the larger the solubility. For non polar gases in non polar liquids, μ^* is negative, and the Ostwald solubility coefficient, L, is greater than 1. For non polar gases in water, μ^* is large and positive compared to RT so in this case, L is much less than 1. For most solvents, μ^* increases linearly (becomes less negative) as the temperature increases [55]. Less work is therefore needed to remove a solute molecule from a hot solvent than a cold one.

If V is the partial molar volume of solute in the solvent, V_g is the molar volume in the gaseous phase and ϕ is the volume fraction of the solution that is occupied by the solute

$$L = \frac{\phi V_g}{V} \tag{3.11}$$

In thermodynamic terms, substituting for L in equation 3.10, the total Gibbs free energy for transferring 1 mol of solute into the solvent is the zero sum of four terms [55]

$$g_{cav}+g_{int}-RTln\frac{V}{V_g}+RTln\phi=0 \tag{3.12}$$

The third term represents the energy associated with isothermal and reversible compression of the solute from its volume in the gas to its volume in solution. The fourth term represents the free energy associated with the entropy on mixing. In effect, the solute gas molecules will dissolve in the solvent up to the volume fraction, ϕ, when the free energy associated with the mixing entropy is enough to overcome the free energies for the processes of the first three terms.

The liquid state is the least understood and most difficult to model of the three main phases, water being the most complex of all. The most successful attempt to model the behaviour of non polar substances in water is the scaled particle theory, developed by Pierotti [56,57] and later modified by subsequent workers. The most revealing parameters in interpreting structures, are the changes in partial molar enthalpy, entropy and heat capacity when a gas dissolves in a liquid. Using the large negative entropies and large positive molar heat capacities of solution observed for aqueous solutions as an indication of the type of solute-solvent interactions, and equations developed by previous workers for calculating the energy and entropy changes involved in each step, Pierroti showed that the thermodynamics of simple gases in water could be accounted for in terms of a simple hard sphere model.

Equations were derived for calculating the reversible work required to introduce a hard sphere into a fluid, and for modelling the second step using a Lennard-Jones pairwise potential to account for the solute-solvent interactions. A Lennard-Jones perturbation potential describes the energy of a non-hydrogen bonding interaction between solvent and solute [58]. Information can then be obtained by considering the perturbation of the energy levels of the species by the presence of a solute molecule. The functional form that is often used to represent the intermolecular potential, as introduced by Lennard-Jones, can be written as

$$V=4\epsilon(\frac{\sigma^{12}}{r}-\frac{\sigma^{6}}{r}) \tag{3.13}$$

where ϵ and σ are a measure of the strength and range of the interaction, measured from scattering experiments. These parameters have been determined for a wide range of molecules and have been used extensively in theoretical interpretations of the properties of gases [59].

By applying the theory of hard-sphere fluids to the cavity model, Pierotti found that the reversible work, or partial molar Gibbs free energy, required to introduce a hard sphere of the same radius as the cavity into a fluid, was the same as that required to create a cavity in the solvent. The reversible work of the second step involving the interaction of the solute molecule with the solvent according to a Lennard-Jones pairwise potential was found to be identical to that of charging the hard sphere, introduced in the first step, to the required potential.

The hard sphere model, as a useful first approximation treated molecules as rigid and perfectly elastic spheres. In this way, Pierotti was able to predict the solubility of simple gases in water with some success, for indeed, when compared to the experimental solubilities, those calculated from the theory showed good agreement. Additional calculations [60], confirmed that the hard sphere perturbation theory described very accurately the thermodynamic process. Since the cavity actually starts growing from a natural void in the liquid, the dissolution of small non polar solutes in water does not involve significant reorientation of the neighbouring water molecules. The interactions existing in the liquid were considered to be strong intermolecular hydrogen bonds among neighbouring water molecules, which resulted in the large positive molar heat capacity observed for non polar gases in water. The magnitude of the change in entropy observed was considered to be a result of the imbalance between the large work necessary to create a cavity in the water, and the very small enthalpy of cavity formation, due to the small expansion of the solvent. The large negative entropy was therefore a result of the low solubility in aqueous solutions, rather than the cause.

In summary, the change in chemical potential of the solute, in going from an ideal gas to a dilute aqueous solution, can be expressed as the sum of the contributions from the formation of a cavity in the hard sphere fluid large enough to hold the solute particle, the attractive solute-solvent interactions and the change in the density of an ideal gas in going from its standard state to the density of the fluid. The excess chemical potential can be calculated from g_{cav} and g_{int}, where g_{cav} can be calculated from the scaled particle theory of liquids. The term g_{int} can be calculated from the enthalpic and entropic contributions, but entropic contributions for interactions are difficult to calculate, and many workers often calculate it from equation 3.10 in terms of g_{cav} and the Ostwald coefficient, L.

3.4 Equations of state: modelling the solubility of gases in oil, water and salt solutions

For dilute solutions at low pressures (<10 bar), the solubility of gases may be determined using Henry's law, a simple equation relating solubility to the partial pressure of the gas. At higher pressures, large deviations from linearity occur, due to the non-ideal behaviour of the gases, and the measured solubility fails to obey Henry's law. At the temperatures and pressures experienced in oil and gas recovery, equations of state, relating volumes to pressures and temperatures must be used.

Thermodynamic models are widely used in the modelling of oil recovery processes. Equations of state are used for predicting the extent of the solubility of a gas or gases over a wide range of temperatures, pressures, gas partial pressures and ionic strength of brines, and for predicting the phase behaviour and thermodynamic properties, such as compressibility factors, densities and enthalpies, of mixtures of liquids and gases. One of the first to be developed was the van der Waals' equation in 1873

$$(p+\frac{a}{V_M^2})(V_M-b)=RT \tag{3.14}$$

The equation is based on that for an ideal gas

$$pV=nRT \tag{3.15}$$

where V is the volume of n moles of gas at temperature, T and pressure, p.

An ideal gas has three main properties, in that the volume occupied by the molecules is insignificant with respect to the volume occupied by the gas, there are no attractive or repulsive forces between the molecules or between the molecules and the walls of the container, and all collisions of molecules are perfectly elastic, hence no loss of internal energy upon collision. No known gas behaves as an ideal gas, although the equation can be used to describe the behaviour of real gases at low pressures. Corrections were therefore made to the ideal gas equation, to account for the behaviour of real gases at higher pressures, by the addition of a term to the pressure, to represent the forces of attraction between the molecules, and the subtraction of a term from the molar volume. The actual pressure exerted on the walls of the vessel by the impinging molecules of a real gas is less, by the amount a/V_M^2, than that exerted by an ideal gas, due to the attraction by the mass molecules in the bulk gas. The attraction rises with density. The subtraction of the constant, b, in the equation represents the correction to the molar volume due to the volume occupied by the molecules. The constants, a and b, are characteristic of each particular gas.

The law of corresponding states proposed by van der Waals, expressed the generalization that equilibrium properties which depend on intermolecular forces are related to the critical properties in a universal way. In this way, the pVT properties of pure substances could be expressed by a two-constant equation of state. The pressure-volume relationships at constant temperature are different for different substances. The law holds well for fluids containing simple spherically symmetrical molecules, and by simple adjustment, for fluids containing non spherical molecules, which are not strongly polar or hydrogen-bonded. Reliable correlations for strongly polar molecules, however, are not possible, particularly at high pressures.

Since the appearance of van der Waals' equation, many authors have proposed variations to the basic ideal gas equation, with varying degrees of success, in an attempt to increase the range of temperatures and pressures to which the equation can be applied. Generally, equations of state have been used to represent the behaviour of the oil and gas phases, which are relatively easy to model.

The two most common and frequently used methods for predicting gas solubilities, physical properties and the vapour-liquid equilibria ratios of hydrocarbon mixtures in the oil industry are the Soave-Redlich-Kwong equation of state [61]

$$(p+\frac{a_T}{V_M(V_M+b)})(V_M-b)=RT \qquad \textbf{(3.16)}$$

and the Peng-Robinson equation of state [62]

$$(p+\frac{a_T}{V_M(V_M+b)+b(V_M-b)})(V_M-b)=RT \qquad \textbf{(3.17)}$$

Both are variations of the van der Waals' equation, modifying the attractive pressure term of the van der Waals' equation to take into account the temperature dependence of the molecular attraction. Although the two are similar, the coefficients do not have the same value. They are both 2-parameter EOS and the values of these parameters for each pure component are obtained from the critical temperature, critical pressure and a term known as the acentric factor. The definitions and calculations for these coefficients, and how they are used can be found in appendix II. Since there is also a lot of interest in the behaviour of mixtures of gases, particularly in the oil industry, mixing rules have also been developed which are recommended for use with both of the above equations of state. The interaction coefficients of the mixed gases are incorporated into the terms a and b. These coefficients can be calculated as shown in appendix II, together with an example of how they can be applied to real life conditions.

Solubility and equilibrium predictions have been carried out by the author for single component gas systems and for mixed gas compositions in liquids, and are described in appendix III. This has particular significance not only to the experimental work carried out on mixed gases, which is discussed in more detail in chapter 6.17, but also to mixed gas behaviour in the oil industry, for the equilibrium calculations are made more complicated due to the complex nature of petroleum reservoir fluids and the complicated phase behaviour observed at elevated pressures and temperatures. This complex behaviour arises because of the wide variety of compounds encountered, for example, non spherical molecules such as heavy alkanes and aromatic hydrocarbons, as well as non hydrocarbons, such as CO_2 and H_2S.

Real mixtures also contain large amounts of water. Therefore, modelling of phase behaviour must include liquid-liquid equilibria, which is much more difficult to represent with an EOS than vapour-liquid equilibria. So, whilst modelling of the oil and gas phases proved reliable using equations of state, accurate predictions of the aqueous phase composition were more difficult to make, especially when attempts were made to model the aqueous phase using the same equation of state [63,64]. However, Peng and Robinson [65] were able to achieve predictions of the composition of the aqueous phase by modifying the EOS parameters. The use of an EOS for both liquid and vapour phases may become prominent when relatively simple solutions are considered, but in focusing on anisotropic molecules in dilute aqueous solutions the use of a single EOS is not really reliable or feasible. The alternative method, which is more commonly practised, involves using adaptations of Henry's law to model the gas solubility in the aqueous phase, and using an EOS for the other phase(s) [66,67].

More recently, correlations for the solubility of CO_2 in brine have been developed [68-71], as the effects of salt in the water cannot be represented by a cubic equation of state. Salt has a strong effect on the solubility of the gas. Using the experimental data available, the phase behaviour of oil, gas and water or brine was predicted. In each case the Peng-Robinson equation of state was used to model the oil and gas phases, and the gas solubility in the aqueous phase was determined from correlations for Henry's law constants. By modifying the Henry's law constants derived for pure water, they were able to account for the effect of salt on the gas solubility in the aqueous phase. The change of the Henry's law constant due to the presence of salt was predicted using the scaled particle theory, by adjusting the solute molecular diameter. Indeed, the correlations and proposed models using this method have accurately predicted the carbon dioxide solubility in the CO_2-NaCl and CO_2-water systems over the wide range of temperatures and pressures considered. The Henry's law approach for the aqueous phase is considered to be superior, with, at present, little likelihood of replacement.

3.5 Solubility trends and predictions for gases in liquids

Section 3.3 has addressed the thermodynamics of the dissolution of simple non polar gases in water. The structure of the liquid mixture must be known before its thermodynamic properties and indeed before the solubility of the gases in the liquid can be predicted. The physical properties of fluids depend directly on the nature of the molecules. All macroscopic properties are related to the molecular structure, which determines the magnitude and predominant type of intermolecular forces, which in turn influences the solubility properties. Thermodynamic and transport properties can also be related to molecular size and speed.

In a solid, molecules are close packed with a definite structure, whereas in a gas, there is no apparent structure and the molecules can move about freely. A liquid lies between the two, for the packing arrangement of the molecules is such that a structure is apparent over short distances over a few molecular diameters, but disappears at greater distances. This can be explained by the fact that the forces between molecules are insufficient to prevent the continual breaking and reforming of the local structure. As a result, when the liquid contains dissolved gas, the molecules have some freedom to move about in the liquid. Most pure solvents, therefore, have some degree of short range ordering of molecules, particularly if hydrogen bonding can occur between the molecules. Solvents with strong hydrogen bonding are generally poor solvents for a gas unless there is a strong tendency for hydrogen bonding to occur between the solvent and the gas molecules [25].

Small non polar inert molecules, such as N_2 and O_2, have dimensions enabling them to fit in the cavities or interstitial sites of the water structure. The behaviour of CO_2, however, is very different, for CO_2, unlike most other dissolved gases, undergoes a chemical reaction with water according to the equilibria

$$CO_{2(g)} \rightleftharpoons CO_{2(aq)} + H_2O \rightleftharpoons H_2CO_3 \rightleftharpoons HCO_3^- + H^+ \qquad (3.18)$$

Several characteristic features can be explained by the dissociation reaction. Being an endothermic reaction in which bonds are formed, a drop in the temperature of the liquid is observed when CO_2 is dissolved in water. A drop in pH is also observed owing to the presence of H^+ ions in the dissociated form. The dissociation reaction of CO_2 in water, and how the equilibria are affected by changes in conditions, particularly to a rapid reduction in pressure, is discussed in more detail in appendix IV.

Figures I-1 to I-6 in appendix I show the effects of temperature and pressure on the solubility of the gases of interest in this study in water over the range 1-30 bara, and 290-350K, compiled from the literature [25-48]. The solubility of CO_2 in water, at 1 bara and 298K is approximately 30 times that of Ar, O_2 and CH_4. The solubility of Ar is approximately twice that of N_2 under the same conditions. The solubility of CO_2 in organic solvents is 3-5 times that for CO_2 in water, although in general, the solubility of gases in water at a high or low pressure is smaller than in other solvents by an order of magnitude [23]. Solvents generally have an affinity for 'like' gas molecules. This preferential solubility is demonstrated in comparing the solubilities of N_2 and CH_4 in water and, for example, hexane (C_6H_{14}). In water, N_2 and CH_4 have similar solubilities. In hexane, however, the solubility of CH_4 is ~ 6 times that of N_2 [25]. The mole fraction solubility of gaseous hydrocarbons, in hydrocarbons, tends to increase with increasing solute chain length [25].

The solubility of gases increases with gas partial pressure for all systems, as more solute gas dissolves in the liquid owing to the increase in the gas density with increasing partial pressure. Whilst the solubility of most gases in water generally decreases with increasing temperature to somewhere approaching the critical temperature of the solvent, beyond which the solubility increases with temperature, in other solvents the solubility of many gases increases with increasing temperature [21,25]. Although equations have been derived to describe the behaviour of solvent with temperature [55,72], the solubility of gases in water and other solvents is not really understood [73]. In general, the solubility data of gases in water and other solvents over a narrow temperature range of $\sim$200-600K can be fitted to an equation of the type [25]

$$\ln x = A + \frac{B}{T} + C \ln T + DT \qquad (3.19)$$

for which the values of A to D are different for each gas-liquid combination.

The solubility of CO_2 and indeed other gases, decreases as salinity increases. The difference in solubility between the water and the salt solution becomes smaller with increasing temperature. Electrolytes cause the break up or build up of the molecular structure of water, according to their ionic radius and charge. Ions which break the structure decrease the viscosity of water. On the other hand small ions and the hydroxyl group build up the structure and therefore increase the viscosity of the solution. A fully saturated NaCl salt solution, in which the Na^+ and Cl^- ions, sheathed in water, move freely and randomly throughout the solution, has a viscosity approximately twice that of water.

Similarly, Ar, for example, is ~20% less soluble in sea water than pure water [36]. At low temperatures, the dissolved electrolyte interferes with the formation of the cage of solvent molecules around the Ar atom. At higher temperatures, the local environment of the gas atom in brine appeared to be slightly more ordered than in pure water, reflecting the longer effective range of the ionic fields at higher temperatures. The Ar solubility in brines of constant salt concentration decreases with increasing temperature. The differences between the solubilities in pure water and brine are greatest at low temperatures. For a 100% salt saturated solution, the solubility of Ar at 0°C is ~7 times smaller than in water, whereas at 65°C, the difference is a factor of ~4 [38].

Solubility calculations and equations of state to model the pVT relationships provide a substantial understanding of the equilibrium state existing between liquids and gases in relation to the oil industry, but there has been very little work done on systems exposed to a non equilibrium state, which are particularly important for the reasons discussed in chapter 2, and where equations of state cannot feasibly be applied. Using the theoretical framework derived for the equilibrium state as a basis upon which to work, the author has used the equations of state for CO_2 in water and brine solutions to establish the amount of gas in solution at the initial and final equilibrium states, appendix III, and has carried out a thorough experimental investigation to explore the behaviour of gases during the non steady state conditions. The following sections address the behaviour of such a system, exposed to a large and sudden reduction in pressure.

3.6 Thermodynamics of gas evolution from liquids

Consider the relationships which can exist between the saturation pressure and the gas pressure above a saturated liquid in a vessel. At equilibrium, the flux of gas molecules entering the liquid balances the flux leaving the liquid. A rapid and continual exchange takes place at the liquid surface, but overall, the liquid neither releases or absorbs gas. At equilibrium, therefore, the dissolved gas content is constant with respect to time. The gas molecules are uniformly distributed throughout the liquid and each gas molecule is closely packed by liquid molecules. The radius for the volume that a single gas molecule occupies in solution is a well defined quantity, and varies with temperature and gas-solvent combination [59].

If there is a change in either the pressure or the temperature, a non equilibrium situation is created. Le Chatelier's principle and thermodynamics indicate that if the sum of the partial pressures of solute and solvent exceeds the ambient pressure, the system will tend to shift towards a re-establishment of equality of pressures. Under approximately isothermal conditions at constant volume, this can only occur by gas and vapour evolution. In the case where the amount of gas dissolved in the liquid is less than the corresponding existing gas pressure, i.e. undersaturation, gas absorption takes place. When the amount of gas dissolved in the liquid is greater than the amount which would correspond to the existing gas pressure, i.e. supersaturation, evolution takes place.

Supersaturation occurs when the sum of the partial pressures of the gases dissolved in the liquid, exceeds the total pressure of gas above the liquid surface, which includes the solvent vapour pressure. For gases which satisfy Henry's law, this condition can be written by using the inequality [74]

$$\pi_{(x)}=\frac{\dfrac{\sum C_{iL(x)}}{H_{i(T)}}}{p}-1>0 \tag{3.20}$$

where $C_{iL(x)}$ denotes the molar concentration of component, i, in the liquid at a distance, x, from the interface, and $\pi_{(x)}$ is the supersaturation function. The total pressure of the gas phase comprises the partial pressures of gases dissolved in the liquid phase

$$p=\frac{\sum C^{*}_{iL}}{H_{i(T)}} \tag{3.21}$$

where C^{*}_{iL} is the molar concentration of component, i, at the interface on the liquid side. It therefore follows, that a sufficiently large drop in pressure above the liquid must always result in satisfying the supersaturation condition $\pi_{(x)} > 0$ in the entire bulk liquid.

Two mechanisms, which often occur simultaneously are used to describe the gas desorption process accompanying a drop in pressure. The first is by diffusion (quiescent desorption), and the second is by bubble formation and growth (bubble desorption). Gas evolution by diffusion, in the absence of mixing and in the absence of bubbling, is analogous to gas absorption. The diffusion process takes place when the degree of supersaturation is reasonably low and when the rate of pressure reduction is slow. In the absence of bubbling, the gas from a supersaturated solution reaches and leaves the surface by diffusion through the liquid, driven by pressure, temperature and concentration gradients set up between the bulk and the surface. The concentration of dissolved gas in the bulk of the liquid is greater than that at the surface. Although the rapid depressurization of saturated liquids is more relevant to this study, quiescent desorption may be significant in the latter stages of the depressurization process, for when the pressure difference has fallen, and surface bubbling ceases, further desorption can then only take place by diffusion. The subject of gaseous diffusion and mass transfer is discussed in more detail in section 3.10.

Following an abrupt fall in pressure, a pressure gradient is immediately set up between the total pressure at the surface and the partial pressure which was in equilibrium with the bulk. In this case, much of the gas is released by diffusing to the surface of bubbles which form in the bulk and rise to the surface to destroy the gas supersaturation caused within the liquid. The physical chemistry of such a process may be illustrated by carbonated beverages. Carbon dioxide is dissolved in an aqueous solution at a pressure of 3 bara, at which the volume of gas dissolved by unit volume of liquid (α) is about one for carbon dioxide in water at 15°C [75]. When the pressure is released, the concentration of dissolved gas in the bulk liquid is greater than at the surface, thus the partial pressure of gas which would be in equilibrium with the bulk liquid is greater than the partial pressure at the surface. The beverage releases an amount of gaseous carbon dioxide equal to twice the volume of the liquid, corresponding to the two bar drop in pressure. The mechanisms of gas molecule aggregation, spontaneous nucleation and bubble growth are discussed in section 3.9. As the pressurized gas escapes from the bottle, the temperature in the bottle neck drops. The kinetic energy of the escaping gas molecules doing work on the surroundings determines the temperature at the bottle neck. Indeed, the temperature may drop to as little as 240K, which is low enough to condense the water vapour at the neck, thus forming water droplets.

Once the initial pressure in the vessel has been released, on replacing the cap, the pressure in the gas space again builds up to a new equilibrium state, but without the occurrence of bubbling. If some of the beverage is then poured into a glass, the contents of the glass froth violently, yet the contents of the bottle remain devoid of bubbles. Left undisturbed, bubbles continue to be released until the beverage is flat. Fluid mechanics and the availability of nucleation sites play an important role in initiating and maintaining bubbling.

3.7 Bubble dynamics

The viscosity of the liquid, compressibility, surface tension, and heat and mass transfer all contribute to the phenomenon of bubble growth. The dynamics of bubbles in a liquid responding to an imposed pressure fluctuation have been considered with varying degrees of complexity, and equations describing how the radius of a single cavity changes with time, under the influence of imposed pressure changes, have been established. The theories of bubble dynamics, taking into account the fact that the boundary layer between the liquid and gas must be treated as a separate phase, with properties between those of the liquid and the gas, have been reviewed in a number of texts [76-78].

The theories, combined with time histories of the bubble radius, the vapour pressure and the gas pressure in the bubble and the pressure distribution in the liquid, together with the temperature profiles of the contents and the bulk liquid have revealed non uniform distributions of temperature and vapour concentration in the bubble during the growth and collapse of a bubble, owing to heat conduction through the interface. Indeed, the influence of internal phenomena, such as thermal diffusion, diffusion between vapour and gas, and heat and mass transfer through the bubble wall on the cavitation process has recently been demonstrated [79]. Other recent developments have included the derivation of equations to describe the collapse of clusters containing large numbers of cavities, in which bubble interactions result in the successive collapse from the outer boundary of the cluster, those collapsing first strengthening the collapse of successive ones [80-82]. Such theories and developments have demonstrated the complexity of bubble formation and collapse, and are beyond the scope of this study. Some basic knowledge of bubble dynamics is, however, necessary to describe the spontaneous growth of bubbles.

The process of bubble formation following the rapid depressurization of a liquid containing large amounts of dissolved gas is different from that which occurs when vapour bubbles are formed [78].

Formation refers to the creation of a new cavity, or the expansion of a pre-existing cavity to such a size where macroscopic effects can be observed. In the absence of any dissolved gas, i.e. vaporous cavitation, a bubble is formed in the body of a liquid by the vaporization of molecules of the liquid into a cavity, which may be considered as any space within the liquid phase unoccupied by liquid molecules, either empty or occupied by vapour. The cavity may be the space vacated by a liquid molecule from its equilibrium position, formed under the influence of localized thermal fluctuations. When a certain critical bubble size is reached, the bubble grows spontaneously without requiring further vaporization of molecules into it.

When the growth of a bubble is determined by the diffusion of dissolved gas into the bubble from the surrounding liquid, the cavitation is called gaseous cavitation, and is not as explosive as in the case of vaporous cavitation. Gas comes out of solution when the partial pressure of gas in the bubble, p_g, is less than the equilibrium pressure of dissolved gas in the solution. The growth can be brought about by a reduction in pressure or a rise in temperature.

As with the onset of vaporous cavitation, the diffusion of gas out of solution to generate gaseous cavitation, or the growth of gas filled bubbles involves a critical pressure. This pressure depends on both the size of the bubbles in suspension and the concentration of dissolved gas. For example, in a fully saturated solution of gas in water at a pressure of 1 atm and relatively large bubbles in suspension, any reduction of the pressure below 1 atm will cause the gas to diffuse out of solution and the bubble to grow to macroscopic size [77]. In the case of very small bubbles, however, with a smaller surface area across which diffusion may occur, a reduction in ambient pressure to somewhat less than 1 atm will be required.

One complication arises in that it is not yet possible to distinguish between the amount of gas and the amount of vapour in a cavity. The vapour pressure inside a cavity can be calculated using the Kelvin equation [174]

$$p_g = p_l\, e^{(\frac{-2\sigma V_m}{rRT})} \tag{3.22}$$

where p_g is the pressure of gas in the bubble, p_l is the ambient liquid pressure, σ is the surface tension of the liquid-gas interface, V_m is the molar volume of the liquid and r is the radius of the bubble.

In the case of droplets of water of radius 10^{-3} mm, the ratio p_g/p_l is approximately 1. Such a value shows that the effect is usually small. In the present study in which the liquid is saturated with gas, only dissolved gas in the bubble really need be considered in the spontaneous bubble formation process which occurs after the saturated liquid-gas solution is rapidly decompressed. In this type of experiment, the bubbles consist mainly of dissolved gases, assuming the temperature is not too high, since the vapour pressure of the solvent is very small compared to the equilibrium gas pressure. The vapour pressure becomes more significant at increased temperatures due to the lowering of the surface tension. The rate of growth and collapse of bubbles containing dissolved gases may be expected to be much slower than that of bubbles containing a single vapour phase.

The condition necessary for a gas bubble in equilibrium with a liquid, is given by

$$p_g = p_l + \frac{2\sigma}{r} \qquad \textbf{(3.23)}$$

In general, the gas pressure, p_g, is the combined sum of partial pressures of solvent molecules in the bubble (vapour pressure), p_v, and the corresponding quantity for the solute molecules (the total equilibrium partial pressure of gas which is dissolved in the liquid), p_s

$$p_g = p_v + p_s \qquad \textbf{(3.24)}$$

During the bubble motion the gas is compressed or expanded so that the partial pressure varies with the bubble radius. The critical radius, r_c, required for stability is

$$r_c = \frac{2\sigma}{p_g} - p_l \qquad \textbf{(3.25)}$$

It follows from eqn 3.25 that for $r < r_c$, the surface tension dominates and the bubble contracts, and at $r > r_c$, the gas pressure, p_g, dominates and the bubble expands indefinitely. In fact, a bubble in a liquid is never in equilibrium. Gas phases larger than the equilibrium size ($\sim 1\mu$m in radius) float to the surface due to buoyancy effects, while the smaller bubbles should dissolve within a few seconds due to the surface tension. Even the one radius at which a bubble would be in equilibrium is unstable. The following section looks at the theories proposed to explain how spherical gas phases are small enough to remain in solution yet strong enough to resist collapse.

3.8 Theories for the pre-existence of microbubbles

Although it is now generally accepted that bubble formation in aqueous media is initiated by the presence of stable gas nuclei in the liquid, there still remains a certain amount of controversy as to how large numbers of microbubbles or pockets of gas can exist in solution, especially as their detection is very difficult. The two difficulties which arise in attempting to explain how microbubbles can exist in the liquid for substantial periods of time, are that either the surface tension would cause these bubbles to dissolve, or the internal pressure would cause the bubbles to grow and rise to the surface.

There is, however, some evidence for the existence of a large number of minute spherical gas bubbles. Solutions of gases in water can be kept in a state of high supersaturation in the absence of gas nuclei [83], requiring external agitation to form bubbles. The actual tensile strength of water is difficult to determine, since it is more than likely that bubble formation begins at the wall of the container, which represents the weakest spot of the system, rather than in the bulk liquid. Theoretical calculations of the tensile strength of 'pure' water give values of around 1000 atm. Ordinary tap water, and even distilled water samples, when measured experimentally, form visible bubbles following the application of tensile or supersaturation pressures as low as 1 atm. The large discrepancy between the theoretical tensile strength of a pure liquid and the actual tension required to initiate bubble formation can be explained by the existence of cavitation nuclei which significantly lower the cavitation threshold [84,85]. It is also accepted that the application of a large positive pressure of ~ 1000 atm for a period of ~half an hour, to a liquid significantly raises the bubble nucleation threshold by eliminating the cavitation nuclei in the liquid, therefore withstanding a greater tension before it cavitates. Experiments with the Berthelot tube [86] have achieved tensile stresses up to ~300 atm. Once the nuclei have been removed from the liquid, the liquid remains denucleated for a substantial period.

The question still remains, therefore, as to how the large number of minute spherical gas bubbles can exist in a liquid. Two models have been proposed which explain the presence of nuclei in the liquid. The widely accepted theory behind crevices in the container walls and in suspended particles was first introduced by Harvey, and can be found in a number of texts [76,78,87]. Harvey suggested that very small gas bubbles could become stabilized in cracks and crevices in the container surface or on the surface of imperfectly wetted, small solid particles in the liquid, of which there are many thousands per cubic centimetre in tap water [78]. Indeed, investigations using a scanning electron microscope to observe the surfaces of solid impurities ($< 3\mu$m), clearly illustrated the numerous potential nucleation sites on the ragged surfaces [88], whilst interference photomicrographs of the surface of a finely polished stainless steel pressure vessel [89], showed conical pits about 1.5μm in size, and scratches about 1μm in width and up to a few mm in length.

A pocket of gas trapped in a crevice can exist in stable equilibrium. As the liquid is subjected to a negative pressure, a critical stage is reached when the pressure of the trapped gas combined with the negative pressure in the liquid overcomes the inward stress due to the surface tension. At this stage the interface (convex on the liquid side) is drawn out of the crevice and breaks off to form a cavity in the liquid. If the liquid is subjected to pre-pressurization the interface becomes concave on the liquid side, and is forced deeper in to the crevice. As this happens some of the gas diffuses across the interface into the liquid. When the pressure is then reduced, the pocket of gas is smaller requiring a greater tension (negative pressure) in the liquid to cause the cavity to grow from the crevice.

Kenning [90], carried out a study into the bubble nucleation characteristics of surfaces, and found a lack of reproducibility in the nucleation processes from a cleaned stainless steel surface under constant conditions. A few sites would remain active and then disappear while other sites became active. On cleaning the surface and repeating, active sites disappeared whilst new sites appeared. Artificial sites were made, firstly by soldering a metal foil containing an optical pinhole 12.5μm in diameter to the surface and then by drilling directly into the stainless steel surface to produce a hole 25μm in diameter. Neither method produced any bubbles, which is not too surprising since the essence of a natural crevice is that it is vee-shaped (conical). In addition, on surfaces which would be expected to possess large numbers of nucleation sites, only small numbers of nucleation sites were observed ($\sim 5/\text{cm}^2$). Different conditions were investigated using different metal surfaces, roughened and polished surfaces, by treating the water, and by varying the procedures for filling the rig. None of these led to an increase in the number of sites nor in improvement of reproducibility. Kenning suggested that clean well-wetted metal surfaces actually possessed few nucleation sites, and that the rewetting rate of a surface could affect the number of available sites.

A theory recently proposed by Morch [91], could be used to explain why nucleation starts at the vessel walls if, indeed, there are few nucleation sites available. Scanning tunnelling microscopy (STM) was used to investigate if cavitation nuclei could be distinguished at the interfaces. Morch suggested that when the solid surfaces were studied by microscopic techniques, which tunnel or scan the surface, they did not exhibit cracks or conical holes. Oxide layers and contamination covered the surface forming a more or less smooth structure. Morch also suggested that near the surface, water has a structure similar to that of ice, which is particularly significant at liquid-solid interfaces, where voids appear due to the imperfect match between the two crystalline planes of the vessel wall and the well defined liquid structure. The suggestion that surfaces in contact with water are smooth was further investigated [92]. A direct STM comparison of non planar solid surfaces exposed to air and water at identical locations, in order to determine the effects of water on the surface topography, did indeed show smoother surfaces in water. Whilst it might be argued that the smoothness of the surface in water compared with the same surface in air was due to a larger tip-to-specimen distance in water than air, Morch claimed that this was insignificant and considered the recorded smoothness to be real. A number of experimental findings, such as Kenning's work, which could not be satisfactorily explained by previous models, could be explained by this model, based on consideration of the water structure due to intermolecular forces at the free surfaces and interfaces.

The alternative theory is the stabilization of the gas bubbles against gaseous diffusion by an immiscible skin of organic impurity, such as fatty acid in water or protein in oils. The elastic skin, composed of surface active molecules surrounding the gas bubble, formed by adsorption onto the surface, gradually thickens as the bubble decreases in size until it becomes sufficiently rigid to inhibit any further shrinkage of the bubble, thereby providing the compression strength necessary to resist collapse and gas loss into the liquid, thus stabilizing the bubble. This model for stabilizing gas nuclei was further developed and modified by Yount [93,94], who used light and electron microscopy to investigate bubble formation, and was able to provide evidence for spherical gas microbubbles. The varying-permeability membranes are usually gas permeable, but when subjected to large compressions, exceeding ~8 atm, they become effectively impermeable. At a later stage, subjected to tension, the skin will be torn apart, followed by diffusion of gas into the bubble. The theory of organic impurity is valid for an air bubble in water [95], but for other liquids, such as hydrocarbons, which also show cavitation behaviour, the bubble is believed to have a protein skin, since this would not dissolve in an organic liquid.

There is evidence to support both theories. Gas filled crevices can act as nucleation sites and are believed to be the main factor responsible for the occurrence of bubble formation on solid surfaces and container walls. The theory behind crevices in the walls has long been established, and will certainly play a role in explaining the nucleation phenomena in the vessel, as the presence of numerous pits and crevices in the inside walls, which may act as potential nucleation sites has been confirmed using a scanning electron microscope. A selection of photographs taken of the inside walls of the stainless steel pressure vessel are shown in plate I. Crevices up to a few mm in length were measured, and in some areas, the surface actually appeared to have a flaky texture. Photomicrographs of the surface of the 5μm uni-sized silica flour particles, used in the experimental programme to investigate the effect of solid impurities on the gas evolution process, can be seen in plate II. There is still some uncertainty as to whether gas filled crevices in suspended particles or spherical bubbles surrounded by a varying permeability membrane or a combination of the two are responsible for bubble formation in the bulk. The crevice theory appears to be more realistic, although there is still a limited knowledge of the mechanism of nucleus generation.

3.9 Bubble nucleation

Spontaneous nucleation of bubbles occurs when a saturated liquid at high pressure is rapidly decompressed. The phenomena of bubble nucleation plays an important part in the depressurization process, for the rates of gas release from the liquid are too rapid to occur by diffusion. The extremely rapid growth of vapour bubbles in the liquid can be explained by nucleation, both homogeneous and heterogeneous. Following the sudden release of pressure above the liquid, a depressurization wave is created at the liquid surface which propagates down into the bulk liquid. The pressure in this wave falls from the pressure, p_i, to a value well below the saturation pressure. The progression of the nucleation front through the liquid occurs at a substantially lower rate than the sonic velocity. Thus for a certain amount of time the liquid is in a metastable state before the nucleation process is triggered.

The first step in forming a macroscopic bubble within a liquid is the grouping of several dissolved molecules to form a cluster. Nucleation occurs when a cluster of two, three, or some other small number of particles grows to a size large enough that it then continues to grow rather than shrink. Depressurization is stopped abruptly by the explosive and extremely rapid growth of these clusters, which, in turn, causes a sharp increase in pressure. The clusters spontaneously expand, for a given driving force p_i-p_f, until the critical size is reached allowing the gas to come out of solution. A critical size nucleus is a cluster of such a size that its rate of growth is equal to its rate of decay, and only clusters larger than a certain size are likely to grow rather than decay. A snapshot of molecules present in a supersaturated state would show small clusters of a new phase containing two or more molecules, as well as occasional clusters containing larger numbers. Most of the larger clusters are short lived, rapidly growing and shrinking. In dilute solutions the concentration of trimers and dimers are less than the concentration of monomers. The low concentration of trimers suggest that clusters rarely collide. As a result it is generally accepted that clusters grow by the addition of single molecules [96].

Where the bubbling is initiated depends on the presence of nuclei in the liquid. In the absence of nuclei, bubble formation starts from the liquid surface and travels downwards. When potential nucleation sites are present in the vessel, such as crevices and pits in the vessel wall, on projections into the vessel and on impurities in the liquid, nucleation starts where these nuclei are highly concentrated. The thermodynamic disequilibrium and extent of the limit of supersaturation depends on the number and character of nuclei in the vessel. Nucleation rates are extremely sensitive to small changes in conditions such as temperature, pressure and presence of impurities, making calculations of nucleation rates quite difficult. In order to have more control over the nucleation rates, a greater understanding of the microscopic events occurring is required. Indeed, nucleation experiments provide a very sensitive probe of microscopic events. Phase transitions generally occur in an irreproducible fashion as a result of the variety and number of heterogeneous nuclei that are present. It is therefore quite difficult to accurately characterize crucial experimental parameters, except in experiments specially designed to study homogeneous and heterogeneous nucleation.

The original theories mentioned in the following section refer to vaporous nucleation, for the presence of dissolved gas significantly changes the pressure at which nucleation occurs. For a given solvent, the value of p_i-p_f for the spontaneous bubble formation depends on the solute gas [97]. The effects of dissolved gas on bubble nucleation are discussed in section 3.9.3.

3.9.1 Homogeneous nucleation

Homogeneous nucleation only occurs in the heart of the bulk liquid, where the influence of any interface in the system is negligible. The new phase arises spontaneously because of thermal fluctuations and intermolecular interactions. In the absence of nucleation aids such as the container walls and particles, the formation of the initial vapour bubbles which are of such a size that they are in thermodynamic equilibrium with the surrounding liquid occurs by the random molecular processes proposed by homogeneous nucleation theory.

The energy, rate of formation and growth of such 'critical size nuclei' strongly depends on the physical properties of the liquid in which the bubbles form. The rate of nucleation depends on the temperature and the supersaturation i.e. the ratio of the partial pressure of a pure substance to its equilibrium vapour pressure, for at supersaturations only a few percent below the critical supersaturation, no homogeneous nucleation occurs, whereas at a few percent above the critical value, very rapid nucleation occurs [98]. For pure liquids, the important physical properties are easy to predict, whereas those of mixtures cannot be predicted as easily.

The first complete theory of homogeneous nucleation, known as the classical theory, was developed by Volmer and Weber, and Becker and Döring to express the rate of formation of cavitation nuclei as a function of temperature and supersaturation and can be found in most nucleation texts [99,100]. The original approach represents the process as a fluctuation phenomena where small droplets, or clusters, overcome a Gibbs free energy barrier given by volume and surface tension. The kinetic part of the theory assumes that clusters grow or shrink via attachment or loss of single molecules, which is a reasonable approximation at low pressures where almost all the molecules are isolated monomers. The principle of microscopic reversibility states that at equilibrium, every forward process must be matched by its corresponding reverse process. The net rate, therefore, at which a cluster of size i, grows to size i+1, is the difference between the rate at which an additional molecule attaches to the cluster and the rate at which the cluster loses a molecule. The impingement of monomers onto the surface of critical size clusters transforms the thermodynamically unstable cluster into a more stable nucleus [96].

The Gibbs free energy of the system is a maximum for the critical size bubble and therefore the formation of a viable nucleus involves overcoming a barrier. Close to equilibrium, the phase remains metastable and fluctuations, such as thermal fluctuations, are required to cause the appearance of a new phase [100]. The rate of nucleation is dependent on the height of the free energy barrier. The height of the maximum is governed by the surface tension of the fluid and the difference between the vapour pressure and the ambient pressure. The pressure in a bubble of radius, r, is greater than the surrounding pressure by $2\sigma/r$, where σ is the surface tension of the liquid, as expressed in equation 3.23. The surface tension effectively controls the size of nucleus available for further growth.

As the temperature of a pure liquid is increased, the surface tension decreases and the vapour pressure increases. Both factors lead to a lowering of the barrier to bubble nucleation, and an increase of the probability of a bubble surmounting this barrier. The term, J, used in bubble nucleation theory represents the rate of formation of bubbles which surmount the barrier and continue to grow spontaneously. A condition for the formation of a critical bubble is given by the Laplace equation, given in equation 3.25, which states that the critical bubble is in mechanical, thermal and chemical equilibrium with the liquid, for which

$$\mu_l(p,T)=\mu_g(p,T) \tag{3.26}$$

The saturation line is defined by the equality of the chemical potentials relating to the liquid and the gas, and can be represented as the line on the phase diagram which decides the regions of stable and unstable states of the homogeneous mass.

The formation of a new phase requires an expenditure of work, which must be supplied by the environment surrounding the spot at which the nucleus will appear. A cavity will grow to a nucleus providing there is sufficient energy to supply the required work of nucleus formation, which can be written as

$$W=\sum(\mu_i-\mu_l)=\sigma A-(p_g-p_l)V \tag{3.27}$$

where μ_i is the thermodynamic potential of a bubble containing i molecules, μ_l is the thermodynamic potential of the liquid phase, and A and V are the surface area and volume of the nucleus, respectively.

Introducing the volume of the nucleus as

$$V=\frac{4}{3}\pi r^3 \tag{3.28}$$

and the radius as

$$r=\frac{2\sigma}{(p_g-p_l)} \tag{3.29}$$

into equation 3.27 and rearranging, gives the free energy, originally proposed by Gibbs, needed to form the critical size bubble

$$W=4\pi r^2\sigma-\frac{2\sigma}{r}(\frac{4}{3}\pi r^3)=\frac{4}{3}\pi r^2\sigma=\frac{1}{3}A\sigma=\frac{16\pi\sigma^3}{3(p_g-p_l)^2} \tag{3.30}$$

Therefore, the work of nucleus formation is dependent on the surface tension and size of the nucleus, which is greater within the bulk than at an interface.

The bubble nucleation rate, J, defined as the number of bubbles generated in a unit volume/unit time, can be written as [101]

$$J=N\left(\frac{\sigma}{\pi mB}\right)^{\frac{1}{2}}\exp\left[-\frac{16\pi\sigma^3}{3kT(p_g-p_l)^2}\right] \tag{3.31}$$

where m is the mass of a molecule, and B is the pre-exponential constant, which is determined by the number of molecular collisions with the nuclei surface and the monomer concentration, and is constant with varying external conditions and substrate. It is generally assumed that experimental observation of bubble nucleation in a liquid is possible when the nucleation rate is between $J=1$ and $J=10^6$ bubbles/cm^3 sec.

In simplified terms,

$$J=ND\exp\left(-\frac{W}{kT}\right) \tag{3.32}$$

where N is the number of molecules in a unit volume, D is the kinetic coefficient, k is Boltzmann's constant, T is the thermodynamic temperature and W is the work necessary to create a bubble capable of further growth.

The theory combines molecular dynamics of the cluster formation process with the thermodynamics of curved surfaces and the kinetic theory of gases, providing a simple physical model, relating the nucleation rate to interfacial tension and surface properties, to describe the formation of a new phase from a supersaturated phase in the heart of the bulk liquid. The theory is based on the assumption that the very small bubbles, which cause nucleation, can be described as if they were macroscopic, with a well defined radius. As a result, the cluster of molecules can be represented as a droplet whose properties, such as surface tension and density, are the same as the bulk liquid. The free energy is assumed to be the sum of two terms, a negative contribution proportional to the droplet volume, and a positive contribution proportional to the droplet surface area. The radius and free energy of the critical droplet which forms the barrier to nucleation can then be calculated as a function of supersaturation, and the rate can be found from the kinetic model for the rate of growth of a critical nucleus due to collisions with supersaturated molecules.

The classical theory is extremely useful in the quantitative understanding of nucleation, providing the rate equation for the appearance of particles of a new phase, and is attractive since the nucleation rates are predicted in terms of measurable macroscopic quantities, used to calculate the free energy barrier for the formation of microscopic nuclei. A major controversy, however, surrounded the nucleation theory, in relation to the free energy change associated with forming a critical nucleus, and whether terms in addition to the surface free energy contribution should be included.

Attempts were made to improve the classical theory [102,103], although they were not too successful. It was suggested by Lothe and Pound [102], that a nucleating cluster should be treated like a large molecule, having translational and rotational degrees of freedom, and therefore additions should be made to the free energy of the cluster to account for the kinetic energy contributions from the rotational and transitional movements. In doing so, the nucleation rate increased by factors ranging from 10^{14} to 10^{20} compared to the conventional theory, therefore worsening the agreement between theory and experiment. Reiss [103] argued that the use of the surface tension in the approximation already included most of the fluctuation effects in the centre of the mass and the rotation of the liquid-like cluster, and therefore the Lothe and Pounde theory double counted certain contributions to the free energy. The corrections made by Reiss reduced the difference between theoretical and experimental to a factor of 10^3. Workers have supported both the Lothe-Pound theory and the Reiss-Katz-Cohen theory and indeed the classical theory, but the controversy has still not been completely resolved [104,105].

Major breakthroughs in the understanding of nucleation and in the prediction of nucleation rates have only really occurred in the last decade, for recent advances in experimental technique have enabled nucleation rates to be measured directly and recorded with greater accuracy, allowing theories and modifications to be tested and compared to reliable and reproducible data. Several comprehensive sets of data for the isothermal rates of homogeneous nucleation in water and other solvents, as a function of supersaturation, measured over a range of temperatures and rates, $10 < J\ cm^{-3}s^{-1} < 10^8$, now exist [106-110], and indeed, several systematic deviations from the behaviour predicted by classical theory have been revealed. The classical nucleation theory was found to consistently underestimate the nucleation rates by 1-2 orders of magnitude and in some cases, the difference between measured and predicted nucleation rates was found to be several orders of magnitude. The data showed that the classical theory failed to account for the correct temperature dependence of the nucleation rate, for there appeared to be a weaker dependence on temperature than predicted by the classical theory. Absolute agreement was observed between theoretical and experimental rates for a temperature close to 300K, but at high temperatures the predicted rates were too high and at low temperatures, were too low. This was also observed for solvents other than water. The theoretical explanation has yet to be discovered, and theories are still being developed, both modifications to the classical theory and proposals for new models, in an attempt to explain the temperature dependence of the nucleation rate. One approach was to introduce a temperature dependent correction factor to the classical theory, with apparent success [111,112].

As the question of which free energy terms should be included remains unanswered, new theoretical approaches using microscopic molecular interactions have been developed which leave out the macroscopic assumption altogether, and are hence termed as the non classical approach. Such theories have included, for example [113,114], using density functions with potential perturbation theories rather than droplet radius functions to calculate the free energies of small droplets in unstable equilibrium with their surroundings. The density functional theory thus provided a means of evaluating the work of formation of the critical nucleus together with the excess number of molecules in the nucleus, simply by calculating the density profile of that nucleus. These more realistic theories take into account the finite size of the critical nucleus and the effects of curvature on the surface free energies of clusters. Indeed, in comparing classical and non classical theories, the non classical approaches [113-117], which allow for translational, rotational and vibrational degrees of freedom of a cluster as well as the variation of surface tension with cluster size, give better predictions of observed nucleation rates in water and various hydrocarbons, as a function of supersaturation and temperature, than the classical theory.

Another recent and significant development was proposed by Oxtoby [96], who, by focusing primarily on the rates and mechanisms by which small clusters of the new phase gained and lost particles, proposed a theory relating the variation in the work of formation of a critical nucleus with the size and composition of that nucleus. Since the theory did not rely on either the classical theory nor the macroscopic assumption, it could be applied to very small critical nuclei containing only a few molecules, which in itself, is significant, because the theories based on macroscopic properties, in terms of surface energy and density, cannot be expected to describe clusters containing only a few particles. Similar calculations [118], which did not include the surface tension and were therefore not limited in size range, also showed close agreement with experiments.

Despite efforts to obtain accurate experimental data and to develop theories and computer simulations of simple systems to describe the nucleation process, homogeneous nucleation is still not fully understood. Large discrepancies still exist between the threshold nucleation conditions predicted theoretically and those indicated experimentally. The theoretical approach has been hampered by inadequate understanding of many of the submicroscopic and molecular properties of the liquid, and experimental approaches have been hampered by the difficulty in controlling the interference from these pre-existing nuclei and in characterizing the cavitation due to vapour and that due to dissolved gas.

Until recently the theories have only really considered single component strongly non ideal mixtures, as opposed to binary mixtures. In addition, neither events in which pre-existing clusters collide and fuse, nor events in which clusters may break into smaller clusters have really been investigated in any great detail. In fact, only recently has it been suggested that the wave action and motion of neighbouring non critical bubbles may affect the rate of nucleation, due to the lowering of the local liquid pressure and the critical work required for cluster formation [119]. The latest research into homogeneous nucleation has also investigated the effects of background gases on the nucleation of vapours [120], in which it was suggested that at elevated temperatures and pressures, the presence of a secondary gas may be significant and may need to be incorporated into the existing theories since at the low pressures used in the original theories, it was assumed that the presence of a second gas could be ignored.

New and modified theories are continually being published and reviewed [121-123], although many have not yet been widely accepted. As a result, the classical theory is still the only widely accepted method to predict the nucleation behaviour of real substances at least in a qualitatively correct theory, and in predicting the supersaturation limit of liquids with nucleation rates of $J = 10$-10^8 bubbles/cm^3 sec.

3.9.2 Heterogeneous nucleation

Nucleation usually occurs at the walls where there are surface imperfections. Rough surfaces, sharp edges, grooves or points do not cause the release of supersaturation as such, since gas evolution and nucleation takes place in molecular dimensions and therefore cannot be connected with macroscopic roughness [101]. The real cause for rough surfaces enhancing bubble formation lies in the fact that they more easily retain entrapped air bubbles or greasy contaminations which are the primary causes for gas nucleation.

Heterogeneous nucleation is more common than homogeneous nucleation, for it occurs at temperatures well below that for homogeneous nucleation and at lower degrees of supersaturation.

It is, however, a more complicated phenomena to explain. As a result, the equations developed for homogeneous nucleation may be in error when applied to heterogeneous nucleation, for the nucleation rates may be determined by, for example, the detachment rate of the bubbles from the surface, which, if slow, may be the rate determining step. Another limiting factor may be the size of the contact angle. If the contact angle is large, favouring the formation of a critical sized bubble, the bubble will have more difficulty in becoming detached from the surface, and whilst the growing bubble is attached to the nucleation site, no further nucleation can take place there. For small or indeed zero contact angles, nucleation becomes more difficult. Once a certain threshold level is achieved, the contact angle is no longer a function of the cluster size, and is thus a thermodynamic property. Under the same conditions, homogeneous nucleation occurs at a much slower rate than heterogeneous nucleation, causing a significant lowering of the overall rate of bubble release.

Although more attention has been focused on the processes of homogeneous nucleation, most materials actually nucleate heterogeneously, upon impurity sites. The study of heterogeneous nucleation is hindered by the lack of control of material impurities, but it is necessary, particularly in systems which do not appear to exhibit homogeneous nucleation. In order to study heterogeneous nucleation, the number and size distribution of effective heterogeneous sites must be determined.

Heterogeneous nucleation was studied in an orderly fashion [124] by the introduction of small concentrations of noble metal salts into the liquid which form metallic particles on heating, serving as effective heterogeneous nucleation sites. The number and size distribution of such particles can be determined experimentally. The influence of multiple nucleation events on impurities on the overall heterogeneous nucleation rate was studied, for it was proposed, that whereas one nucleation event per site was generally assumed, if the critical radius was small compared to the radius of the nucleating particle, then multiple nucleation events could and did occur. The effectiveness of the spherical nucleating particle was shown to be a strong function of the ratio of the particle radius to the critical nucleus radius (when the ratio was less than 10), decreasing as the ratio decreases. Investigations into the size and surface properties of a spherical nucleating particle, with respect to the nucleation efficiency [125], demonstrated that size becomes important in the 10-100 nm particle radius. For larger values of the ratio, the nucleation efficiency becomes independent of particle size.

Ward [126,127] looked at the conditions under which heterogeneous nucleation takes place in a conical pit, and was able to predict the size to which the bubbles grew. In fact, Ward proposed there to be four possible equilibrium states in the process of heterogeneous nucleation from a conical pit, based on thermodynamic potentials. The existence of two unstable, one metastable and one stable state was proposed, rather than just the one unstable equilibrium state, corresponding to the smallest equilibrium size, in the case of a bubble in an unbound volume of a liquid gas solution, as proposed by Gibbs. Previous workers had considered bubble nucleation in a conical pit [101], but did not consider the thermodynamics in enough detail to identify the equilibrium states.

The stability of the bubble was predicted on the basis of a property of a liquid-gas solution, that being the critical radius, r_c. The nature of the state was determined by examining whether the thermodynamic potential at the equilibrium state, for which the radius, r, is equal to the critical radius, is a minimum, a maximum, or a point of inflection. Ward proposed that the unstable state represents the threshold size which must be exceeded in a nucleation event, whilst the second unstable state is encountered as the bubble emerges from the pit. When the gas-liquid interface reached the mouth of the pit, the bubble was considered to be in a metastable state, whilst the stable state corresponded to the largest equilibrium size of the bubble.

The classical nucleation theory, therefore has been modified by various workers to produce equations corrected for heterogeneous nucleation, to account for the decreased activation energy of the heterogeneous nucleation sites. Treating the intermolecular and vibrational motions between water molecules in a similar manner to that for homogeneous water clusters, the energy of formation of water clusters attached to a foreign particle surface can be evaluated. As long as the nucleation is initiated by molecular disturbances, as indeed it is, the critical work, calculated from equation 3.30, being much lower for heterogeneous nucleation compared to the value for homogeneous nucleation, can be multiplied by a correction factor ϕ, to reduce it to a conventional homogeneous nucleation value [128], such that

$$W' = W\phi \tag{3.33}$$

The heterogeneous nucleation factor is a function of the contact angle between the solid surface and the interface of a critical cluster which grows on it. In practice, ϕ reflects the percentage of the bubble surface exposed to the liquid, i.e. how well the critical cluster is protected by the wall and therefore the type of nucleation can be defined by [129]

$$\phi = 1 \qquad \textit{homogeneous nucleation} \tag{3.34}$$

$$1 > \phi > 0 \qquad \textit{heterogeneous nucleation} \tag{3.35}$$

The factor, ϕ, can be calculated from experimental data. The state in which $\phi < 1$, implies that the molecular clusters formed on a rough surface or suspended particles need less energy to survive. In other words, ϕ accounts for the role of the wall and impurity surfaces which can protect the nuclei. The value of ϕ is well defined for an isolated bubble, but not so for bubble swarms [130], since it is statistical in nature and becomes difficult to determine for more than one bubble. There are also other effects making ϕ more difficult to predict, such as the irreproducibility of nucleation sites on the surface, as discussed by Kenning [90], who showed the importance of surface roughness, cavity size, shape and wetting characteristics.

The correction factor has been calculated for water for a number of controlled pressure releases, up to 0.3 Mbar/sec [129,131], using previously published experimental data [132]. In order to quantify ϕ, the calculated value of ϕ was correlated with the rate of depressurization and the initial temperature of the liquid. A typical value of $\sim 10^{-3}$ was obtained. The results showed that the heterogeneous factor, ϕ, was strongly dependent on both the rate of depressurization and the ratio of the initial liquid temperature and the critical temperature of the liquid, which is not too surprising since both factors affect the size of the critical cluster characterized by

$$r_c = \frac{2\sigma}{\Delta p_{sat}} \tag{3.36}$$

The temperature dependencies arise through the surface tension and the molecular energy. Since ϕ is a geometric factor associated with the contact angle between the critical bubble and the surface [129] it is clear that as r_c changes, so will ϕ. Therefore, ϕ depends not so much on the rate of pressure release in the vessel, but more on the pressure and temperature at the point where nucleation is most dominant, which is generally when the pressure is a minimum.

3.9.3 Effect of dissolved gas on bubble nucleation rates

The presence of dissolved gas significantly changes the pressure at which nucleation occurs. Theoretical and experimental studies into the effects of dissolved gases have been carried out by several workers [133-143]. Ward discussed the role of dissolved gases in the homogeneous nucleation of the gaseous phase, both experimentally and theoretically [133,134], and showed how the thermodynamic potential, eqn 3.30, required for the formation of a nucleate bubble, changed when a dissolved gas is present in the liquid. The format of the equation is the same as that for a pure liquid. The difference, however, is in the expression for the critical radius. The presence of dissolved gas significantly reduces the value of the critical radius compared with that for the pure liquid, thus changing the conditions under which nucleation occurs.

The major reduction in the value of the critical radius stems from an additional term, which appears in the presence of a dissolved gas, and is related to the partial pressure of the gas inside the nucleate bubble. A homogeneous pure liquid becomes metastable i.e. goes into a state in which the nucleation of a new phase is possible, only when the pressure is reduced below the saturation or vapour pressure. The dissolved gas changes the conditions under which a liquid phase is metastable, and therefore reduces the extent of supersaturation to which a liquid can be subjected without nucleation. The regions in which the liquid is metastable are expanded, compared to those of a pure liquid, and therefore nucleation can occur at pressures above the saturation pressure where in a pure liquid, the state is still stable. Indeed in some cases, homogeneous nucleation was predicted and shown to occur at pressure above the saturation pressure.

Ward assumed, however, that the dissolved gas affected only the total pressure in the critical bubble nucleus, and did not take into account the effect on the surface tension by the dissolved gas, nor the change in the rate of nucleation by the dissolved gas. Mori [135] also carried out an experimental study, using CO_2 in liquid freon, isobutane and propane, making a slight adjustment for the change in surface tension, into the effect of dissolved gas on the supersaturation limit of the liquid, which was then compared to predictions of bubble nucleation. Again, the results showed that with an increase in dissolved gas content, homogeneous nucleation occurred at lower temperatures, and in the presence of sufficient dissolved gas, at pressures above the saturation pressure of the pure solvent.

It is, however, difficult to precisely establish the minimum saturation pressure necessary for spontaneous cavitation and to know the supersaturation (saturation pressure - decompression pressure) which exists in the liquid at the moment of nucleation due to the lack of detailed pressure measurements during decompression and the time delay between the moment of nucleation and the moment of first detection.

Whereas Ward studied the behaviour of a single gas, N_2 in previously degassed ethyl ether, Hemmingsen performed experiments using water supersaturated with Ar, O_2, N_2 and He [136,137]. To achieve the conditions in which the interference from pre-existing nuclei was minimized, the nuclei were subject to dissolution under 1000 atm pressure, prior to saturation of the water. As a result, high supersaturations (170-300 atm) without any cavitation were possible.

Bubble formation was observed during and after decompression from high (100-300 bara) to atmospheric pressure. Again, the results showed that the concentration of dissolved gas played a significant role in the cavitation process. It was apparent that Ar and O_2, which have similar solubilities, showed similar cavitation properties and required lower degrees of supersaturation, before cavitation occurred, than that for N_2, which has approximately half the solubility of O_2 and Ar. The increase in stability with decreased concentration was similarly evident with He, which has the lowest solubility. The maximum supersaturation tensions without cavitation, which represent the lowest possible limit of spontaneous bubble formation, were 140 bara for O_2 and Ar, 190 bara for N_2 and 300 bara for He.

Yet it was necessary to consider other factors, such as water properties, since certain additional results could not be put down to the presence of dissolved gas. The supersaturation tensions of, for example, N_2 changed only slightly in ethanol, in which N_2 is ~ 9 times more soluble. In addition, the observed effect of temperature on the cavitation did not reflect the increase in gas solubility with decreasing temperature, for over the temperature range 5-40°C, only a small change in cavitation properties was observed. The evidence also pointed to the fact that, in the absence of pre-existing nuclei, spontaneous nucleation was originating from the water-glass interface rather than in the bulk, for which no explanation could be given other than it may be due to weak spots of adhesion at the water-glass interface. Experiments were not carried out using other interfaces, which could have provided an explanation.

A model based on these results was developed [138], which predicted the pressure reduction required for the threshold of bubble formation, which showed good agreement with experiments for various gases in water. A model was also proposed by Finkelstein [139] to predict the tolerable degree of supersaturation of gas-water solutions, based on the key parameter associated with bubble nucleation, that being the difference between the initial saturation pressure and the pressure at which bubbles first appeared when the pressure was gradually released from equilibrium. The correlations fitted well with the results obtained for the gases tested by Hemmingsen, showing that the decrease in pressure below the saturation pressure required to induce bubble nucleation was characteristic of the gas. In addition, the values were not influenced by temperature, solution density, presence of electrolyte, the initial pressure from which the pressure release began, nor indeed, the gas solubility, for the concentration of dissolved gas increases with increasing pressure, yet the pressure difference for that particular gas remained constant.

The model proposed, was of a liquid at rest, in which clusters of gas molecules serving as nuclei for bubble formation, exist as a concentration dependent upon temperature. A spherical region, of radius, r, centred on the cluster, surrounds each cluster, from which, at nucleation, molecules are driven towards the cluster, aggregate and form a bubble. The radius was found to be characteristic of water. Below the critical pressure difference value, the process takes place by diffusion of gas molecules to the cluster. At values above the pressure difference required for bubble formation, the nature of the process changes to one of forced convection, as a result of the pressure differences set up in the liquid between the gas molecules dissolved in the water, which is equal to the initial equilibrium pressure, and the pressure inside the bubble, which is equal to the total pressure above the solution at the point when the bubbles appear.

The diffusional mechanism for the process of gas entering the cavity during the spontaneous gas bubble nucleation in supersaturated solutions, which occurs when ready nuclei are not available, was also considered by Chirkov [140,141]. A theoretical model was proposed for the probability of spontaneous nucleation, based on the timescale required to gather gas by diffusion into a nucleus and the lifetime of a cavity filled with vapour, taking into account the fact that because of the low gas concentration in the liquid, the gas must be gathered from large solution volumes.

The surface tension did not appear to play such a major role as suggested by Hemmingsen. Similar conclusions were reached by Rubin [142], again using N_2, whose results showed that surfactants greatly reduce the surface tension of aqueous solutions, but have little effect on the thresholds for homogeneous nucleation in bulk solution. Indeed the nucleation thresholds in various solvents showed little correlation with either the surface tension or the viscosity.

The work discussed so far, has investigated the effects of dissolved gas on spontaneous homogeneous nucleation in supersaturated solutions in the absence of pre-existing nuclei. In contrast, Wilt [143] studied the effect of dissolved gas on both homogeneous and heterogeneous nucleation, in which, at these lower supersaturations, the number of bubbles is relatively small, and nuclei play a major role. Homogeneous and heterogeneous nucleation rates on smooth surfaces and conical and spherical cavities and projections were calculated for water solutions containing dissolved gas. Using the equations derived for homogeneous and heterogeneous nucleation, together with the modification to r_c, as suggested by Ward for the presence of dissolved gas, Wilt looked at the effect of dissolved gases on both homogeneous and heterogeneous nucleation. At a supersaturation ratio of 5, typical of a carbonated beverage, Wilt concluded, in terms of geometry, bubble radius and the work required to form a critical size bubble, that homogeneous nucleation cannot occur in an opened carbonated beverage, and also predicted that heterogeneous nucleation at a smooth surface, at conical or spherical projections will not occur, but will occur in conical cavities. Wilt also agreed with the theory proposed by Ward [126,127] in which more than one equilibrium state can exist in a finite closed volume of liquid-gas solution.

3.10 Desorption of gases and mass transfer

In the final two sections, bubble desorption is considered in terms of the overall rate of desorption from supersaturated liquids, which increases rapidly with increasing supersaturation, rather than on the mechanism of bubble formation and nucleation. This section briefly addresses the desorption of gases from liquids at low pressures, with small and gradual pressure changes, in which diffusion plays an important role. The following section, 3.11, which is more significant and indeed directly relevant to the study looks at rapid depressurization processes, in which the rates of evolution are many thousand times greater than evolution in quiescent conditions.

The desorption of gases from solution is an important mode of mass transfer. Gases do not readily desorb from undisturbed saturated or supersaturated liquids [144]. During, for example, a drop in pressure from the initial pressure to the saturation pressure of the liquid, no gas evolves and the solubility remains constant. Below the saturation pressure, the dissolved gas is liberated. The mechanisms of gas release, be it with or without bubbling, depend on the degree of supersaturation of the solution and depend very much on the rate at which the pressure is released.

In the absence of bubbling, mass transfer is purely diffusional. The mechanism is controlled by the rate of diffusion of gas through the liquid up to the liquid-gas interface and as a result, is considerably slower than the rate of gas evolved by bubble desorption. Indeed, desorption is up to 10 times faster than absorption owing to bubble formation [145]. With quiescent desorption, the partial pressure of dissolved gas is less than the total system pressure. Bubbling begins when the partial pressure of dissolved gas plus the vapour pressure of solvent exceeds the total system pressure [146]. For a CO_2 in water system,

$$r_p = \frac{(pCO_2 + pH_2O)}{p_T} \tag{3.37}$$

where r_p is the pressure reduction ratio. Although a small amount of bubbling occurs when the sum of the partial pressure of components is greater than the total pressure, bubbling does not effectively begin until the partial pressure of the dissolved gas alone, is greater than the total pressure. In other words, bubbling occurs when the pressure reduction ratio is ~1, but is only dominant when $r_p^* = 1$, where

$$r_p^* = \frac{p_{CO_2}}{p_T} \tag{3.38}$$

in which case the partial pressure of CO_2 in solution is much greater than the system pressure.

For some gases, such as air, with a slow reduction of pressure, quiescent desorption can take place for a pressure reduction ratio of up to 2 [147]. The same study showed that the transition from quiescence to bubbling was not observed using CO_2. With CO_2 desorption bubbling always occurred when the partial pressure of the dissolved CO_2 exceeded the system pressure, suggesting that p_{CO2}/p_T must be greater than one for desorption to occur. In focusing on the phase transition between quiescent and bubbling desorption, it became evident that the supersaturation is a major factor for determining the rate, and its importance increases with increasing liquid temperature.

The theory of mass and heat transfer and transfer of momentum between the phases is strongly dependent on the bubble size distribution. Studies of mass transfer coefficients during the desorption of CO_2 from liquids have shown that the liquid phase mass transfer coefficients for bubbles are increased by the presence of electrolyte in water [148,149], which can be explained due to the increase in interfacial area caused by the occurrence of small bubbles, owing to the coalescence hindering property of electrolyte solutions. Independent tests [150] demonstrated that with air bubbles less than ~450μm in diameter, there was no difference in the rise velocity of the bubbles in water or brine. For bubbles with diameters greater than 450μm, the velocity was indeed higher in pure water than in brine solutions. The rise velocity for CO_2 in water and other liquids has been shown to be generally independent of liquid viscosity, except for solutions with high viscosities (> 100 cP), which did cause some retardation especially with smaller bubbles [151]. The results of investigations into CO_2 and air bubbles with diameters ranging from 60 to 1200μm, rising in quiescent liquids [152,153] indicated that very small bubbles behaved like rigid spheres due to their surfaces being covered with surface active contaminants, an effect which decreased with an increase in bubble diameter.

In terms of the factors affecting the mass transfer coefficients, fluid agitation plays a significant role, since mixing induces more gas into the liquid and effectively shears large bubbles into several smaller ones, thus increasing the gas-liquid interfacial area and hence the mass transfer coefficients. The effect of pressure is still under debate [154]. The increase of pressure lowers the liquid surface tension due to the increased solubility of the gas and may reduce the liquid viscosity due to the increased dissolved gas. Since the mass transfer coefficient is inversely proportional to viscosity, an increase in the coefficient would be expected. On the other hand, higher pressures may shrink the gas bubbles, enhancing their coalescence, reducing the interfacial area and consequently reducing the mass transfer coefficient. Temperature effects are also inconclusive [154]. Higher temperatures increase the gas diffusivity and hence the mass transfer coefficient. Yet increased temperatures may promote bubble coalescence, thus decreasing the gas-liquid interfacial area and hence the mass transfer coefficients. The effects of temperature and pressure, therefore, are determined by the competing processes in the particular gas-liquid system. As a result, an increase in pressure or temperature may result in an increase, a decrease, or indeed, may not change the mass transfer coefficients.

The properties of the liquid and gas can also affect the mass transfer coefficients. Gases generally have higher mass transfer coefficients in water than in organic solvents. The gas diffusivities are higher in organic solvents than in water [155], suggesting gas bubble coalescence plays a significant role in organic solvents, resulting in the lowering of the gas-liquid interfacial tension and thus the mass transfer coefficients. In terms of the gas nature, it is generally found that the more soluble the gas, the lower the mass transfer coefficients. The main reason for this, is the fact that low solubility gases have a tendency to form a large number small rigid gas bubbles in the liquid resulting in a large gas-liquid interfacial area and hence higher mass transfer coefficients.

3.11 Rapid depressurization studies

Most studies of sudden high pressure reductions have been concerned with the potentially hazardous situations occurring as a result of the sudden rupture of hot water pipes in nuclear reactors. As a result, the data has generally been collected using small open ended pipes, with diameters of less than 50 mm. In these pipes, the rapid depressurization of the hot water from temperatures up to 300°C and rates up to 2 Mbar/sec, is halted or greatly attenuated by the explosive like generation of vapour bubbles in the liquid, leading to a steep short term rapid increase in pressure, ranging from 0.1 to 1 ms, followed by a relatively long period, ranging from 10 to 100 ms, of quasistatic pressure. The two most important parameters affecting the magnitude of the pressure drop below the saturation pressure, are the initial temperature and the depressurization rate. The nucleation of the bubbles was described by several workers using the homogeneous nucleation theory after introducing the correction factor, ϕ.

Alamgir [132,156] followed the initial response over the first 20 ms, of two pressurized hot water pipes ($\sim$1.3 and 5.1 cm ID) to sudden depressurization, using oscilloscope pressure-time histories under varying experimental conditions. The experiments involved initial pressures of around 150 atm, temperatures up to 300°C, and depressurization rates up to 1.62×10^6 bar/sec, achieved using a quick-opening plug mechanism. The initiation of depressurization is accompanied by the generation of a rarefaction wave that propagates away from the pipe break location. At any point in the pipe, the pressure starts to change upon arrival of this wave. Characteristic features of the pressure transients showed an initial slow pressure drop, which was put down to the initial slow movement of the plug, followed by a rapid fall, almost linearly with time, to well below the saturation pressure. The extent to which it is possible to depress a liquid beyond the saturation point depends on how quickly it is done and as a result of the rapidity of depressurization in these cases, the water reached pressures well below saturation before nucleation occurred. The drop in pressure below p_{sat} was correlated by the authors as a strong function of the initial water temperature and a weaker function of the depressurization rate in the supersaturated liquid, which in turn is a strong function of the initial pressure and temperature.

In most cases, following the rapid drop in pressure, bubble growth causes the pressure to recover, nearly exponentially with time, to a quasi-static level well below the saturation pressure, over a period of a few milliseconds. The level p_{qs} persists for $\sim$20 ms or longer. The pressure did not recover beyond 20 ms, as material was expelled from the pipe during depressurization. The time dependence of the pressure recovery process appeared to be related to the bubble growth rate, and to the gross liquid motion around the region of interest. The speed of the wave was measured from oscilloscope traces and found to be significantly faster than the speed of sound under the same conditions. A reason for this was suggested to be due to the heavy thick walled pipe surrounding the water, and hence the coupling between the liquid and the steel pipe wall, which was less for the larger pipe and hence a smaller velocity, although still faster than the speed of sound, was observed.

The study also looked at the water purity during rapid depressurization, in terms of boiling and comparing distilled and tap water, although the system response did not appear to be influenced in any way by the method of water preparation. Nor did the dimensional scale, in terms of the size of pipe, appear to influence the response, except with regard to a slight change in the rarefaction wave speed.

Bartak [157] carried out an experimental investigation into the rapid depressurization of hot water, from initial pressures of 80-160 bar and depressurization rates around 0.2 Mbar/sec, which closely simulated the geometric and thermodynamic conditions of a pressurized water reactor. A method was devised to calculate the pressure undershoot, i.e. the decrease of pressure below the corresponding saturation pressure. With a 90 mm ID pipe, the velocity of the rarefaction waves were within 20% of the local sound velocity. It was shown by Alamgir [131], that eqs 3.30 and 3.33 could be used to derive a correlation for the pressure undershoot if Gb, the Gibbs number, and ϕ were known, where

$$Gb=\frac{W'}{kT} \tag{3.39}$$

But whereas Alamgir made an assumption about Gb and calculated ϕ from experimental data, Bartak was able to develop a correlation for the unknown variable Gb/ϕ as a function of temperature and depressurization rate, which are the two most important parameters affecting the pressure undershoot.

An area which has been only been briefly addressed in the literature is the apparent 'finite' time between the saturation state of the liquid and the first appearance of detectable bubbles. Reasons for such delay times, ranging from 0.1 ms to 1.6 seconds in some cases, have been put down to the diffusion of dissolved gas towards the bubble nucleation sites, the finite time necessary for vapour to fill the cavity at which the bubble originates [158], and the metastability, irreversibility and the random nature of the state of the supersaturated liquid [99]. Kendoush [159] looked into the delay time during depressurization, after the liquid has passed through the saturation state up to the first appearance of detectable bubbles. He showed both experimentally and analytically, using water from initial saturation pressures of 3-60 bara, that the delay time decreased as the initial saturation pressure of water increased. The model proposed in the paper was based on the existence of a state of thermal non equilibrium during depressurization of the fluid, due to the growth of bubbles, which tended to destabilize the thermal equilibrium of the system. The simultaneous measurement of pressure and temperature transients enabled Kendoush to determine the degree of non equilibrium in terms of the difference in temperature between that measured, and the saturation temperature, corresponding to the pressure measurement. But he was unable to give a precise reason for the delay time, other than to confirm that the delay time decreased as the initial saturation pressure increased.

The time delay between nucleation and significant bubble growth for the rapid depressurization of distilled water, at 130°C, in a stainless steel vessel, was also noted by Wang and Bankoff [160,161] which they put down to the slow growth of microbubbles dominated by the surface tension, which becomes negligible for macroscopic bubbles. High speed motion photography was used to show that nearly all the initial bubbles were nucleated on the solid walls rather than in the bulk liquid. Bubble growth rates on a stainless steel vertical rod with a milled flat surface using deionized and distilled water were measured.

The main factor controlling the rate of growth of the bubble, was considered to be the degree of non equilibrium between the vapour in the bubbles and the bulk liquid. In the very earliest stage, as the bubble first starts to grow the rate is determined by the surface tension, but this becomes negligible before the bubble becomes visible to the naked eye. This is the slow growth period resulting in a time delay of several milliseconds between nucleation and significant bubble growth. The next stage is momentum controlled, and finally diffusion of heat through the thermal boundary controls the bubble growth. The final stage, whilst important for bubbles that are predominantly vapour filled, is considered less significant for predominantly gas filled bubbles. A bubble growth equation, taking into account the contact with the solid surface was developed. Again, empirical correction factors were introduced to the basic homogeneous nucleation theory framework, to account for the decreased activation energy of the heterogeneous nucleation sites.

One final area which must be considered, whilst not directly related to the present study, is the behaviour of the vessel during the sudden and rapid release of pressure [162-164]. This has been investigated with particular relation to the potentially hazardous operation of rapidly depressurizing vessels containing hydrocarbons [165], for which computer programs have been developed to simulate the rapid depressurization process, enabling the temperature histories for the vessel walls and the fluid to be predicted. The physical process which occur in the vessel are a complicated mix of several phenomena, and a number of competing processes must all be taken into account, particularly for predominantly gas filled vessels. These processes include heat transfer by convection from the vessel wall to the cold gas inside the vessel and from the vessel wall to the liquid, heat conduction through the wall of the vessel, heat transfer by convection between the surrounding and the vessel, and heat transfer between the liquid and the bubbles.

Vessels operating under pressure may be horizontal or vertical, and may be subjected to slow or rapid depressurization. As a result a potential hazard may arise due to the low temperatures generated within the fluid, particularly if very large vapour volumes are produced, which leads to a reduction in the temperature of the vessel itself. In some extreme cases, particularly for cheaper grade steel, the temperature can drop to well below the ductile-brittle transition temperature of the steel from which the vessel was fabricated. Under certain circumstances, for example, on offshore platforms, it may therefore be a necessity to predict precisely what happens when a vessel containing hydrocarbons is rapidly depressurized.

4.0 DESIGN AND INSTRUMENTATION OF THE RIG FACILITY

4.1 Introduction

The original specifications and criteria upon which to work were *a thermodynamically enclosed system, bench scale (~5 litres) apparatus with a maximum operating pressure of around 30 bar, controllable rates of pressure let-down and with a facility for simply changing the flow regime.* A closed system, rather than an open system, was favoured, largely to have more control over the variables, to obtain reproducible operating conditions fairly easily, and to keep instrumentation costs down.

The first concepts were of a small pressure vessel approximately 600 mm in length, preferably a cut off from a piece of pipework with a 200 mm bore. Although sensitive to chloride ion corrosion, stainless steel 316L was chosen, for reasons of cost and because the exposure to concentrated NaCl salt solutions would be minimal. It was quickly appreciated that in order for the vessel to accommodate the necessary instrumentation, the length of pipe would have to be extended. To keep down costs, it was felt that there was no reason why the bore could not be reduced in size. The final dimensions were chosen as a compromise between cost and valid experimentation. Too small a capacity would have multiplied scaling problems, and too large a bore, together with the appropriate pressure rated end flanges would have increased costs and handling weight considerably. Figures 4.1 and 4.2 show the general arrangement of the pressure vessel and a schematic of the systems set-up. A selection of photographs taken during the manufacture of the vessel can be seen in plate III, and plate IV shows a selection of photographs of the completed rig facility.

At the beginning of the project, the intended schedule for the duration of the three years was set down in the form of a bar chart. The bar chart, to which the actual schedule has been added, can be seen in figure 4.3. The initial ideas for the design of the pressure vessel were put on paper in March of 1992. By considering the parameters which would provide vital information, and therefore need monitoring, the vessel was designed and instrumentation selected accordingly. Over the course of the following three months, thoughts on the instrumentation began to take shape. At this stage, stress calculations of the vessel body, flanges and inserts were in the process of being carried out, and contact was made with the fabricators. Numerous discussions followed with the fabricators and with various manufacturers of measuring instruments.

The final set of drawings were completed in July 1992, and sent to National Vulcan Insurance for assessment, as required by the safety regulations for pressure vessels. Three months later a positive response from National Vulcan was given for the go ahead of the vessel. The necessary amendments to the drawings were made, and in November 1992 the drawings were issued to the fabricators. The overall design of the rig facility was maintained throughout the design and construction, but the specifications were refined and modifications continually made.

The vessel was delivered to the University towards the end of May 1993, having been promised for February 1993. By the end of June 1993, the schedule was running behind by about 6 months. The main reason was the lack of practical experience in allowing enough time for each stage of design and production. What was thought to be a reasonable period, both by the author and the relevant companies, for delivery, and, for example, vessel fabrication, tended to be delayed for one reason or another. Several jobs which were necessary to allow the next stage to continue were not accounted for in the original time schedule and many were time consuming. In particular, it was a necessity, being a pressure vessel, that each and every stage of manufacture had to be approved by a qualified insurance inspector, and feedback with the insurance inspector was very slow. In addition, on many occasions the technical departments of many firms would freely give verbal information over the telephone, but were reluctant to back up such information on paper. This was understandable in certain cases, since the equipment was not really designed to operate under the conditions experienced in the vessel, particularly during depressurization.

Despite buying, where possible, 'off the shelf' items and therefore reducing the design and manufacturing costs, the budget was still excessively under estimated. The reason was a result of the complexity of the vessel required, both in terms of manufacturing the vessel and in the instrumentation necessary to monitor the various parameters. A little more money was made available as a lot of interest has been shown by the oil companies, and the brewing industry, into the research being carried out on gas dissolution phenomena.

4.2 Materials and instrumentation

4.2.1 Vessel body

A 150 mm bore pipe, 10 mm thick, was deemed to be the most suitable in terms of effective liquid capacity, setting up for machining, matching piston seals, pipe flanges and end flanges. With all the bosses provisionally positioned for instrumentation, the final length, flange to flange, stood at just over 1000 mm. This was the minimum length possible, allowing for reasonable clearance between the pH electrode and the heater, and meeting the clearance necessary for the full penetrative welding required between inserts. The whole unit, complete with pneumatic cylinder, stood just under 2000 mm high, with an estimated mass of ~350 kg. The capacity of the vessel below the piston, at its lowest position, was ~ 11 litres, with a length/diameter ratio of ~5:1. The corresponding volume above the piston was ~5 litres. The complete set of drawings for the pressure vessel were done by M.E. Cox of the Central Design Service of the Mechanical Engineering Department.

For the appropriate insurance cover, a standard procedure had to be followed in order to meet the safety standards required for a pressure vessel. The vessel was certified to the ASME V111 Division 1 pressure code. A full set of stress calculations were required for the vessel, including all inserts and end flanges. A recognised fabricator, licensed to weld to the appropriate code was used, and all welding procedures and welders qualifications had to be checked by the insurance company. In addition all stock material and components had to be inspected and analyzed before manufacture. The welding at various stages of construction was inspected until completion, and the 'tack-up' of welded parts was examined. The written reports of all the Dye Penetrant Tests were examined, and the hydraulic testing of the finished pressure vessel to 58.63 barg for 30 minutes was witnessed, which satisfied the requirement that the vessel must be able to withstand a pressure of 45 barg (1.5 times that of the maximum working pressure).

The local company chosen for fabricating the vessel, PTR fabrications Ltd., had a vast experience in the manufacture of pressure vessels, particularly for oil companies and offshore rigs. Even so, the vessel proved to be one of the most complicated pieces of equipment made at the site. As a result, the fabrication took four months longer than originally estimated. The pressure vessel and instrumentation details can be found in appendix V.

4.2.2 Observation windows

It was envisaged that a key feature in the programme would be the visual observations and photographic evidence portraying the events occurring in the vessel during the rapid depressurization process. The original design incorporated a row of six 50 mm diameter circular windows down each side of the vessel. Consultation with the fabricators led to the belief that it would be easier and indeed simpler, in terms of construction, and more effective to accommodate two large slotted windows instead of the smaller circular windows. Two large vertical rectangular glass windows were therefore located in the sides of the vessel. In fact, this proved an immense problem during fabrication, the reason being that since such a large surface area of the main vessel body had been removed to accommodate the windows, the vessel 'bowed like a banana', as reported by the insurance representative during the initial stages of welding. The assurances of the manufacturers that the bowing would be rectified once the flanges had been welded onto the main body, proved correct, and indeed the alignment of the top flange, piston shaft and piston bore, which was critical for a smooth operation and to avoid any unnecessary wear was almost perfect.

In addition, two circular windows, were located at the liquid surface, to allow the events at the surface and the process of foam formation to be studied. A window was also incorporated in to the base flange, for two reasons. Firstly, since the method selected for stirring the liquid in the vessel was by a magnetic stirrer plate, inducing the rotation of a magnetic stirrer bar situated inside the vessel, it was necessary to have a window in the base. Secondly, the window would also allow either the vessel contents to be lit from the base, using a high powered light source, or indeed the events in the vessel to be viewed from below, if necessary, or advantageous. In order to let as much light through as possible and to provide a large area over which the stirrer could operate, therefore enabling the use of a larger stirrer bar, the size of the hole cut out of the base flange was calculated to achieve the maximum area acceptable within the pressure coding regulations. A toughened perspex window was then ordered to fit.

4.2.3 Pneumatics

A key feature in the design and operation of the vessel was to find the most effective way of releasing the pressure built up in the system as fast as possible, and being able to do it repeatedly, and reproducibly. Various options were considered, the most suitable being a pneumatics system. The main reasons for this was the cost, and the fact that a relatively easy means of measuring the free gas volume during depressurization could be incorporated into the design.

A withdrawable piston was chosen as a means of varying the set volume. The piston was machined from a stainless steel plate and sealed using a rubber 'o' ring seal encased in an outer PTFE low friction ring to reduce the friction between the piston and the wall. With the piston at its lowest position, there was a free gas space of ~ 0.8 litres between the piston and the liquid surface, for the liquid was always filled to the same level, 10 mm from the top of the window. During saturation, the gas was vented out of the lower chamber through the 4 mm diameter channel bored through the centre of the bronze shaft.

The use of the pneumatic cylinder, figure 4.2, enabled the rate of pressure release to be controlled rather than solely governed by the rate at which the hydraulic fluid left the upper chamber. The arrangement was such that the pneumatics controlled the dumping of the hydraulic fluid from the upper chamber to the reservoir using a solenoid valve, whilst simultaneously aiding the upward movement of the piston, as air was supplied to the lower section of the double acting cylinder. A potentiometric type linear distance transducer was attached to the cylinder to monitor the piston position with time and hence the rapidly changing gas volume.

The piston could be withdrawn a total distance of ~240 mm. The initial rate of movement during the design stages was estimated to be around 200 mm/sec corresponding to an increase in the free gas volume of 3.5 l/sec. The pneumatic cylinder, with a 250 mm stroke, was also fitted with a reed switch for the point detection of the piston. The reed switch was positioned ~40 mm from the end of the cylinder stroke, such that when the piston hit the reed switch, a supply of air into the upper section of the double acting cylinder would provide a cushioning effect and hence slow the piston down before it hit the end wall. Since a potential problem was envisaged to be in stopping the piston before it reached the top flange, particularly for large initial pressures in the lower chamber of the vessel, the top flange was further protected from any unforseen operational problems by a rubber buffer. The buffer was positioned to prevent the piston coming in contact with the underside of the top flange, and to cushion at least some of the impact, if, as a result of a malfunction, the piston should suddenly shoot back without warning. The pneumatic cylinder was also intended to be effective at the lower pressures in providing some assistance in withdrawing the piston, ensuring the rapid movement be maintained over the whole distance travelled by the piston.

It was essential that there was no leakage of pressure between the lower chamber and the upper chamber, nor of hydraulic fluid from the upper chamber to the lower chamber, which may contaminate the liquid under investigation in the lower chamber. The surface finish of the machined and honed bore was an important feature in governing the efficiency and indeed, life time of the seal, by ensuring the smooth running of the seal in the bore. The recommendation by the manufacturer of the seals was a surface roughness of $0.6\mu m$ to $6.0\mu m$ Ra. Surface roughness measurements were taken on a number of stainless steel samples and on replicas of the inside walls of the pressure vessel both in the piston bore and further down the vessel. The stainless steel samples, taken from the sections bored out of the main vessel body to enable the window mountings to be inserted, had the same surface finish as that of the inside walls of the pressure vessel. More details on the technique and the results can be found in appendix VI. The samples taken in the piston bore ranged in value from 1.3μm to 3.0μm, well within the specified range.

4.2.4 Hydraulics

A standard hydraulic hand pump was used to pressurize the vessel. The pump had a pressure rating of 100 bar, and a double stroke of 50 cm^3. A diffuser, to reduce the aeration of the hydraulic fluid, and a tank breather were fitted to the dump tank. A pressure gauge and adjustable relief valve were also fitted to the unit for safety reasons. The maximum capacity of the hydraulic fluid in the upper chamber was $\sim$5.1 litres. The fluid, expelled from the upper chamber on the opening of the solenoid valve, flowed back to the 20 litre portable reservoir via a dump tank, as shown in figure 4.2. As the rate of pressure release may have been limited by the rate at which the hydraulic fluid left the upper chamber, provision was made for an additional two outlets, if necessary, to increase the speed at which the hydraulic fluid left the vessel. It was indeed decided, in order to exhaust the hydraulic fluid from the upper chamber as fast as possible, to have three 25 mm outlets in the top flange, rather than just the one. The hydraulic valves were capable of handling a flow rate of 800 l/min, although the flow rate was only anticipated to be around 600 l/min, allowing for friction and the mass of the piston. It was originally estimated that the time taken for the piston to travel the maximum 241 mm distance with the simultaneous exhaustion of the hydraulic fluid from the upper chamber at a rate of 600 l/min would be of the order of a second. The valves chosen were compatible with both hydraulic oil and water. A 95% water, 5% hydraulic oil mixture was chosen, to work effectively with the valves and seals, and to reduce microbial contamination.

4.2.5 Pressure measurements

The pressure of the liquid was measured using a strain gauge pressure transducer. The transducer, unaffected by rapid depressurization, was suitable for use in brine and had an operating range of -20 to 80°C. The transducer could be inserted into the liquid in any of three places, allowing the changes, if significant, in the pressure readings recorded at various liquid depths to be noted. There was also the possibility of measuring any pressure changes in the gas by inserting the transducer into the link pin at the head of the piston shaft. Using two pressure transducers, the pressure in the liquid and gas phase could be recorded simultaneously.

The pressure transducer and linear position transducer were linked to a data logging software package, which has a maximum sample rate of 15,000 samples/sec. The pressure and the piston position, and hence the rapidly changing gas volume, were recorded during the course of a run using an 11 channel 10 bit ADC converter. Each channel measures a voltage representing the parameters, such as pressure and temperature, being monitored.

Whilst it was anticipated that the main event, the depressurization process, would only take a few secs, it was necessary to log the data over a longer period in order to monitor the pressure recovery process. It was decided to monitor the process over a period of 1200 secs. In most cases this was sufficient for the system to reach equilibrium. Unfortunately, the sampling interval could not be changed during a run, for it would have been ideal to have a small sampling interval for the first two mins, followed by a longer sampling interval for the remainder of the run. In order to select the most suitable sampling interval, two identical runs were carried out, one with a 100 ms sampling interval, the other with a 1 ms sampling interval, to observe if there was any significant change to the shape of the curves over the depressurization period, and hence to determine if any information would be 'lost' with a longer sampling interval. The results showed identical curves and therefore a sampling interval of 100 ms was chosen. As a result, over the 20 min period, 1,200,000 samples were collected, many of which were unnecessary. A programme, listed in appendix V, was therefore written, to shrink the data over the latter stages to a more manageable size of 120-150 data points. By recognizing the large blocks of data which remained constant over a given period, the programme was written such that the bulk of the data in the latter stages was disregarded whilst the data in the initial stages was left untouched. When the interest was focused on the latter stages of the run and the rise to the new equilibrium pressure, over a period of 1-2 hours, the sampling interval was changed to 5 secs, and occasionally to 1 min.

4.2.6 Temperature measurements

It was originally hoped that a rod heater could be used to keep the surface area available for bubble nucleation to a minimum. Unfortunately this proved impractical. Rod heaters 150 mm in length, such that they could be positioned horizontally into the vessel were available, yet were not recommended, for they would not effectively heat 10.5 litres of liquid to 70°C. Vertical insertion of a longer rod heater either from the top or the bottom was also impractical. Instead, a coiled heating element had to be used to provide the necessary heating. As the same heater was required to heat oil and water, a 500 watt, 240 volt incoloy sheathed electric immersion heater, inserted near the base of the vessel was used to obtain temperatures up to 70 °C. The heating time required was estimated to be as much as two to three hours. The temperature of the liquid, controlled by a thermostat incorporated in the element, was monitored using a platinum resistance thermometer situated near the liquid surface.

4.2.7 Magnetic stirrer

Some sort of stirring mechanism was required in the vessel, firstly to ensure uniform heating of the liquid and saturation of the liquid by the gas as it was bubbled into the vessel, and secondly to look at the degree of agitation on the rate of gas release during and after depressurization. It was anticipated that agitation of the liquid in the vessel both before and after depressurization might influence the rate of gas uptake into solution initially and, more importantly, the rate of gas evolution from the liquid following depressurization.

Whilst it would have been ideal to have some sort of impeller inside the vessel itself to stir the liquid, this proved impractical. The requirement to successfully seal a rotating rod capable of withstanding a pressure of 30 bara would have introduced major design problems. Other stirring methods, such as submersible and steady flow pumps were considered, but in terms of simplicity and effective sealing of the vessel, a magnetic stirrer was considered to be the most suitable option. It was hoped that the magnetic plate, sitting flush to the base flange, would provide the necessary flux to rotate a magnetic stirrer bar, 30 mm in length, situated in the bottom of the vessel.

4.2.8 pH Probe

It was considered that measurement of the pH of a CO_2/water system, during saturation and during the evolution of CO_2 following depressurization, might provide a valuable means of monitoring the uptake of CO_2 in solution. Water has a neutral pH of ~7.0, which, when saturated with carbon dioxide drops to a pH of ~5. It was considered that the interpretation of the measurements obtained might be used to help to determine the degree of saturation of the liquid in the vessel.

The determination of pH involves two separate potential measurements, one on an unknown sample and one on a standard. A thin membrane of glass separates the two solutions. When the probe comes in contact with the liquid sample an electric potential difference is established across the glass which is dependent on the ions present in the solution. Unfortunately there were no pH probes commercially available capable of withstanding pressures of 30 bara, so a series of experiments were carried out at lower pressures with smaller pressure reductions, 6 bara to atmospheric pressure. Since the pH probe was only rated to pressures up to 6 bara, a 6 bara pressure relief valve was incorporated into the rig, to be used when the pH probe was in operation.

The probe, according to the manufacturer's specification, had to be inserted at an angle of between 15° and 90° from the horizontal position, to ensure the filament at the tip of the probe was always surrounded by liquid. In addition, it was considered that the probe, although not adversely affected by small temperature changes, should not be positioned too close to the heater, especially under conditions approaching 70°C. Provision was therefore made to allow adequate space between the heating element and the angled pH probe.

4.2.9 Dissolved gas measurements

The rig was designed to incorporate two potential methods for determining the dissolved gas content in the liquid. The first is based on partial pressure measurements, using a piece of equipment already available in the department, which monitors the CO_2 content in a flowing liquid. The Carbocheck device monitors the build up of pressure in a periodically evacuated chamber, which is separated from the bulk fluid by a silicon rubber gas permeable membrane. After a short period of time, the pressure in the evacuated chamber approaches an equilibrium value, reflecting the partial pressure of the gas in the liquid. Analysis of the data provides quantitative information on the amount of gas dissolved at a particular temperature, at the time the data is collected. Although other gases may permeate the membrane, they do so at a slower rate. Providing the venting operation is repeated at regular intervals, the pressure readings can be converted to a function of CO_2 content only.

The second method for measuring the dissolved gas content uses an infra red technique which relies on transmission of infra red radiation through an optically pure crystalline sensor in contact with the liquid. As an infra red beam is internally reflected along the crystal probe, a portion of the energy in the beam projects slightly beyond the reflecting surface, before returning to the crystal. The total amount of absorption of the beam is a function of the gas concentration, and as a result, the local dissolved gas content in the liquid can be monitored directly and rapidly. This technique has been discussed in detail in appendix IV.4, since it was used by the author to monitor the dissolved gas content of CO_2 in water and hydrocarbons during saturation.

4.3 Rig commissioning and modifications

There were no major problems or changes associated with turning the drawings into a fully operational rig, the commissioning of which proved quite successful. A significant amount of time was spent commissioning the rig to ensure the instrumentation was fully operational and repeatable pressure reductions were achieved. Initially it was hoped that up to four runs a day could be achieved. During the commissioning of the rig, it was found that 5-6 runs a day could be accommodated, each run taking approximately 1 hour from start to finish, except for those where recovery to equilibrium was monitored over a period of 2-3 hours. When the heater was in operation, a period of up to two hours was required to heat the water to a temperature of 60°C.

There were far fewer problems than expected. The main problem which became evident early on, was the leakage of hydraulic fluid past the piston seal, resulting in an oily sheen on the liquid surface. It followed that, more likely than not, gas was also leaking past the seal in the opposite direction. The original piston seal consisted of a rubber o-ring, seated in the groove of the piston, encased by a PTFE seal. The intention was to keep the friction to a minimum as the piston moved up and down, thereby increasing the rate at which the piston moved. The rig was stripped down, and the seal replaced. The new seal was similar to the original seal, except an I-section PTFE ring was used, with o-ring inserts either side to provide a better seal between the piston and the vessel wall. The new seal proved very effective, and the rate of the piston movement did not appear to be significantly different. The piston, as calculated, moved the 241 mm distance in 1-2 secs, at an initial rate well over 100 mm/sec.

Another problem was the stirrer. In the original design, a recess in the base of the flange was intended to prevent the magnetic stirrer bar from jumping away from the perspex window during depressurization, and thus losing the effect of the magnetic flux through the window. After testing the stirrer, it was considered that this might actually restrict the effectiveness of the stirrer bar. To overcome this, a perspex disc was fitted into the recess, making the base of the vessel flat. A more powerful magnetic stirrer was also used to provide a stronger flux. It appeared that some flux was getting through the perspex window, but rather than turning, the bar was jumping about on the spot. Several shapes of stirrer inside the vessel were used. A disc shaped stirrer proved to be the most effective design. Unfortunately it was still not possible to effectively stir the liquid in the vessel.

Whilst this method worked to some extent, it did, however, have its limitations, the main two being the large volume of liquid to be stirred, and the lowering of the effective stirring rate as the magnetic flux had to travel through 25 mm of air space and 12 mm of perspex. Tests by the author, however, had shown that 12 litres of water could be stirred effectively through 25 mm of perspex. The problem was considered to be that the flux was spreading out before it reached the stirrer, being absorbed by the steel, with the result that the stirrer was effectively sitting in a 'no flux zone'. Six ferrite rods, each 25 mm long and 6 mm in diameter, were then located in the air space between the perspex window and the stirrer plate, in an attempt to focus the flux onto the stirrer, still to no avail. Next, the magnetic stirrer device, itself, was dismantled, and the rotating magnetic disc, which was fortunately less than 50 mm in diameter was fitted flush to the window, such that the flux only had to go through 12 mm perspex. But the flux was still not focusing directly on the stirrer bar.

Stirring the liquid using a magnetic stirrer was eventually abandoned, and instead, a pump, able to operate up to 10 bara pressure was used. The pump was actually a dosing pump, which, when connected to the inlet and outlet valves in the base flange, provided a pulsed jet, through a 2 mm orifice, into the bulk liquid. Owing to the large volume of water, and the fact that the pump was being used for a purpose it was not strictly designed for, the pump was set at its maximum setting in terms of stroke and frequency, so a range of agitated conditions was not really possible. The pump, however, was effective in agitating the liquid. Although the jet died away before reaching the observation windows, so the bulk liquid appeared to be motionless, there were signs of agitation at the liquid surface due to the periodic displacement of the liquid surface, at a frequency of ~60 Hz. The velocity of the emergent jet was estimated to be about 1-2 m/sec.

Midway through the experimental programme, it became necessary to actually slow down the rate of piston movement. It was decided that valuable information could be obtained by changing the rate at which the piston moved its full distance of travel. Two methods were investigated to achieve three controlled and reproducible rates. The piston could be slowed by either restricting the flow of hydraulic fluid out of the upper chamber, or by reducing the air pressure supplied to the lower section of the double-acting pneumatic cylinder.

Ideally, the flow of hydraulic fluid out of the upper chamber should be changed by inserting a control valve into the outlet pipe. Unfortunately this was not that simple, as three 25 mm pipes were used to satisfy the design criteria. This would mean two or three control valves would be required. This was investigated, but disregarded for two reasons. Firstly, there was not enough room to accommodate the control valves in the pipework, as the hydraulic hoses were too tightly packed, and secondly this method would have proved expensive. One control valve below the solenoid valve was considered, slowing the flow to the dump tank, but it was felt that this may influence the flow of the fluid, passing through both the solenoid valve and a control valve. Another alternative was to plug first one hose, and then two, giving three rates of release. Again, more fittings would be required, and as the solenoid and hydraulics had been designed to cope with the flow and pressures from three 25 mm outlets, this method was not selected.

The method opted for, was actually regulating the air pressure into the lower section of the pneumatic cylinder. The only drawback was that in reducing the air pressure in the lower section, the pressure in the upper section, providing the cushioning, would also be reduced. At the higher initial saturation pressures, care was taken to prevent the piston shooting up and impacting the top flange. The air pressure was generally regulated to 6 barg. In order to investigate the effect of piston rate, the regulator pressure was reduced to 4, 2 and 0 barg. This effectively reduced the piston velocity from a maximum of 240 mm/sec at 6 barg to 20 mm/sec with no air pressure supporting the piston movement upwards.

Throughout the duration of the research, there were no signs of gas leakage, tested using a soap solution on the joints and valves, and by monitoring the pressure over a period of time whilst the vessel was left standing at a pressure of 10 bara, nor were there any signs of hydraulic fluid passing the seal. Diffusion of gas through the piston seal was also considered negligible. Careful monitoring of the pressure in the lower chamber and the upper chamber, above the piston, indicated that there was no significant pressure difference across the piston. A typical run was regularly repeated throughout the trials, to ensure reproducibility with time. There were also no signs of wear, or degradation. Samples of the hydraulic fluid were regularly observed for signs of any reaction or contamination, which would have been particularly apparent in the smell of the fluid. Nothing unusual was observed.

5.0 EXPERIMENTAL PROGRAMME

5.1 Introduction

The variables which may influence the events likely to occur in the vessel were carefully considered, and the experimental programme devised such that, where possible, each variable could be considered independently. Naturally, there was going to be some overlap between variables, and this was taken into account. In order to determine the length of time to be spent studying each variable, the vessel operation had to be considered, together with the volume of data required for each changing variable.

5.2 Operating conditions and procedure

The sequence of events involved firstly, the saturation or part saturation of the liquid, in the lower chamber, with gas. Once the vessel had been filled with liquid to the required level, the piston was lowered to its lowest position using the hand pump. The lower chamber venting valve was then shut, the gas inlet valve opened, and the lower chamber pressurized to the required pressure, set by the pressure regulator head on the gas cylinder. The vent was then opened slightly, the extent of which was determined by the required flow rate of gas through the vessel. The gas was bubbled through at that pressure for the required length of time.

When the required level of saturation was reached, the system was isolated. The lower chamber vent was shut, the hydraulics locked and the gas supply turned off, in order to establish a steady state in the vessel. The steady state of the vessel was maintained for approximately 15 seconds before the depressurization process was initiated. The rapid depressurization process was initiated by flicking a switch on the control box, which simultaneously opened the solenoid valve for dumping of the hydraulic fluid from the upper chamber, and allowed the flow of air into the lower section of the double acting pneumatic cylinder. As a result of both actions, the piston started travelling. The operating instructions for controlling the pneumatics system during depressurization are given in appendix V.

Following the sudden depressurization, the pressure recovery was monitored over a period of twenty minutes. When the experiment was completed, the lower chamber vent was opened to evacuate the pressure built up in the lower chamber. After draining the liquid, the system was then ready for the next experiment. The vessel was emptied and refilled before each and every run, to ensure that there was no influence on the results from the previous run, and the inside walls were cleaned regularly. The process of refilling was looked at carefully, in terms of bubble nucleation, to determine whether or not reproducibility of data may be affected by the rewetting of the potential nucleation sites on the surface walls.

5.3 Operating variables

The two main variables in the system which were considered to have some influence over the depressurization process for a given gas and solvent, were the pressure, in terms of the initial saturation pressure and the rate of change of pressure with time, and the initial liquid temperature. Keeping the conditions the same and varying one parameter at a time, those parameters which were investigated were

i) the saturation pressure, for which pressures of 5, 10, 20 and 30 bara were selected,

ii) the period of time for which the liquid was exposed to the solute gas, for which bubbling times ranged from 5 to 120 minutes,

iii) the initial temperature of the liquid, for which temperatures of 15, 40 and 60°C were selected,

iv) gas flow rates of 33, 66 and 100 and 160 l/minute atp,

v) the initial free gas volume, for which tests were carried out with initial free gas volumes above the liquid surface of 0.01, 0.8, 2.4 and 3.6 litres.

In most cases, unless otherwise stated, the standard conditions were a bubbling time of 15 mins, at a gas flow rate of 100 l/min measured at atmospheric pressure, ambient temperature, from an initial saturation pressure of 10 bara. Once the capabilities of the rig had been assessed, and the influence the basic parameters, mentioned above, on the gas evolution process were determined, the factors which might further control the rate of gas evolution were investigated. These factors were considered to be the salinity, the presence of insoluble solid nuclei in the vessel and agitation of the liquid.

In terms of salinity, the salt concentrations initially selected for examination were 25, 50 and 100% salt saturation, although a few tests were carried out in 3% salt saturations. The salt saturation of the North Sea is typically around 10%. A certain amount of interaction between salinity and nuclei population was anticipated. Being extremely sensitive to solid impurities such as electrolytes, dust and even bacteria (0.3-30μm), bubble formation was anticipated to be strongly influenced by those parameters which play a role in initiating bubble nucleation. A comparison was made between tap water, containing many thousands of particles/cm^2, and distilled water. At the other extreme, in order to thoroughly investigate the effects of solid nuclei, some tests were carried out in which 500 ppm and 1000 ppm, 5μm uni-sized silica flour particles were added to the liquid. Photoelectron micrographs of the 5μm silica flour particles can be seen in plate II.

The population and size distribution of the solid nuclei were determined using a Coulter counter, the results of which can be seen in figure 5.1. It was apparent from the size distribution spectrum that, in fact, the mean particle size was slightly less than 5μm. Whilst the spectrum only goes down to 3.05μm particle size, owing to the size of the tube in the analyzer, it was not considered necessary to recalibrate the instrument to lower particle sizes since the distribution is clearly a normal distribution, with an estimated volume mean size of around 2.5-3μm, and nothing of any value would be gained by going any lower. The main implication in the experimental work of adding 500 ppm with an average particle size of 3μm, compared to 5μm, would be in calculating the effective surface area of the solid particles available for nucleation. This is carried out in chapter 6.16 and discussed in chapter 7.3.1.2.

In terms of agitation of the liquid, owing to the problems mentioned in chapter 4.3, the effects of agitation were investigated simply in terms of 'agitated' and 'not agitated', since varying degrees of agitation could not be obtained. The operating conditions, variables and accuracy of measurements are summarized in appendix V, table V.2.

5.4 Materials

5.4.1 Solvents

The liquids investigated were essentially tap water, various salt concentrations, using pure vacuum dried NaCl (containing anti-caking agent, sodium hexacyannoferrate), gas oil (ρ 857 kg/m^3, μ 5.74 cS) and kerosene (ρ 787 kg/m^3, μ 1.82 cS). Statfjord crude (ρ 845 kg/m^3) was also used in a few experiments, in order to compare the behaviour of gases in the crude to the behaviour in kerosene. The same parameters were varied for each liquid, and where possible the conditions were kept the same. Some tests were also carried out with distilled water, but this line of investigation was not continued as there were no significant differences in the data recorded to that of tap water. This is discussed in more detail in chapter 7.2.1. Tap water was therefore used in all water-based experiments, which is, in fact, a more realistic model regarding the industrial application, as oilfield waters in the offshore industry contain significant quantities of salts, suspended particles and solid impurities. A few tests were also carried out towards the end of the experimental study into the behaviour of oil/water mixes. Owing to the fact that turbulent conditions could not be achieved, an emulsion could not be maintained in the vessel. As a result, the oil/water mixes separated out with time.

5.4.2 Solute gases

The gases investigated in the study were selected as a representative sample of the wide range of gases, in terms of polarity, solubility in hydrocarbons and water-based liquids, molecular size, and molecular behaviour. Availability, cost and safety were also factors which required some consideration. The gases investigated in this study were CO_2, CH_4, Ar, O_2, N_2 and two combined gas mixtures of CO_2 (70%) and N_2 (30%), and CO_2 (30%) and N_2 (70%). The purity of the gases ranged from 99.5% for CH_4 and O_2 to 99.99% for Ar and N_2. The purity of the CO_2 used was 99.8%. The physical properties of these gases are tabulated in appendix I, table I-1. The solubilities of these gases in water, salt solutions and hydrocarbons can be seen in figures I-1 to I-8.

Where possible, the conditions were kept the same for each gas, in order to make valid comparisons. Oxygen was not included in the tests involving hydrocarbons since oil, grease and other materials can ignite and burn violently in the presence of O_2. There is also the possibility of seal damage, degradation and film formation on the vessel walls using O_2.

5.5 Data analysis

The instrumentation on the rig enabled the careful monitoring of a number of variables, the key parameters under investigation being pressure and temperature- both in the liquid and the gas phase, and the free gas volume. The simplest and most informative way to display pVT data is in the form of pressure-time histories. The typical pressure-time history obtained in this study is shown in figure 5.2. The pressure-time history can be divided into three stages, the initial steady state, the rapid depressurization process, figure 5.3a, and the pressure recovery following depressurization.

In all cases, the data logging was started as soon as the system was isolated, 15 secs before the depressurization event. During the initial steady state period, the pressure, p_i, the temperature, and the gas volume remains constant. The rapid depressurization of the vessel, from p_i to p_{min} generally takes of the order of 1-3 secs, depending upon conditions. The pressure recovery of the isolated system, p_{min} to the final pressure, p_f, occurs over two distinct timescales. For CO_2 in water, the initial growth is rapid, occurring over a period of around 10 secs, during which approximately half of the total pressure recovery takes place. Beyond 20 secs, when the pressure has recovered to around 2/3 of the pressure recovery, the growth recovery slows enormously and follows an exponential. In chapter 6, the pressure recoveries have generally been reported in terms of the time taken for 50 and 80% of the total pressure recovery to have taken place, where

$$\frac{p-p_{\min}}{p_{eqm}-p_{\min}}=0.5\ (or\ 0.8) \tag{5.1}$$

enabling comparisons to be made between one or more systems, during both the initial rapid recovery (50%) and the slower rate of approach to equilibrium (80%).

The main differences in the pressure-time histories, from direct comparisons of the various gases under the various conditions, were evident in terms of the rate of approach to equilibrium, reflected in the shape of the curve from p_{min} to p_f, and the final equilibrium pressure, p_f, which reflects the amount of gas dissolved in solution. The significance of these values and timescales, and how they are influenced by the various parameters and conditions in the vessel are reported in chapter 6 and discussed in chapter 7.

The pressure-time histories for most of the experiments were recorded over a period of 20 minutes, which, in most cases is sufficient for equilibrium to be established. However, under certain conditions, particularly with CO_2, the pressure continued to recover beyond this period, albeit slowly. In the following chapters, p_f represents the final equilibrium pressure, unless otherwise stated. In the instances where the pressure was still obviously climbing, the equilibrium pressure was estimated, where necessary, by extrapolation, as described in chapter 6.3.

The $p-p_{eqm}$ versus time traces are directly related to the pressure-time histories and represent the drive to equilibrium, with respect to time, of a gas-liquid system, determined by the extent of disequilibrium in the vessel. The driving force to equilibrium is a maximum at p_{min}. A typical $p-p_{eqm}$ against time trace for CO_2 in water is shown in figure 5.3b.

The pressure-volume relationship during the rapid depressurization process is an important one, both in determining whether the process is isothermal, polytropic or adiabatic, and indeed in giving some idea of when bubble evolution begins. The p-V histories were recorded during the period of movement of the piston. At its lowest position the initial free gas volume was generally 0.8 litres, which expanded over the full distance of travel, to 5.1 litres. Each mm the piston travelled upwards represented a volume increase of ~0.018 litres. The typical p-V plot is shown in figure 5.4a.

For a constant mass system, as is the system during depressurization, before bubbling begins, the equation pV^n=constant can be fitted to the p-V plot obtained to determine the value of n. The constant, C, is related to RT, where R is the universal gas constant and T is the temperature. The value of n lies somewhere between 1 and γ, where γ is the ratio of the specific heat at constant pressure to that at constant volume. The values of γ for the gases used in the study, at the test conditions, are 1.28 for CO_2, 1.4 for N_2 and O_2 and 1.675 for Ar. Figure 5.4b shows, for a set of data, the equation pV^n=constant for different values of n. In this case the values chosen were 1.0, 1.2 and 1.4 and 1.6. Strictly speaking, values of $n > 1.28$ would not be expected for CO_2, the figure just gives an indication of how the plot changes for different values of n. Also included in the plot, is the actual data obtained for CO_2, from an initial saturation pressure of 20 bara. The value of n in that experiment was ~1.16. The effects of pressure, volume and temperature on the value of the index, n, are discussed in detail in chapter 7.2.2. In general, the p-V plots obtained show a close fit with the line representing the equation pV^n=constant, where n is approximately one, suggesting a nearly isothermal reaction, owing largely to the bulk mass of steel and liquid.

The specific heat, or thermal capacity, of water is large compared to that of most other substances, and as a result the value of n would be expected to tend towards unity. In comparison, however, the specific heat for oil is much lower than for water, by a factor of around two. The implication of this is that the index would tend towards γ. In some cases, particularly with CO_2 in kerosene, the p-V relationship moves away from the reference line, indicating that under these conditions, the dissolution of gas starts whilst the piston is still travelling. The bubble evolution causes the pressure to rise, thus moving away from the line of best fit. In those instances where this occurred, the data used to obtain the line of best fit did not include the deviated data. The effects of bubble evolution before volume expansion is completed is also apparent in the free gas volume-time plots for CO_2 in kerosene, in which there is a sudden change in the gradient of the line, as reported in chapter 6.19.

Two other useful traces which could be obtained from the recorded data were the velocity of the piston against distance travelled, and the piston velocity with respect to time. The traces can be seen in figure 5.5. These plots were particularly useful in showing how the velocity of the piston varied according to, for example, the initial saturation pressure, the viscosity of the liquid and the initial free gas volume.

5.6 Reproducibility of measurements

A standard test procedure was adhered to, in an attempt to ensure reproducibility. In fact, reproducibility was not a problem. In two identical experiments, using CO_2 in water, the traces obtained were almost identical in all respects. From an initial starting pressure of 10.18 bara ($\pm$0.06 bar), the minimum pressure recorded, 1.82 secs after depressurization was initiated, was the same for both runs ($\pm$0.02 secs). Both the pressure-time and velocity-time plots, recorded during the depressurization process, were identical within 0.1 bar and 5 mm/sec. The approaches to equilibrium were also identical, reaching the same final equilibrium pressure ($\pm$0.02 bar).

6.0 EXPERIMENTAL RESULTS

6.1 Introduction

The experimental results of the present study are documented in this chapter. The interpretation and discussion of these results then follows in chapter 7. Sections 6.2-6.17 explore the behaviour of gases in water. Initially, from the visual and photographic observations capturing the events occurring in the vessel, on a macroscopic level, and then by reporting the effects various parameters, such as initial saturation pressure and temperature, salinity, fluid agitation and presence of solid nuclei have on these events, in terms of the key features which can be gleaned from each history. Sections 6.18-6.27, describe the results obtained from the evolution of the same gases from the three hydrocarbons, gas oil, kerosene and Statfjord crude, under the same experimental conditions as with water. In the following sections, the effects have generally been described using the CO_2 data, since the effects are more pronounced, and then compared with the behaviour of the other less soluble gases.

6.2 Visual and photographic observations in water

The rapid depressurization of a gas saturated liquid in the vessel took place too quickly to be observed in any detail by the human eye. A video camera, therefore, was used to capture the sequence of events occurring during and immediately after depressurization. The video camera had a shutter speed 1/1000 of a second, enabling 25 frames a second to be recorded. The process was observed by back lighting the vessel with a 1000W halogen lamp through the rear slot window. It was considered that the heating-up of the liquid by the lamp would be negligible, for the lamp was only turned on whilst the video camera was in action, over a period of 1-2 mins.

The activity in the vessel during a typical CO_2 in water run has been captured in plate V. The CO_2 was initially bubbled through the liquid for a period of 15 minutes at a saturation pressure of 10 bara, and a gas flow rate of 100 l/min. The temperature was 18.6°C. The numbers below each photograph represent the timescale, in secs. During saturation of the liquid, a certain degree of agitation was provided in the vessel by the steady streams of gas bubbles flowing through the liquid. Very few bubbles were observed on the vessel walls or observation windows. Once the liquid had been exposed to the gas for the required length of time, and the desired saturation level reached, the vent was shut and the system isolated. At this point the data collection was started.

During the first 3-4 seconds of isolation, an occasional solitary bubble was observed rising to the surface from somewhere near the base of the vessel, probably from gas trapped at the inlet. There were still very few bubbles on the vessel walls or windows. During the following 10 secs, a steady state was being established in the vessel, in which there were no visible bubbles in the liquid. When the saturated liquid, prior to depressurization, was motionless (plate V, 1), the video recorder was started. A period of 15 secs was considered adequate time for the system to reach a reasonably steady state before depressurization, for over the latter part of the isolation time, there was no signs of any macromolecular bubble activity. It was anticipated that at this stage the gas molecules were reasonably uniformly spaced in the liquid, and any movement of gas took place on a molecular scale by diffusion.

The first signs of activity at the surface, following the sudden release of pressure from the upper chamber, occurred after just 20 ms (plate V, 2). Time $t=0$, was taken to be the point immediately prior to the first signs of any activity in the vessel, corresponding to the opening of the solenoid valve. This progression of the bubble front into the bulk liquid, to a maximum depth of ~ 50 mm, took place over the course of 100 ms (plate V, 2-7). The event at the surface cannot be termed as a pressure wave, as such, for pressure waves in liquids travel at very much greater velocities than observed in this experimental study. A more precise term is a bubble front, defining the edge of the zone within which bubbles are rapidly evolving, which is observed moving in the opposite direction to the bubble motion. The progression of the bubble front into the liquid appeared to be slightly off-centre, travelling down one side of the vessel. Repeated runs, under the same test conditions, however, indicated that the geometry of the bubble front was susceptible to random local disturbances, for there was no apparent consistency to the asymmetry.

There were signs of symmetry of timescale as the bubble front retreated back up to the surface (plate V, 8-13). Over the next 200 ms, the only activity apparent in the vessel was the periodic displacement of the meniscus (plate V, 14-16). Following this, there was evidence of small bubbles evolving in the surface layers of the liquid. These bubbles first became visible at the liquid surface and gradually evolved from further into the bulk liquid (plate V, 17-22) to a maximum depth of ~ 30 mm. The lifetime of this stage (from the appearance of the first bubbles to the disappearance/bursting of the last few bubbles) was of the order of a second. The bulk liquid and indeed the surface of the liquid became almost motionless again (plate V, 23) before a large 'mushroom' of gas was observed rising from somewhere near the base of the vessel, followed by a number of bubbles in its wake (plate V, 24 and 25). Unfortunately it was not possible to determine exactly where in the vessel the evolution of gas started, even by visual observations through the base window. The mushroom was estimated to be travelling at around 1.0 m/sec (±0.05 m/sec). This event took place ~1.7 seconds after the initial signs of bubble evolution. Over the following 4-5 secs there was extremely rapid mass evolution of bubbles from the bulk liquid (plate V, 26).

After the sudden rush had passed, and the mass of bubbles at the surface had died away, some order became apparent in the vessel, as streams of bubbles from the bulk liquid rose to the surface (plate V, 27 and 28). The steady streams of rising bubbles continued for anything from one minute, for the less soluble gases, to half an hour for CO_2 in water, depending upon conditions, and gradually diminished with time.

During and immediately after the mass evolution of bubbles to the surface, the walls were not visible. Once visible, however, ~10 secs after depressurization, the walls were completely coated with bubbles of various sizes, from the barely visible to those of a few mm in diameter. Most of the bubbles seemed to remain on the vessel wall, neither growing, nor moving. Some activity, however, was evident. These bubbles rose to the surface, during the pressure recovery period either by being 'sucked' off and dragged up in the wake of large bubbles rising to the surface in the bulk liquid, or by coalescing with bubbles which were gradually moving up the vessel wall encompassing the smaller bubbles in its path. The latter process was very slow, of the order of several minutes for a bubble to travel a relatively short distance of a few mm. The bubbles either continued up the wall, or grew large enough to leave the wall.

By focusing on a small area of the vessel wall it was possible to observe bubbles explosively appearing on the vessel wall. This was particularly apparent and frequent in the first minute or two following depressurization, due to the dissolved gas trapped in the pits and crevices in the walls, being drawn out from the vessel walls. It was also evident during pressure recovery, that when bubbles left the vessel walls they were immediately replaced by other bubbles. This appeared to happen either by bubbles shifting along the wall surface, or by bubbles explosively growing from the crevices. Even when the run was completed, and the streams in the bulk liquid had virtually ceased, bubbles still remained coated on the vessel walls.

It was apparent, therefore, from the events captured by the video camera that there were three definite stages in the evolution of CO_2 from water. The first stage (plate V, 2-13), is the progression of a bubble front into the bulk liquid. The second stage (plate V, 17-22), is the evolution of bubbles in the top 30 mm of the liquid. The third stage in the sequence (plate V, 24-26), is the mass evolution of bubbles from the bulk liquid. A detailed discussion of the events can be found in chapter 7.2.1.

Although the photographs themselves provided a detailed picture of the events occurring in the vessel, it is essential to be able to relate those events to the changes in pressure, piston movement and hence free gas volume occurring over the same time period. Figure 6.1 shows the plots obtained using the data recorded for this particular run. The numbers on figure 6.1a correspond to the numbered photographs in plate V.

During the initial steady state period, the initial pressure was 9.4 bara, and the piston was at rest. During depressurization, over a period of 1.4 secs, the pressure dropped from 9.4 bara to 1.93 bara, figure 6.1a. In that time the piston had virtually travelled the complete distance from rest to the end of its stroke, resulting in the evacuation of 5.1 litres of hydraulic fluid. The maximum velocity of the piston, 237 mm/sec, was reached 0.3 secs into its travel, figure 6.1b, at which point the piston had travelled ~40 mm, corresponding with plate V, 15. The piston position, and hence free gas volume increased approximately uniformly with time, over the depressurization period.

The minimum pressure recorded over the whole run, 1.93 bara, coincided with plate V, 23, showing the bulk liquid to be still, prior to the mass evolution of gas from the bulk liquid. As the mushroom of gas rose to the surface, initiating mass evolution, the pressure started to rise. The rapid initial growth, over approximately 10 secs, corresponded to the gross bubble activity in the vessel (plate V, 24-26), beyond which a marked change in the rate of pressure recovery was observed. As mass evolution was replaced by steady streams (plate V, 27 and 28), the pressure slowed, following an exponential towards equilibrium over a period of ~30 mins.

In general, the behaviour observed for CO_2 in water was broadly characteristic of that observed for other gases and liquids. Dependent upon experimental conditions, however, and the gases used, there were slight differences in terms of timescales, bubble sizes and bubble activity. Selective photographs from a typical N_2 in water run can be seen in plate VI, which show the characteristic features of the less soluble gases in water. The corresponding p-t data for the N_2/water system recorded during the depressurization can be seen in figure 6.2. The conditions were the same as for CO_2, 100 l/min, 15 mins and 17.8 °C. The numbers on figure 6.2a correspond with the numbered photographs in plate VI. The bulk liquid, and surface, was motionless prior to depressurization (plate VI, 1). Following the opening of the solenoid dump valve, a bubble front was again observed progressing into the bulk liquid at an estimated velocity of 0.75 m/sec (±0.05 m/sec), to a maximum depth of 26 mm (±2 mm) over a period of ~ 100 ms (plate VI, 2). The depressurization from p_i to p_{min} took place over 2.9 secs. The piston came to rest at the same time as p_{min} was reached, figure 6.2a. The maximum velocity recorded was 103 mm/sec, after the piston had travelled 50 mm, figure 6.2b. This was 0.7 secs after depressurization was initiated. With fewer bubbles creating a disturbance at the liquid surface, it was clear to see the 'dome' shape of the periodic displacement of the surface (plate VI, 3), which occurred over a 1/2 second period. Most significant, however, was the absence of stage II in the evolution of N_2 from water. Over a 1 sec period, there was virtually no activity in the vessel (plate VI, 4 and 5). A few small solitary bubbles, 1-2 mm in diameter, were observed rising to the surface from the bulk liquid, but the evolution of bubbles at the surface of the liquid, which occurred with CO_2 in water (plate V, 17-22), was not evident.

Approximately 1.76 secs after depressurization was initiated, a mushroom of gas was observed rising through the bulk liquid to the surface (plate VI, 6). There were, however, relatively few bubbles travelling in its wake (plate VI, 7). There was another 1 sec period, after the mushroom has reached the surface, whilst the piston was still moving, in which there was little activity in the vessel. When the piston was stationary, 3.3 secs after depressurization, bubbles appeared with increasing frequency in the bulk liquid (plate VI, 8-10), before gradually dying away (plate VI, 11 and 12). Approximately 30 secs after depressurization, all bubble activity had virtually ceased, since the new equilibrium state had almost been established. With CO_2 the activity in the vessel occurred for many minutes. It was also evident from visual observations, that the bubbles evolving from a N_2/water solution ~ 15 secs after depressurization, were generally smaller, in diameter, by a factor of 3-4, than those evolving from a CO_2/water solution. The visual observations, comparing CO_2 and N_2, are discussed in detail in chapter 7.2.1.

6.3 Effect of bubbling time

The amount of gas which can be dissolved in solution would be expected to increase with bubbling time until a state of saturation is reached, beyond which, the mass of gas in the liquid and gas phases are no longer a function of the length of bubbling time. A series of experiments were carried out to study the behaviour of an isolated, but pressurized, saturated or part saturated solution. In these experiments, the saturation procedure was carried out as normal, and the system isolated, but rather than carry out the depressurization, the system was left and the pressure monitored over a period of up to 6 hours.

For a partly saturated system in an enclosed environment, assuming negligible diffusion of gas through the piston seal, the pressure would be expected to drop to that equilibrium pressure where the concentration of gas, in the gas phase, was in equilibrium with the concentration of gas in the liquid phase. For a fully saturated solution, at equilibrium, the pressure drop with time would be expected to be minimal. This is demonstrated in figure 6.3. Figure 6.3a shows the drop in pressure after the liquid, in this case, water, had been exposed to the solute gas, argon, for the time indicated, and then isolated. In each case the piston did not move, so any drop in pressure observed was due to the movement of gas in and between the liquid and gas phases, to establish a system which was in a reasonably steady state. The bulk liquid was still, suggesting any movement of gas was by molecular diffusion. The time required to fully saturate a liquid is strongly dependent on the solubility of the gas. With sparingly soluble gases, a fully saturated solution is achieved within minutes of bubbling. The situation, however, is very different for the more soluble gases, where bubbling times of several hours are often necessary in order to achieve a fully saturated solution. Figure 6.3b shows the same plot for CO_2 in water. The time necessary for the steady state to be established was much greater than for the less soluble gases.

Following the operating procedure described in chapter 5.2, a series of experiments were carried out to determine the effect increasing the bubbling time had on the evolution of gas using the pVT data recorded. With an initial saturation pressure of 10 bara and gas flow rate of 100 l/min, at ambient temperature, the pressure-time histories obtained for each gas in water, with respect to the bubbling time, were recorded. The final equilibrium pressure is strongly dependent on the amount of gas in solution initially. As the amount of gas in solution increases, so does the new equilibrium pressure, until the point is reached, beyond which the value of p_{eqm} is independent of bubbling time, indicating that complete saturation of the liquid has occurred.

Figure 6.4 shows a plot of the new equilibrium pressure obtained as a function of bubbling time. For those gases which are sparingly soluble in water, namely Ar, CH_4, O_2 and N_2, the length of bubbling time required to reach the plateau increases with increasing solubility of gas. The plateau for the least soluble gas, N_2 occurred after just 5 mins, compared to 12-15 minutes for Ar, CH_4 and O_2. With CO_2 in water, however, although after bubbling for 120 mins, some levelling off was apparent, the plateau had not been reached, suggesting that the liquid was still not fully saturated. Taking the plateaued equilibrium pressure, obtained after depressurization, for each gas, to represent virtually 100% saturation, the degree of saturation can be estimated with respect to bubbling time, as shown in figure 6.5.

In most of the experiments carried out, a period of 20 mins after depressurization was considered adequate for the new equilibrium to be established. Indeed this was the case for all the gases except CO_2, where, in most cases, the pressure was still recovering beyond the twenty minute period and therefore equilibrium conditions had clearly not been established. In order, therefore, to identify the new equilibrium values for CO_2, several runs were carried out, and left for several hours. Figure 6.6 shows the pressure recovery for two different operating conditions. In the first case, figure 6.6a, CO_2 was bubbled through the water for 120 minutes, at a pressure of 10 barg, ambient temperature, and a gas flow rate of 100 l/min. The steady state was reached just after an hour later. In fact, the curve, although steep until 1200 secs, levelled off quite suddenly. The reading recorded at 1200 secs was 97% of the true equilibrium value. This degree of equilibrium was also observed in the second case, figure 6.6b, where CO_2 was bubbled through the liquid for 60 minutes at a pressure of 5 barg. The reading at 1200 secs was 94% of the true equilibrium value. It was neither feasible, nor practical, when the main region of interest took place in the first few minutes to leave each CO_2 experiment for several hours in order to reach equilibrium. For those experiments where the run was recorded for a period of 20 minutes after depressurization only, the true equilibrium value, when required, was determined by extrapolation. Similarly, obtaining a fully saturated solution of CO_2 every time was not feasible, and would have proved costly. Experiments were carried out with a bubbling time of 15 minutes as standard, and the degree of saturation when required, was estimated.

Having established that CO_2 is not fully saturated, even after bubbling for 2 hours, increasing the time for which the liquid is exposed to the gas increases the amount of gas in solution initially, which is reflected in the increasing values of p_f with degree of saturation. Figure 6.7 shows the plots obtained by increasing the bubbling time for CO_2 in water. The increased amount of gas in solution, and thus the volume evolving, was significant in terms of the final pressure recorded and the gross mass evolution during the initial rapid pressure recovery. The initial rates of recovery ranged from 0.12 bar/sec for an initial bubbling time of 5 mins, to 0.41 bar/sec for a bubbling time of 120 mins. The driving force, being the extent of disequilibrium, which is larger for the increased bubbling times. The degree of saturation had no significant influence over the velocity of the piston. The maximum velocities recorded in each case were reached within the first quarter of the piston travel, ~0.4 secs of starting out. The minimum pressure, p_{min}, in each case, was reached within 1.5 secs of starting depressurization. The p-V plots were not influenced by the degree of saturation. The values of n were in the region 1.07 ±0.04. The deviation of the curves beyond 4.5 litres, was a result of the piston hitting the reed switch and slowing down the piston over the final part of its journey. Up to that point the free gas volume increased approximately uniformly with time.

The same set of experiments were then carried out with CO_2 in water at an initial saturation pressure of 20 bara, gas flow rate of 100 l/min and ambient temperature, figure 6.8. The characteristics were found to be much the same. The piston velocity-time and p-V plots were the same for the three bubbling times, giving a value of n around 1.16. The effects of pressure, volume and temperature on the value of the index, n, are discussed in chapter 7.2.2.

Similarly, for the less soluble gases it was established that for the same initial saturation pressure, the length of bubbling time, and hence degree of saturation had no influence over the velocity of the piston, the initial growth rate, nor the approach to equilibrium. The value of p_{eqm} increased up to full liquid saturation, beyond which it remained constant, regardless of increased bubbling times. Since the plots, obtained for N_2, O_2 CH_4 and Ar showed similar characteristics as a result of increasing the bubbling time, only the plots for O_2 have been included, figure 6.9.

6.4 Comparison of gases in water

A comparison of the various gases in water, under the same bubbling conditions of 15 mins, at a flow rate of 100 l/min, saturation pressure of 10 bara and ambient temperature, can be seen in figure 6.10. With CO_2, in addition to being more soluble, and therefore recovering to a higher pressure, the most significant difference was the length of time taken to reach the new equilibrium. With the other gases, under all conditions, the final equilibrium was reached within 30 secs of depressurization. Using CO_2, however, the pressure recovery was still continuing at 1000 secs. The approach to equilibrium of CO_2 was ~2 orders of magnitude slower than for the other gases. The p-V plots showed the same approximately isothermal behaviour, with a value of n of 1.07 for CO_2, 1.15 ±0.05 for N_2, O_2 and CH_4, and 1.28 for Ar.

There was also a reasonable difference in the velocity of the piston. The velocity-time plot indicated that in comparison with Ar, CH_4, and O_2, the piston reached a greater velocity with CO_2

in solution, and a lower velocity with N_2 in solution, which would appear to be a function of the gas in solution and not a function of the system, for in all the tests, the velocity of the piston was significantly and consistently lower for N_2 than for CO_2. This was slightly unexpected, since it was anticipated that the gas in solution would not influence the rate of piston movement, particularly since mass gas evolution occurs after the piston has stopped moving. The effects of gas on the piston velocity are discussed in detail in chapter 7.2.3. In each case, the maximum velocity was reached within 40 mm of the piston travel, figure 6.10c, and within 0.3 secs of the piston starting out for CO_2, Ar, CH_4, and O_2, and within 0.6 secs for N_2. The velocity-time and volume-time plots also showed a significant difference in the time taken for the piston to complete 80% of the full distance of travel, ranging from 1 sec for CO_2, to 1.4 secs for Ar, CH_4 and O_2 to 2.3 secs for N_2. The increase in volume with time was reasonably uniform over 80% of the distance of travel of the piston, figure 6.10e. The change in volume with time was calculated in each case, and found to be 3.66 l/sec for CO_2, 2.82 ± 0.04 l/sec for Ar, CH_4 and O_2, and 1.84 l/sec for N_2.

Similar trends were also observed from an initial saturation pressure of 5 bara, figure 6.11. The p-V plots for each gas could be superimposed and produced a value of n around 1.03. The velocities of the piston ranged from 78 mm/sec for CO_2 to around 50 mm/sec for Ar, CH_4 and O_2, and 37 mm/sec for N_2. The time taken for CO_2 to reach the new equilibrium state was again slower by ~2 orders of magnitude.

6.5 Effect of gas flow rate

For a partly saturated solution, the effect of increasing the flow rate of gas through the liquid, and hence the mass transfer rate, for a given saturation period, is to increase the amount of gas dissolved in solution. This is observed for CO_2 in water, figure 6.12, where the final pressure, p_f, was significantly larger for 133 l/min than for 33 l/min, as was the timescale of approach to equilibrium over the initial pressure recovery period. The reduction in pressure, p_i to p_{min}, was the same for each flow rate, but the initial growth rate following depressurization increased with increasing flow rate, ranging from 0.17 to 0.49 bar/sec for gas flow rates of 33 and 133 l/min respectively. The timescale of approach to equilibrium over the long term, however, was the same for each gas flow rate, taking ~200 secs to reach 80% of the total pressure recovery. The p-V plots and velocity-time plots showed identical behaviour, irrespective of flow rate.

The behaviour for saturated solutions was different. Following exposure for 15 minutes, solutions of Ar, CH_4, O_2 and N_2 in water were completely saturated, and as a result, increasing the flow rate of gas through the liquid would have no effect on p_{eqm} and indeed, this was found to be the case. Increasing the gas flow rate during saturation had no significant effect on the p-t, p-V or velocity time plots for the less soluble gases.

6.6 Effect of initial saturation pressure

The solubilities of gases increase with increasing pressure. The data obtained for CO_2, with increasing saturation pressure is shown in figure 6.13. The main differences observed in the pressure-time histories, as a result of increasing the initial saturation pressure were evident in terms of the minimum pressure, p_{min} recorded, and the final equilibrium position, p_{eqm}, reflecting the amount of gas in solution initially. The increased pressure in the lower chamber was found to have a drastic effect on the velocity of the piston, figure 6.13c, and hence the time taken for depressurization to occur. From an initial pressure of 28 bara, the piston reached a maximum velocity of 433 mm/sec compared to that of 237 mm/sec from 11 bara, and 78 mm/sec from 6 bara. In each case, the maximum velocity of the piston was reached within the first 1/4 of the full distance travelled (~60 mm), after the pressure had dropped by at least 50% (70% for 28 bara), beyond which it dropped off steadily. The piston came to rest at its final position within 1-4 seconds of p_{min} being reached.

In each case, the increase in the free gas volume during depressurization was reasonably uniform over the initial 80% of the piston travel, but occurred at different rates. Those rates for 28, 20, 11 and 6 bara were 7.1, 6.1, 3.7 and 0.6 l/sec. As shown in figure 6.6, recovery, although still climbing steadily at 1200 secs, does drop off quite rapidly beyond 2000 secs, reaching a plateau soon after. The slopes of the p-t plots in the latter stages of pressure recovery ran reasonably parallel. There appeared to be no significant changes to the shape of the p-V curve, when normalized, although the equation when fitted to each set of data showed a small increase in the value of the index, n, with increasing initial saturation pressure, ranging from 1.03 from an initial pressure of 6 bara to 1.15 from 28 bara.

The same effects on the rapid depressurization and pressure recovery occurring as a result of increasing the initial saturation pressure from 10 to 20 bara would be expected for the other gases, if not quite so significant. This was not carried out for two reasons. Firstly the standard regulators for N_2, O_2 and Ar are not designed for pressures exceeding 12 bara, and secondly, being sparingly soluble, an excessive amount of gas would be required as most of the gas would go straight through the liquid and out of the vessel. Safety restrictions prevented the use of CH_4 at 20 bara. Instead, experiments were carried from initial pressures of around 5 bara initial pressure, and the results were pretty much as expected, as shown in figure 6.14, for Ar. At 5 bara initial pressure, the smooth operation of the piston indicated that there were no signs of stick slip. For each gas, increasing the initial saturation pressure had the effect of increasing p_f. There was no significant change in the shape of the p-V plots with increasing initial saturation pressure, and the velocity-time plots showed a decrease in the velocity of the piston by a factor of around 4. The maximum velocity was reached within 30 mm of the piston travel, irrespective of saturation pressure.

6.7 Effect of initial temperature

The solubility of gases in water decreases with an increase in temperature. It would be feasible, therefore, to expect the results recorded at elevated temperatures to show significant signs of a decrease in gas solubility. In fact, the final equilibrium pressures recorded after 20 mins showed signs of reaching the same value of around 5.2 bara, figure 6.15. Also significant, was the increase in the rate approach to equilibrium with increasing temperature. Looking at the approach to equilibrium in more detail, at 60°C, the time taken for 20, 50 and 80% of the total pressure recovery was 1.4, 2.5 and 4.5 secs respectively, compared with 1.4, 5 and 180 secs respectively at ambient temperature. During the latter stages, 100-1000 secs, the approach to equilibrium at elevated temperatures was faster by a factor of 40. There were no significant differences in the p-V or velocity-time plots with increasing temperature.

The heater was usually turned off immediately prior to depressurization to reduce the influence the convection currents may have had on the rate of bubble evolution, since the thermal mass of the bulk liquid and the stainless steel maintained the temperature sufficiently over the 20 minute period. An experimental procedure was carried out at the elevated temperature to study the effects, if any, convection currents from the heating element had on the approach to equilibrium. The heater was left on during the whole run. Not unexpectedly, there were no significant differences in the plots obtained, although convection currents were visible over the latter stages of the run, but by then equilibrium had been reached.

Similar characteristics were apparent as a result of increasing the initial temperature for a CO_2 in water system from an initial saturation pressure of 20 bara, figure 6.16. Towards the end of the recorded pressure recovery period, the final pressures were approaching the same equilibrium value. From an initial pressure of 20 bara, and liquid temperatures of 45°C and 60°C, 80% of the total pressure recovery had occurred within 10 secs of depressurization, compared to 280 secs for CO_2 at ambient temperature. Again, there were no significant differences in the velocity-time and volume-time plots with an increase in temperature. For the sparingly soluble gases in water, the data recorded at the two temperatures, 20 and 60°C showed similar characteristics in all respects.

6.8 Investigation of gas temperature

In all the previous experiments, the temperature of the liquid was monitored during each run and had shown no signs of a change in the temperature of the bulk liquid during depressurization. A series of tests were also carried out, to investigate any significant changes in temperature which may occur in the gas phase during depressurization.

In order to get some idea of the change in gas temperature during gas expansion, the vessel was filled to two different levels below the platinum resistance temperature probe. The gas expansions in each case were 2.4 litres to 6.6 litres and 3.6 litres to 7.8 litres. Gas temperatures were monitored during depressurization from two initial saturation pressures of 10 and 20 bara, and for the two gases, CO_2 and N_2. The data recorded from these experiments can be seen in figure 6.17. The readings in the gas phase during depressurization and during subsequent pressure recovery confirmed a temperature drop of a few degrees (4-7°C), over a period of 30-40 seconds following depressurization, followed by a gradual recovery to, or somewhere approaching, the initial temperature. The temperature drop was found to be dependent upon the initial temperature, figure 6.17a, and pressure, figure 6.17b, of the system and the initial free gas volume, figure 6.17c. Using N_2 instead of CO_2, figure 6.17d, had no apparent effect on the gas temperature. During the depressurization of the vessel, as the pressure dropped from p_i to p_{min}, the temperature remained relatively constant. The temperature dropped significantly as the pressure was recovering, by which time the volume expansion had been completed and the piston was at rest. The minimum temperatures in each case were recorded ~ 30 seconds after p_{min} was reached. This delayed reaction of the temperature in the vessel was probably due to the thermal inertia and impedance of the heat flow through the steel pocket to the probe.

Immediately after the depressurization process was initiated, a thick mist was seen above the liquid. In the case of CO_2, the mist seemed to clear ~6 minutes after depressurization, and was completely gone after 10 minutes. With N_2, the mist was not quite so heavy, and had cleared after just 4 minutes. The mists had probably formed as a result of the water vapour in the gas phase dropping below the dew point, thus condensing to form liquid droplets. In fact, the temperature drop recorded in the gas phase was very much less than the actual temperature drop calculated for the volume expansion and pressure drop occurring in the vessel. The main reason being that the mass of gas in the system is extremely small (~0.01%) in comparison with the surrounding mass of steel and indeed the bulk liquid.

6.9 Investigation of gas pressure

It was investigated early on whether the pressure readings recorded in the gas phase were identical at all times during an experimental run, particularly during the depressurization process, with the pressure recorded in the liquid phase. The interest lay in the rates at which the pressure in the gas and liquid phases dropped and to what pressures the gas and liquid phases dropped, and indeed, if there were any time delays between the pressure recorded in the gas phase and that recorded in the liquid phase. The transducer in the liquid phase was situated approximately half way down the bulk liquid in the vessel. A transducer screwed into the link pin at the head of the piston shaft confirmed that the pressure readings in the liquid and gas phase were more or less identical (±0.01 bar), under all initial conditions of starting pressures, 5,10 and 20 bara, temperatures, 18 and 40°C, and gas volumes, 0.8, 2.4 and 3.6 litres. In fact, any differences could only really be caused by hydrostatic or temporal acceleration effects, and would therefore be very small. The differences may, however, be measurable during the mushrooming effect, using more sensitive instrumentation.

6.10 Effect of initial free gas volume

The effect of the initial free gas volume above the liquid was determined simply by changing the level to which the vessel was filled. A state of minimum initial gas volume between the piston, at its lowest position, and the water level was achieved by initially filling both the piston shaft and the hydraulic hose leading to the lower chamber vent valve with water. Naturally, as the gas was bubbled through, a small volume of water, estimated to be ~0.01 litres, was displaced out of the vent. The series of tests were carried out using CO_2, with initial free gas volumes of 0.01, 0.8

(standard), 2.4 and 3.6 litres, from an initial saturation pressure of 20 bara. The results can be seen in figure 6.18. Equilibrium was clearly reached much sooner when the gas volume was minimal. The pressure-time history shows that equilibrium pressure was reached after ~600 secs with an initial free gas volume of 0.01 litres, compared to those obtained with initial gas volumes of 0.8, 2.4 and 3.6 litres, where the pressures were still recovering beyond 20 minutes. The p-V plots were also shown to be influenced by the free gas volume initially. The value of n in the equation pV^n=constant became smaller with increasing free gas volume, ranging from 1.16 for 0.01 litres of free gas to 1.02 for 3.6 litres of free gas initially.

Similar results were obtained in comparing a N_2 in water system from two initial starting volumes of 0.8 and 0.01 litres, figure 6.19. The most striking differences in the p-t histories were in the values of p_{min}, the velocity of the piston, and the final pressure readings. Figure 6.19b shows the rapid depressurization of the two systems. The pressure drop, p_i to p_{min}, occurred over a period of 2.9 secs with an initial free gas volume of 0.8 litres, compared to 4 secs with a minimum free gas space. The velocity-time traces show the maximum velocity recorded with an initial gas volume of ~0.01 litres was approximately the same as that recorded with 0.8 litres of free gas initially. What was significant, with an initial free gas volume of 0.01 litres, was the rapid drop in velocity, beyond the initial 50 mm of travelled, as the pressure in the vessel was approaching atmospheric pressure, indicating a sub-atmospheric vacuum was being drawn in the lower chamber, and the fact that the piston did not reach the top, stopping 50 mm short. Again the value of n obtained from the p-V plots became smaller with increasing free gas volume initially.

6.11 Effect of piston velocity

To date, the velocity had so far only changed as a result of changing the initial test conditions, in terms of, for example, the initial saturation pressure and the particular gas in solution. In addition to investigating the effects these parameters had on the rate of piston movement, some interesting results were obtained by controlling the rate at which the piston moved the full distance of travel. The effect of piston velocity on the evolution of CO_2 can be seen in figure 6.20. Besides the normal 6 barg air pressure supplied to the pneumatic cylinder, the regulator was also set to 4, 2 and 0 barg. The velocity of the piston was reduced from a maximum of 240 mm/sec with 6 barg pressure, to 28 mm/sec with no supply of air to the cylinder. In all cases the maximum velocity was reached ~0.4 secs after depressurization was initiated. The effect of reducing the velocity was apparent in the value of p_{min} recorded, and more significantly, in the shapes of the pressure-time histories obtained. The visual observations of the activity in the vessel with 6 barg and 0 bar air regulator pressure were also markedly different.

With the air regulator pressure set at 4 barg, the traces were similar to those recorded with a 6 barg pressure. In both cases the piston came to rest ~2 secs after depressurization. The pressure drop, p_i to p_{min} was, however, smaller, and the initial volume of bubbles rising to the surface following depressurization appeared to be less. The rising mushroom of gas was evident, together with the small rush of bubbles to the surface. When the air pressure was reduced to 2 barg, however, different characteristics were observed.

The characteristics of the plots obtained at 2 and 0 barg air regulator pressure were similar. There were very few signs of gas evolution immediately after the opening of the solenoid dump valve. During the first minute, as the pressure in the vessel dropped from the initial 10 bara pressure to ~5 bara, a few occasional small bubbles rose to the surface, but the bulk of the liquid was still. A mushroom of gas, as such, was not observed, indicating that the mushroom of gas is a function of the rate of pressure release. As the pressure carried on dropping, several large bubbles (5-8 mm) started to rise from somewhere near the base of the vessel to the surface. With time, as the pressure dropped to p_{min}, the frequency of the bubbles significantly increased, resulting in steady streams of bubbles, ~ 1-3 mm in diameter, rising to the surface. With no external air supply, the pressure reached a minimum around 200 seconds, remaining there until the piston came to rest. From then onwards, the pressure rose, and the frequency of bubbles gradually slowed. Throughout the course of the run, there very few bubbles and hence very little activity on the vessel walls. With a 2 barg air supply to the pneumatic cylinder, the piston took less time to travel the full distance, during which time the pressure dropped gradually. Beyond 100 secs, once the piston had stopped moving, the pressure rose to the same equilibrium position. The pressure-volume plots followed approximately the same curve over the initial part of the gas expansion (up to ~2.5 litres).

Not unexpectedly, in all cases, the pressure recovered to the same equilibrium pressure, confirming that the equilibrium pressure is a function of the amount of gas in solution initially, which is the same in each case. From ~300 secs onwards, the traces all followed the same course, figure 6.20a. It is in the 15-300 second period during which the behaviour differed, which can be related to the piston position with respect to time, for, in nearly all cases, the piston was at rest beyond 200 secs.

From an initial saturation pressure of 20 bara, the p-t traces for CO_2 in water, obtained with the regulator pressure set to 6 barg and 0 barg, were similar in all respects. The maximum velocity dropped from 343 mm/sec with 6 barg air pressure to only 253 mm/sec with no air pressure, owing to the larger initial pressure in the lower chamber supporting the upward movement of the piston. The piston came to a complete stop after 3 secs, compared to that of 4 secs for 6 barg air pressure.

The effect of the piston rate on bubble evolution was also monitored for all the other gases, from an initial saturation pressure of 10 bara, ambient temperature and with the air pressure regulator set to 0 barg. Figure 6.21 shows the results obtained for CH_4. The initial pressure drop was the same ($\sim$4.5 bar) in all cases, suggesting that the larger part of the volume of gas in solution (more for CO_2 than, for example, N_2) does not participate at this stage. Again, there seemed to be a point, related to the drop in pressure, beyond which the bubbles started evolving. This threshold was likely determined by the actual magnitude of the pressure drop, which appeared to be around 6 bar. The maximum velocity of the piston was also reduced by a factor of $\sim$10.

In each case, over a period of 1000 secs, the pressure dropped, as the piston continued to move upwards, to a pressure somewhere close to the equilibrium pressure and remained there. The main significance with the less soluble gases was the fact that the piston did not travel the full distance. There was not enough upward force, from the gas coming out of solution, to complete the journey. With N_2 and no air regulator pressure, the maximum velocity recorded was only 6.2 mm/sec. The piston came to rest 400 secs after depressurization, after travelling only 130 mm, 110 mm short of the end, indicative of a very low pressure in the cylinder. At this point, the free gas volume was only 2.75 litres. Similarly with Ar, CH_4 and O_2, the piston stopped around 1000 secs after depressurization, 40 mm short of the total distance. At the end of the CH_4 experiment, the piston was raised manually by providing some air flow into the lower section of the pneumatic cylinder. When the final 40 mm of the piston movement was completed, the pressure reading was 2.06 bara, which corresponded to that recorded with a 6 barg air regulator pressure during depressurization.

The visual observations were the same for these gases as for CO_2. There was a very small bubble front at the surface, followed by 2 or 3 bubbles, approximately 3-5 mm in diameter, rising to the surface. The bulk liquid was then still for many seconds, and as the pressure continued to drop, very small bubbles, $\sim$0.5 mm in diameter (smallest visible to the human eye) were observed in the liquid, rising to the surface, not, however, breaking it. These bubbles again appeared with increasing frequency, with time. There did not appear to be as many bubbles in comparison to CO_2, and they appeared to die away sooner. Occasional larger bubbles, ~5 mm in diameter, rose to the surface. During the period, 5-15 minutes following depressurization, around 50 of these larger bubbles were recorded per minute. The frequency of the bubbles gradually died away, (~500 secs+), although even at p_f, a few bubbles were still visible, but had no effect on the pressure or piston position.

6.12 Effect of salinity

An interesting reproducible set of data was collected for CO_2 in tap water and various salt solutions. Data was collected for CO_2 from an initial saturation pressure of 10 barg, ambient temperature and flow rate of 100 l/min, in tap water and 3, 25, 50 and 100 saturated salt solutions. The North Sea typically has a salt saturation of around 10%. The equilibrium pressures, recorded after 20 mins, were found to increase slightly, with increasing salinity up to 25% saturation beyond which the equilibrium pressures dropped off with increasing salt saturation, figure 6.22. This was slightly unusual, as the solubility of CO_2 in salt solutions decreases with increasing salt saturation, figure I-6. It would seem feasible, therefore, to expect the equilibrium pressures to decrease with increasing salt saturation. It was also interesting to note that the relative degree of saturation with respect to bubbling time for a 50% saturated salt solution was strikingly similar to that using tap water, figure 6.23. For the same bubbling time, a higher degree of CO_2 saturation is reached in a fully saturated salt solution than in tap water.

Figure 6.24 shows the plots obtained with increasing salinity. It has been established that the final equilibrium pressure for CO_2 in water under these conditions would continue to rise to 5.2 bara, an increase of 0.2 bar on the reading obtained at 1200 secs. This equilibrium value of 5.2 bara was still less than that obtained for a 3, 25 or 50% saturated salt solution. In terms of the approach to equilibrium, recovery to 80% of the final equilibrium pressure in tap water was slower than that of 3, 25 or 50% salt solutions by a factor of nearly 20, 180 secs in tap water and 8-10 secs in 3, 25, and 50% saturated salt solutions. In a 100% saturated salt solution, recovery to 80% of equilibrium was slower by a factor of 3 compared to that for CO_2 in tap water. The effects of salinity on the equilibrium values and the rates of approach to equilibrium are discussed in chapter 7.3.1.4.

In terms of the visual observations with salt solutions, the most significant differences observed were in the sizes of the bubbles. In the presence of salt, the bubbles were very much smaller and appeared to be more numerous after rapid depressurization. Being smaller, their movement to the surface was a lot slower. Indeed, the tiny bubbles seemed almost 'suspended' in solution. In comparison to a CO_2/water solution, everything appeared to be in slow motion. There was also much less activity on the walls, very few, if any explosive bubble growths, and no bubble coalescence on the walls. The bubbles which occupied the vessel wall space remained there throughout. The majority of bubbles in the bulk liquid, following the sudden initial rush, upon reaching the surface, did not cause a break in the surface. Looking at the liquid surface from below, it was possible to see the very small bubbles bursting as they hit the underside of the surface, whereas, from above, the surface remained still, suggesting a larger interfacial tension.

The same experiments were carried out with CH_4, figure 6.25, N_2 and Ar in tap water and NaCl salt saturations of 25, 50 and 100%. Whilst a very small increase in p_f, (1-2%) was observed in a 25% saturated salt solution compared to that in water it cannot really be considered significant. It would appear, therefore, that the addition of salt to these inert, non polar gases in water has no influence on the amount of gas in solution nor on the rate of approach to equilibrium. In terms of visual observations, again, there were a number of very small bubbles rising slowly to the surface. The bubbles appeared to be more numerous for Ar and CH_4 and to continue for longer, in comparison with N_2. Again, the bubbles did not break through the surface.

In terms of the temperature effects on the rate of evolution of CO_2 from a 25% saturated salt solution, the characteristics were similar to those observed for CO_2 in water. An increase in the timescale of approach to equilibrium was observed. The time taken to reach 80% of the total pressure recovery, with CO_2 in a 25% saturated salt solution, was halved at 58°C compared to the time taken at ambient temperature. The final equilibrium value was the same (within 0.3 bar). The effect of temperature had no influence over the p-V plots nor the velocity of the piston.

6.13 Effect of gas evolution on pH

The data obtained with regard to pH was somewhat disappointing. The pH of tap water is generally around 7. In these experiments, the pH was 6.7. The pH of a saturated CO_2 in tap water solution is around 5. The pH was logged during saturation at 5 bara and ambient temperature, at a gas flow rate of 100 l/min, for bubbling periods of 15 and 120 mins. The pH was also monitored during depressurization and during the approach to equilibrium. During saturation, the pH dropped steadily over a period of 10 mins to the new pH, where it remained over the rest of the saturation period, even after 120 mins bubbling. It was thought that there might be a small increase in the pH after depressurization as CO_2 left solution. There was, however, no increase observed, under any circumstances. The only change in pH observed over the whole duration of the run was the drop of ~1.5 units, from 6.7 to 5.1, during the initial saturation period, where it remained regardless of the activity in the vessel.

6.14 Effect of solid nuclei

The intention of adding insoluble nuclei into the system was to significantly increase the number of nucleation sites available for the evolution of gas. As a rough estimate, the surface area of the inside walls of the vessel in contact with the water was calculated to be approximately 0.4 m^2. With the addition of 500 ppm 5μm uni-sized silica flour particles into the water, the surface area available for nucleation was estimated to increase by a factor of 4, to 1.6 m^2. The surface texture of individual 5μm particles, viewed under an electron microscope, can be seen in plate II.

Figure 6.26 shows the effects the presence of 500 ppm and 1000 ppm insoluble nuclei have on the rate of gas evolution following depressurization. Of particular interest was the initial rate of gas evolution from the solution over the first few secs, and, indeed, there were signs of a significant increase in the rate of evolution due to the presence of solids. The initial pressure recovery rate over the first 2 secs was 0.4 bar/sec in water compared to 0.1 bar/sec with 500 ppm solids. The time taken to reach 50% and indeed 80% of the total pressure recovery was halved in the presence of 500 ppm solids compared to water. There were no significant differences, in terms of the equilibrium pressure, the p-V plots or the velocity of the piston, due to the addition of the solid nuclei into the vessel. With a solids concentration of 1000 ppm, the characteristics were similar, in all respects, to those observed for 500 ppm, suggesting there exists a threshold level beyond which increasing the concentration of nuclei has no effect on the rate of gas evolution. This is discussed in chapter 7.3.1.2.

With the other less soluble gases, such as N_2 and CH_4, there were no significant increases observed in the rate of evolution with the addition of solid nuclei. This, again, is discussed in chapter 7.3.1.2. There were also no significant changes to the value of p_f, the p-V plots, or the velocity-time plots with increasing solids concentration.

6.15 Effect of fluid agitation

This section explores the effect of fluid agitation in the vessel. The main aim was to achieve a system which was in a dynamic state, in order to study the evolution of gas from solution when the process was largely diffusion controlled (quiescent evolution) compared to one which was dynamically controlled (agitated evolution). Unfortunately, due to the problems mentioned in chapter 4.3, a state of reproducible and variable turbulence could not be achieved. Instead, a dosing pump, connected to the inlet and outlet in the base flange, provided a pulsed jet into the vessel at a frequency of ~60 Hz.

Figure 6.27 shows the effects of fluid agitation on the evolution of CO_2 from water. In addition to a condition of no agitation (case 1), and agitation of the liquid over the course of the whole run, (case 4), the plots also show the results for agitation during saturation only (case 2), and during the approach to equilibrium only (case 3). In the latter case, the pump was turned on immediately prior to the opening of the control valve. These plots, especially, helped to determine the effects the pump had on gas dissolution and evolution.

Clearly, agitation had a significant effect on the evolution of CO_2 from the solution. An increase of 25% in the final equilibrium pressure was achieved as a result of applying a degree of agitation to the system in the vessel over the course of the whole run. Figure 6.27d shows the relative rates of approach to equilibrium in each case, in terms of the percentage pressure recovery. In the latter stages of pressure recovery, the approach to equilibrium was ~ 5 times faster in the dynamic conditions. There were no significant differences in terms of the piston velocity, the p-V plots, nor in the time taken for depressurization to take place.

In order to investigate whether the rise in the equilibrium value was a result of agitation during saturation or a result of agitation after depressurization or indeed a combination of the two, comparisons had to be made with the partly agitated systems, in which two systems with the same initial free and dissolved gas content could be compared. Whereas it cannot be assumed, at this stage, that there was the same quantity of dissolved gas present initially in cases 1 and 4, it could be assumed that the total mass of gas initially present in cases 1 and 3, under the same bubbling conditions, was the same. A comparison of the two sets of data show a dramatic increase in both the value of p_f itself, and the timescale of approach to equilibrium, demonstrating the differences must be a result of the agitation after depressurization, since neither systems were agitated before depressurization, nor were there any significant increases in p_f or the rate as a direct result of agitation during saturation only (comparing cases 1 and 2). An increase of 23% in the final equilibrium pressure was recorded in the agitated approach to equilibrium. The approach to equilibrium was ~5 times faster as a result of fluid agitation. Similarly, in cases 2 and 4, for the same initial quantity of dissolved gas, the rate of approach to equilibrium was faster in a dynamic system, by a factor of 6, compared to that in a system with no external agitation.

The effects of fluid agitation on the other gas/water systems tested were found to be similar. With gases such as CH_4 and N_2, in which the system was assumed to be fully saturated, fluid agitation had no influence over the amount of gas in solution initially. What was apparent, however, was the increase in p_f with agitation after depressurization. In N_2, for example, an increase of 22% in the final equilibrium pressure was observed. The timescale of approach to equilibrium was not visibly increased, for in a system with no external agitation, equilibrium is reached relatively quickly anyway. In accordance with the effects of fluid agitation on the evolution of CO_2 in water, and indeed as expected, agitation after depressurization had no influence over the p-V plots or the velocity-time plots recorded during depressurization.

6.16 Effect of fluid agitation and solid nuclei

In this section, the agitation of a CO_2/water system containing 500 ppm insoluble nuclei, in the form of 5μm silica flour particles, was investigated. It has been established, section 6.14, that the rate of approach to the new equilibrium state is doubled in the presence of solids. Figure 6.28 shows the plots obtained as a result of agitating the same system, water containing 500 ppm solid nuclei, and confirmed the behaviour observed for CO_2 in tap water as a direct result of fluid agitation, figure 6.27. As predicted, a significant increase in the rate of pressure recovery, by a factor of 5, was observed as a result of fluid agitation.

Figure 6.29 combines the data obtained from a system with no additional nuclei or agitation (case 1), from a system with 500 ppm solids and no agitation (case 2), a system using tap water, no additional solids, which was agitated over the duration of the whole run (case 3) and a system in which water, containing additional solids was agitated, again over the whole run (case 4). In both a system with no agitation, (cases 1 and 2) and a dynamic system (cases 3 and 4), the new equilibrium value was not affected by the presence of solids. In addition, the effects of solids and agitation on the rate of gas evolution did not appear to be additive, for the addition of solids to an already agitated system (cases 3 and 4), did not increase the rate of gas evolution any further. The effects of agitation during the approach to equilibrium using other gases, such as CH_4, figure 6.30, and N_2, showed similar characteristics as that for CO_2 in water.

6.17 Effect of mixed gases

This section explores the behaviour of a system in which the liquid has been saturated with a gas of mixed composition. The pre-mixed gas compositions selected were a 30% N_2 in CO_2 composition, and a 30% CO_2 in N_2 composition. The behaviour of these two mixed gas compositions in water were investigated and the results shown in figures 6.31 and 6.32. Saturation of the liquid with gas is a key factor when calculating the masses of free and dissolved gas initially. Exploratory tests into the degree of saturation of the 70% CO_2/30% N_2 mixed gas composition with bubbling time indicated saturation was achieved after 30 mins bubbling. The following tests were therefore carried out after bubbling for 30 mins.

Figure 6.31 shows the plots obtained following the depressurization of the 70:30 CO_2:N_2 mixed gas composition. Also displayed in the figure is the data obtained for a CO_2 in water system from an initial pressure of 7 bara, and a N_2 in water system from an initial pressure of 3 bara. It cannot be assumed, and indeed has been shown not to be the case, that the ratio of CO_2:N_2 in the gas phase at the final equilibrium state is in the ratio 70%:30%. The calculations to determine the ratios of CO_2:N_2 in the final equilibrium state, have been described in appendix III. Briefly, assuming the liquid in the vessel was fully saturated, using a gas cylinder containing the mixed gas composition in the ratio 70:30, it can be assumed that at the initial steady state conditions, before depressurization, the partial pressures of the gases in the gas phase, and hence in the liquid phase, are in the ratio 7:3. The masses of free gas and dissolved gas initially can therefore be calculated. Assuming conservation of the total mass of gas during depressurization, the partial pressures of the gases in the gas phase at the new equilibrium can be calculated for each possible percentage CO_2:N_2 composition. By a process of deduction, explained in the appendix, the gas ratios at equilibrium can be calculated. In this case, the final equilibrium ratio was calculated to be in the ratio 88% CO_2 to 12% N_2.

The results showed that the equilibrium was reached faster with a mixed gas composition. With CO_2 alone, the equilibrium pressure was still rising after 20 mins. The rate of approach to equilibrium for the mixed gas composition was faster by a factor of ~5, compared to that for the 7 bara CO_2 system. In terms of the final equilibrium pressures, the pressure reached by the mixed composition was found to be approximately equal, within 10%, to the sum of the equilibrium pressures of the two individual components at the same pressure as they appeared in the mixed composition initially.

In the same way, the data for the 70% N_2: 30% CO_2 mixed gas composition was analysed. The p-t plots for depressurization of a fully saturated solution of the mixed gas, together with the plots obtained for a CO_2 in water system from an initial pressure of 3 bara, and a N_2 in water system from an initial pressure of 7 bara are shown in figure 6.32. The final gas composition was calculated to be in the approximate ratio 60% CO_2:40% N_2. The plots showed similar characteristics to that of the 70% CO_2:30% N_2. Again, equilibrium was reached much sooner with the mixed gas system. As a result of the increased pressure in the lower chamber, the velocity of the piston was faster for the mixed gas composition than for 7 bara CO_2 and 3 bara N_2. Again, the final pressure of the mixed gas composition was approximately equal to the sum of the equilibrium pressures obtained in the single component systems, from that initial pressure at which they existed in the mixed composition initially.

The effects of initial temperature and saturation pressure, flow rate, piston velocity and salinity on the mixed gas composition in water were all investigated and shown to follow the trends observed for a single gas in water. The behaviour of the 70% N_2 mix tended to follow the behaviour characteristic of N_2 and the 70% CO_2 mix tended to follow the behaviour characteristic of CO_2. This was particularly evident in the results obtained by reducing the piston velocity, figure 6.33. With CO_2 as the major component, figure 6.33a, with no external air supply, the pressure dropped to a value below that obtained with 6 barg air regulator pressure. The minimum pressure, p_{min}, was recorded at ~600 secs, by which time the piston had reached the end of its full distance of travel, beyond which the pressure started to climb to the new equilibrium state, coinciding with that pressure observed with 6 barg regulator pressure. With N_2 as the major component, figure 6.33b, with no external air supply to the pneumatic cylinder, the pressure dropped to a value just above that predicted, since the piston, which reached a maximum velocity of 20 mm/sec, again stopped short of the end.

6.18 Visual and photographic observations in kerosene

The sequence of events occurring in the vessel during depressurization were captured using a video camera. The set up of the camera was the same as that used to record the process in water. The process was observed by back lighting the vessel using a 500W lamp. As the lamp was only turned on for ~30 secs for each run, the heating of the liquid by the lamp was considered negligible. The oil used in the study was kerosene, being transparent. With gas oil and Statfjord crude being highly coloured, it was difficult to observe any of the events in gas oil and crude, even with powerful back-, side, or front- lighting. The operating conditions and procedure were kept the same as used for water. The two gases used were CO_2 and N_2. The system was isolated, establishing a steady state in the vessel before the control valve was opened, initiating depressurization. The still photographs, taken from the television screen, can be seen in plate VII for CO_2, and plate VIII for N_2. The timescale, in secs, is given below each photograph.

The mechanisms of gas release, following the opening of the control valve, showed certain characteristics similar to that of water, and certain features characteristic only of oil. After saturating for 15 mins with CO_2, and releasing the pressure, the propagation of a bubble front into the bulk liquid was observed. This front travelled a maximum of ~30 mm (±2 mm) into the bulk liquid (plate VII, 1-3), over a period of 0.12 secs, with an initial velocity of 0.75 m/sec (±0.05 m/sec), before retreating back to the surface (plate VII, 4 and 5). As observed with CO_2 in water, there was a short period of ~0.24 secs (plate VII, 6-10), during which there was relatively little activity in the vessel. There were very few bubbles on the vessel walls at any time.

The most significant difference, in comparison with water as the solvent, was the absence of the mushroom of gas from the base of the vessel. Instead, over a period of a second, bubbles appeared with increasing frequency, first from the vessel walls, (plate VII, 11-17), and then with mass evolution from the bulk liquid (plate VII, 18-30). During this time, the back lighting was gradually blocked, firstly from the densely populated regions at the vessel walls, (plate VII, 18-21), and then by the mass of bubbles evolving in the bulk (plate VII, 22-30). The light was completely blocked for ~3 secs, following which light became visible from the base upwards as the mass of bubbles started to clear (plate VII, 31-34). Once the tail end of the bubble mass had reached the surface, streams of bubbles rising to the surface became apparent, which gradually died away over the following 10 secs (plate VII, 35-40). Approximately 30 secs after the depressurization event had taken place, the bulk liquid was virtually motionless. Occasional bubbles were observed, however, travelling at ~150 mm/sec (plate VII, 41 and 42).

In terms of the pressure-time history recorded for that particular run, figure 6.34, the time taken for the pressure to drop from the initial to the minimum pressure was 1 sec. The photographs, 1-

20, in plate VII depict the activity in the vessel during that 1 sec. Beyond that single second, as a result of the mass evolution from the walls and the bulk, the pressure starts rising, whilst the piston is still moving upwards. The piston came to rest 2.3 secs after depressurization was initiated. Beyond this point, (plate VII, 30), the population density of the bubbles starts to decrease. What was particularly evident from the p-t plot, was that evolution of CO_2 in oil occurred well before the piston had finished travelling, figure 6.34a. Indeed the minimum pressure was reached before the piston had completed even half the complete distance of travel. By the time the piston had come to rest, 70% of the pressure recovery had already taken place. This helps to explain the shape of the velocity-travel plot, figure 6.34b. The minimum pressure, p_{min}, recorded occurred at 98 mm. From that point onwards, the mass evolution of gas occurred and consequently, the velocity of the piston increased.

For a less soluble gas, the time taken to reach p_{min} was slightly longer. With N_2 in kerosene, figure 6.35, p_{min} was reached after 1.6 secs, at which point the piston had travelled 218 mm. The maximum velocity of the piston was recorded after just 0.4 secs, during which time the piston had travelled 40 mm. The piston took 2.5 secs to travel the complete distance, following which the pressure increased with time to the new equilibrium value over a period of around 30 secs. A significant difference between CO_2 and a less soluble gas such as N_2 in kerosene, was that whereas with CO_2 in kerosene a completely clear liquid was obtained immediately prior to depressurization, with N_2, (plate VIII, 1), on each of four runs recorded, using fresh batches of kerosene, tiny bubbles were visible in the bulk during saturation. There was little activity associated with these bubbles for they appeared to be almost suspended in the liquid. The bubble front at the surface was observed immediately after depressurization, progressing to a depth of 15 mm into the bulk liquid (plate VIII, 2-5), at a velocity of 0.375 m/sec (±0.05 m/sec).

Since there were bubbles already present in the liquid, the increasing frequency of bubbles appeared uniformly throughout the liquid rather than at the walls (plate VIII, 6-10). The dark patches did however appear first at the walls (plate VIII, 11-14), as the increasing density of bubbles blocked the back lighting. As with CO_2 the light was completely blocked for ~4 secs (plate VIII, 15-17), following which light became visible as the bubble mass cleared from the base of the vessel upwards (plate VIII, 18-21). The interface between the bulk mass and the liquid was estimated to be travelling up at ~80-100 mm/sec. Over the next 5-10 secs, the streams of bubbles gradually ceased (plate VIII, 22-26). Approximately 20 secs after depressurization, the new equilibrium value had been reached. The photographic observations of CO_2 and N_2 in kerosene and in water are discussed in more detail in chapter 7.2.1.

6.19 Comparison of CO_2 evolution from water, gas oil, kerosene and Statfjord crude

The data recorded during the rapid evolution of CO_2 from water, gas oil, kerosene and Statfjord crude (degassed for safety reasons) is displayed in the pVT plots shown in figure 6.36. In water, the pressure dropped to 1.87 bara compared, to 3.49 bara in kerosene. This was due to the fact that in kerosene, the pressure was recovering before gas expansion was complete. The value of p_{min} for CO_2 in kerosene was recorded when the piston had travelled 100 mm, whereas in water the distance travelled by the piston was 210 mm. By time the piston had travelled 80% of its journey, the pressure in the water was still dropping whereas in kerosene, just over 50% of the total pressure recovery had taken place.

The maximum velocity of the piston in water, 237 mm/sec, occurred 0.2 secs into depressurization, when the piston had travelled 40 mm. In kerosene, the peak velocity initially, was 100 mm/sec, which occurred ~1 sec into depressurization, when the piston had travelled 41 mm. Due to the rapid massive bubble evolution, however, the velocity of the piston increased towards the end of its travel, recording a maximum velocity of 137 mm/sec, 25 mm short of the complete distance. This is demonstrated quite effectively in the volume-time plot, figure 6.36c. The free gas volume increased reasonably uniformly with time, during depressurization, for both liquids. The gradients for water and kerosene were ~1.85 and 3.8 l/sec respectively. The gradient for kerosene, however, increased from 1.85 to 2.35 l/sec at the point where the velocity of the piston changed markedly, marked with a * on figure 6.36c, ~4 secs after depressurization.

The rate of approach to equilibrium in water was slower than in kerosene by ~2 orders of magnitude. The evolution of CO_2 from Statfjord crude showed much the same characteristics as CO_2 in kerosene, in terms of p_{min}, p_f and piston velocity. The approach to equilibrium, however, was slightly slower. Pressure recoveries were slower by a factor of ~2 in the crude compared with those in kerosene. The behaviour of CO_2 in gas oil showed tendencies similar to that of water, in terms of the piston velocity and the approach to equilibrium. The p-V plots, figure 6.36d, gave a value of n for kerosene (up to 2.8 litres volume) of 1.27 and for water of 1.07. In gas oil and Statfjord crude the values of n were 1.16 and 1.22 respectively.

6.20 Effect of bubbling time in gas oil and kerosene

Figure 6.37 demonstrates quite effectively the effects observed as a result of increasing the bubbling time of CO_2 through gas oil. As expected, the characteristics were similar to those observed in water, in that the equilibrium pressure increased with increasing degree of saturation, up to full saturation. The degree of saturation did not influence the piston velocity or p-V plots.

With CO_2 in kerosene, figure 6.38, or indeed Statfjord crude, there was comparatively little difference in the shape of the p-t plots or indeed the final equilibrium values, with increased bubbling time. Each plot had similar interesting velocity-travel plots, owing to the increased bubble activity in the vessel during depressurization, as reported in section 6.18. The p-V plot, for CO_2 in kerosene, over the initial volume expansion was independent of bubbling time and gave a value of n of 1.26 ± 0.02. Under certain conditions, particularly for large concentrations of gas in oil, light foaming was observed at the surface, but had completely cleared within one minute. The equilibrium value obtained, as a result of 15 mins bubbling CO_2 through kerosene, was 80% higher than in gas oil, owing largely to the increase in gas solubility.

The pressure-time traces were also recorded for Ar and N_2 in gas oil and CH_4 and N_2 in kerosene. The new equilibrium value for N_2, under the same bubbling conditions, was 20% higher in kerosene than in gas oil. There was little difference in the time taken to saturate water or kerosene with N_2. Indeed, if anything, saturation of kerosene took longer. The equilibrium plateau was reached sooner, but only by a matter of minutes, in kerosene, and crude, than in gas oil or water, which is not surprising due to the inert, sparingly soluble behaviour of N_2 in water. What was particularly evident with N_2 and Ar was the inactivity of the bulk liquid approximately 20-30 secs after depressurization, by which time the new equilibrium state had virtually been reached. A small amount of foaming was observed, but had cleared within seconds.

6.21 Effect of gas flow rate, saturation pressure and initial temperature in gas oil

The effects of these parameters on the evolution of gas from gas oil, figure 6.39, are not dissimilar to the behaviour observed in water. The aim of this section is really to verify that the behaviour in oil is similar to that in water, accounting for the increased solubility. In terms of the flow rate, as predicted, increasing the flow rate of gas through gas oil, figure 6.39a, increased the final equilibrium pressure. This confirmed that after 15 mins of bubbling CO_2 through the gas oil at 33 l/min, the liquid was not fully saturated. The p-V plot nor the velocity of the piston was influenced by the amount of gas in solution.

Figure 6.39b shows the comparison of CO_2 in gas oil at 5, 10 and 20 bara. Again the characteristic features were similar to those observed for CO_2 in water as a result of increasing the saturation pressure. In accordance with the effect of temperature in water, the final equilibrium pressure did not decrease with increasing temperature, figure 6.39c, despite the fact that the solubility of CO_2 in gas oil decreases with increasing temperature. Similar features in the rate of approach to equilibrium were observed, for on increasing the temperature, equilibrium was reached much faster.

In comparing the behaviour of CO_2 to that of N_2 and CH_4, figure 6.40 shows the plots obtained for each gas in kerosene. Indeed, similar trends were observed from an initial saturation pressure of 10 bara. Even at 5 bara, the evolution of CO_2 starts well before the piston has finished moving. The p-V plots for each gas were similar over the initial expansion, and the velocities of the piston ranged from 60 mm/sec for CO_2 to 30 mm/sec for N_2.

6.22 Effect of piston velocity in gas oil and kerosene

The effect of reducing the velocity of the piston, by a factor of 10, on the behaviour of CO_2 in gas oil was found to be basically the same as that of CO_2 in water, in terms of an initial pressure drop of ~ 5 bar pressure, a continued slow drop to p_{min}, and then an increase in pressure to the new equilibrium value. The pressure minimum was several bar below that of p_f and occurred around 200 secs after depressurization. At this point the piston was still moving, albeit slowly. Once the piston had completed its journey and come to rest, the pressure steadily rose, coming to rest at the predicted pressure after 1200 secs. The visual observations in the vessel were also similar to those observed for CO_2 in water. During the initial 5 bar pressure drop there was little sign of any activity in the vessel. As the pressure continued to drop gas evolution started, very slowly, but with increasing frequency. From around 400 secs, steady streams of bubbles were observed rising to the surface. Bubble evolution continued for many minutes, before gradually dying away over the latter stages of pressure recovery.

The same study was then carried out in kerosene, in which CO_2 is more soluble. This was evident not only in the value of p_f, but also in the shape of the curves. Figure 6.41 shows the pressure-time, velocity-time and p-V plots for CO_2 in kerosene, with and without an external air supply.

The piston velocity with no external air supply was 25 mm/sec, compared to that of 137 mm/sec. Following the initial pressure drop of ~5 bar, the evolution of gas from the vessel was apparent. Over the period 20-200 secs the pressure in the system was virtually stationary. This was because of the two opposing effects in the vessel, for over that period, the drop in pressure as the piston moved upwards, as observed with gas oil and with CO_2 in water, was being compensated by the evolution of CO_2 from the kerosene. Over the latter stages, once the volume expansion had been completed, the pressure rapidly rose to the new equilibrium value, coinciding with the plot obtained from a 6 barg air supply. The pressure recovery was more rapid than with gas oil, due to the increased solubility of CO_2 in kerosene compared to gas oil.

The behaviour of other gases in gas oil and kerosene showed similar characteristics, figure 6.42. For example, in the case of N_2 in gas oil, figure 6.42a, the behaviour was similar to that in water. The pressure with no air regulator pressure dropped to the equilibrium pressure and stayed there. The piston velocity was slower by a factor of ~10 without the aid of the pneumatic cylinder. The piston came to rest after ~1000 secs. As with water, when the experiment had finished, the piston was taken back manually. The pressure dropped a further 0.23 bar to coincide with the same value obtained with a 6 barg air supply. With CH_4 in kerosene, figure 6.42b, in which the gases are more soluble, the pressures dropped to a p_{min} below the equilibrium pressure, and then rose to the new equilibrium value. Being that much more soluble than N_2 in kerosene, the piston did reach the top before the piston came to rest.

6.23 Effect of insoluble nuclei in gas oil

The effect of insoluble solid nuclei in gas oil was investigated, without success. In water, there exists a colloidal stabilizing force which holds the particles in suspension. In oil, in the absence of any electrical surface charge, there is nothing to keep the solid nuclei in suspension. Even with agitation, the solid nuclei remained at the bottom of the vessel.

6.24 Effect of fluid agitation in kerosene and Statfjord crude

The effects of fluid agitation before and after depressurization are shown in figure 6.43, for a CO_2/kerosene system, and in figure 6.44, for a CO_2/Statfjord crude system. In both the CO_2/kerosene, and CO_2/Statfjord crude systems the final equilibrium pressure had increased by ~10% as a result of fluid agitation over the whole run. Fluid agitation had no significant influence on the p-t histories ~ 10 secs after depressurization, for, as can be seen from figures 6.43a and 6.44a, the equilibrium plateau is reached ~ 10 secs after depressurization and remains there, irrespective of the continued agitation. The time taken for 80% of the total pressure recovery, however, which occurs during gas expansion as reported in section 6.18, with agitation, was 0.4 secs, compared to that of 0.86 secs with no agitation. This faster rate of gas evolution is also apparent in terms of the differences observed in the p-V plots, with and without agitation, figures 6.43b and 6.44b. In both kerosene and Statfjord crude, the p-V plots showed that with agitation, there was significant gas evolution occurring before the piston had travelled a third of its journey. This rapid change in the shape of the curve at around 2.4 litres, strongly suggests that with agitation during saturation, the rate of uptake of CO_2 in kerosene and crude, for a given bubbling time, may be increased.

The effects of fluid agitation over the whole run (case 1), before (case 2) and after (case 3) depressurization, on a N_2/kerosene system are shown in figure 6.45. The plots obtained as a result of agitation during saturation only (case 2) and with no agitation at all (figure 6.35) are similar in all respects. With agitation after depressurization, the equilibrium value, for the same initial total mass of gas in the system, had increased by 35%. It took 15 secs from depressurization for 80% of the total pressure recovery to occur, compared to that of 3 secs with no agitation. Equilibrium was reached after 36 secs with no agitation, and 500 secs after depressurization with agitation. Fluid agitation, therefore, did not increase the overall rate of gas evolution, but did encourage more gas out of solution. Unlike the p-V plots for CO_2 in kerosene, the p-V plot for N_2 in kerosene, figure 6.45c, was shown not to be influenced by fluid agitation.

6.25 Effect of mixed gases in gas oil and kerosene

Figures 6.46 and 6.47 show the p-t histories obtained using the same mixed gas compositions as used in water. It was considered that a period of 30 mins bubbling was sufficient, in order to achieve a fully saturated solution, for which it can be assumed that the partial pressures of CO_2 and N_2 in the gas phase and thus in the liquid phase are in the ratio, 70:30.

Figure 6.46 shows the pressure-time history obtained in kerosene, for the 70:30 CO_2/N_2 initial composition, together with the plots obtained from the individual components at the partial pressures at which they existed in the mixed gas composition. The initial mass of, for example, CO_2, in the liquid and gas phase at an initial pressure of 7 bara, is the same as the mass of CO_2

initially in a mixed gas composition of 70% CO_2:30% N_2 at an initial pressure of 10 bara. Figure 6.47 shows the same information for the 70:30 N_2/CO_2 initial mixed gas composition in gas oil. In both cases, a faster rate of approach to equilibrium, by a factor of 3-5, was observed in a mixed gas system, compared with that recorded for the individual components. In terms of the equilibrium pressures, in both cases, the equilibrium pressure of the mixed component system was approximately equal to the sum of the equilibrium pressures of the two individual components at the same pressure at which they existed in the mixed component system initially.

The influence of parameters such as the initial temperature, saturation pressure and piston rate on the behaviour of the mixed gas compositions in oil were then investigated. Again, the effects on the gas evolution were similar to those observed by the individual gases. The same equilibrium value was reached as a result of increasing the temperature, but the rate of recovery was much faster at the increased temperatures. As observed with mixed gases in water, the difference in behaviour of the two mixed gas compositions was demonstrated quite effectively by changing the piston rate. With CO_2 as the major component, figure 6.48a, the plot had the same characteristics as those observed for CO_2 in kerosene with and without an external air supply, figure 6.41. During the period 20-400 secs, the upward movement of the piston was being compensated by the evolution of gas from the oil. As a result the pressure was relatively constant. Once the piston had stopped, the pressure started to rise to the new equilibrium value. With N_2 as the major component, figure 6.48b, the plots obtained with and without an air supply were characteristic of that of N_2 in oil, figure 6.42.

6.26 Gas evolution in oil/water mixes

A few exploratory tests were carried out at the end of the study to investigate the evolution of CO_2 from an oil/water mix, figure 6.49. The testing conditions were not ideal as it was extremely difficult to establish and maintain an emulsion. Indeed, with the degree of agitation available in the vessel, it would be more accurate to describe the system in the vessel as an oil/water dispersion as opposed to an emulsion. The oil/water mix was maintained during saturation by the flow of gas through the fluid. As soon as the gas supply was turned off, the control valve was opened, to prevent the two phases separating out during the 15 second steady state period, which is standard in the water studies.

In the series of tests, CO_2 was bubbled through a 50:50 v/v mix of gas oil and water for bubbling times of 15 mins, figure 6.49a, and 120 minutes, figure 6.49b, and from an initial starting pressure of 20 bara, figure 6.49c. In each case, there was no agitation after depressurization. It was found that in comparison to oil and water, the final equilibrium pressures under all conditions were less in an emulsion than the respective values in oil and in water, which is not surprising since only half the respective volumes of gas oil and water were present. Estimations of the predicted equilibrium pressure with the relative masses of oil and water in the vessel indicated that the pressure in each case, fell within the expected range. The evolution of gas from oil/water mixes is discussed in a little more detail in chapter 7.5.

What was more significant, was that the shape of the p-t plot took the form of the oil plot. Equilibrium was reached within ~ 10 secs in all cases. Shortly after that period, the two phases had separated out. Bubble evolution was still visible, with bubbles rising through the water, to the oil-water interface, and through the oil phase, to the liquid surface. It was not possible to see a continuation of the streams of bubbles in the water phase through the interface to the oil phase, for the bubbles in the water phase appeared to burst, as they hit the oil-water interface. The frequency of the streams and rise velocity of the bubbles appeared to be larger in the oil phase than the water phase. The activity at the interface would, however, be better observed using a video camera.

6.27 Effect of surfactants in oil/water mixes

Again exploratory tests were carried out to investigate the effects a surfactant had, if any, on the gas evolution process. Figure 6.50 shows the plots obtained with, and without surfactant, in two kerosene/water mixes. The first was a kerosene/water mix in the ratio, 50:50 v/v, whilst the second was in the ratio, 1:20 v/v. The surfactant used was Span 80, also known as sorbitan monooleate. The concentration of surfactant was 500 ppm of the oil phase, being oil soluble. When the surfactant was dissolved in the oil in the vessel, both the oil and the water went completely white, as a cloudy precipitate, probably a calcium salt, was formed, making any visual observations impossible.

There was complete agitation during each run. In both cases, the final equilibrium pressure increased with the presence of surfactant, by 3% for the 50:50 mix and 18% for the 1:20 mix. In both cases, the plots obtained with and without surfactant were similar over the first 10-20 secs after depressurization. The significant region occurred, for the 1:20 mix, ~40 secs after depressurization, where the pressure levelled off with no surfactant, yet continued to rise with surfactant. Similarly, but less significantly, the same was observed for the 50:50 mix. The p-V plots and velocity-time plots were also similar, which was to be expected, since the presence of surfactant was only significant after depressurization, during the separation of the phases.

7.0 INTERPRETATION AND DISCUSSION OF RESULTS

The key areas of interest in this study lay in the non steady state conditions created in the vessel during and immediately after depressurization and indeed during the steady, and sometimes slow approach to the new equilibrium where once again steady state conditions are established. Drawing on the available literature where appropriate, and drawing on the experimental results given in chapter 6, to provide information on response times and pressure recovery behaviour, the following discussion aims to present a picture of the behaviour of a saturated or part saturated system when exposed to a rapid reduction in pressure. In investigating this, the characteristic behaviour of the various gases, which could be related to their solubility, and the distinctive influencing features of the solvent, which could be related to the physical characteristics of the liquids, became evident.

7.1 Steady state conditions

The state of liquid-gas systems at equilibrium, in terms of the liquid structure and bonding between molecules and how it may be affected by parameters such as pressure, temperature and salinity, is briefly discussed in this section, as it is these factors, which determine the initial steady state conditions established at the start of each experiment.

The general consensus of opinion in the literature [58,59] supports the theory that the structure of liquid water contains molecular clusters or 'cages', which form spaces in the bulk liquid where dissolved molecules are concentrated. In other words, each gas molecule is surrounded by a sphere of water molecules. When a gas is dissolved in a liquid, a small proportion of the gas is held as free microbubbles, which are able to move in the interstices of the liquid structure, whilst the larger proportion of gas molecules, particularly when the number of gas molecules is small, are locked into the liquid structure [139]. The radii of the free microbubbles in solution are distributed over a wide range ($1\mu m$ to $1000\mu m$).

Molecular attraction between gas molecules results in the grouping of several dissolved gas molecules to form clusters. In a saturated system at equilibrium, the clusters are short lived, continually forming and breaking. The rate of growth is equal to the rate of decay and usually occurs by the addition or detachment of just one molecule at a time [123]. As a result, the microbubbles are unable to grow to that critical size, beyond which bubbles form and rise to the surface. A driving force, such as a rapid change in conditions, in terms of temperature or pressure is required for the formation of macroscopic bubbles. At room temperature, aggregates in water can generally reach sizes up to about 100 molecules [166]. An increase in temperature breaks down the short range ordering present in water [25], and allows the molecules which were trapped in the local structure to move about freely, therefore increasing the number of microbubbles and hence the concentration of available nuclei.

The amount of dissolved gas going into solution generally obeys Henry's law, as given in equation 3.4. Thus the amount of gas dissolved in solution and hence the amount of gas released upon pressure reduction are both direct functions of the initial pressure. The solubility of gases in solution, for a given solvent, is also dependent on the temperature and dissolved solids concentration. The solubility of air, for example, is reduced by 45% as the temperature is raised from 0 to 30°C, whilst the solubility of O_2 decreases by 20% as salinity is increased from 0 to 20,000 mg/l (10% salt saturation) [6]. The length of time required to fully saturate a liquid is dependent on the dissolved gas. Indeed, saturation of the less soluble gases, CH_4, Ar, O_2 and N_2 in water took several minutes compared to CO_2 in water, figure 6.5, in which several hours was necessary. This was in agreement with the length of time considered necessary, by several authors in the literature, to saturate a volume of water with CO_2, which ranged from a period of 1-2 hours to 16-48 hours [49].

Once equilibrium has been reached, it is relatively easy and straightforward to provide quantitative information for systems in steady state conditions. The equations and calculations are well documented and well established in the literature [4]. The solubilities of gases in liquids under all conditions of temperature, pressure and salinity, have been determined using various adaptations of equations of state and Henry's law [61,62,71]. Indeed, in this study, calculations to determine the mass of gas in the liquid and gas phases in the steady state initially, before depressurization, and at the new established equilibrium state, after depressurization, were carried out, when required, for the gases in water. Using basic thermodynamic principles and the standard gas equations and solubility data given in the literature, the equations were used to determine the dissolved and free gas content initially, as a function of temperature, pressure and salinity, and to calculate how much gas changed phase following depressurization. The same equations were particularly useful in relation to mixed gases, in predicting the final gas compositions of mixed component systems following depressurization. The method and calculations, together with the assumptions made are shown in appendix III.

The following sections focus on the non equilibrium conditions created in the vessel. Firstly, during rapid depressurization, in terms of visual and photographic observations and factors affecting the rate of depressurization, and secondly, during the pressure recovery to the new equilibrium, in terms of the factors influencing both the rate of gas evolution and indeed, the actual equilibrium pressure.

7.2 Rapid depressurization

7.2.1 Visual and photographic observations

The video sequences capturing the evolution of the gases, CO_2 and N_2 from the solvents, water and kerosene, when exposed to a sudden reduction in pressure provided some valuable information on the gas evolution process in terms of timescale of events and the mass macromolecular movement of gas, in the form of bubbles, between phases. A more complex gas evolution process was observed with CO_2 in water (plate V), compared to that for N_2 in water (plate VI). In interpreting the sequence of events occurring during the evolution of CO_2 in water, it became apparent that there were three definite stages. The first stage was the progression of a bubble front,as described in chapter 6.2, into the bulk liquid (plate V, 2-13), the second stage was the evolution of bubbles in the top 30 mm of the liquid (plate V, 17-22), whilst the third stage in the sequence was the mass evolution of bubbles from the bulk liquid (plate V, 24-26). With N_2 in water, only two stages were apparent, for there was no evidence of the evolution of bubbles in the surface layers of the liquid, which were clearly visible with CO_2.

In terms of timescale of events for the two gases, the depressurization, p_i-p_{min}, of the CO_2/water system, figure 6.1a, was faster by a factor of 2 than that for N_2, figure 6.2a. It might therefore have been expected that CO_2 evolution occurs well before N_2 evolution under the same conditions. Closer analysis of the photographs, however, showed that right up until the evolution of the mushroom of gas from the base of the vessel (plate VI, 24 and plate VII, 6), the two systems were relatively evenly matched in relation to the timescale of events. In both cases stage I, the advancement of the bubble front into the bulk liquid, occurred over the same period of time (~ 100 ms). Whereas with CO_2 in water, the bubble front reached a depth of 47 mm (±2 mm) at a velocity of 1.3 m/sec (±0.05 m/sec), in N_2, the depth of propagation into the liquid, at a velocity of 0.7 m/sec (±0.05 m/sec), was only 26 mm (±2 mm), as shown in table 7.1. The values were calculated directly from the video sequence. The velocity of the bubble front and the depth to which the front propagated could also be related to the maximum velocity of the piston recorded during depressurization, as discussed in more detail in section 7.2.3.

Gas	Liquid	Max depth of propagation mm (±2 mm)	Max velocity of bubble front m/sec (±0.05 m/sec)	Max velocity of piston mm/sec (±10 mm/sec)
CO_2	water	47	1.3	237
N_2	water	26	0.75	100
CO_2	kerosene	30	0.5	100
N_2	kerosene	15	0.375	90

Table 7.1 Calculated depths of propagation and velocities of the bubble front for CO_2 and N_2 in water and kerosene during depressurization, from a saturation pressure of 10 bara and ambient temperature

Whilst stage II was taking place in the CO_2/water system, over a period of a second (plate V, 17-22), there was virtually no activity in the N_2/water system (plate VI, 4 and 5). With CO_2, stage III was visible ~1:72 secs (plate V, 24) after initiation of depressurization, and with N_2, stage III was visible ~1:76 secs after initiation (plate VI, 6). In both cases, the mushroom was estimated to be rising at 1.0 m/sec (±0.1 m/sec). With CO_2, immediately after the mushroom had reached the surface, continuing mass evolution was clearly evident, for there were a number of bubbles in the wake of the mushroom of gas (plate V, 24 and 25). With N_2, however, there were relatively few bubbles trailing in the wake of the leading gas volume (plate VI, 7). This was probably due to the increased solubility and hence increased amount of CO_2 in water compared to N_2, and the fact that by this point, with CO_2, p_{min} had been reached, and the piston movement was completed, figure 6.1b, whereas with N_2 the pressure was still dropping and the piston still had to travel the last 40 mm, figure 6.2b.

A few calculations were carried out to determine the volume of gas in the initial mushroom of gas. Taking N_2 as an example, (plate VI), the volume of the mushroom was estimated to be ~90 cm^3, ~1% of the total liquid volume. The mass of N_2 in that volume was calculated to be 0.11g (0.04 mole), ~7% of the total mass of N_2 in solution initially. A similar value of around 7-10%, for the mass of gas in the initial mushroom (as a % of the total mass of gas in the liquid phase initially) was also calculated for the other gases.

With N_2, whilst there was no mass evolution as such, as observed with CO_2 (plate V, 26), bubbles appeared with increasing frequency, ~1 sec after the mushroom had reached the surface (plate VI, 8-12). During that 1 sec period, as the piston was still travelling upwards, apart from the occasional bubble, 2-4 mm in diameter, rising to the surface, there was, again, very little activity in the vessel. With CO_2, mass evolution continued for several secs, before some order was apparent, in the form of steady streams of bubbles rising to the surface. Bubble evolution occurred for many mins with CO_2 (plate V, 27 and 28), compared to that of many secs for N_2, (plate VI, 8-12), owing largely to their respective solubilities, figure I-1. The visual observations and indeed the estimated sizes of evolving bubbles in water, ~15 secs after depressurization, showed that using N_2, the bubbles were generally smaller, by a factor of 3-4, than with CO_2.

It seems reasonable to assume that this second stage, observed with CO_2, which resulted in the evolution of a small percentage of the total gas evolved (~5%), may be related to the dissociation reaction of CO_2 in water, for stage II was not apparent in either the evolution of N_2 in water, in which there is no chemical bonding, nor in the evolution of CO_2 from oil, in which CO_2 does not dissociate. It could be predicted, therefore, that stage II would not be apparent with Ar, O_2 or CH_4, but would be expected with, for example, NO_2 in water.

When CO_2 is dissolved in water, several characteristic features are observed, which can be related to the dissociation reaction which takes place. The first is a drop in the liquid temperature, observed immediately the liquid is exposed to the gas. Unlike the other gases in water, the dissolution of CO_2 in water is an endothermic reaction. Energy is required for the dissociation reaction of CO_2, in which bonds are formed between CO_2, in its ionic form, and the water molecules. This energy comes from the surroundings, and as a result, at the start of saturation, the measured temperature of the bulk liquid immediately drops by 2-3°C, and remains at that temperature throughout the rest of the saturation period. This also gives an indication of the degree of ionization, for once the temperature has dropped, it remains there, suggesting the extent of ionization is complete. Whilst the measured temperature did not change significantly during depressurization or immediately after depressurization, a small and gradual rise in temperature accompanied the slow approach to equilibrium during the evolution of CO_2 from water, for the measured temperature of the liquid at equilibrium was generally the same as that recorded before saturation (± 0.2°C).

Another feature characteristic of CO_2, is the drop in pH measured when CO_2 is dissolved in water, as reported in chapter 6.13. Again, the drop is observed during the first few minutes of saturation, beyond which the pH remains constant, regardless of the changing conditions in the vessel. At pH 5, the proportion of CO_2 existing in dissociated form in tap water is 3-5% [167]. This corresponds quite well with the small amount of CO_2 evolved in stage II. However, in order to be convinced that the small amount of gas evolving is actually a direct result of the dissociation reaction, the carbonate equilibria must be considered more carefully. This is discussed in detail in section 7.4 and appendix IV.

The video observations, capturing the evolution of CO_2 and N_2 from water during rapid depressurization, clearly showed that the bulk of the dissolved gas left solution after the piston had finished travelling and expansion was complete. Although a small percentage of the gas volume (~5%) had evolved in the CO_2-water system before this point, it can be assumed that during gas expansion, the mass of gas in solution stays reasonably constant. The mass of gas in both the gas and liquid phases is particularly important when using equations of state to calculate and predict the new equilibrium pressures, as discussed in appendix III, and indeed when interpreting the p-V plots during gas expansion, which applies only to systems of fixed mass. The significance of the p-V plots during the rapid depressurization process, in terms of how the parameters such as initial pressure, temperature and free gas volume influence the plots, have been discussed in detail in section 7.2.2.

A very different picture emerged using kerosene as the solvent. The key differences observed, in terms of the rate and extent of bubble evolution of the same gases, CO_2 and N_2 from kerosene compared with water, under the same conditions, can largely be explained by the fact that gases are more soluble in hydrocarbons compared to water [25]. During the rapid depressurization of a CO_2 in kerosene system (plate VII), the advancement of a bubble front into the bulk liquid was again observed (plate VII, 1-5). As shown in table 7.1, however, the distance travelled into the bulk, 30 mm (±2 mm) and the velocity of the bubble front, 0.5 m/sec (±0.05 m/sec), were much less than that for CO_2 in water, by approximately 35% and 60% respectively.

In both kerosene and water, the advancement of the bubble front to the respective maximum depths, occurred over a period of 100 ms. Similar behaviour was observed with N_2 in the same two solvents. The depth of propagation and velocity of the bubble front were reduced in kerosene by approximately 40% and 50% respectively, compared to that in water. This suggests that the physical characteristics of the kerosene, particularly in terms of the increased viscosity, could be a factor influencing the bubble front characteristics, possibly providing some sort of damping effect.

Whereas with CO_2 in water, mass evolution was initiated by the rising of a large mushroom of gas through the bulk liquid, the absence of this mushroom in kerosene was markedly noticeable. Instead, bubble evolution clearly started, with increasing frequency, from the vessel walls (plate VII, 11-17) and indeed well before the piston had finished travelling. As a result, from approximately the same initial pressure, the minimum pressure recorded in kerosene was approximately twice that recorded in water, figures 6.1 and 6.34. Depressurization in kerosene occurred in just 1 second (plate VII, 1-19), beyond which massive evolution took place. The minimum pressure, p_{min}, was reached before the piston had travelled even half of the complete distance, figure 6.34. More significantly, over 70% of the total pressure recovery had taken place by time the piston had come to rest, whereas in water, pressure recovery occurred only after expansion was complete, figure 6.1a. In comparison to that in water, massive bubble evolution started over a second earlier in kerosene. In kerosene, approximately 30 secs after depressurization had taken place, the new equilibrium had been established and the bulk liquid was virtually motionless (plate VII, 40).

Similar characteristics were observed with N_2 in kerosene. Evolution of N_2 also occurred over a second earlier in kerosene than in water. One of the most significant differences between N_2 and that of CO_2 in kerosene was that despite using fresh batches of kerosene, when saturated with N_2, small bubbles, no more than 0.5 mm in diameter, were always visible in the liquid prior to depressurization (plate VIII, 1). This was also observed for the other gases in kerosene, but was not observed with CO_2 in kerosene, where the liquid was completely clear prior to depressurization, suggesting that it could be related to the relative solubilities of the gases. The main implication of this is that these minute bubbles undoubtedly acting as nucleation sites, effectively lower the nucleation threshold, and nucleation from the vessel walls therefore becomes less significant. This effect would be particularly significant in larger vessels containing the less soluble gases, as nucleation in the bulk liquid may occur more readily.

Bubble nucleation, therefore, might be expected to occur earlier in with N_2 in kerosene, compared with CO_2 in kerosene. Using the blocking of the back-lighting, as a means of comparison to give an indication of the lowering of the nucleation threshold, in N_2 the light is completely blocked after 1:32 secs (plate VIII, 15) compared to 1:48 secs (plate VII, 30) with CO_2. In addition, the rapid evolution of the less soluble gases in mixed gas component systems could well act as a triggering mechanism for evolution of other gases. The behaviour of mixed gas systems on the rate of evolution is discussed in section 7.3.1.5. It should be noted that immediately after mass evolution of N_2 from kerosene, the 'haze' of bubbles had disappeared (plate VIII, 18-26), and the kerosene had returned to the same clear state it was in before saturation with N_2.

Certain aspects of the process of bubble nucleation reviewed in the literature, therefore, were clearly visible in the vessel. It became apparent from the work carried out by previous workers that homogeneous nucleation occurred at much higher pressures than those experienced in the vessel [3,15] and was generally only observed when a large proportion of the stable microbubbles existing in solution were degassed prior to depressurization. This was not carried out in the programme since very large pressures (> 1000 atm) are required at temperatures over 100°C [97]. It was therefore anticipated that nucleation would occur predominantly heterogeneously, from pre-existing microbubbles and small suspended particles in the liquid, and from the vessel walls, which, like most machined metal surfaces, were shown to contain numerous pits and crevices (plate I).

The presence of microbubbles and particles in the water, and indeed the crevices and pits at the walls were considered to be the reasons why, in carrying out experiments using distilled water, there were no significant differences in the time histories recorded. Although the number of potential nucleation sites in the liquid had been reduced, there were still numerous potential sites available for bubble nucleation on both the vessel walls and in the liquid. Indeed, the mushroom of gas, initiating bubble evolution, was observed using treated water. Video analysis would, however, be necessary to make a detailed comparison of the sequence and timescale of events in treated water and in tap water. As most industrial applications do not use purified and treated water, this line of investigation was not continued. In contrast, significantly increasing the number of nucleation sites in the liquid, by the addition of silica flour particles, significantly increases the rate of gas evolution, as discussed in section 7.3.1.2.

The clearest picture of heterogeneous nucleation phenomena was observed with CO_2 in kerosene, in which the bubbles clearly formed at the vessel walls. In the case of N_2 in kerosene, nucleation was still heterogeneous, but was starting from pre-formed sites in the liquid, in the form of N_2 bubbles existing in solution following saturation. With water, in which pre-existing microbubbles and suspended particles are more significant and indeed more numerous, it was more difficult to determine where bubble evolution originated. With CO_2, the rising of the mushroom through the bulk of the liquid appeared to be a strong influencing factor in triggering the nucleation process as bubbles formed in its wake, in regions of high velocity gradient. The effects of the mushroom of gas initiating gas evolution are not so significant with N_2 in water, as there is a 1 sec delay between the mushroom reaching the surface and p_{min} being reached. As a result, mass evolution, as such, is not observed.

The origin and mechanism of the evolution of this initial volume of gas, considered to be a reaction to the pressure release, was investigated, but without too much success. The phenomenon was not in evidence in oil, largely due to the increased solubility and hence the mechanism of rapid evolution of gas. The mushroom of gas in water for both CO_2 and N_2 occurred ~ 1.76 secs after initiation of depressurization. In kerosene, rapid evolution from the vessel walls started after just 0.7 secs and after 1.76 secs, massive evolution was already evident with both CO_2 and N_2 (plate VII, 30 and plate VIII, 17). It was very difficult to determine where the mushroom originated from, even by viewing the vessel contents through the window in the base of the vessel. It was considered that the volume of gas might be originating from, or indeed influenced by, the heating element situated near the base of the vessel. This theory was tested and abandoned, since removal of the heating element from the vessel did not appear to influence the size or shape of the mushroom of gas. The mushroom of gas did not appear to originate from the vessel walls, as observed with gas evolution in kerosene, for the initial gas volume was observed rising through the heart of the bulk liquid. Immediately after mass evolution, however, when the walls became visible, nucleation from the vessel walls was very much in evidence, for it was possible to see bubbles explosively appearing on the inside walls, where the dissolved trapped in the pits and crevices in the wall was drawn out, according to the theory introduced by Harvey [168], as discussed in chapter 3.8.

The mushroom effect occurs in water, with all gases tested and under all initial conditions tested. Unfortunately, nothing conclusive, regarding its origin or cause, other than a reaction to the pressure release, could be discovered. The mushroom of gas is, however, considered to be an artefact of the rig, in terms of the size and length/diameter aspect ratio of the vessel. Taking a simple case of opening a bottle of carbonated water, there is no evidence of an initial volume of gas rising from the base of the bottle. In the vessel, even at initial pressures of 5 bara, the mushroom was observed. The phenomena has been discussed in chapter 8, in terms of further investigations to determine the origin and cause of the mushroom, and regarding the effects scaling up might have on the gas evolution process.

7.2.2 Pressure-volume plots recorded during rapid depressurization

The significance of the p-V plots obtained during depressurization, assuming a fixed mass system, was briefly introduced in chapter 5.5, and in the light of the results is discussed in a little more detail in this section. It was proposed in chapter 5.5, that the gas expansion would probably be nearly isothermal, owing to the bulk mass of steel and liquid. The equation pV^n=constant was fitted to the p-V data plots to determine the value of n. The value of n was anticipated to lie somewhere between 1, for an isothermal reaction and γ, where γ is the ratio of the specific heat at constant pressure to that at constant volume. The values of γ for the gases used are 1.28 for CO_2, 1.4 for N_2 and O_2 and 1.675 for Ar. The values of n calculated, under the test conditions, for the depressurization of the gases in water ranged from 1.07 for CO_2, to 1.28 for Ar, figure 6.10b.

The specific heat of water is large, compared to that of most other substances, indicating that the value of n would tend more towards unity than, for example kerosene, for which the specific heat is approximately half that for water, suggesting that the value of n would tend towards γ. This indeed was found to be the case in practice. With CO_2, the value of the index, n, was found to be 1.07 in water, and 1.27 in kerosene, figure 6.36d. In gas oil and Statfjord crude, the values of n for CO_2 were 1.16 and 1.22 respectively.

In terms of the factors affecting the p-V relationships during gas expansion, upon changing the initial conditions, the results obtained can be related to the nearly isothermal expansion in the vessel and can be explained relatively easily. Investigations of the gas phase temperature showed that a larger drop in temperature was observed as the initial pressure was increased from 10 bara to 20 bara, figure 6.17b, since the ratio p_i/p_{min} increases with increasing p_i. Similarly, a larger drop in the temperature of the gas phase was observed with a smaller initial free gas space initially, figure 6.17c. This, again, can be explained in terms of the simple gas equations. For a system in which the ratio of the free gas space initially to the final gas volume is small, i.e. a larger free gas space initially, the ratio of the initial to final temperature would also be smaller, than compared with a system with a large initial to final volume ratio. With an increasingly larger temperature drop in the gas phase, the value of the index, n, would be expected to move further from unity. Indeed this was observed both with an increase in pressure, as reported in chapter 6.6 and a decrease in initial free gas volume, as reported in chapter 6.10.

The p-V plots also provide a strong indication of when bubble evolution begins in the vessel, particularly when the solvent is a hydrocarbon. This is demonstrated quite effectively in figure 6.36d. As the pressure in the vessel rises due to significant bubble evolution, the p-V plot tends to deviate from the expected curve. In figure 6.39cii, for example, at the increased temperature, the p-V plot indicates that bubble evolution occurs approximately half way through the gas expansion, when the free gas volume is ~2.5l. Indeed, analysis of the p-V plots obtained with and without agitation of a CO_2 in kerosene system, figure 6.43b, provided an indication of how agitation during saturation influenced the rate of uptake of CO_2 in kerosene, as discussed in section 7.3.1.3. Bubble evolution during gas expansion is not so evident with the gases in water, for, as discussed in section 7.2, a comparison of the photographs and the pVT plots show that gas evolution, even with CO_2, does not occur until after the piston has finished moving and gas expansion is complete.

7.2.1.3 Factors influencing the rapid depressurization process

The rapid depressurization of the liquid in the vessel was considered to be dependent on a number of variables. The rate of depressurization is governed by the rate at which the piston moves upwards. Every effort was made during the design stages of the pressure release mechanism to ensure the piston moved upwards as fast as possible. The main factor which was considered to have a significant effect on the rate of piston movement was the initial saturation pressure of the liquid below the piston, and indeed the results showed a significant increase in the velocity of the piston with increasing pressure below the piston, figure 6.13d.

In addition, the rate at which the piston moved upwards was also strongly dependent on the volume of free gas above the liquid initially. This was particularly significant with the less soluble gases in water. With N_2, for example, the pressure drop, p_i to p_{min} occurred over a period of 2.9 secs with an initial free gas volume of 0.8 litres, compared to that of 4 secs with a free gas volume of 0.01 litres, figure 6.19b. What was perhaps more significant was the rapid drop in the velocity of the piston, figure 6.19c, as the pressure in the vessel was approaching atmospheric pressure, indicating a sub-atmospheric vacuum was being drawn in the lower chamber. As a result, the piston did not actually travel the complete distance, figure 6.19d, stopping 40 mm short of the end wall. Additional data confirmed that the rate of piston movement was independent of the variables such as the bubbling time, figure 6.8b, the gas flow rate, figure 6.12c, and the initial temperature of the liquid, figure 6.16b, suggesting that increasing the amount of gas in solution, for a particular gas, did not affect the velocity of the piston.

What was somewhat surprising, however, was the influence the particular gas under test had on the rate. The velocity-time plots indicated that in comparison with Ar, CH_4 and O_2, the piston reached a greater average velocity with CO_2 in solution and a lower velocity with N_2 in solution, figure 6.10c. This would appear to be a function of the gas in solution and not a function of the system, for the data showed that throughout the experimental programme, under all conditions, the velocity of the piston was significantly and consistently higher for CO_2 than N_2, figures 6.11c and 6.40c. In both CO_2 in water and N_2 in water, the maximum velocity was recorded when the pressure in the lower chamber had dropped by 65% (±2%). This was also true for the other gases in water. For a number of repeated runs from 10 bara initial pressure, the maximum velocity of the piston recorded with CO_2 was in the range 237 mm/sec ±10 mm, and for N_2 was 100 mm/sec ±5 mm. The velocity of the piston was also influenced to a certain extent by the liquid being investigated. Indeed, lower maximum velocities, of around 200 mm/sec, were recorded for CO_2 in saturated salt solutions, figure 6.24b, and even slower velocities, of around 100 mm/sec, were recorded in hydrocarbons, figure 6.36b. It had previously been considered that the velocity of the piston would not be influenced either by the liquid or by the gas used in each experiment.

Originally, the differences in piston velocities for the gases in water were thought to be due to the amount of gas evolving from solution during depressurization, since the relative piston velocities of the various gas systems showed some relation to the relative solubilities. But closer analysis of the video evidence and the data showed that at the point of maximum velocity, around 0.4-0.6 secs into depressurization and 40 mm into the piston travel, there was no significant evolution of gas. The reproducibility of the air supply to the air cylinder and the reliability of results was questioned, but the results were consistent and reproducible. Several other factors were considered as a possible explanation, but were neglected. Simple calculations of the density of each gas in the 0.8 litres of free gas space initially, bore no relation to the piston velocity. The temperature of the gas was shown not to change significantly during depressurization, figure 6.17, largely owing to the large mass of surrounding steel, suggesting there would be no significant difference in the gas expansion rates of the gases.

Diffusion of any gas through the PTFE seal of the piston was considered negligible for two reasons. Firstly, there were no signs of any gas bubbles in the hydraulic fluid after depressurization, nor were there any signs of pressure loss through the seal, as discussed in chapter

4.3. In addition, the surface area of the PTFE seal in contact with the gas was so small to be considered negligible in terms of a significant difference between the diffusion rate of the gases through the seal. Although not very predictable, the friction of the piston, which would only really be in the PTFE seal itself, was considered insignificant, and even more so the difference in the friction due to the particular gas in the vessel. Friction may, however, become more significant for the lower initial starting pressures (slower piston velocity).

The only reasonable explanation, therefore, appears to be in the progression of the bubble front, for in that 0.4 secs taken to reach the maximum velocity, the bubble front was the only visible activity in the vessel for any gas-liquid combination. In that initial half a second, the bubble front had progressed to a depth into the bulk liquid, dependent on the liquid and the gas used, at a speed well below sonic velocity, before regressing back to the surface. Analysis of the data given in table 7.1, comparing the bubble front velocities and depth of propagation with the maximum velocity recorded by the piston for each gas-liquid combination did indeed show some relationships.

Video analysis in both water and kerosene, showed that the depth of propagation into the bulk and the maximum velocity of the bubble front for CO_2 was approaching twice that for N_2. Similar relationships were apparent for each gas in water compared with kerosene. The pVT data for the same two gases showed an increase by a factor of ~ 2 in the piston velocity for CO_2 in water compared with N_2, figure 6.10c, and indeed the same increase for CO_2 in water compared to that in kerosene, figure 6.40c. So whilst there is no significant evolution of gas at the point of maximum velocity of the piston, the piston velocity appears to be related to the depth of propagation and velocity of the bubble front, which in turn is related to the solubility of the gas. Video evidence of the bubble front using CO_2 in both water and kerosene, from an initial pressure of, for example, 20 bara, would help to establish the relationship between the bubble front characteristics and the piston velocity which is higher at the increased saturation pressures, figure 6.13d.

Putting things into perspective, however, the fact that the piston velocity is influenced by the gas under test is a relatively minor point, which does not affect the results too significantly. More importantly, the effect is, again, an artefact of the rig, in terms of the mechanism used to release the pressure built up in the system, and as a result may not be such a significant influence in the industrial context, as discussed in chapter 8. The influence of the gas and indeed, the liquid, on the piston velocity is also discussed in chapter 8, in terms of modifications to the rig which would produce a constant velocity piston withdrawal, which is independent of test conditions.

The mechanism of gas evolution from a liquid exposed to a reduction depends largely on the rate at which the pressure is released, as discussed in chapter 3.10. Under the conditions in which the pressure dropped from p_i to p_{min} in approximately 1-2 secs, with a rate of 10-20 bar/sec, depending on initial conditions, bubbling was the dominant form of pressure release. Even from an initial pressure of 5 bara, in which the pressure dropped at a rate of approximately 3 bar/sec, bubbling was observed. The evolution of gas from a system exposed to a reduction in pressure occurs once a certain threshold limit is exceeded. This limit, determined by the ratio of the partial pressure of the dissolved gas to the total pressure, was demonstrated during the slow release of pressure from the system, from an initial pressure of 10 bara, in which the rate of piston movement was reduced by a factor of 10, figures 6.20 and 6.21. Under those conditions, over the first few seconds, there was no visible evolution of gas. The initial drop in pressure of around 5 bar occurred due to the force exerted on the piston as a result of the initial pressure built up in the lower chamber. As the pressure continued to drop, bubbles 2-3 mm in diameter, started appearing and rising to the surface. Only after a significant drop in pressure, of around 6 bar, did the significant evolution of bubbles start. It was not, however, a sudden mass evolution, since there was a gradual increase in the frequency of bubbles up to that point. Threshold limits, in terms of the absolute pressure required for bubble formation, were observed by other authors, particularly in relation to homogeneous nucleation for the much higher pressures (>100 bara), where it was observed that a significant drop in pressure to a pressure, characteristic of the gas-liquid combination, was required before bubble nucleation occurred [97,137,139].

It was not possible to reduce the rate of piston movement any further and hence desorption in which mass transfer was purely diffusional, as discussed in chapter 3.10, was not investigated. In an enclosed system, for any gas or liquid combination, from the same initial conditions, whether the depressurization process is rapid, of the order of 2 secs, thus producing a supersaturated state, or very slow, of the order of 1000 secs, the same final pressure, representing the established equilibrium state, is eventually reached, figures 6.33 and 6.42. This was to be expected, since the final equilibrium pressure is a function of the initial amount of gas in solution. This may not however be the case in the industrial environment, in which open systems are more commonly encountered.

7.3 Pressure recovery and rate of approach to equilibrium

The previous section, 7.2, has discussed the rapid depressurization event in terms of the visual observations and the factors affecting the rapid depressurization process. Attention is now focused on the pressure recovery process and the rate of approach to equilibrium. Immediately after the depressurization of the vessel has occurred, pressure recovery takes place. The time dependence of the pressure recovery process is related to the individual and cumulative bubble growth rate. An initial rapid pressure recovery period, corresponding to the rapid gross macromolecular bubble movement, was observed in *all* systems, for any gas-liquid combination. The evolution of bubbles, a macromolecular event, was due to the pressure imbalance created, as a result of the pressure release above the liquid, between the partial pressure of the gas in the liquid and the pressure above the liquid. The extent of mass evolution is clearly influenced by the amount of gas in solution, and the rate of depressurization, for the pressure recovery to a new equilibrium is driven by the extent of disequilibrium in the vessel. As the degree of bubble activity slows, so does the rate of pressure recovery.

In terms of quantifying the rate of gas evolution, the mass of gas evolved and the rate of gas evolved with time, for the two systems, CO_2 in water and N_2 in water, as observed in plates V and VI, can be seen in figure 7.1. The masses of gas in each case were calculated using the equations given in appendix III. For approximately isothermal conditions, if

$$pV=mRT \tag{7.1}$$

then

$$\frac{dm}{dt}=\frac{1}{RT}[p\frac{dV}{dt}+V\frac{dp}{dt}] \tag{7.2}$$

Also, as

$$V=Al \tag{7.3}$$

where l is the piston displacement, eqn 7.2 may be rewritten as

$$\frac{dm}{dt}=\frac{A}{RT}[p\frac{dl}{dt}+l\frac{dp}{dt}] \tag{7.4}$$

where dl/dt is effectively the piston velocity.

As discussed in section 7.2, the bulk of the gas evolves once the piston has finished moving, and hence the velocity term ceases to be significant. After depressurization, therefore, the rate of mass evolution is a function only of dp/dt. In addition, over the initial 0.5-1 secs of depressurization, in which the mass of gas evolved is negligible, the two terms can be shown to sum to approximately zero. Reliable data for the mass of gas evolved during the piston movement could not really be obtained. So whilst a small volume of gas was evolved during depressurization for all gases in water, in the form of the mushroom of gas, as described in section 7.2, this has not been included in the plots shown in figure 7.1. It could be predicted, however, that a small peak would be apparent immediately prior to mass gas evolution.

For the less soluble gases in water and for all gases in kerosene, the new equilibrium state is effectively reached within 30 secs of depressurization, and hence pressure recovery virtually ceases, figures 6.9a and 6.38a. Indeed, during the initial rapid recovery period, lasting between 5 and 20 secs, around 95% of the total pressure recovery has already taken place. It is apparent from figure 7.1b, however, that for N_2 in water, gas evolution is still occurring 100 secs after depressurization. This would indicate that over the latter stages of pressure recovery, molecular processes take over, for towards the end of the pressure recovery process, gas evolution is still occurring, albeit slowly, yet there are no bubbles visible in the bulk of the liquid. Under these conditions the final pressure recovery to equilibrium occurs by molecular diffusion, generally as a result of concentration gradients existing in the bulk. For all gases, only a small proportion of gas (~3-5%) evolved by diffusion, and only after approximately 95% of the total pressure recovery had taken place.

For CO_2 in water systems, there were two distinct rates of pressure recovery associated with evolution by bubbling, figures 6.7a and 6.8a, the initial rapid recovery, followed by a slow, exponential recovery to equilibrium. The slow gradual approach, recorded over a period of 1000 secs, corresponded to the change in bubble activity observed in the vessel, as mass evolution was replaced by steady streams of bubbles rising to the surface. Again, once the steady streams had eventually died away, gas evolution by diffusion was apparent, for the pressure was still recovering.

7.3.1 Factors influencing the rate of gas evolution

The period of time over which the enclosed system was in a state of non equilibrium was found to be strongly dependent on the nature of the gas and liquid used, as discussed above. Indeed, the rate of approach to the new equilibrium for a CO_2 in water system was generally slower by 2 orders of magnitude than that of the less soluble gases, where equilibrium was generally reached within 30 secs, figures 6.10a and 6.11a. The differences observed in the rate of approach to equilibrium were largely due to the dissociation reaction of CO_2 in water. This is discussed in detail in section 7.4. With CO_2, a period of around 2000 secs was necessary for the new equilibrium state to be established, figure 6.13. The approach to equilibrium of a CO_2 in water system was also slower, again by ~2 orders of magnitude, compared to that for CO_2 in kerosene and Statfjord crude, figure 6.36a.

In terms of enhancing the rate of evolution following depressurization several factors were shown to influence the rate of approach to equilibrium. The main factors were considered to be the initial temperature of the liquid, the presence of solids, fluid agitation and the salinity.

7.3.1.1 Initial temperature

Increasing the initial temperature of the CO_2/water system increased the rate of approach to equilibrium and significantly so. Indeed, the approach to equilibrium from an initial temperature of ~60°C, was faster by a factor of 40, compared to that at ambient temperature, figure 15a, which is much faster than would be expected for a change in a single property. Similarly, increases in the rate of approach to equilibrium were observed under different starting conditions, figure 6.16, and using gas oil, figure 6.39c. This has significant implications in the context of offshore field operations, for warmer liquid temperatures are generally experienced during processing and therefore higher rates of gas evolution and indeed higher levels of bubble-induced turbulence may be expected. Video analysis at higher temperatures would give an indication of the cumulative bubble growth following depressurization.

It was also apparent that the final equilibrium value, which is a reflection on the amount of gas in solution initially, was effectively independent of temperature. The solubility of CO_2 in water at 15°C is nearly twice that at 60°C [25]. The solubility of CO_2 in gas oil at 20°C is also approximately twice that at 60°C [35]. Simple calculations were carried out, to determine the masses of gas in the liquid and gas phases in water, saturated with CO_2, at 10 bara, at initial liquid temperatures of 20°C and 60°C, as described in appendix III, and using solubility data given in the literature [29]. The masses of gas at 20° and 60°C were calculated to be 175.8 g and 72.0 g respectively in the liquid, and 14.6 g and 12.8 g respectively in the gas phase, indicating a predicted decrease of ~20% in the equilibrium pressure at 60°C. Yet, for CO_2 in water, figures

6.15a and 6.16a, or in gas oil, figure 6.39c, this decrease in solubility with increasing temperature was not apparent in the pressure-time plots recorded as a result of varying the temperature.

The model used in the literature, based on Henry's law, to calculate the mole fraction solubilities was derived using a large data base consisting of CO_2 solubility data in water from several sources. Whilst solubility data does deviate from Henry's law at higher pressures, the model used was shown to be valid for temperatures in the range 273 to 433K (0 to 160°C) and pressures up to 10 bara. It may be assumed, therefore, that there is indeed, approximately twice as much gas in solution initially at 20°C than at 60°C. Although not carried out, it may be predicted that the relative degree of saturation with respect to bubbling time for water at 60°C is higher than that at 20°C. In other words, the time required to fully saturate the liquid with CO_2 at 60°C would be less than that required for saturation at 20°C.

A simple explanation for why the equilibrium pressure at 60°C and 40°C is higher than expected, would be to suggest that although the temperature probe was reading 60°C the bulk liquid temperature could have been a lot less. There were, however, several indications that the liquid in the vessel was uniformly heated to the temperature recorded by the indicator. Firstly, the probe was situated near the top of the bulk, whilst the heating element was near the base of the vessel. Secondly, although there was no agitation during heating, there were visible convection currents in the bulk, suggesting uniform heating. Finally, the bulk liquid is surrounded by a 10 mm thickness of stainless steel, which would have aided in the uniform heating. A period of two hours was generally required to reach a temperature of 60°C, which ensured the stainless steel mass was also heated. Simply by feeling the outside walls, it was clearly evident that the steel body and indeed the flanges were heated to the same temperature. The temperature of the liquid was also tested using a mercury thermometer when the resistance thermometer probe recorded a reading of 60°C, and found to be accurate within 0.2°C.

It should be noted that in fact, the temperature of the water was generally heated to around 65°C before saturation with CO_2 was started, because when first exposed to the gas, the temperature of the liquid generally dropped by 3-4°C. After the initial temperature drop, the temperature remained constant during continued saturation. It appears, therefore, that during saturation, there are no apparent reasons to explain the unusual behaviour. Attention must now be turned to the rapid depressurization and subsequent pressure recovery process. Neither at 20°C, nor at 60°C, was there any significant drop in the temperature of the liquid during the depressurization of the vessel. As discussed in section 7.2.2, the temperature drop in the gas phase for an expansion from 0.8 litres to 5.1 litres at 20°C during a pressure reduction of 8 bar is minimal, owing largely to the bulk mass of surrounding steel and liquid, compared to the mass of gas (~0.01%).

The initial rapid pressure recovery at 60°C may largely be explained by the gas diffusivities, which generally increase with increasing temperature. Due to the additional energy in the system at the increased temperatures, the velocity of the gas molecules is larger and the ability to escape from solution increases. Indeed the p-V plot obtained using gas oil, figure 6.31cii, clearly indicates that gas evolution at the higher temperatures occurs whilst the piston is still moving and the gas volume is still expanding. The major part of the pressure recovery to equilibrium occurs during the initial rapid stage, corresponding to the macromolecular bubble activity.

Whilst there appears to be no single major factor influencing the equilibrium results, several factors do change with temperature, which may contribute in some way. The surface tension, generally decreases with increasing temperature, and is an important factor since it determines whether or not a bubble will start growing. The vapour pressure of water, and indeed hydrocarbons (of the same order of magnitude as water) increases with increasing temperature. Indeed, the vapour pressure of water at 60°C is ~10 times that at 20°C [169]. Another more significant contribution may lie in considering the mass of gas required at the two temperatures to reach the same final pressure. At a higher temperature, the pressure of a given mass of gas will be higher, but by nothing like the extent of the solubility change with temperature.

Whilst the suggested explanations are not conclusive, it should, however, be pointed out that the decrease in gas solubility with increasing temperature was also not reflected in observations of the homogeneous nucleation behaviour of gases in water [137]. Over the temperature range 5-40°C, only a small change in cavitation behaviour with increasing temperature was observed. The unexpected behaviour was put down to the properties of the water, but no explanation was provided. In addition, as discussed in chapter 3.5, the temperature effects of the solubility of gases in liquids are not fully understood.

In terms of the other less soluble gases, Ar and N_2, there were no significant differences in the rate of approach to equilibrium or the final equilibrium pressure with increasing temperature, either in water, kerosene or gas oil. This was not too surprising, since equilibrium was reached within ~30 secs anyway, and these gases are only sparingly soluble in water even at 20°C, so the effects would be very much less. It may therefore be predicted, that at the higher temperatures experienced in offshore operations, the rate of gas evolution of CO_2 may become comparable to the rate of evolution of the other less soluble gases. Gases which have similar properties to those of CO_2 in kerosene and water, would be expected to show similar behaviour at the increased temperatures as observed with CO_2.

7.3.1.2 Solid nuclei

The addition of insoluble solid nuclei to the system significantly increases the surface area available for nucleation and hence the rate of approach to equilibrium. Indeed, this was shown to be the case in practice. The addition of 500 ppm 5μm uni-sized silica flour particles to a CO_2 in water solution increased the surface area available for nucleation, by a factor of $\sim$4, whilst the time taken to reach equilibrium was halved, figure 6.26. This has significant industrial implications relating to reservoir solids. Oil field waters can also contain high concentrations of dissolved solids. In addition to the more common salts, Na^+, Ca^{2+}, Cl^- and SO_4^{2-}, quantities of Sr^{2+} and Fe^{2+} are also present. Mixing of brines, caused by, for example, sea water injection or indeed, leaky casing, can cause the precipitation of sulphates of barium, strontium and calcium, typically known as hard scale, which can be a nuisance in oilfield flow lines. Soft scale, composed of calcium carbonate, is usually caused by the loss of dissolved CO_2 from brine during pressure reduction [4].

As mentioned in chapter 5.3, and shown in the Coulter counter size distribution spectrum, figure 5.1, the particle size appeared to follow a normal distribution with a volume mean particle size of around 2.5-3μm. Although not affecting the overall behaviour of the system on addition of solid nuclei, the surface area available for nucleation will be affected. Indeed, the addition of 500 ppm 3μm silica flour particles to a CO_2 in water solution results in an estimated additional increase in the surface area of the particles of approximately 60%, compared with the addition of 500 ppm, 5μm particles. The surface area available for nucleation would therefore be increased by a factor of around 6.5, compared with an increase of $\sim$4 for 500 ppm 5μm particles.

The results obtained using 500 and 1000 ppm concentrations could also have significant industrial implications, for the results showed that the plots for the two solid concentrations were similar in all respects, despite the fact that the surface area available for nucleation was effectively doubled. This suggests that the rate of gas evolution can only be enhanced to a certain degree, above which the presence of additional nucleation sites has no significant effect. If this were the case, then there may not actually be any significant differences between the pressure-time plots obtained with the addition of $3\mu m$ uni-sized particles or $5\mu m$ uni-sized particles.

Whilst it could be argued that, being uniformly distributed in suspension, the presence of the particles could effectively reduce the distance necessary for the gas molecules to travel, particularly for the less soluble gases, since the distances between gas molecules is greater, this was not found to be the case. There was no significant effect observed on addition of 500 ppm solid nuclei using the less soluble gases tested, as shown in figure 6.30 for CH_4. This suggests that diffusion of gas molecules to the nucleation sites may not be a rate limiting factor. The factors associated with the mechanisms of bubble nucleation, which are more likely to be rate limiting, are the number of active sites on the nucleating particle, and the contact angle. For small contact angles, nucleation becomes difficult, but if the contact angle is large, favouring the formation of a critical size bubble, the bubble has more difficulty in becoming detached from the surface of the nucleating particle, and whilst the growing bubble is attached to the site, no further nucleation can take place there. The detachment rate, if slow, may be the rate determining step. The nucleation rate is also dependent on the size and surface properties of the nucleating particle, the smaller the radius of the nucleating particle, the less effective the nucleation efficiency [125].

7.3.1.3 Fluid agitation

In a dynamic system, in which agitation was provided in the form of a pulsed jet at a frequency of ~60 Hz, as described in chapter 4.3, it was clearly evident that there was an improvement in both the new equilibrium value and the rate of evolution. A 25% increase in the final equilibrium pressure was observed for an agitated CO_2 in water system, figure 6.27a, together with an increase in the rate of approach to equilibrium by a factor of ~5, figure 6.27d.

Tests were carried out on each gas-liquid system, to determine whether the effects observed in a system in which there was agitation over the complete run were largely influenced by agitation during saturation, or largely due to agitation during the pressure recovery period, or indeed a combination of the two. In a system such as CO_2 in water, the water is not fully saturated after 15 mins bubbling. It was considered possible that more gas may be dissolved in solution, over the same bubbling duration, as a result of fluid agitation during saturation, which would have the effect of increasing the mass transfer rate and hence the rate of uptake of gas.

For the less soluble gases, in both water and kerosene, saturation is reached after bubbling for 15 mins. Fluid agitation during saturation would not be expected to influence the results in any way, since it is not possible to dissolve any more gas in the liquid above the saturation point, and indeed this was shown to be the case, figures 6.30 and 6.45. In fact, tests showed that agitation during saturation of water with CO_2, also did not influence the amount of gas in solution initially, and therefore had no effect on the p-t traces recorded, figure 6.27. This, however, is probably due to the effectiveness, or indeed, ineffectiveness, of the jet, for turbulent conditions, although not possible to achieve in the present study, may be expected to decrease the time required for saturation. The test results indicated that whilst the intermittent jet pump is effective in encouraging the dissolved gas to come out of solution, it is less effective in increasing the rate of uptake of gas into solution.

With CO_2 in water, therefore, the increase in the new equilibrium value and indeed the time taken to reach this new value for a dynamic state compared to that obtained from a system with no agitation was found to be due to agitation after depressurization, figure 6.27. The increases observed in the timescale of approach to equilibrium can be accounted for by a number of reasons. The aggregation of dissolved gas molecules in the liquid following depressurization would appear to be the key factor, both in terms of gas microbubble aggregation, and in terms of macroscopic bubble coalescence. With agitation, the likelihood of a depleted domain next to a concentrated domain is increased, and as a result, the diffusion rates are likely to be increased, the clustering and growth of microbubbles is increased and hence the rate of gas evolution increases.

Since the equilibrium pressure recorded is influenced by agitation of the liquid, if the agitation source were turned off at equilibrium, the pressure would be expected to drop to that equilibrium pressure recorded with no external agitation. This reduction in pressure would be very slow, because the process is diffusion controlled. Indeed, the pressure was monitored for ~40 mins after equilibrium in an agitated CO_2 in water system was reached and the pump was turned off. In that time the pressure dropped by ~0.2 bar. For a CO_2 in water system, the actual drop expected would be ~0.6 bar, suggesting that a period of 2-3 hours would be required for equilibrium to be established.

It was established in section 7.3.1.2 that the addition of solid nuclei to a CO_2 in water system, with no agitation, effectively doubles the rate of approach to equilibrium, but does not significantly influence the final equilibrium pressure, figure 6.26. Agitation of a CO_2 in water system, with no additional solids, under the same bubbling conditions, increases the rate of approach to equilibrium by a factor of 5, figure 6.27. A comparison of an agitated CO_2 in water system with an agitated CO_2 in water system containing 500 ppm solids, figure 6.29, shows virtually identical behaviour, indicating that the effects of fluid agitation and solids are not additive. In other words, in a system in which there is agitation, and there are additional solids, the rate of approach is determined by the agitation rather than the solids.

An increase of 22-25% in the final equilibrium pressure was also observed for the less soluble gases, Ar, CH_4, figure 6.30a, N_2 and O_2 in water, as a result of agitation after depressurization. The timescale of approach to equilibrium was not significantly reduced, for equilibrium in a system with no external agitation is reached within approximately 30 secs.

One of the main differences observed between oil and water, using CO_2, is the initial rate of gas evolution, and hence the rate of approach to equilibrium. With CO_2 in kerosene, in which there was no external agitation, equilibrium was reached within a few secs of p_{min} being reached, figure 6.43a. It was therefore unlikely that fluid agitation would have much effect $\sim$10 secs after p_{min} was reached. An improvement, however, was observed during the initial rapid stage of pressure recovery, since 80% of the total pressure recovery with agitation took 0.4 secs, compared to 0.86 secs without agitation. If the increase in the equilibrium pressure, figure 6.43a, was not as a result of agitation after depressurization, since equilibrium was reached within seconds, then the 10% increase must have been a result of agitation during saturation and hence more gas going into solution for the given bubbling time. Indeed, this was supported by the p-V data, figure 6.43b, which strongly suggests there is more gas initially in the agitated system, as gas evolution and hence pressure recovery occurred much earlier than in a system with no external agitation. Since it was calculated from figure 6.38a, that after 15 mins, CO_2 in kerosene was $\sim$95% saturated, the increase in the equilibrium pressure was due to an increase of a few % in the initial dissolved gas content. The same characteristics were observed with CO_2 in Statfjord crude, figure 6.44. The effects of fluid agitation could be verified fairy easily by ensuring a completely saturated solution initially.

In kerosene, the increase in the equilibrium pressure, as a result of fluid agitation, was 35-40% for N_2, figure 6.45a, and CH_4, which is particularly important given the industrial context. As discussed in chapter 2.2, over 75% of natural gas is methane. Unlike CO_2 in kerosene, there was no indication from the p-V plots that any gas evolved during depressurization, figure 6.45c, and fluid agitation after depressurization clearly influenced the rate of gas evolution. This would also help to explain why an increase in p_f of only 10% was observed for CO_2 in kerosene and crude, figures 6.43a and 6.44a, compared to an increase in p_f of 35-40% for CH_4 and N_2, figure 6.45a. In the first two cases the increase was largely due to the small increase (5-10%) in the dissolved gas content initially, and so only a small increase would be expected. Whereas, with CH_4 and N_2, for which complete saturation of kerosene with these gases is achieved within minutes, the results were largely a result of agitation after depressurization.

Putting the results into context, the energy dissipation rate of the pulsed jet, in terms of the loss of kinetic energy, was estimated to be smaller, by a factor of ~2-3, than the energy dissipated in a pipeline of unit length (1 m), 50 mm in diameter, with a moderately rough internal surface (0.001 friction factor) and a liquid velocity of 2 m/s. In the industrial context, with higher flow velocities and larger liquid volumes, the effects of fluid agitation and indeed turbulence, would be expected to be much more significant.

7.3.1.4 Salinity

The rate of approach to equilibrium, using CO_2 as the solute gas, was significantly increased by the presence of NaCl salt, figure 6.24a. Indeed, the pVT data obtained in tap water and the various salt concentrations showed a somewhat surprising increase in magnitude in the time taken to reach the new equilibrium value, in that the rate of approach to equilibrium in 3% and 25% saturated salt solutions was faster by a factor of nearly 20, than that in tap water and faster by a factor of 3, in a fully saturated salt solution compared to that in water. The rate of approach to equilibrium can be increased in the presence of solids, as discussed in section 7.3.1.2, and indeed the presence of excess insoluble salt in the liquid could act as potential nucleation sites for the evolving gas. This would undoubtedly increase the rate of gas evolution, by a factor of 2-3. Yet this would only really be feasible approaching a fully saturated salt solution, it can not really be used to explain the increased rate at 3% or 25% salt saturations, in which the salt exists in a soluble state.

An explanation for the increase in rate with salinity was briefly mentioned in section 7.2.1, where the equilibrium state of the dissociation reaction of CO_2 in water was addressed, and is discussed in detail in section 7.4. The rates can be explained due to the significant difference in the extent of the dissociation reaction which occurs between CO_2 in tap water and CO_2 in salt water. As discussed in appendix IV, whereas with CO_2 in tap water, the equilibrium in eqn 3.18 lies over to the left hand side, with ~95% of the dissolved CO_2 existing in the form of weak carbonic acid, in salt water, the equilibrium lies far over to the right hand side, with the dominant species being the dissociated bicarbonate ions. As discussed in appendix IV, gaseous CO_2 can be evolved directly from the bicarbonate ions, and indeed the rate constant for the conversion of HCO_3^- ions to gaseous CO_2 is many times faster than the conversion of H_2CO_3 to gaseous CO_2, by ~4 orders of magnitude, although this is influenced by the solution composition. The significant difference in the conversion rates are largely due to the change in molecular configuration of H_2CO_3 (bent) to CO_2 (linear), as discussed in section 7.4. In terms of diffusion coefficients, information in the literature tends to indicate that there is no ionic drag associated with ion mobility [170]. In other words, even though CO_2 exists largely in ionic form in salt solutions, and largely in the undissociated form in tap water, the diffusion coefficients of the two species are of the same order of magnitude. Indeed, in general, the differences observed in the diffusion coefficients between molecules and ions are largely a reflection of the size of the species.

If the dissociation reaction of CO_2 is the probable cause for the increased rate of evolution, then an increase in the rate would not be expected for the other gases in salt water, and indeed, this was shown to be the case, for there were no significant increases in the rate of gas evolution with increasing salt saturation with any of the other gases tested, figure 6.25a.

At the larger salt saturations, approaching 100% salt saturation, other factors may also influence the gas evolution process, and could explain why the rate of approach to equilibrium for a fully saturated salt solution is not so fast as that for a 25% saturated salt solution. At 20°C, the density rises from 998 kg/m^3 for pure water to 1201 kg/m^3 for a 100% saturated salt solution, figure I-7. The viscosity is effectively doubled from water to a salt saturated condition, rising from 1 cP for pure water to 1.95 cP for a 100% saturated salt solution at 20°C, figure I-8. There is also a small increase in surface tension with salinity [171]. In addition, the diffusion coefficient may be expected to decrease with increasing salt saturation, due to the increased number of ions in solution. Indeed, the diffusion rate of dissolved CO_2 in water at 25°C is 1.92×10^{-9} m^2/sec compared to 1.60×10^{-9} m^2/sec approaching a fully saturated NaCl salt solution [149].

In terms of visual observations, there was a noticeable difference in both the size and hence the rise velocity of the bubbles in tap water compared to salt water solutions. There is very little difference in the rise velocity of bubbles in tap water and salt solutions for bubbles less than 450μm in diameter, yet the difference in the velocity in water and brine becomes increasingly significant for bubbles with diameters greater than 450μm [150]. Approximately 15-20 secs after depressurization, those in salt solutions appeared to be much smaller and to be travelling much slower, by a factor of ~4, in comparison to those in water. This also indicates less bubble-induced turbulence in high concentration NaCl salt solutions. It was difficult to establish visually, without video evidence, whether there was a difference in bubble sizes and velocities in a 3% salt solution compared to a fully saturated salt solution.

The solubility of gases tends to decrease with increasing salt saturation over the range of interest. With the less soluble gases, the decrease in solubility with increasing salt saturation is not so significant and indeed this was reflected in the equilibrium pressures recorded, figure 6.25. It is apparent from the results obtained using CO_2 in water, however, that the decrease in solubility with increasing salt saturation is only reflected with salt saturations above ~40%, figure 6.22. Above this salt saturation, the equilibrium pressures recorded, reflecting how much gas is in solution initially, decrease with increasing salinity. The equilibrium pressures recorded over the 3-25% salt saturation tended to show a small increase with increasing salinity.

It should be noted, however, that whilst the non linear behaviour was observed, and was reproducible, there was only an increase of 4% in the equilibrium pressure obtained in a 25% saturated salt solution, compared to that in tap water. The 10% reduction in the equilibrium pressure obtained in a fully saturated salt solution, compared to that obtained in tap water, was more significant, and indeed was expected from solubility predictions. In addition, complete saturation of a fully saturated salt solution (100%) with CO_2 occurred in a much shorter time than compared to tap water under the same bubbling conditions. Since much of the industrial interest lies in the 0-10% salt saturation range, it seems apparent that over that range, increasing the salt concentration does not really influence the final equilibrium pressure obtained after depressurization.

Due to the sparingly soluble behaviour of N_2 and Ar in water, it is inconclusive whether the non linear behaviour observed with CO_2 in salt water solutions is characteristic of all gases or characteristic only of gases which dissociate in water. It seems more feasible, that the small increase in p_f observed, with increasing salinity to 25% salt saturation, is simply related to the dissociation reaction and hence the increase in the initial rates of gas evolution observed at 3 and 25%.

7.3.1.5 Mixed gases

An area which has particular significance in the oil industry is the behaviour of mixed gas compositions. In both water and kerosene, the rate of gas evolution using mixed gases was significantly enhanced compared to the rates obtained using the individual component gases. In water, an improvement, by a factor of ~3-5, was observed in the initial rate of approach to equilibrium of the mixed gas system, compared to the rate of approach of the equivalent single component systems, figures 6.31 and 6.32. A similar increase was apparent in the rates of approach to equilibrium for the same mixed gases in hydrocarbons, figures 6.46 and 6.47.

The principle behind testing mixed gas compositions, in this case, CO_2 and N_2, was that the evolution of CO_2 from a saturated solution during depressurization might be enhanced by the presence of a small amount of a sparingly soluble, inert gas such as N_2. Being less soluble, and inert, and therefore leaving solution more readily, the evolution of N_2 may well trigger the CO_2 evolution process. In practice, an increase in the rate of gas evolution was observed, in both water and hydrocarbons. In oil, analysis of the video sequences in CO_2 and N_2 indicated that evolution of N_2 does indeed occur slightly earlier than evolution of CO_2, as discussed in section 7.2. Careful examination of the video frames capturing the two systems, N_2 and CO_2, individually in water (plates V and VI), from an initial pressure of 10 bara, however, showed that during depressurization the mass evolution of gas, initiated by the rise of the mushroom of gas to the surface, occurred at approximately the same time, yet equilibrium of a mixed gas system compared to that of CO_2 in water or oil is established much sooner. This suggests that the effect may be more significant immediately after depressurization, during the initial stages of rapid pressure recovery. Video evidence during and immediately after the depressurization of a mixed gas system in water, is necessary, however, in order to fully understand the mechanisms of mixed gas evolution.

Being a thermodynamically enclosed system, following the release of pressure from the vessel, gas is evolved from solution. It was considered that the composition of the gas in the gas phase following depressurization would not be in the same ratio as the initial composition in the liquid phase, particularly for the mixed gas containing 70% N_2 and 30% CO_2. This was shown to be the case in practice. Calculations of the final gas composition in the gas phase, given in appendix III, indicated that the composition tended to swing in favour of the more soluble gas. The final gas composition of the 70% CO_2/30% N_2 mixed gas was calculated to be in the ratio 88% CO_2:12% N_2, whilst the final composition of the 70% N_2/ 30% CO_2 mixed gas was calculated to be in the ratio 40% N_2:60% CO_2.

As discussed in appendix III, it may be assumed that at the low pressures ($\leq$10 bara) experienced in the vessel, each constituent gas may be considered to behave as an ideal gas, independent of its composition in the mixture. As a result, the total pressure of the mixture may be calculated, according to Dalton's rule of additive pressures, as the linear sum of the pressures exerted by each constituent at the temperature and total volume of the mixture. This was reflected in the equilibrium pressures obtained in the mixed gas systems. For each mixed gas, in both oil and water, the results tended to show that the equilibrium pressure obtained was approximately the sum of the equilibrium pressures of the two individual components at the same pressure as they appeared in the mixed composition initially.

As discussed in appendix III, the same general behaviour may be expected at the higher pressures, although the component pressures and volumes would need to be evaluated using equations of state to account for the deviation from ideality. In terms of the extensive properties of a gas mixture, such as the internal energy, entropy and enthalpy changes, during a process, these can generally be determined by summing the contributions of each component in a mixture [172]. The evaluation of intensive properties of a gas mixture, per unit mass or per unit mole, however, involves averaging in terms of mass or mole fractions.

It should be noted, however, that the results obtained in this study, give an indication of the behaviour of mixed gas systems in an enclosed system, and are an imperfect analogue to steady flow systems. In an industrial application, such as flow through control valves, the reduction in pressure and hence the change in gas composition would only be apparent in a very short period of time, of the order of a few secs, as the stream passes through the control valve. As a result, the results obtained can only really be applied during and immediately after the rapid initial depressurization period, over a period of perhaps 0.1-5 secs.

7.4 Dissociation reaction of CO_2 in water

There are three key features which occur with CO_2 in water, which do not occur with CO_2 in hydrocarbons, nor with the less soluble gases in water or hydrocarbons. These can all be shown to be related to the dissociation reaction which occurs when CO_2 is dissolved in water. The first of these is a more complex evolution pattern observed in water (plate VI), compared with N_2 in water (plate VII). The second is that the rate of approach to equilibrium for a CO_2 in water system is approximately two orders of magnitude slower than for the other gases in water, figure 6.10a, and indeed, two orders of magnitude slower than CO_2 in kerosene or Statfjord crude, figure 6.36a. The third, but no less significant feature is that the rate of approach to equilibrium for CO_2 in water is generally slower by a factor of 20 compared to that in saturated salt solutions, figure 6.24a. This difference in the rate of approach was not observed for any of the less soluble gases in water and salt water, which again suggests that it is related to the dissociation reaction of CO_2.

The equilibria describing the dissociation reaction of CO_2 in water is generally given in the form

$$CO_{2(g)} \rightleftharpoons CO_{2(aq)} \rightleftharpoons H_2CO_3 \rightleftharpoons HCO_3^- + H^+ \qquad (7.5)$$

It is more correct, and indeed necessary, in order to explain the evolution behaviour of CO_2 in water, to write the equilibria in the form [170,173]

$$\begin{tikzcd} (a)\ CO_2 + H_2O \arrow[rr, leftrightharpoons] \arrow[dr, leftrightharpoons] & & H_2CO_3\ (b) \arrow[dl, leftrightharpoons] \\ & HCO_3^- + H^+\ (c) & \end{tikzcd} \qquad (7.6)$$

In this way, it can be seen that gaseous CO_2 can be formed directly from the dissociated ions, without being converted back into H_2CO_3, as depicted in eqn 7.5. It is therefore quite feasible for the small volume of gas evolved in the second stage of CO_2 dissolution (plate VI, 17-22), as discussed in section 7.2.1 and appendix IV, to be the evolution of the 3-5% of dissolved CO_2 water existing in the form of dissociated ions, particularly if the rate constants for the reactions are considered. The rate constants for the reaction (b) to (a) and (c) to (a) at 25°C, are 26.9 sec^{-1} and 10.2×10^4 l mol^{-1} sec^{-1} respectively, indicating that the path taken by the bicarbonate ions, (c) to (a), occurs very much faster than the path taken by the weak carbonic acid form (b) to (a). The rate constants for the forward and reverse reactions are discussed in more detail in appendix IV. The slow hydration rate of CO_2 in water, path (a) to (b), with a rate constant of 3.0×10^{-2} sec^{-1} at 25°C, lies largely in the change of molecular configuration which must occur. The $CO_{2(aq)}$ molecule is linear, O=C=O, with waters of hydration attached, whilst H_2CO_3 has the form

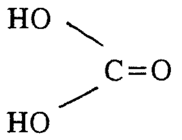

with associated waters of hydration [166]. It is due to this effective 'slow step', in both the forward and reverse direction, occurring as a result of the chemical reaction between CO_2 and H_2O, that the rate of gas evolution is very much slower than in kerosene, in which CO_2 does not dissociate, or with the other gases, in which the rate constants would be expected to be 3-4 orders of magnitude faster than for the reaction (b) to (a) occurring with CO_2 in water.

The form of eqn 7.6, and the associated rate constants, also help to explain the differences observed in the rates of approach to equilibrium in saturated NaCl salt solutions and in water. As discussed in section 7.3.1.4, and in more detail in appendix IV, the equilibrium in eqn 7.5 lies far over to the right hand side in salt solutions, for the dominant species is bicarbonate ions, with only a small proportion of carbonic acid. In a 3% salt solution, ~95% of dissolved CO_2 exists in the dissociated form [170]. As explained above, using the rate constants given, the route available for the bicarbonate ions, resulting in gas evolution, is very much faster than that taken by the carbonic acid form, and it therefore follows, that the rate of gas evolution in salt water, path (c) to (a) would be very much faster than that in tap water, path (b) to (a).

7.5 Gas evolution in oil/water mixes

This section briefly discusses the results of the tests described in chapter 6, sections 6.26 and 6.27, investigating the behaviour of gas evolution in oil/water mixes and the use of surfactants. Whilst not actually significantly enhancing the rate of approach to equilibrium, the addition of surfactant to the contents in the vessel were shown to influence the gas evolution process in some way. Unfortunately the tests were only simple, for emulsions could not be maintained in the vessel, although they may have been stabilized to a certain extent by the addition of surfactants. It was decided that there would be no significant differences in the time traces using additives, for the typical additives used in the oil industry, such as deoxygents, defoaming agents and descaling agents are generally small, water soluble, simple molecules. In terms of using surfactants, it was anticipated that if indeed there was any change it would be during the slow recovery to equilibrium, as the surfactant would effectively reduce the interfacial tension of the oil-water interface. This, therefore, would only really be effective with regard to CO_2, and was indeed observed, in a saturated 1:20 v/v kerosene/water mix, figure 6.50. The final equilibrium pressure was found to increase on addition of 500 ppm of surfactant, Span 80. The surfactant was found to have no significant effect during the first 10-20 secs after depressurization, but approximately 40 secs after depressurization, the pressure levelled off with no surfactant, yet continued to rise, by an additional 20%, with surfactant.

In terms of the oil/water mixes in which agitation was not used, this could have implications in primary separators in which the oil/water systems are left to settle out under gravity. In order to get any quantitative data in the existing rig, it may be necessary to block a significant amount of gas space, using, for example, a plastic coated bung, such that direct comparisons can be made with oil/water mixes and systems containing the equivalent volume of either oil or water, i.e. 5 litres of liquid, compared with 10 litres. In that way, it would be possible to validate the predicted equilibrium pressures, and to predict the outcome of these and other results, relating to surfactants, more easily. There is scope to study oil/water mixes and emulsions, by improving the stirring mechanism as discussed in chapter 8.3, and to explore the use of surfactants in the rig, in more detail, focusing on particular applications, although there was inadequate time to carry out any substantial research in these areas.

8.0 FURTHER WORK

A period of three years, in which a significant period of time was set aside for the design and manufacture of a suitably instrumented rig facility, was not sufficient to carry out a complete investigation into gas dissolution behaviour. The experimental results obtained in the present study, however, can be used to establish an overall framework which fits the experimental data and hence enables predictions to be made. One particular area in which predictions would prove useful relate to how other gases may behave under the same conditions. Indeed, several suggestions and proposals concerning the nature and behaviour of other gases were put forward during the interpretation and discussion of results. By carrying out a few additional experiments, as outlined in section 8.1, the validity of the theories and predictions can be established. In thinking ahead, slight modifications to the rig would be necessary, not only to improve data collection, but also to improve the understanding of various phenomena. The rig modifications are discussed in section 8.2. Section 8.3 gives a brief outline of three suggested areas, using the existing rig facility, around which an experimental programme could be based, but which were out of the scope of the present study. The final section, 8.4, focuses on the application to the oil industry. In this area, predictions are necessary regarding the geometry and size of the vessel, in terms of scaling up, and in developing an open system, which is a more realistic representation of offshore conditions.

8.1 Theoretical framework and predictions

In terms of the nature of the gases tested in water, it became apparent that there were two distinct types of behaviour. The gases CH_4, Ar, O_2 and N_2 were shown to behave in a similar fashion in all respects, whereas CO_2 clearly stood apart, owing largely to the increased solubility, being ~ 50 times more soluble than N_2 in water and ~ 30 times more soluble in water than CH_4, Ar and O_2, and the fact that CO_2 dissociates in water.

A significant input to the discussion came from the video evidence, which captured the sequence of events in water and kerosene using CO_2 and N_2. Whilst it was predicted that the same experiments in O_2, Ar and CH_4 may not have produced anything new, a useful exercise would be to carry out the same experiments using, for example NO_2 or SO_2. The complex gas evolution pattern observed only with CO_2 in water was put down to the dissociation reaction of CO_2 in water. It could therefore be predicted that the same gas evolution pattern would be observed with SO_2 and NO_2 in water. In addition, the slower rate of approach to equilibrium using CO_2 in water compared to the other gases tested, the much faster rate of approach to equilibrium using CO_2 in kerosene than in water, and the slower rate of approach to equilibrium using CO_2 in saturated NaCl salt solutions compared to tap water, were all considered to be due to the dissociation reaction, as discussed in chapter 7.4. These characteristics would, therefore, also be expected with NO_2 and SO_2 in water, together with a small drop in pH and in the liquid temperature during saturation.

The theory that the extent of dissociation of CO_2 in tap water and salt water is the major factor influencing the rate of evolution of CO_2, can be substantiated by capturing the sequence of events during and immediately after depressurization of a salt water solution saturated with CO_2. In water, it was suggested that the small amount of gas evolving before mass evolution was due to the small proportion of bicarbonate ions ($\sim 5\%$) existing in solution, backed up by comparing the rate constants for the conversion of carbonic acid to gaseous CO_2 and the conversion of bicarbonate ions to gaseous CO_2. The route taken by the bicarbonate ions has a very much faster rate constant, as discussed in chapter 7.4 and appendix IV, and as dissolved CO_2 in salt water exists largely in the dissociated form (95%), compared to the carbonic acid form, differences may be expected both in terms of the stages of gas evolution, as discussed in chapter 7.2, and in terms of timescale of events.

Time, cost and easy access to a suitable video camera prevented a thorough investigation of the effects the initial conditions, in terms of liquid temperature and saturation pressure, had on the sequence of events during depressurization. The key features which were obtained from the video sequences, and could therefore be compared relatively easily under different conditions, were the depth of propagation and velocity of the bubble front, the mushroom effect in water, and the timescale of events. Some tentative relationship was apparent between the piston velocity and the depth of propagation and velocity of the bubble front, but could only really be verified by comparing the velocities and depths of the bubble front from higher initial saturation pressures, in which the velocity of the piston is significantly increased.

The effect of the initial saturation pressure would also be valuable on both a CO_2 in kerosene system, in terms of the timescale of events, and the percentage of pressure recovery during depressurization, and on a CO_2 in water system containing insoluble solid nuclei, in terms of the rate of pressure recovery. At higher initial pressures, there is more gas in solution, and hence the rate limiting phenomena relating to solid nuclei may be investigated further.

One area in which questions remain unanswered is the origin and cause of the initial mushroom of gas, which occurs under all conditions, with all gases in water. Video analysis from different starting conditions may give an indication of the factors affecting, for example, the rise velocity and size of the mushroom of gas. Visual observations through the base window were not conclusive, as the events were too rapid to be observed in any detail by the human eye, but video analysis of the pressure release through the base window, with careful use of lighting, and if necessary, mirrors, may also give some indication of where and how the volume of gas forms.

In terms of the behaviour of other gases, the noble gases, such as Kr and Xe, would be predicted to show the same characteristic behaviour as Ar. For the gases more commonly found in offshore processes, such as the light hydrocarbons, C_1-C_{10}, these alkanes may be expected to show the same characteristic behaviour as CH_4. In water, the behaviour of the gases tested fell into two categories, CO_2, being a polar molecule capable of hydrogen bonding, and 'all the other gases', being non polar and inert. In hydrocarbons, such as kerosene and gas oil, however, there was a distinct difference in the behaviour of CH_4 compared to that of Ar and N_2. A property of gas solubility is that 'like' dissolves 'like', as discussed in chapter 3.5. The preferential solubility of CH_4 in hydrocarbons is clearly evident in the results, in terms of the increase in solubility and hence the increase in the equilibrium pressure, in comparison to N_2. This would also be expected for other hydrocarbons, and indeed more so, for the heavier hydrocarbons in kerosene, because the solubility of alkanes increases with increasing solute chain length. As an indication of the relative solubilities of hydrocarbons compared to CO_2 in kerosene, it would be predicted that ethane, C_2H_6, would produce similar p-t plots to that of CO_2, whilst the heavier hydrocarbons, C_4-C_{10} may reach higher equilibrium values, reflecting the increased amount of gas in solution initially. Another gas commonly found offshore is H_2S. Although out of the scope of the present study (safety restrictions), the results of a study using H_2S could have significant implications to the offshore oil industry.

Valuable information would also be gained in using carefully chosen combinations of gases. Timing allowed only the brief analysis of a mixed gas composition of CO_2 and N_2. The reasoning being that the presence of a small quantity of a less soluble gas might trigger the evolution of CO_2, and indeed, the results showed a faster rate of approach to equilibrium for the mixed composition, in comparison to a single component system, in both water and kerosene. In order to fully understand the behaviour of mixed gases, and the mechanisms of gas evolution, video evidence should be obtained for the CO_2/N_2 system and compared to both the pVT data for the mixed gas composition and the video evidence of the single component systems.

The fact that CO_2 dissociates in water did not seem to influence the behaviour of the mixed gas, for similar characteristics were observed in kerosene. In order to validate the predictions, it would be worth carrying out the same experiments using gases which have similar solubilities. A suitable choice would be CO_2 and C_2H_6 in kerosene, or two similar hydrocarbons in kerosene, focusing on the pVT data, the video events during depressurization, the rate of approach to equilibrium and the equilibrium pressure.

8.2 Rig modifications

The few rig modifications and suggested improvements to the rig would include a piston mechanism in which the piston is mechanically driven and not influenced by the conditions in the vessel, thereby obtaining a piston movement with a constant velocity; a better method for obtaining more accurate gas temperature measurements, which would require an instrument with a faster response time than the platinum resistance thermometer; and a method for achieving turbulent conditions, as opposed to agitated conditions.

During the design stages of the rig, several methods for obtaining a fast rate of release of pressure in the vessel were considered. Attention was mainly focused on achieving as fast a rate of pressure release as possible, with some means of monitoring the rate of release and the free gas volume with respect to time, and in being able to do it repeatedly and reproducibly. Another key factor was, of course, cost. In fact, the pneumatic cylinder has not actually been used to its full effect, as the air pressure used to drive the cylinder up was only rated at 6 barg, which was the on-line air supply to the laboratory. If a compressor was used to increase the flow of gas into the lower chamber of the double acting cylinder, the velocity at which the piston moved upwards could be increased.

It was not originally envisaged that the gas dissolved in the liquid would have some influence over the piston velocity. Although not a major problem, and not affecting the general trend of results, in some instances it would be an advantage to have a piston which operates independently of conditions in the vessel. Using a line pressure of, say, 15 barg, with a feed-back loop, incorporated into the existing rig set-up, thereby altering the air pressure in the pneumatic cylinder, may prove effective. Alternatively, some sort of mechanical rack driven piston could be used, which would also result in a constant rate of pressure release.

In terms of temperature measuring devices, when considering the instrumentation required during the design stages of the vessel, the thermometer was only intended to measure the temperature of the liquid, and a resistance thermometer was considered suitable. At that stage, the change in gas temperature was considered, but owing to such a large mass of steel in comparison to the small mass of gas (~0.01%), the drop in temperature was anticipated to be negligible. In terms of accurately measuring the temperature of the gas during depressurization, the use of an instrument, such as an IR thermometer, with a sensitivity of 0.1 °C, and a response time many times less than that of the resistance thermometer would be necessary. It might also be useful to have the device in the vessel on a mobile arm, such that by monitoring the temperature of the gas phase at various positions, a temperature profile, with increasing distance from the vessel wall, can be established. This would be more significant with larger free gas volumes than generally used in the existing programme.

Whilst the results in an agitated system have provided an insight into response times in a dynamic system, compared to that in a system with no external agitation, there is still scope for more investigation into turbulent flow, which is a more perfect analogue of industrial systems. It was hoped, originally, that a simple system might be the most effective, but the use of a magnetic stirrer bar in the vessel, controlled by a magnetic plate underneath the vessel proved a little optimistic, even though the method had been tested and shown by the author to be capable of stirring 12 litres of liquid, and that the flux was capable of passing through 25 mm of perspex and still operating effectively. The problems were encountered when surrounded by several mm of stainless steel. This method, being cheaper, and being easier to accommodate in the vessel was chosen above that of a motor driven paddle on a shaft inserted in the base of the vessel. Enquiries were made regarding the use of a paddle and shaft, but the difficulty lay in sealing a rotating shaft at pressures up to 30 bara. One suggested, and indeed, effective solution, would involve modifying the lower flange to incorporate a completely enclosed fluid mixing unit, similar to that of the standard Kenwood mixers.

8.3 Extended programme

Three areas upon which an extended experimental programme could be focused, include more detailed image analysis of bubble sizes and cumulative bubble growth, the development of an infra red technique to measure dissolved gas concentrations during depressurization, and the use of ultrasonic vibrations and acoustic techniques to initiate and monitor bubble evolution.

The video sequences were extremely useful in providing an overall picture of the gas evolution process, in terms of timescale of events and in relation to the pressure-time histories and piston velocity-time traces recorded. There is, however, scope for more investigation in that area, in terms of the quantitative analysis of bubble sizes during and immediately after depressurization, which were not considered in any great detail in the existing programme. A few preliminary calculations were carried out, as discussed in chapter 7.3, in an attempt to quantify the rate of gas evolution from solution, based on the ideal gas equation. Use of a high speed video camera, thus obtaining pictures with a higher resolution and therefore better definition in those first few seconds, would enable more detailed analysis of bubble size distributions and cumulative gas volumes as gas is released. By quantifying the amount of gas coming out of solution, during and immediately after depressurization, it should then be possible to develop a method for predicting the rate of gas evolution for any gas-liquid combination.

The monitoring of the dissolved gas content of CO_2, in particular, was considered useful in several respects. The first was to validate the predictions made as to the degree of saturation of water with CO_2 with respect to bubbling time, and hence establish the amount of gas in solution initially, and more importantly, at any time during depressurization. The dissolved gas content measurements would also provide a valuable means of monitoring the transfer of gas between phases, which would be particularly useful in relation to mixed gases. As discussed in chapter 4.2.9, provision was made during the design stages to incorporate two instruments which could be used to measure the dissolved gas concentration in the vessel. Unfortunately, it was decided that the Carbocheck device would not be very useful in an enclosed system, since it was really designed for use in a flowing system, and did not have an adequate response time for the changing conditions in the vessel.

The second method, an on-line infra red technique, described in more detail in appendix IV proved far more hopeful. Some initial experiments were carried out by the author to look at the infra red bands of CO_2 when dissolved in water and hydrocarbons. The method and results have been documented in appendix IV. The technique has so far been developed for the brewing industry to determine the CO_2 content of beer and other carbonated beverages. The effects of brine, other gases and indeed the harsher conditions experienced offshore, have not, as yet been tested. The vessel itself was considered to be ideal for doing this type of research, of interest to both the PhD programme and to the manufacturers themselves.

Discussions with Procal, the manufacturers, regarding the development of the system to monitor directly the dissolved gas content in oil well fluids, in pipelines and separators were optimistic, particularly due to the robust nature of the sensor and the negligible effect the presence of suspended solids in the liquid have. Unfortunately, this research could not be carried out in the timescale or the budget of the existing programme. It may however, be worth exploring, particularly in relation to mixed gases for the characteristic wave bands on an infra red spectrum are specific to each particular gas, and the intensity of each wave band is not affected by the presence of any other gas in the system.

The final area, for which there is significant scope and interest for research is in the use of ultrasonic vibrations to initiate and control bubble evolution. In instances where systems in a state of supersaturation can prove potentially dangerous, it may be necessary to have some controllable means of initiating, or indeed accelerating the gas evolution process. One such method, which is both reliable and controllable is the use of ultrasonic energy. Tentative investigations showed that the equipment necessary to investigate this phenomena more closely, under finely controlled conditions, could be relatively easily accommodated in the rig facility by installing small hydrophones at various points inside the vessel. Indeed, given adequate coupling, the hydrophones could even be located outside the vessel.

8.4 Application to industry

This final section addresses the application of this work to industry, and more directly in relation to offshore facilities. The research programme, being experimental in nature, has provided a vast amount of data for many operating conditions, and for a range of gases and liquids. This, in itself, should prove useful for a process designer operator, working on a pilot scale scheme, by indicating which variables must be considered, and indeed those factors which may play a significant role. In the light of the results obtained in the present study, and indeed using this work as a basis upon which to work, two areas need to be considered. The first focuses on the scaling up of the system, in terms of how the results may be affected by, for example, increasing the size of the vessel, or indeed changing the shape of the vessel. The second area involves considering a thermodynamically open system, which is undoubtedly a more effective representation of offshore separating conditions.

The main objective of the research was to investigate the mechanisms of gas evolution from saturated liquids. A thermodynamically enclosed small scale pressure vessel was chosen, largely to have more control over the variables, and therefore to gain a thorough understanding of the processes involved. Open systems, and indeed larger scale systems become more difficult to control, instrument and replicate. In addition, in industrial systems, boundary levels are often required, which are more often set as a function of the set pressure following depressurization, rather than as a function of the set volume, as in the case of this experimental work. It may therefore be necessary to know, for example, how the voidage, as a result of gas evolution following a pressure reduction, increases with time for set conditions.

In terms of the geometry of the vessel, keeping approximately the same length/diameter aspect ratio, predictions can be made regarding the gas evolution process in larger vessels. In for example, a vessel with dimensions larger by a factor of 10, scaling effects would probably be most significant during and immediately after rapid depressurization. The dimensions of the vessel would be expected to have very little influence over the state of the dissolved gas molecules at the initial saturation pressure, in terms of the dissolved gas concentration and the distance between gas molecules in a saturated liquid, or indeed, the latter stages of pressure recovery to equilibrium. In addition, the bubble front and mushroom of gas may not be dependent on the size of the vessel. As it was difficult to establish anything conclusive about the bubble front, predictions relating to the effects of vessel size and shape are difficult.

The main differences expected on increasing the size would probably be anticipated in terms of an increase in the timescale of events. This might be particularly apparent with gases in kerosene, in which nucleation from the vessel walls is particularly significant. Although the surface area available for nucleation is increased, the response time of bubble nucleation in the heart of the bulk may be slower. With smaller vessels, the vessel walls also have a significant influence on, for example, stabilizing foams, or influencing bubble behaviour. In fact, under the conditions tested, foaming in the rig was not observed to any great extent (see chapter 6.20). The rig, however, is an ideal facility in which to study foaming, and could be particularly significant to the oil industry in relation to the sensing and control problems encountered as a result of foaming, as described in chapter 2.2.

It is more difficult to predict the gas evolution behaviour in vessels which have significantly different length/diameter aspect ratios. Under these conditions, a change in the bubble front and mushroom of gas may well be expected, becoming more significant with larger length/diameter ratios, together with an increasingly significant influence of the vessel walls on the nucleation behaviour, particularly in hydrocarbons. A change in the time scale of events might also be predicted. In terms of the material of the vessel, the main difference would be apparent in relation to nucleation at the vessel walls, which would be strongly dependent on the surface finish of the inside walls.

The length/diameter aspect ratio can be investigated to a certain extent, by slight modifications to the existing rig. Impermeable liners, located in the vessel, could be used to alter the length/diameter ratio, to see how the various phenomena in the vessel are affected. It should be taken into consideration, however, that the use of liners would effectively reduce the vessel volume, and may affect both the surface area and the texture of the surface available for bubble nucleation. The latter effects may be particularly significant when using hydrocarbons as the solvent.

In developing a thermodynamically open system, the test rig could be modified by, for example, having a circulating liquid system, incorporating a storage tank for the water, or oil. Similar test conditions can be established, and the influence of various parameters investigated. In an open system, the turbulence intensity level can be raised, and an organized velocity profile can be established, by, for example, the use of perforated plates. Under these conditions, attention is focused solely on the macroscopic level. An alternative would be to bleed off, and measure, the gas coming off, which is again a more realistic representation of the real situation. Under these conditions, it could be predicted that the p-t profile may not change significantly until the beginning of the diffusion stages, for with gas being bled off, the diffusion gradients would be higher, and hence the rates of diffusion more significant.

9.0 CONCLUDING COMMENTS

The purpose of the research was to investigate the phenomena of gas evolution from saturated liquids exposed to a sudden and rapid reduction in pressure. The rapid depressurization of various gas-saturated liquids were studied in terms of the gas evolution mechanisms involved, how the initial conditions influenced the processes involved, and how certain external factors influenced the rate of evolution. Combining visual and photographic observations with data collected using several gases and solvents under a range of test conditions in a thermodynamically enclosed pressure vessel, a number of key points were established, in terms of the nature of the gas and the liquid, and the underlying phenomena.

(1) Following the rapid depressurization of a gas-saturated liquid, gas evolution and hence pressure recovery occurred predominantly by bubbling for all gas-liquid combinations. Gas evolution by diffusion was apparent, however, over the latter stages of the approach to equilibrium, after ~95% of the total pressure recovery had taken place.

The rate of depressurization in the vessel was determined largely by the initial saturation pressure, and to a lesser extent by the initial free gas volume. The rate of depressurization, which was varied by altering the velocity of the piston, had no influence over the equilibrium pressures obtained.

(2) In water, the behaviour of the gases can be characterized in terms of those gases, such as CO_2, which dissociate, and those gases, Ar, CH_4, O_2 and N_2, which do not. Owing to the dissociation reaction of CO_2 in water, (i) a more complex evolution pattern was observed with CO_2, (ii) the rate of approach to equilibrium was approximately two orders of magnitude slower with CO_2 than with the other gases, and (iii) the rate of approach to equilibrium for a 25% saturated salt solution was faster, by a factor of 20, compared to that in tap water.

The rate determining step in the gas evolution process was considered to be the change in the molecular configuration of CO_2, as a result of the chemical reaction which takes place with water. Consequently, dissolution and evolution of CO_2 takes several hours, compared to several minutes as observed with Ar, CH_4, O_2 and N_2. The extent of dissociation of CO_2 in salt solutions, is very much greater than in tap water. The rate constants for the interconversion of bicarbonate ions to gaseous CO_2 are 3-4 orders of magnitude faster than for the interconversion of the non-dissociated form to gaseous CO_2. As a result, gas evolution from salt solutions is very much faster. The rate of approach to equilibrium using CO_2 in a fully saturated (100%) salt solution was faster than in tap water by a factor of only 3, because at the larger saturations, other factors such as an increase in the viscosity and density of the liquid, together with an increase in the surface tension become more significant. An increase in the rates of approach to equilibrium in salt solutions was not apparent for the other gases tested, for no dissociation reaction occurs.

(3) In hydrocarbons, CO_2 was found to behave in a similar fashion to that of the other gases. With CO_2 in kerosene, the rate of approach to equilibrium was approximately two orders of magnitude faster than in water, which is comparable to that of the other gases in kerosene, where equilibrium was generally reached within $\sim$30 secs of depressurization.

(4) The increased solubilities of gases in hydrocarbons, in comparison to water, were particularly apparent during evolution. With CO_2 in water, under all conditions, gas evolution and hence pressure recovery occurred once gas expansion was completed and the piston had stopped moving, whereas with CO_2 in kerosene, under all conditions, around 70% of the total pressure recovery had occurred before gas expansion was completed. As a result, the minimum pressures recorded with CO_2 in kerosene, from the same initial starting conditions, were generally twice those recorded in water. With the other gases in kerosene, evolution also started $\sim$1 sec earlier than in water.

(5) The phenomena of heterogeneous nucleation from the vessel walls and from pre-existing gas microbubbles and suspended particles in the liquid were observed following depressurization. For all gases in water, gas evolution appeared to be initiated by the rising of a ‘mushroom’ of gas in the bulk liquid. The origin and cause of the initial volume of gas, however, besides being a reaction to the pressure release, could not be established. In kerosene, the influence of the surface walls was more significant, for bubble evolution clearly started from the vessel walls.

It was also apparent, following saturation of kerosene with the less soluble gases, that bubbles of gas ($\leq$0.5 mm) were already present in the liquid. These bubbles, acting as nucleation sites, effectively lower the nucleation threshold. This effect would be particularly significant in larger vessels, as nucleation in the bulk liquid may occur more readily.

(6) The equilibrium pressures, reflecting the amount of gas in solution initially, were successfully predicted using Henry's law and basic thermodynamic principles. The masses of gas in both the liquid and gas phases were also calculated, based on the ideal gas equation and solubility data given in the literature, enabling the rate of gas evolution immediately after depressurization to be quantified.

(7) In terms of the factors influencing the rate of gas evolution, a significant increase in the rate of CO_2 evolution was observed, under all conditions, with increasing initial liquid temperature. The rate of approach to equilibrium during the evolution of CO_2 from water at a temperature of 60°C was faster, by a factor of 40, compared to that at 20°C. Such significant increases in rate with increasing temperature were not so apparent for the less soluble gases.

It may be surmised, therefore, that at even higher temperatures, the rate of gas evolution of CO_2 in water, may become comparable with that of the other, less soluble gases. The temperature dependence of solubility on liquid temperature, however, was not reflected in the equilibrium pressures recorded. Under all conditions, for any gas-liquid combination, there was no significant decrease in equilibrium pressure with increasing temperature. The behaviour of the liquid and gas at increased temperatures, together with those factors, such as vapour pressure, which become more significant at higher temperatures were considered and discussed, but a satisfactory explanation for why this was so, could not be found.

(8) Fluid agitation also significantly increased the rate of gas evolution. With agitation, using CO_2, the rate of approach to equilibrium was increased by a factor of 5 in water, and by a factor of 2 in kerosene. In all cases, for all gas-liquid combinations, an increase of 10-40% in the equilibrium value was observed with agitation.

The increases in the rate of gas evolution were considered to be largely due to the aggregation of gas molecules in the liquid, both in terms of gas microbubble aggregation and in terms of macroscopic bubble coalescence. With agitation, the likelihood of a depleted zone next to a concentrated zone is increased, effectively increasing the gas diffusion rates, the clustering and growth of microbubbles, and hence the rate of gas evolution. The equilibrium values obtained with agitation, however, would be expected to drop, when the agitation source was turned off, to that equilibrium recorded for the same gas-liquid system with no external agitation. This process would be very slow (~2-3 hours), as the equilibrium is re-established by molecular diffusion.

(9) The third major factor which significantly increases the rate of gas evolution, is the presence of inert solids. The addition of 500 ppm 5μm silica flour particles to water can effectively double the rate of approach to equilibrium, largely owing to an increase, by a factor of around 4, in the surface area available for nucleation.

The addition of 1000 ppm 5μm silica flour particles to a CO_2 in water system also doubled the rate of approach to equilibrium, despite the additional increase in surface area. The rate limiting phenomena, regarding nucleation sites, were considered to be associated with the mechanisms of bubble nucleation, in terms of the number of active sites on the nucleating particle, the size of the nucleating particle and the contact angle. Diffusion and aggregation of gas molecules was not considered to be a strong influencing factor, as there were no significant improvements in the rates of approach on addition of solids, using the less soluble gases, where in comparison to CO_2, the distances between gas molecules are larger, and the concentrations of gas molecules in solution are smaller.

(10) Exploratory tests using the mixed gas compositions, 30% N_2 in CO_2, and 30% CO_2 in N_2, showed, for both compositions, in oil and in water, (i) an increase in the rate of approach to equilibrium, by a factor of 3-5, compared to that for the dominant gas in a single gas component system, under the same conditions, (ii) the equilibrium pressure of the mixed gas composition to be approximately the additive sum of the final pressures obtained for the individual components at that pressure at which they existed in the mixed composition, and (iii) that the composition of the mixed gas in the gas phase after depressurization was not the same as the composition of the gas phase before depressurization.

The composition of the mixed gas at equilibrium tended to swing in favour of the more soluble gas. The composition of the 30% N_2 in CO_2 at equilibrium was calculated to be in the ratio, 12% N_2 to 84% CO_2, whilst the composition of the 30% CO_2 in N_2 at equilibrium was calculated to be in the ratio, 60% CO_2 to 40% N_2. In terms of the rate of approach to equilibrium, it was considered that the rate of evolution of CO_2 from solution may be enhanced by the presence of a sparingly soluble, inert gas, such as N_2, which, leaving solution more readily, may trigger the CO_2 evolution process. Whilst an increase in the rate was observed with a mixed gas system, more research, which would ideally include video analysis, needs to be carried out to further test the theory.

APPENDICES

I Physical properties of liquids and gases

The following figures and tables have been included to provide some useful background information into the gases and liquids used in the experimental programme.

	Mol Wt	T_c (K)	p_c (bara)	Viscosity (μPas)		Density (kg/m^3) 1bara, 298K	Mole fraction solubility in water, 298K
				298K	373K		
Ar	40	151	49	22.9	28.8	1.68	$2.519\text{x}10^{-5}$
CO_2	44	304	73	15.0	19.7	1.80	$6.150\text{x}10^{-4}$
N_2	28	126	34	17.9	22.2	1.16	$1.183\text{x}10^{-5}$
O_2	32	155	50	20.8	26.1	1.31	$2.293\text{x}10^{-5}$
CH_4	16	190	46	11.2	14.3	0.71	$2.552\text{x}10^{-5}$

	Van der Waal constants		Lennard-Jones parameters		Diff coeff in water	Henry const in water	
	a atm.l^2/mol^2	b l/mol	ϵ_l/k (K)	σ (A)	m^2/sec 298K	x10^8 Pa 288K	303K
Ar	1.345	0.0322	124	3.418	$2.00\text{x}10^{-9}$	33.5	43.2
CO_2	3.592	0.0427	190	3.996	$1.92\text{x}10^{-9}$	1.24	1.87
N_2	1.390	0.0391	91.5	3.681	$2.41\text{x}10^{-9}$	74.8	93.6
O_2	1.360	0.0318	113	3.433	$2.49\text{x}10^{-9}$	39.2	52.1
CH_4	2.253	0.0428	136.5	3.822	$1.49\text{x}10^{-9}$	34.1	45.5

Table I-1 Physical properties of the gases investigated in the experimental programme [59,169,174]

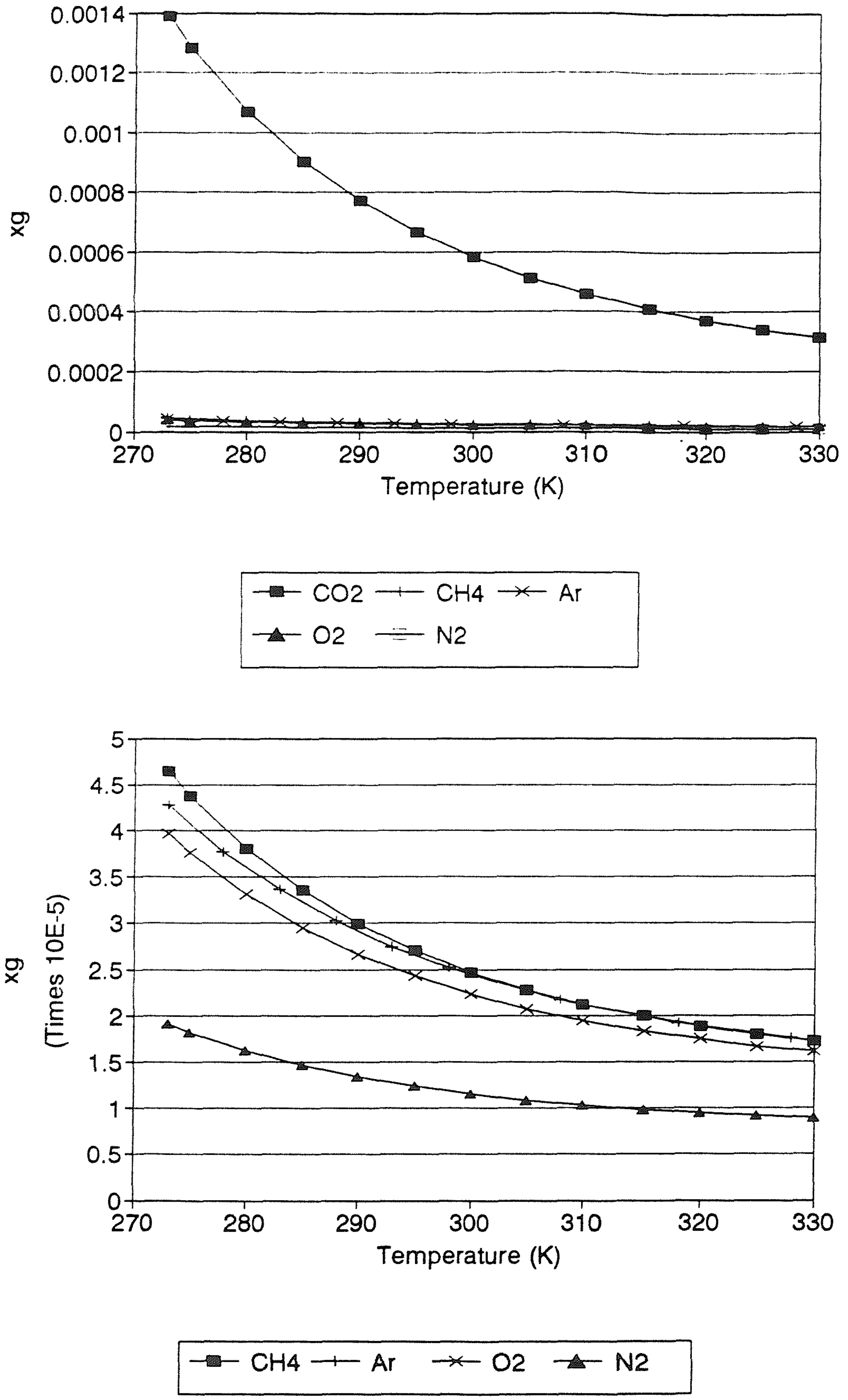

Figure I-1 Mole fraction solubilities in water as a function of temperature, at 1 bara for a) CO_2 and b) CH_4, Ar, O_2 and N_2 [25,27,29,37,41,45,48]

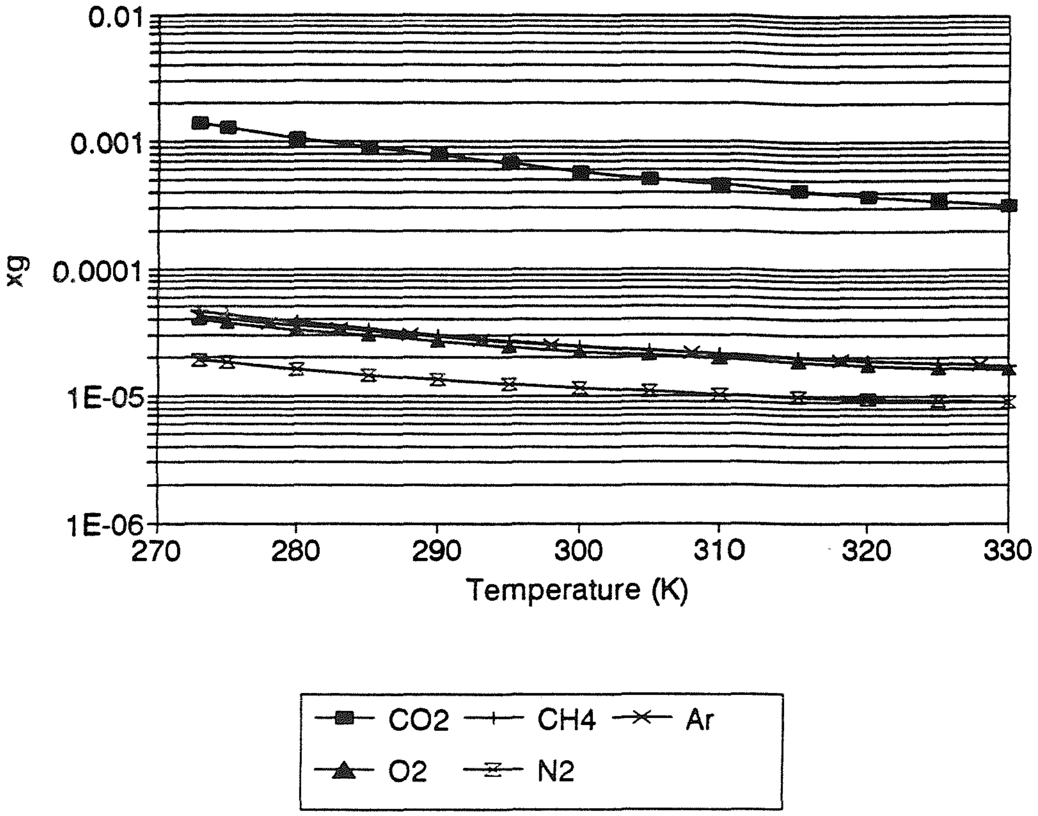

Figure I-2 Mole fraction solubilities for the range of gases in water as a function of temperature at 1 bara, log scale [25,27,29,37,41,45,48]

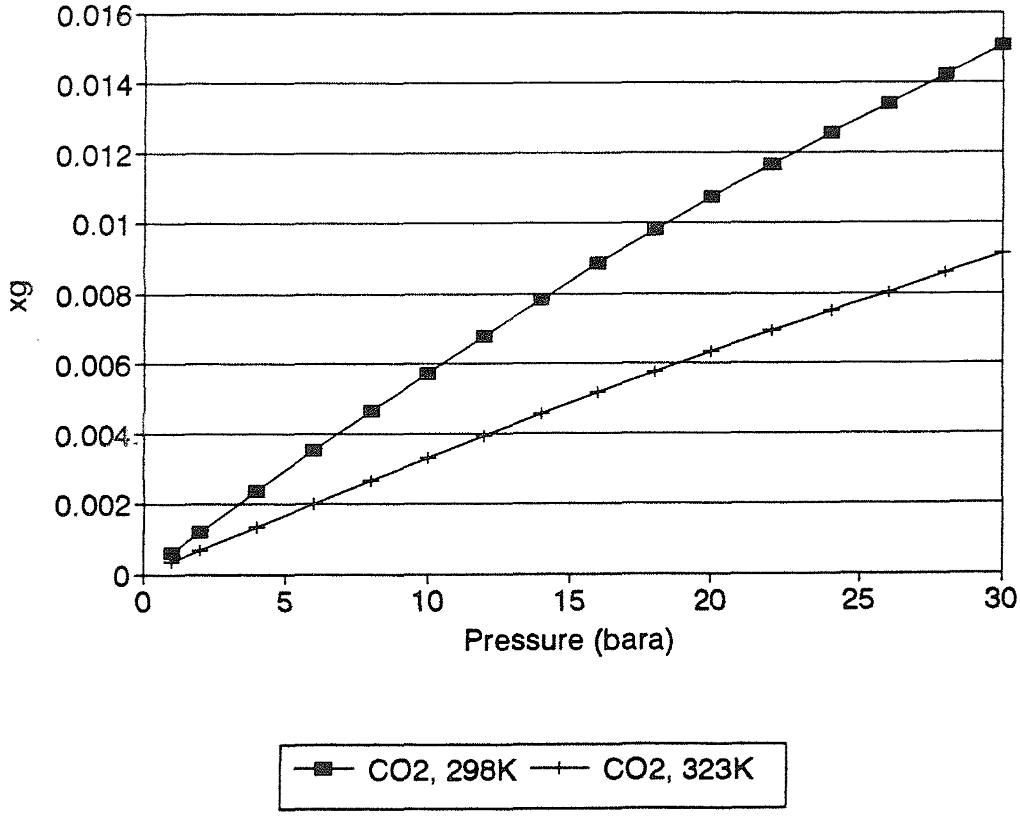

Figure I-3 Mole fraction solubilities of CO_2 in water as a function of pressure [27-29]

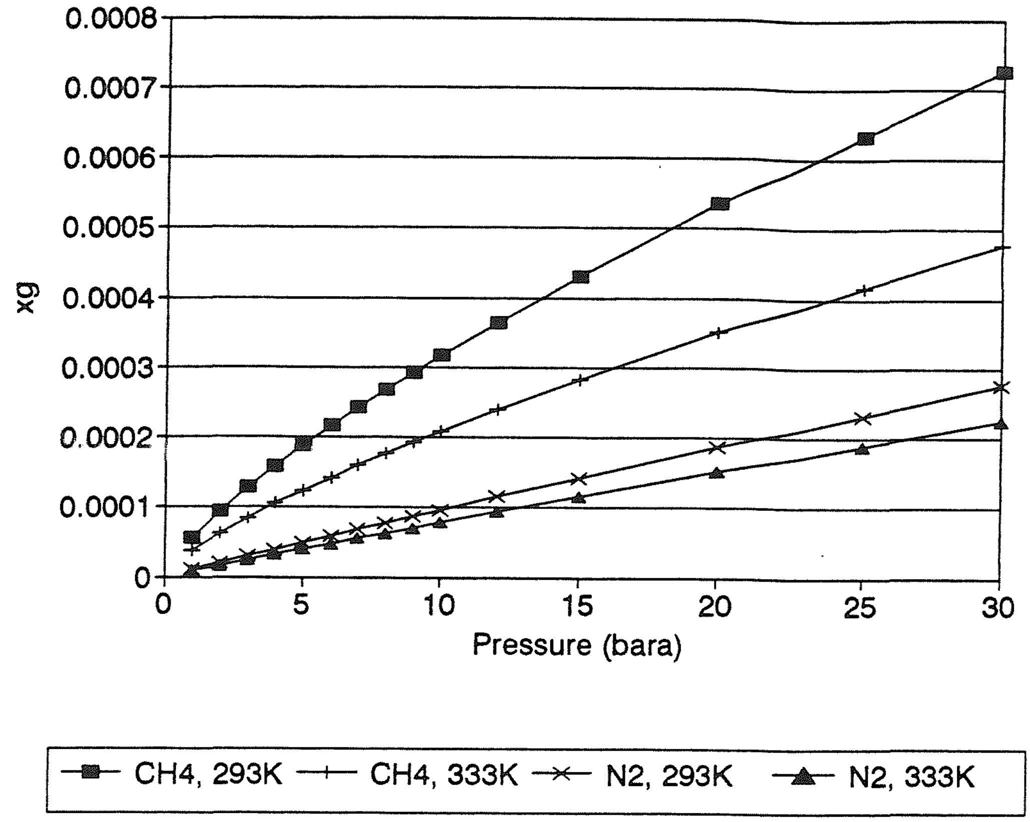

Figure I-4 Mole fraction solubilities of CH_4 and N_2 in water as a function of pressure [37,41]

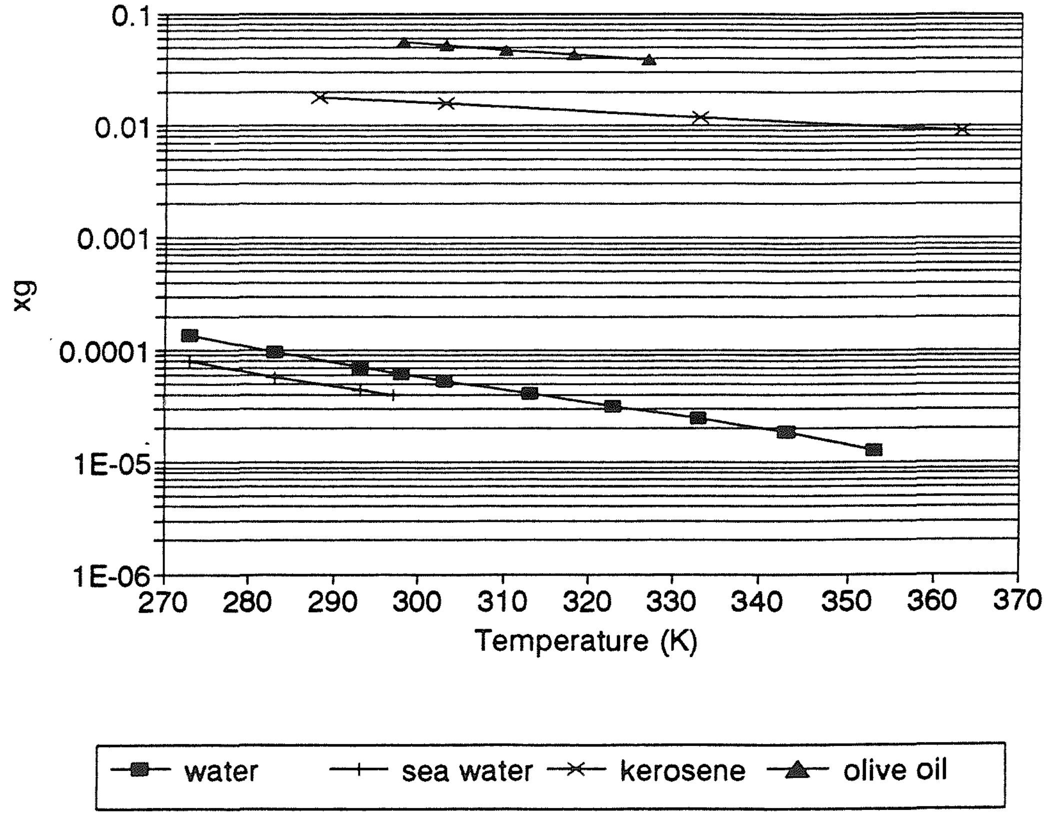

Figure I-5 Mole fraction solubilities of CO_2 in water, seawater, kerosene (ρ=0.8119 kg/cm^3) and olive oil (ρ=0.9076 kg/cm^3), 1 bara [25,30,35]

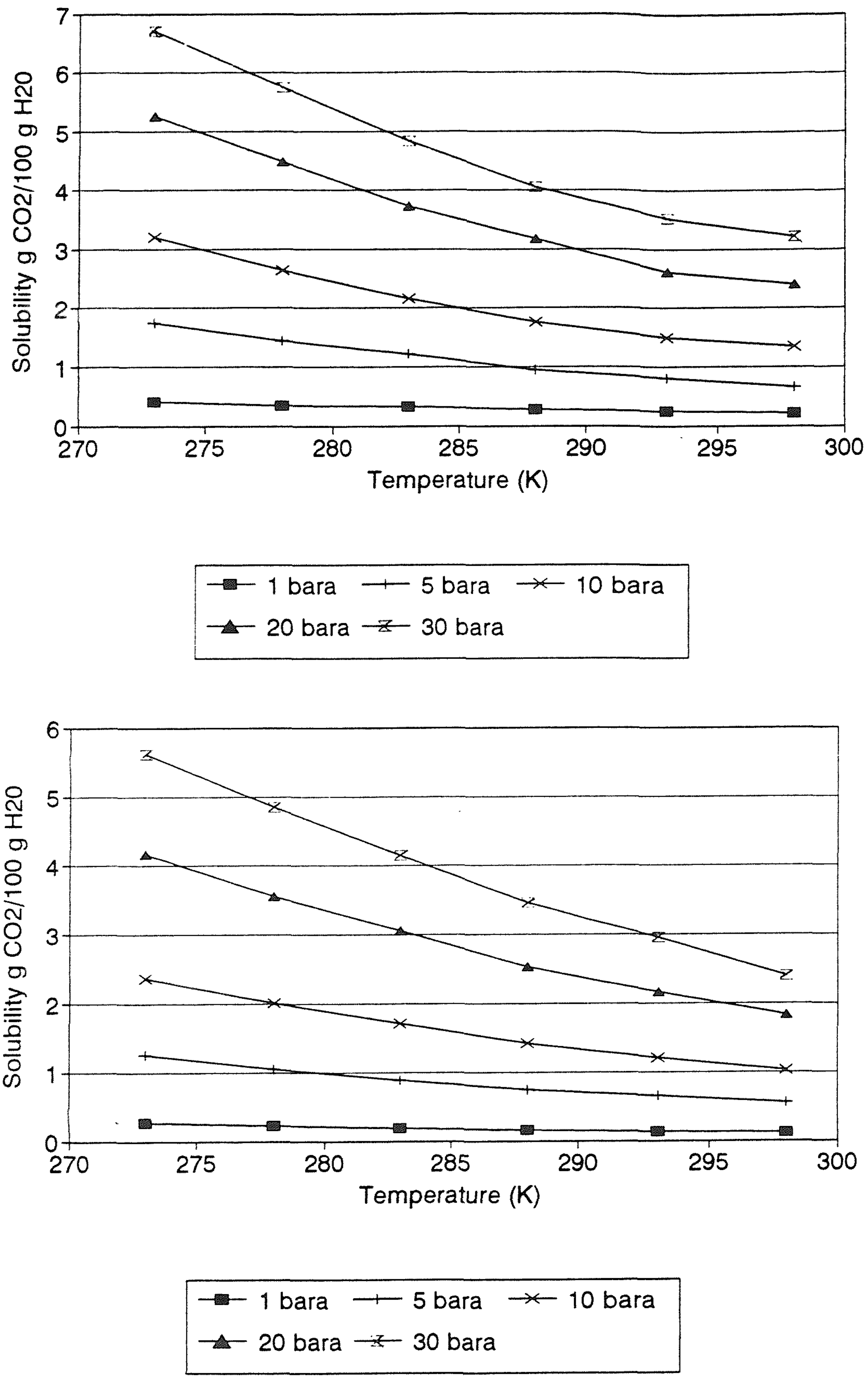

Figure I-6 Solubility isobars for CO_2 in a) water and b) sea water [25,27,29,30,33-35]

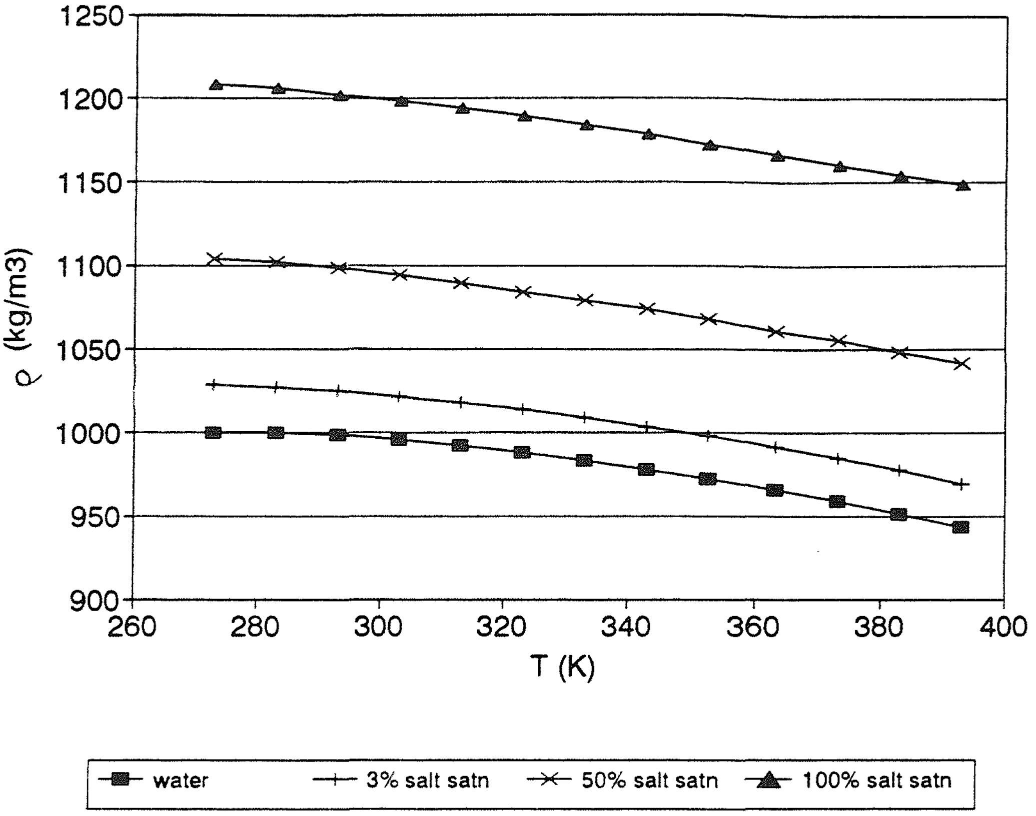

Figure I-7 Density of aqueous NaCl solutions as a function of temperature, 1 bara [175]

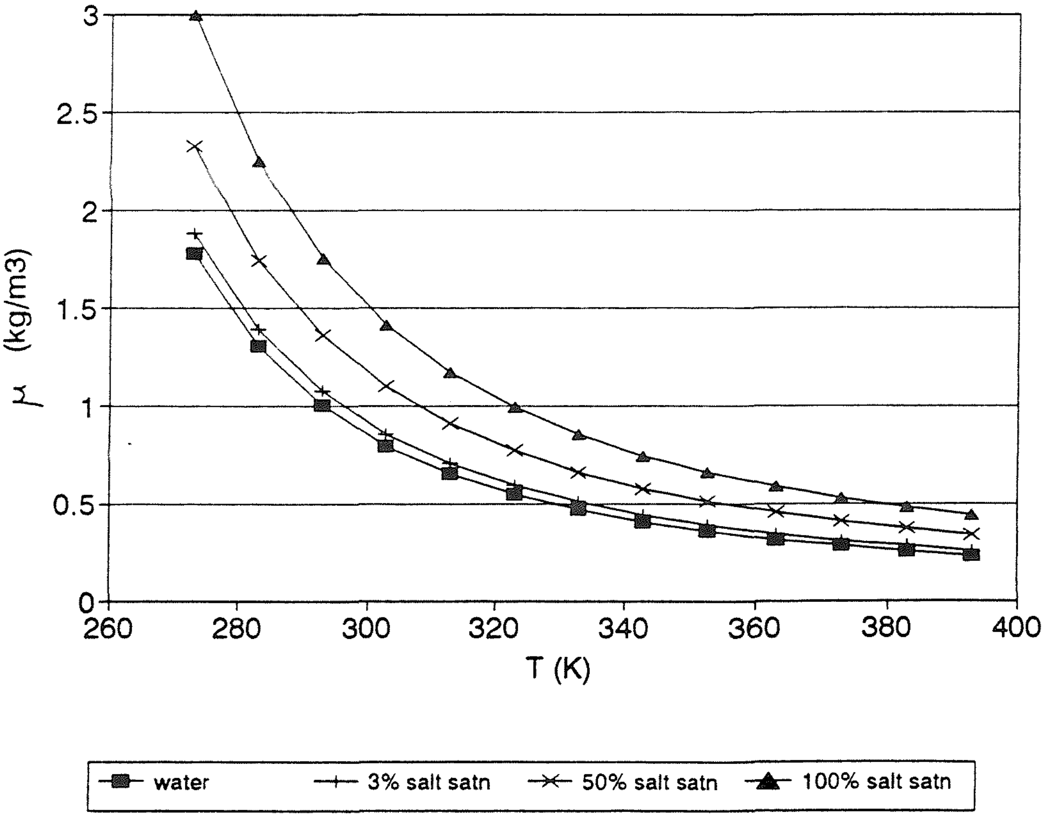

Figure I-8 Viscosity of aqueous NaCl solutions as a function of temperature, 1 bara [175]

II Equations of State

II.1 Soave-Redlich-Kwong Equation of State

The coefficients of the SRK EOS

$$(p+\frac{a_T}{V_M(V_M+b)})(V_M-b)=RT \tag{1}$$

are calculated as follows

$$b=0.08664\frac{RT_c}{p_c} \tag{2}$$

and

$$a_c=0.42747\frac{R^2T_c^2}{p_c} \tag{3}$$

where the suffix term, c, represents the temperature or pressure at the critical point.

The equation for a_T, which varies with temperature, is

$$a_T=a_C\alpha \tag{4}$$

where a_c is the value of a_T at the critical temperature and α is a non dimensional temperature-dependent term which has a value of 1.0 at the critical temperature. Values of α are obtained from

$$\alpha=(1+m(1-T_r^{0.5}))^2 \tag{5}$$

where

$$m=0.480+1.574\infty-0.176\infty^2 \tag{6}$$

where ∞, known as the Pitzer acentric factor, is defined as

$$\infty=-(logp_{vr}+1) \tag{7}$$

at $T_r=0.7$, where T_r is the reduced temperature, T/T_c, and p_{vr} is the reduced vapour pressure, evaluated at $T_r = 0.7$. Thus the acentric factor is a constant for each pure substance. The values can be found in most engineering data books, e.g. Engineering Data Book, 10th Ed., GPSA, Tulsa, 1987.

II.2 Peng-Robinson Equation of State

The coefficients of the PR EOS

$$(p+\frac{a_T}{V_M(V_M+b)}+b(V_M-b))(V_M-b)=RT \tag{8}$$

are calculated as follows

$$b=0.07780\frac{RT_c}{p_c} \tag{9}$$

and

$$a_c=0.45724\frac{R^2T_c^2}{p_c} \tag{10}$$

and

$$a_T=a_c\alpha \tag{11}$$

where

$$\alpha=(1+m(1-T_r^{0.5}))^2 \tag{12}$$

and

$$m=0.37464+1.54226\infty-0.26992\infty^2 \tag{13}$$

II.3 Mixing rules

The same mixing rules can be applied to both the Peng-Robinson Equation of State and the Soave-Redlich-Kwong Equation of State. The parameters, b and a_T, in a system containing more than one component are calculated as

$$b=\Sigma y_j b_j \tag{14}$$

and

$$a_T=\Sigma\Sigma y_i y_j a_{Tij} \tag{15}$$

where

$$a_{Tij}=(1-\delta_{ij})(a_{Ti}a_{Tj})^{0.5} \tag{16}$$

That is

$$a_T=\Sigma\Sigma y_i y_j(a_{Ti}a_{Tj})^{0.5}(1-\delta_{ij}) \tag{17}$$

The subscripts, i and j, refer to the two pure compounds of interest present in the mixture, y represents the mole fraction, and the terms δ_{ij} are binary coefficients, which are assumed to be independent of pressure and temperature. The binary interaction coefficients have different values for each binary pair and also take on different values for each equation of state.

An example taken from [4], shows how the mixing rules and the SRK can be used, in this case, to calculate the pressure expected on raising the temperature of a vessel, containing three gases, to 400°C. The vessel, with a volume of 250 cm^3, contains 79.28g of gas with the mole fraction compositions for methane, ethane and n-butane of 0.65, 0.25 and 0.1 respectively. The binary coefficient is 0.02 between methane and n-butane, 0.01 between ethane and n-butane, and zero between methane and ethane.

Firstly the constants a_j and b_j for each component must be calculated

$$b_j=0.08664\frac{RT_{cj}}{p_{cj}} \tag{18}$$

$$a_{cj}=0.42747\frac{(RT_{cj})^2}{p_{cj}} \tag{19}$$

$$m_j=0.480+1.574\infty-0.176\infty^2 \tag{20}$$

$$\alpha_j^{0.5}=1+m_j(1-T_{rj}^{0.5}) \tag{21}$$

$$a_{Tj}=a_{cj}\alpha_j \tag{22}$$

The critical temperatures, pressures and acentric factors can be found in tables, the rest must be calculated.

	T_{cj}	p_{cj}	b_j	a_{cj}	∞_j	m_j	α_j	a_{Tj}
methane	342.9	666.4	0.4784	8,687	0.0104	0.4964	0.6120	5,317
ethane	549.5	706.5	0.7232	21,042	0.0979	0.6324	0.8349	17,569
n-butane	765.2	550.6	1.2922	52,358	0.1995	0.7870	1.0591	55,453

Table II-1 Constants and coefficients used in the Soave-Redlich-Kwong Equation of State for a three component mixed gas system

Secondly, the mixture constants, b and a_T must be calculated

$$b=\Sigma y_j b_j \tag{23}$$

$$b=(0.65)(0.4784)+(0.25)(0.7232)+(0.10)(1.2922)=0.6210 \tag{24}$$

$$a_T=\Sigma\Sigma y_i y_j (a_{Ti} a_{Tj})^{0.5}(1-\delta_{ij}) \tag{25}$$

$$\begin{gathered} a_T=(0.65)(0.65)(5{,}317*5{,}317)^{0.5}(1-0.0)+ \\ (0.65)(0.25)(5{,}317*17{,}569)^{0.5}(1-0.0)+ \\ (0.65)(0.10)(5{,}317*55{,}453)^{0.5}(1-0.02)+ \\ (0.25)(0.65)(17{,}569*5{,}317)^{0.5}(1-0.0)+ \\ (0.25)(0.25)(17{,}569*17{,}569)^{0.5}(1-0.0)+ \\ (0.25)(0.10)(17{,}569*55{,}453)^{0.5}(1-0.01)+ \\ (0.10)(0.65)(55{,}453*5{,}317)^{0.5}(1-0.02)+ \\ (0.10)(0.25)(55{,}453*17{,}569)^{0.5}(1-0.01)+ \\ (0.10)(0.10)(55{,}453*55{,}453)^{0.5}(1-0.0)=10{,}773 \end{gathered} \tag{26}$$

Finally, the expected pressure can be calculated using the SRK EOS, eqn 1, substituting in the values for a and b to give a final pressure of 8,223 psi.

III Solubility and equilibrium pressure predictions

At the initial starting pressure, for a typical run, the liquid in the vessel is saturated with gas, and thus in equilibrium with the gas phase. As discussed in chapter 3.4, in situations where the ideal gas equation cannot be used to describe the behaviour of real gases, because large deviations occur with increasing pressure above atmospheric, the gas solubilities are generally worked out using the equations of state mentioned in the previous appendix. The initial masses of gas, however, in both the liquid and in the free gas space for the less soluble gases, under the conditions in the vessel ($\leq$ 10 bara), can be readily calculated using the standard equations.

The mass of gas in the gas space above the liquid can be calculated using the ideal gas equation

$$mass\ gas = \frac{pMV}{RT} \tag{27}$$

where p is the initial pressure, M is the molecular mass of the gas used, V is the initial free gas volume, T is the temperature and R is the universal gas constant. Using bara, g, litres and K for units of pressure, mass, volume and temperature, the value of R in this case is 0.083145. Although the equation has limited practical value, as no gas behaves as an ideal gas, the equation does describe the behaviour of most real gases at low pressures ($\leq$ 10 bara).

The mass of gas in the liquid phase can be calculated using the mole fraction solubility, x_g, given in the literature at that particular pressure. The mole fraction solubility is defined as

$$x_g = \frac{n^{\circ}moles\ gas}{(n^{\circ}moles\ gas + n^{\circ}moles\ water)} \tag{28}$$

The mass of gas in a given volume of water can therefore be calculated

$$mass\ gas = \left(\frac{x_g * n^{\circ}moles\ water}{(1 - x_g)}\right)M \tag{29}$$

where M is the molecular mass of the gas.

The same equations can be used to determine the mass of gas in the liquid and gas phases at the final equilibrium pressure. Assuming conservation of mass, the amount of gas changing phase, following depressurization, can therefore be determined. Given the initial pressure and temperature, and the final equilibrium pressure and temperature of the system, a spreadsheet was set up, which could be used to determine the masses of gas in the liquid and gas phases, before and after depressurization, for a range of operating conditions. According to the experimental data obtained for several gases in water, from initial saturation pressures of around 10 bara, the calculations for the masses of gas in both the gas and liquid phases initially, table III-1 and finally, table III-2 are displayed, using the mole fraction solubilities given in the literature, as displayed in figure I-1. The total masses of gas calculated initially, for saturated systems at equilibrium, and finally, after depressurization, are within 4%, in each case.

Gas	p_i, bara	Mass gas in gas phase, g	x_g at p_i, $x10^{-4}$	Mass gas in liquid phase, g	Total mass gas initially, g
CH_4	9.53	5.110	2.29	2.138	7.247
Ar	9.86	13.216	2.07	4.833	18.050
O_2	9.82	10.530	2.16	4.033	14.563
N_2	9.75	9.148	1.17	1.911	11.060

Table III-1 Calculated masses of gas in the liquid and gas phases initially, for a saturated water system at equilibrium, according to actual experimental data

Gas	p_{eqm}, bara	Mass gas in gas phase, g	x_g at p_{eqm}, $x10^{-5}$	Mass gas in liquid phase, g	Total mass gas at eqm, g
CH_4	2.06	6.972	4.94	0.461	7.433
Ar	2.09	17.682	4.39	1.024	18.709
O_2	2.05	13.875	4.51	0.842	14.717
N_2	1.80	10.660	2.16	0.353	11.013

Table III-2 Calculated masses of gas in the liquid and gas phases at the new established equilibrium, following depressurization, according to actual experimental data

The predictions for the masses of gas in each phase, could also be applied to mixed gas systems, in order to determine the percentage composition in the gas phase, following the depressurization of water saturated with a mixed gas. As discussed in chapter 6.17, the composition of a mixed gas system following depressurization in an enclosed system, is unlikely to be the same as the composition of the mixed gas in the gas phase initially. The composition, after depressurization, of the mixed gas system would be expected to swing in favour of the more soluble gas, which, indeed, is demonstrated using a simple method for predicting the final gas phase composition for a mixed gas system.

Predictions of the pVT behaviour of gas mixtures are usually based on two models [172]. Dalton's law of additive pressures states that the pressure of a gas mixture is equal to the sum of the pressures each gas would exert if it existed alone at the mixture temperature and volume. Amagat's law of additive volumes states that the volume of a gas mixture is equal to the sum of the volumes each gas would occupy if it existed alone at the mixture temperature and pressure. The laws hold exactly for ideal gas mixtures, but only approximately for real gas mixtures, due to the intermolecular forces which may be significant for real gases, at high densities. The same laws can, however, be used for real gases, with reasonable accuracy, by evaluating the component pressures and volumes using equations of state, which account for the deviation from ideality.

At the low pressures experienced in the vessel (≤ 10 bara), it may be assumed that the molecules are spaced far apart and molecular force fields do not influence the pressure. Each constituent gas, therefore, may be considered to behave as an ideal gas, independent of its composition in the mixture.

Table III-3 shows the initial calculated masses of CO_2 and N_2, in both the liquid and gas phases, at an initial saturation pressure of 10 bara, using the actual data obtained for the 70/30 CO_2/N_2 and the 70/30 N_2/CO_2 mixed gas compositions in water, assuming that the partial pressures of CO_2 and N_2 in the gas phase initially are in the ratio 7:3 and 3:7 respectively.

	Mass CO_2 in gas phase, g	Mass N_2 in gas phase, g	Mass CO_2 in liquid phase, g	Mass N_2 in liquid phase, g	Total CO_2, g	Total N_2, g	Total mass gas initially, g
70% CO_2/ 30% N_2	10.453	2.852	108.183	0.595	118.636	3.447	122.083
70% N_2/ 30% CO_2	6.542	4.406	45.482	1.367	52.024	5.773	57.797

Table III-3 Calculated masses of gas in the liquid and gas phases initially, for a saturated system at equilibrium, using actual experimental data

At the final equilibrium pressures recorded, which were 4.42 bara for the 70% CO_2 composition, figure 6.32, and 2.13 bara for the 70% N_2 composition, figure 6.33, the predicted partial pressures for each possible composition of CO_2 and N_2 can be calculated. By calculating the masses of each gas from the partial pressures for each predicted composition, it became evident, from tables III-4 and III-5, that many compositions were not possible. Looking at table III-4, for example, a gas composition in which CO_2 is $\geq$ 90% is unrealistic, for in those cases, the final mass of N_2 in the gas phase is less than that in the gas phase initially, as calculated in table III-3. For those final CO_2 compositions $\leq$ 86%, the mass of N_2 in the gas phase exceeds the total mass of N_2 initially, which again is unrealistic. The results therefore indicate a final equilibrium state in which the composition of the gas phase is around 88% CO_2 and 12% N_2, as shown in figure III-1. The same deductions can be made in table III-5, indicating a final equilibrium gas phase of around 60% CO_2 and 40% N_2, as shown in figure III-2.

% CO_2	% N_2	pp CO_2, bara	pp N_2, bara	Mass CO_2 in gas phase, g	Mass N_2 in gas phase, g
99	1	4.38	0.04	40.726	0.262
90	10	3.98	0.44	37.023	2.618
89	11	3.93	0.49	36.612	2.879
88	12	3.89	0.53	36.201	3.141
87	13	3.85	0.57	35.789	3.403
86	14	3.80	0.62	35.378	3.665
85	15	3.76	0.66	34.966	3.926
80	20	3.54	0.88	32.910	5.235
70	30	3.09	1.33	28.796	7.853

Table III-4 Calculated masses of gas in the gas phase, at the final equilibrium pressure, for various possible final gas compositions, from a 70/30 CO_2/N_2 composition initially

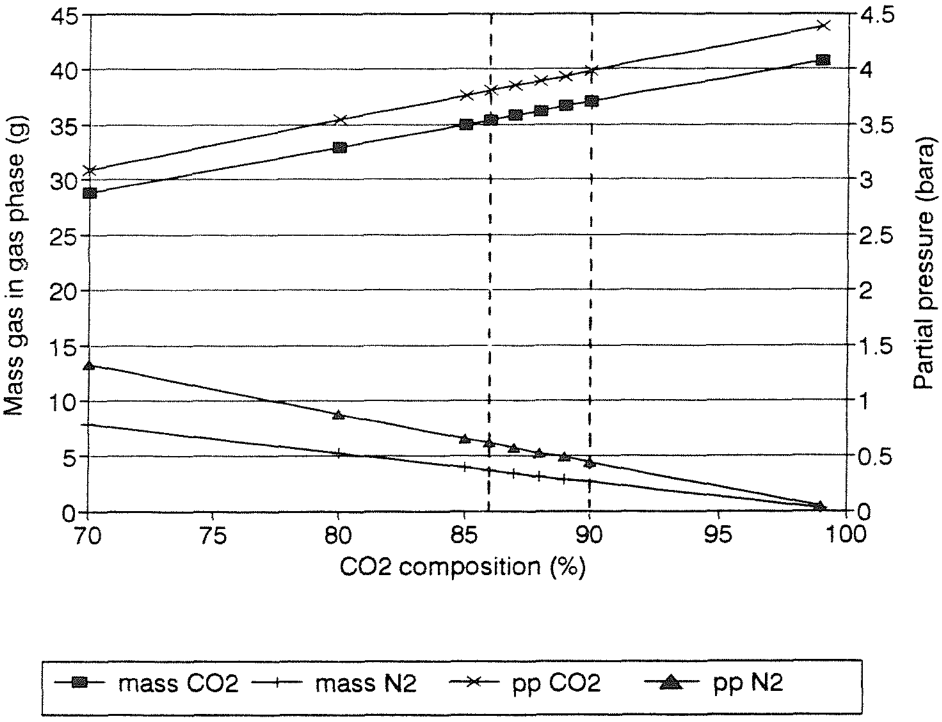

Figure III-1 Graphical representation for the calculated masses of gas in the gas phase, at the final equilibrium pressure, for various possible final gas compositions, from a 70/30 CO_2/N_2 composition initially

% CO_2	% N_2	pp CO_2, bara	pp N_2, bara	Mass CO_2 in gas phase, g	Mass N_2 in gas phase, g
99	1	2.11	0.02	19.626	0.126
80	20	1.70	0.43	15.859	2.523
70	30	1.49	0.64	13.877	3.784
65	35	1.38	0.75	12.886	4.415
61	39	1.30	0.83	12.093	4.919
60	40	1.28	0.85	11.894	5.046
59	41	1.26	0.87	11.696	5.172
55	45	1.17	0.96	10.903	5.676
50	50	1.07	1.07	9.912	6.307
30	70	0.64	1.49	5.947	8.830

Table III-5 Calculated masses of gas in the gas phase, at the final equilibrium pressure, for various possible final gas compositions, from a 70/30 N_2/CO_2 composition initially

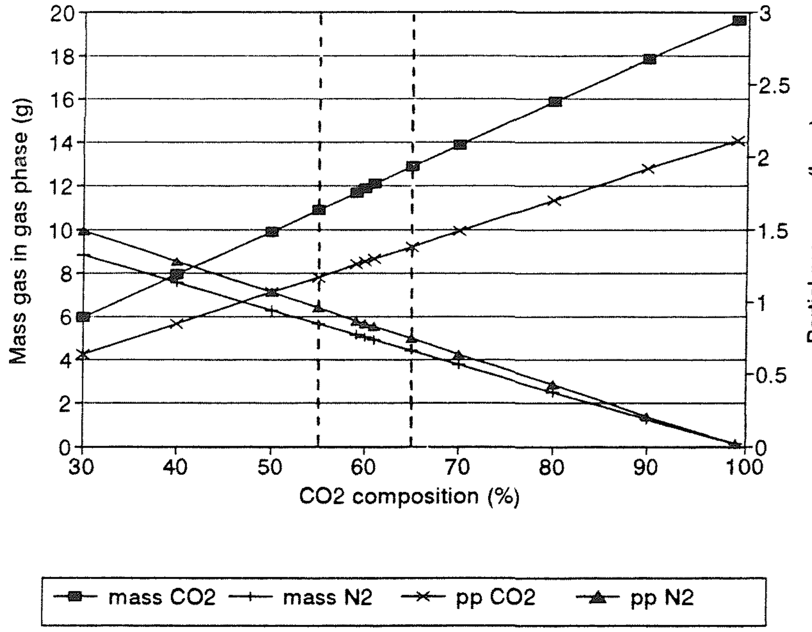

Figure III-2 Graphical representation for the calculated masses of gas in the gas phase, at the final equilibrium pressure, for various possible final gas compositions, from a 70/30 N_2/CO_2 composition initially

IV CO_2 properties and infra red details

IV.1 Carbonate equilibria

Carbon dioxide, unlike most other gases such as nitrogen and oxygen, undergoes a chemical reaction with water to form a weak acid, carbonic acid (H_2CO_3). This, in turn, dissociates into bicarbonate (HCO_3^-) ions, as represented by the equilibria

$$CO_{2(g)} \rightleftharpoons CO_{2(aq)} \tag{30}$$

$$CO_{2(aq)} + H_2O \rightleftharpoons H_2CO_3 \tag{31}$$

$$H_2CO_3 \rightleftharpoons HCO_3^- + H^+ \tag{32}$$

The extent of the dissociation reaction, however, being dependent on variables such as the pH and the concentration of ions in solution is very different in pure water and NaCl salt solutions. For a saturated solution of CO_2 in pure water, or indeed tap water, at around pH 5, the dominant species is dissolved CO_2, whilst only a small proportion (~5%) exists in the dissociated form [176]. The formation of HCO_3^- ions is small below pH 6. In salt water solutions, however, in which the pH is greater than 7, the amount of H_2CO_3 formed from carbon dioxide and water is small in relation to the total dissolved CO_2, for the equilibrium, in eqn 32, lies far over to the right hand side, and the dominant species is HCO_3^- ions (97%).

Each step in the equilibrium sequence can be characterized by an equilibrium constant, which is, in general, temperature dependent [177]. At equilibrium, the forward and reverse reactions proceed at such a rate that the ratio of concentrations of products to reactants, as described by the equilibrium constant, remains constant. For example, the concentration of CO_2 in solution can be expressed in terms of the partial pressure of the gas in solution. That is, that pressure of CO_2 in the gas phase with which the sample would be in equilibrium. The concentration of dissolved $CO_2(aq)$ and pCO_2 are interrelated by Henry's law, and the equilibrium constant derived from eqn 31, can be written as

$$K_H = \frac{(CO_{2(aq)})}{pCO_2} \tag{33}$$

The equilibrium constant derived from eqn 32, known as the first ionization constant, can be defined as

$$K_{H_2CO_3}=\frac{(H^+)(HCO_3^-)}{(H_2CO_3)} \tag{34}$$

An additional step in the carbonate equilibria which occurs in seawater is the further dissociation of bicarbonate (HCO_3^-) ions into carbonate (CO_3^{2-}) ions, according to the equilibria

$$HCO_3^- \rightleftharpoons H^+ + CO_3^{2-} \tag{35}$$

for which the equilibrium constant, known as the second ionization constant can be defined as

$$K_2=\frac{(H^+)(CO_3^{2-})}{(HCO_3^-)} \tag{36}$$

Over the pH range of seawater, 7.8-8.3, the dominant ion is HCO_3^- and at higher pH's the presence of CO_3^{2-} ions become more significant. The equilibrium constants are particularly useful in salt water and sea water calculations, as knowledge of these constants as functions of salinity, temperature and pressure enables values for the concentrations of individual components to be calculated.

IV.2 The effect of pressure on the dissociation reaction of water

Most of the CO_2 entering pure water remains as dissolved gas. At the pH of the solution, ~5, the bicarbonate ion formation is small, and there is no carbonate ion formation. As these are the only two products of the dissociation process, to maintain electrical neutrality,

$$[H^+]=[HCO_3^-] \tag{37}$$

The equilibrium constants for eqns 33 and 34 are $10^{-1.47}$ and $10^{-6.4}$ [176] respectively.

Rearranging eqn 33, and substituting for (H_2CO_3), ($\approx(CO_{2(aq)})$) in eqn 34, and rearranging, gives

$$(HCO3^-)=\frac{K_{H_2CO_3}K_H\,pCO_2}{(H^+)} \tag{38}$$

An effective increase in pressure from, for example, 1 bara to 30 bara, would result in an increase in the partial pressure of CO_2, by a factor of 30. Le Chatelier's principle states that a system at equilibrium, subjected to a perturbation, responds in a way that tends to minimise its effect.

Therefore, although it might be expected that on increasing the pressure, the (HCO_3^-) ions become more significant as the equilibrium is pushed to the right, this is in fact compensated by the increase in (H^+) ions, as shown by eqn 38, which also increase by a factor of 30 on increasing the pressure.

From (37), eqn (38) can be rewritten,

$$(HCO_3^-)=\sqrt{(K_{H_2CO_3}K_H pCO_2)} \tag{39}$$

On increasing the pressure from 1 to 30 bara, therefore, the partial pressure of CO_2 increases by a factor of ~30, and the (HCO_3^-) concentration increases by a factor of ~5.5. The solubility of CO_2 in distilled water at 1 bara and 30 bara is 0.034 and 0.80 moles CO_2/l H_2O respectively at 25°C [30]. These values correspond to the total dissolved CO_2 content

$$\Sigma CO_2=H_2CO_3+HCO_3^-+CO_3^{2-} \tag{40}$$

As mentioned previously, the carbonate ion concentration for CO_2 in water can be neglected, ($pH<7$), and therefore, at 1 bara

$$0.034=CO_{2(aq)}+HCO_3^- \tag{41}$$

and at 30 bara

$$0.80=CO_{2(aq)}+HCO_3^- \tag{42}$$

Substituting for (H_2CO_3) in eqns 33, 34 and 39, gives values for the (HCO_3^-) concentration of 1.23×10^{-4} and 5.96×10^{-4} mols/l at 1 and 30 bara respectively, showing that in pure water, irrespective of pressure the dominant species is (CO_2).

IV.3 Rates of reaction involving dissolved CO_2

In focusing on the rate of gas evolution of gases in water and salt solutions, a key factor concerning the rate of CO_2 evolution must be the rate constants for the forward and reverse reactions occurring in the CO_2/water system. This would have significant implications when comparing the position of the equilibria for CO_2 in water and salt solutions, in which, in water the equilibrium lies far over to the left hand side of eqn 32, whereas in salt solutions, the equilibrium lies far over to the right hand side.

Of the reactions contributing to the equilibria, the passage of CO_2 across the phase boundary, eqn 30, has a rate coefficient sufficiently small to be insignificant in the following discussion. The interconversion routes between dissolved CO_2, H_2CO_3 and HCO_3^- can be depicted by [173,177]

$$\begin{array}{c} (a)\ CO_2 + H_2O \rightleftharpoons H_2CO_3\ (b) \\ \searrow\!\!\nwarrow \qquad\quad \swarrow\!\!\nearrow \\ HCO_3^- + H^+\ (c) \end{array} \tag{43}$$

rather than by

$$CO_2 + H_2O \rightleftharpoons H_2CO_3 \rightleftharpoons HCO_3^- + H^+ \tag{44}$$

The forward and reverse rate constants for reaction (a) to (b), k_{ab} and k_{ba}, have values, at 25°C, of $3.0\mathrm{x}10^{-2}$ sec^{-1} and 26.9 sec^{-1} respectively [166,173]. Since the concentration of water is essentially constant in dilute solutions, and is generally incorporated into the equilibrium constant, the forward reaction can be expressed as a first order reaction with respect to CO_2 [173],

$$\frac{-d\,[CO_{2(aq)}]}{dt} = k_{ab}\,[CO_{2(aq)}] \tag{45}$$

and the reverse reaction, also first order, can be expressed as,

$$\frac{-d\,[H_2CO_3]}{dt} = k_{ba}\,[H_2CO_3] \tag{46}$$

Similarly the rate constants for the reaction (b) to (c), denoted by k_{bc} and k_{cb} have values of $8\mathrm{x}10^6$ sec^{-1} and $4.7\mathrm{x}10^{10}$ l mol^{-1} sec^{-1} respectively [173,177]. The rate law representing the reversible process occurring between (b) and (c) can be expressed as [170]

$$\frac{d[HCO_3^-]}{dt} = k_{bc}\,[H_2CO_3] - k_{cb}\,[HCO_3^-][H^+] \tag{47}$$

Indeed, the rate constant at equilibrium is, in fact, the ratio of the rate constants for the forward and reverse reactions, which in this case, is given in eqn 34.

The rate constants, k_{ac} and k_{ca}, for the forward and reverse reactions linking (a) to (c), have values of 0.03 sec^{-1} and $10.2\mathrm{x}10^4$ l mol^{-1} sec^{-1} respectively [170]. The first rate constant is a first order coefficient, indicating a half life for dissolved CO_2 of several minutes [166]. The reverse process has a second order rate coefficient, depending on experimental conditions, such as the solution composition. The rate law for the disappearance of CO_2 can effectively be written as

$$\frac{-d[CO_2]}{dt} = (k_{ab}+k_{ac})\ [CO_2] - k_{ba}\ [H_2CO_3] - k_{ca}\ [H^+][HCO_3^-] \tag{48}$$

As can be seen from the rate constants, the first and third steps are the rate determining steps. The second step is very rapid. The reactions (a) to (b) and (a) to (c) occur simultaneously [173], and either one can be the dominant reaction, depending on pH. Indeed, the relative importance of the third step to the overall hydration rate increases with increasing pH. This has significant implications in relation to the rate of gas evolution from water and salt solutions, as discussed in chapter 7, sections 7.3.1.4 and 7.4.

IV.4 Use of infra red spectroscopy to measure the dissolved gas content

Every molecule has some form of vibrational spectrum, and hence bonds in the molecule absorb energy at particular frequencies, yielding characteristic absorption peaks. Infra red spectroscopy is a versatile technique for analysis, since spectra can be easily obtained for gases, liquids and solids, under extreme temperature and pressure conditions.

An on-line infra red technique, is, at present, being used in the brewing industry to determine the CO_2 content of beer, and other carbonated beverages. The measurements are taken in situ, without the need for sample extraction or chemical treatment, and hence the analysis is a non destructive, non invasive technique which can provide information almost instantly. The technique is based on the attenuated total reflectance principle, which relies on transmission of infra red radiation through an optically pure crystalline sensor in contact with the liquid. An infra red beam is focused into one end of the crystal, so that it strikes the internal face of the crystal at an oblique angle. At the point of internal reflection, a portion of the energy in the beam projects slightly beyond the reflecting surface, before returning to the crystal. When the probe is inserted into a fluid stream, energy will be absorbed from the beam at those frequencies at which the liquid normally absorbs. The energy of the beam extends only a few micrometers into the sample. Any sample material beyond that point has no effect on the measurement. The beam is finally reflected out of the crystal, close to the point at which it went in, and strikes an infra red detector. Provided the rod remains wetted whilst measurements are being made, the total amount of absorption of the beam is a function of the measured concentration.

By measuring the intensity of the characteristic peak, which for CO_2 is a strong absorption band at 2340 cm^{-1}, the amount of dissolved CO_2 in the sample can be determined. The concentration of the dissolved CO_2 is directly proportional to the amount of IR energy absorbed by the sample. The peaks are characteristic of the gas being studied and are not affected by the presence of other gases in the fluid. The technique can also be used to study other gases present in the fluid, by concentrating on a different region of the infra red spectrum, for each gas, such as CH_4 and H_2S has characteristic peaks which appear at different wavelengths on the IR spectrum.

At the start of the programme, the feasibility of developing and indeed adapting the on-line infra red analyzer used in the brewing industry for use in the oil industry, as a technique to monitor directly the dissolved gas content, not just of CO_2, in oil well fluids at various stages in the separation process was investigated. The conditions experienced during crude oil production are somewhat harsher than those experienced in the brewing industry. Namely pressures up to 60 bar, as opposed to 3 bar, temperatures approaching 100°C compared with 15°C, and levels of CO_2 in water of about 10 v/v as compared to 1 v/v. In addition to which, the fluids often contain a high solids content.

Infra red spectroscopy has been used, in the present study, to monitor the dissolution of carbon dioxide in water and hydrocarbons using a small scale IR cell. The spectra, showing the infra red band positions and relative band intensities for CO_2 in water and oil samples, recorded after bubbling CO_2 into solution at room temperature and 6 bara pressure can be seen in figures IV-1 to IV-4. The spectrum for the CO_2 in water system, figure IV-1, clearly shows a small peak at 2342 cm^{-1}, characteristic of CO_2, on the shoulder of the water band. The actual intensity of the CO_2 peak can be obtained by a subtraction spectrum of a water sample before and after bubbling with CO_2. The lower solubility of CO_2 in water, figure IV-1, than in, for example, hexane, figure IV-2, determined by the intensity of the peak observed at 2340 cm^{-1}, is clearly apparent. Both systems were virtually saturated, for CO_2 was bubbled through hexane, at 6 bara pressure, for 15 mins, and through water, at 6 bara, for 3 hours. Similar results to those in hexane were obtained using kerosene, figure IV-3, and Forties crude oil, figure IV-4. Indeed, the spectra recorded of hexane and crude over the range 4000-1000 cm^{-1} were shown to be very similar. The majority of peaks observed could be put down to the bending and stretching vibrations of O-H and C-H bonds.

During discussions with the manufacturers, it became evident that they had not, as yet, had a need to consider the equilibrium state of CO_2 in water, and therefore the dissociation reaction of CO_2

in water had not been investigated using the infra red analyzer. This however, was not considered to be a major problem. The bicarbonate peaks appear in a different part of the spectrum (2000-600 cm^{-1}) to that of molecular CO_2. The spectrum of HCO_3^- ions was observed, by the author, by recording a spectrum of $NaHCO_3$ suspended in a Nujol mull. The spectrum can be seen in figure IV-5. Table IV-1 shows the wavenumbers and band assignments associated with the HCO_3^- ions. The other bands in the spectrum not assigned, are due to the $[Na^+HCO_3^-]$ lattice vibrations.

After investigating the technique, there appeared to be no apparent reason why the technique could not be adapted for use in the oil and gas industry, and indeed there may be a future in the oil industry for this type of sensor and analyzer to monitor dissolved gas contents in fluids, in pipelines and separators, particularly as the sensor is robust and not affected by the presence of suspended solids in the liquid, nor by moderate increases in pressure and temperature. The probe material, however, would need to be thoroughly investigated at very high pressures and temperatures.

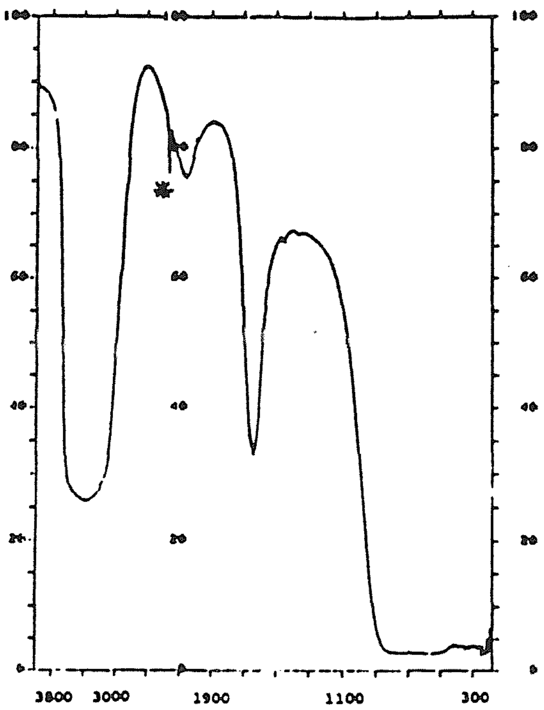

Figure IV-1 Infra red spectrum of water, saturated with CO_2 at 6 bara pressure, ambient temperature, pathlength 1mm, range 4000-1000 cm^{-1}

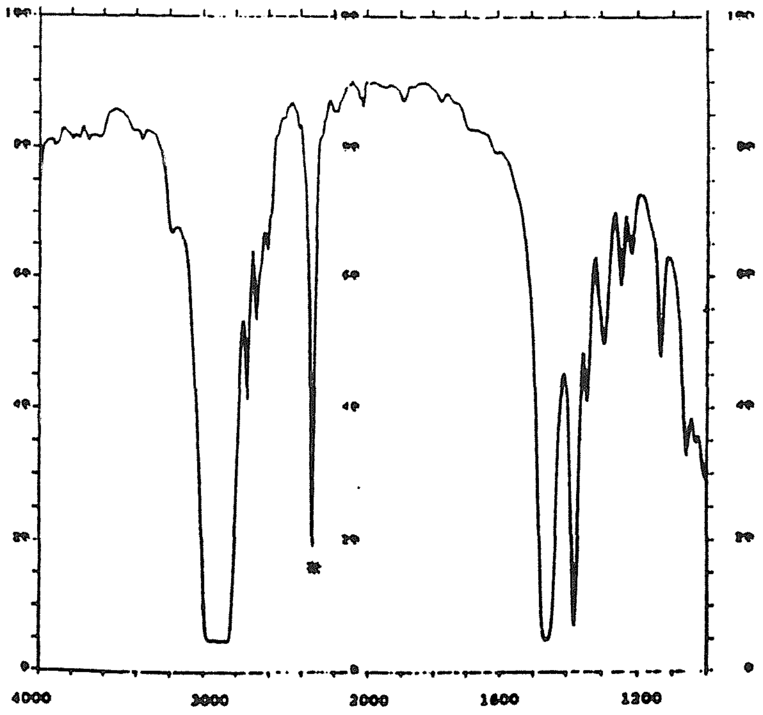

Figure IV-2 Infra red spectrum of hexane, saturated with CO_2 at 6 bara pressure, ambient temperature, pathlength 1mm, range 4000-1000 cm^{-1}

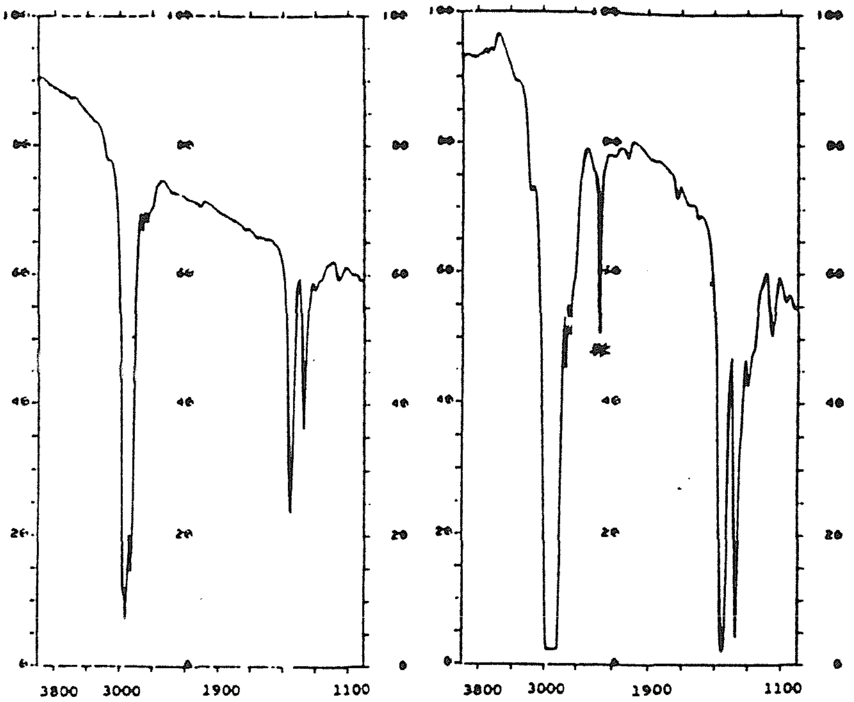

Figure IV-3 Infra red spectrum of kerosene, before and after bubbling for 5 mins with CO_2 at 6 bara, ambient temperature, pathlength 1mm, range 4000-1000 cm^{-1}

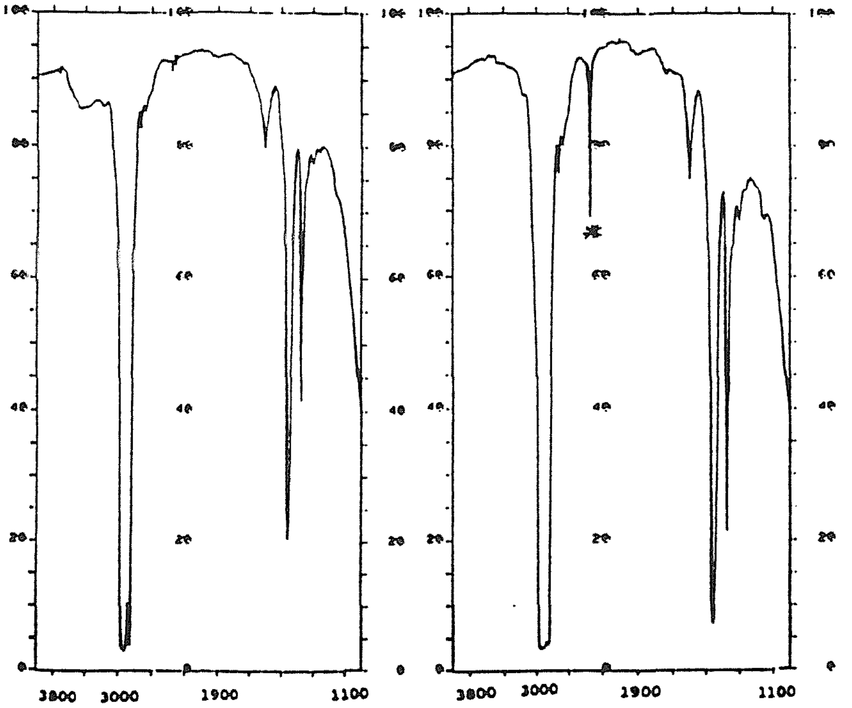

Figure IV-4 Infra red spectrum of Forties crude oil, before and after bubbling for 5 mins with CO_2 at 6 bara pressure and ambient temperature, pathlength 1mm, range 4000-1000 cm^{-1}

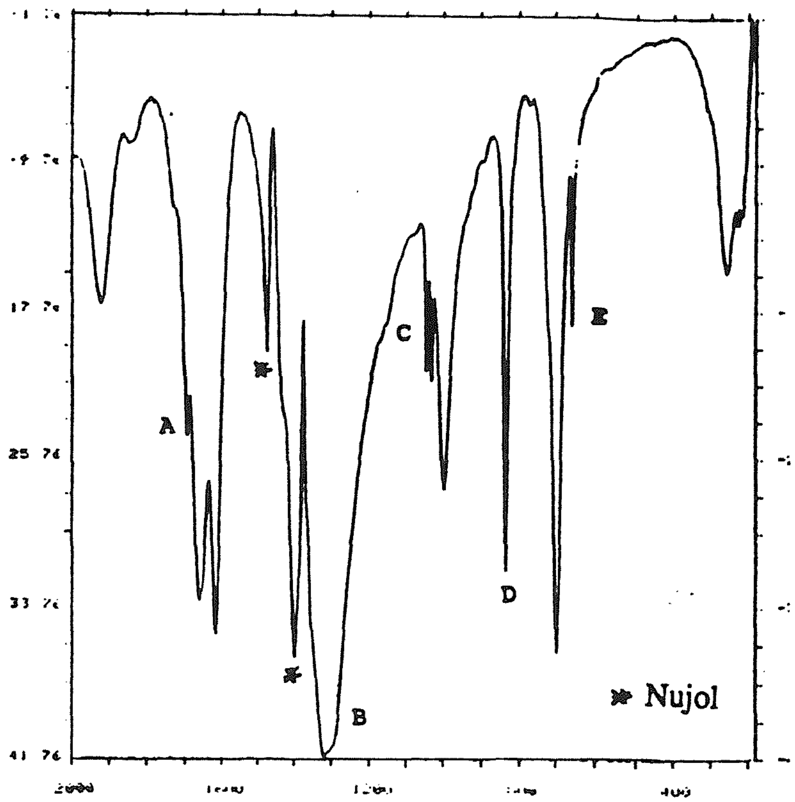

Figure IV-5 Infra red spectrum of $NaHCO_3$, suspended in a Nujol mull, pathlength 0.25 mm, range 2000-180 cm^{-1}

	ν_1 cm^{-1}	ν_2 cm^{-1}	ν_3 cm^{-1}	ν_4 cm^{-1}	ν_5 cm^{-1}	ν_6 cm^{-1}	ν_7 cm^{-1}	ν_8 cm^{-1}	ν_9 cm^{-1}
[HO-CO2]*	3390	1697	1338	1211	960	712	579	835	660
Peak assignment	---	1694	1323	1210	hidden	hidden	---	839	655
	---	A	B	C	---	---	---	D	E

Table IV-1 Infra red absorption peaks of the stretching and vibrating motions of [HCO_3^-] ions

* Data taken from [178]

V Pressure vessel and instrumentation details

V.1 Pressure vessel information

Pressure vessel details	
Material	Stainless steel 316L
Design code/ specifications	ASME VIII Div 1
Design pressure	33 barg
Operating pressure	30 barg
Test pressure	58.63 barg hydro test
Design temperature (maximum)	93°C
Operating temperature	70°C
Internal diameter	150.60 mm ±0.1 mm
Outer diameter	168.30 mm ±0.1 mm
Distance flange to flange	1001.5 mm
Flange thickness	47.6 mm

Table V-1 Pressure vessel details

V.2 Instrumentation details

Parameter	Units	Accuracy	Initial conditions				
Pressure	bar (g)	±0.01	5	10	20	30	
Temperature	°C	±0.1	25	40	60		
Gas flow rate	l/min	±2	33	66	100	160	
Bubbling time	mins	±0.1	5	15	30	60	120
Free gas volume	litres	$\pm 4\text{x}10^{-5}$	0.01	0.8	2.4	3.6	
Fluid velocity			agitation	no agitation			
Nuclei levels			tap water	500 ppm solids	filtered		
Salt saturation	%	±0.5	0	3	25	50	100
Air reg pressure	bar (g)	±0.1	6	4	2	0	

Note: accuracy is given in terms of full scale units

Table V-2 Instrumentation details

V.3 Operating instructions

The operating procedure is given below. The valves are shown in the systems drawing, figure 4.2. Positions 1 and 0 refer to the piston at its highest and lowest positions respectively. The upper and lower chambers of the cylinder are referred to as x and y respectively.

INITIALLY Open: V_9, V_{11}, V_{13}, V_{15}
Closed: V_1, V_2, V_3, V_6, V_7, V_8
Cylinder at position 1.

1. Open V_3 to fill vessel from holding tank. Close V_3 when required level is reached.
2. Open V_8 and bleed air using hand pump to ensure no air is in the system. Close V_8.

3. Apply air on x to drive piston slowly down, i.e. close V_{11} and V_{13}, adjust air restrictor, throw V_{14}. Air in Y dumped via V_{14}. Simultaneously, pump hydraulic fluid into upper chamber, via V_5, using hand pump.
4. When cylinder is in position 0, close V_9 and open V_2. Pressure in lower chamber will rise, observed by the pressure gauges, P_2 and P_3.
5. At required test pressure, bubble gas through for desired length of time, using V_9 to control flow rate of gas.
6. After saturation, use hand pump to ensure piston is still at its lowest position, and centralise V_{14} to lock hydraulics.

AT REQUIRED STARTING PRESSURE, e.g. 10 bara,

Closed: V_1, V_2, V_3, V_6, V_7, V_8, V_9, V_{11}, V_{13}
Cylinder at position 0.

7. Allow air onto Y, open V_{11} and V_{13}, energising V_{10}, i.e. dump x.
8. **Start test**, i.e. throw switch, opening dump valve, V_7, dumping hydraulic fluid. Piston moves upwards, towards position 1. Relay throws V_{10}, thus de-energising V_{10} and energising V_{12}, therefore dumping y and pressurizing x.

The operation can then be repeated.

V.4 Data reduction programme

As discussed in chapter 4.2.5, a data reduction programme was written to reduce the 1,200,000 samples, collected over the duration of a typical run, to a more manageable size of 120-150 data points. The programme was written such that the bulk of the data over the latter stages of the run was stripped out, whilst the data recorded in the initial stages was left untouched. The programme is listed below.

SHRINK.BAS

```
' SHRINK.BAS reads in a comma-delimited data file from Pico-log,
' with an 'x' data set in milliseconds (which it converts to seconds)
' and two 'y' series. It 'strips out' repeated data, leaving 'trends' and
' transient data intact. Compared with the original, the final output file is
' greatly reduced in size.

  DECLARE SUB Pause ()
  DECLARE SUB InputData ()
  DECLARE SUB WriteData ()
  DECLARE SUB WriteVal ()

  COMMON SHARED Ti1, Ti2, Ti3, Pr1, Pr2, Pr3, Po1, Po2, Po3
  Table$ = "c:\pico\tab.dat"
  Result$ = "c:\pico\tab_r.dat"
  Intval = 40               'Interval of repeat sequential data items to ignore
  OPEN Table$ FOR INPUT AS #1
  OPEN Result$ FOR OUTPUT AS #2
  Cycle = 1
  Cnt = 0
  INPUT #1, Ti1, Pr1, Po1   'Input initial data "group"
  INPUT #1, Ti2, Pr2, Po2
  INPUT #1, Ti3, Pr3, Po3
  CLS
  LOCATE 11, 18
  PRINT "*** PROCESSING: PLEASE WAIT ***"
  PRINT
  PRINT "                  (Input file is -  "; Table$; ")"
  PRINT "                  (Output file is -  "; Result$; ")"
  DO
    Ti1 = Ti1 / 1000        'Milliseconds to Seconds
    Ti2 = Ti2 / 1000
    Ti3 = Ti3 / 1000
    Dirn = 0                'Look for a local trend in the data
    Dirn = Dirn + SGN(Pr2 - Pr1)
    Dirn = Dirn + SGN(Pr3 - Pr2)
    REM PRINT Cycle; ")", "Pr1="; Pr1, "Pr2="; Pr2, "Pr3="; Pr3, "Dirn="; Dirn
    IF ABS(Dirn) <> 2 THEN  'If no trend, then..
      Cnt = Cnt + 1
      IF Cnt <> Intval THEN
        GOTO GetNxtVal      '..ignore data group if still within interval..
```

SHRINK.BAS

```
      ELSE
        Cnt = 0
        CALL WriteData          '..otherwise, write the group & start a new interval
      END IF
    ELSE
      CALL WriteData            'If there is a trend, write the data group
    END IF
GetNxtVal:
  Ti1 = Ti3 * 1000 'Make the FIRST set of data in the new group equal to the LAST..
  Pr1 = Pr3       '..set of data in the previous group
  Po1 = Po3
  Cycle = Cycle + 1
  CALL InputData   'Read in the next two sets of data
  LOCATE 16, 30
  PRINT "Line number: "; Cycle; "  "
  LOOP UNTIL EOF(1)
Finish:
  CLOSE #1
  CLOSE #2
  CLS
  BEEP
  LOCATE 11, 18
  PRINT "         *** THERE.. ALL DONE !! ***"
  PRINT "                          (Press a key)"
  SUB InputData
    INPUT #1, Ti2, Pr2, Po2
    IF EOF(1) THEN EXIT SUB
    INPUT #1, Ti3, Pr3, Po3
  END SUB

SUB Pause
  DO
  LOOP UNTIL INKEY$ <> ""
END SUB

  SUB WriteData
    WRITE #2, Ti1, Pr1, Po1
    WRITE #2, Ti2, Pr2, Po2
    WRITE #2, Ti3, Pr3, Po3
  END SUB
```

VI Surface roughness and scanning electron microscopy details

VI.1 Measurement of surface roughness

Roughness is a measure of the irregular, inherent surface in the production process left by the actual machining process used on the surface. An idea of the roughness values for the surface finishes obtained from several manufacturing process can be seen in the table.

Process	Ra, μm
Superfinishing	0.05-0.2
Lapping	0.05-0.4
Polishing	0.1-0.4
Honing	0.1-0.8
Grinding	0.1-1.6
Boring	0.4-6.3
Turning	0.4-6.3
Milling	0.8-6.3

Table VI-1 Roughness values for the surface finishes obtained from manufacturing processes [179]

Roughness measurements are made perpendicular to the direction of the lay, and can be taken directly from the surface or from replicas of the surface if the surface is inaccessible. A replica of the surface is easily obtained, by pouring a small amount of a synthetic resin onto the surface and allowing it to set over a period of 10-15 minutes. The resin can be removed, when set, by using a release agent which assists in the removal of the replica from the surface without damage. Measurements can then be made on the replica. Using a synthetic resin replica, the accuracy attainable on a normal surface approaches 100%. It is generally accepted that an accuracy of within 10% can be obtained from traces of the original and the replica. The accuracy of the replica surface technique was tested using a stainless steel sample and a replica of the same surface. The Ra value for the replica traces carried out by the author were found to be smaller than the Ra values for the original traces by ~6.55%

The replica has an inverted profile, and therefore, a peak on the actual surface is measured as a valley on the replica. But although the profile is inverted, the Ra will not differ, since it represents the average roughness. The stylus is traversed across the surface and the pick-up (transducer) converts the minute vertical movements of the stylus into proportionate variations of electrical signal, which is amplified and used to operate a recorder. The stylus is the only active contact between the surface and the instrument. Although stylus measurements trace a section profile along a line, rather than an area, this is considered to be a representative of the whole surface, as most surfaces produced by common manufacturing processes have a texture that is substantially even over a comparatively large area. It is also possible to take several closely spaced parallel traces to build up a 3D picture of the surface.

Surface roughness measurements, carried out using Rank-Taylor-Hobson Talysurf equipment, were taken on a number of stainless steel samples and on replicas of the inside of the pressure vessel. The assessment length for each measurement of surface roughness was 10 mm. The most important Ra values were those taken from the piston bore, where a fine finish to the surface was essential for the smooth running of the piston. The Ra values obtained from replicas of the piston bore ranged from 1.37μm to 3.03μm, within the roughness values specified by the manufacturers of the piston seal, as discussed in chapter 4.2.3. Traces were also taken from replicas of the stainless steel surface, at various positions lower down in the vessel. These Ra values ranged from 2.99μm to 7.40μm.

Direct roughness measurements were then taken from the stainless steel sections, bored out of the main vessel body to enable the window mountings to be inserted. The samples had the same surface finish as the inside walls of the vessel. The results, together with a description of the various parameters measured are given in table VI-2. The average roughness, Ra, of the 10 samples ranged from 3.58μm to 8.37μm. A typical profile is shown in figure VI-1, on which the parameters are marked, together with two typical 3D samples of the surface texture, figure VI-2.

Sample	Ra, μm	Rp, μm	Rv, μm	Rt, μm	S, μm	Sm, μm
1	3.58	9.85	30.79	40.65	11.47	95.09
2	5.04	13.63	27.22	40.85	13.06	154.02
3	4.61	11.38	25.27	36.64	11.65	134.68
4	3.88	10.77	22.97	33.73	9.35	95.63
5	3.78	18.66	32.30	50.96	13.30	105.75
6	5.41	12.53	30.48	43.01	13.79	180.85
7	8.25	16.62	42.67	59.29	22.92	248.41
8	8.37	16.49	47.03	63.52	20.98	286.91
9	5.13	18.17	26.06	44.23	14.60	128.58
10	4.63	14.05	28.20	42.25	12.54	136.57

Table VI-2 Roughness values for the surface replicas taken from the inside walls of the pressure vessel

Ra is the arithmetic mean of the departure of the roughness profile from the mean line
Rp is the maximum height of the profile above the mean line within the assessment length
Rv is the maximum depth of the profile below the mean line within the assessment length
Rt = Rp+Rv and is the maximum peak to valley height of the profile in the assessment length
S is the mean spacing of adjacent local peaks, measured over the assessment length, where a local peak is the highest part of the profile measured between two adjacent minima, depicted as S_1 in figure VI-1
Sm is the mean spacing between profile peaks at the mean line, measured over the assessment length, where a profile peak is the highest point of the profile between an upwards and downwards crossing of the mean line, depicted as S_{m1} in figure VI-1

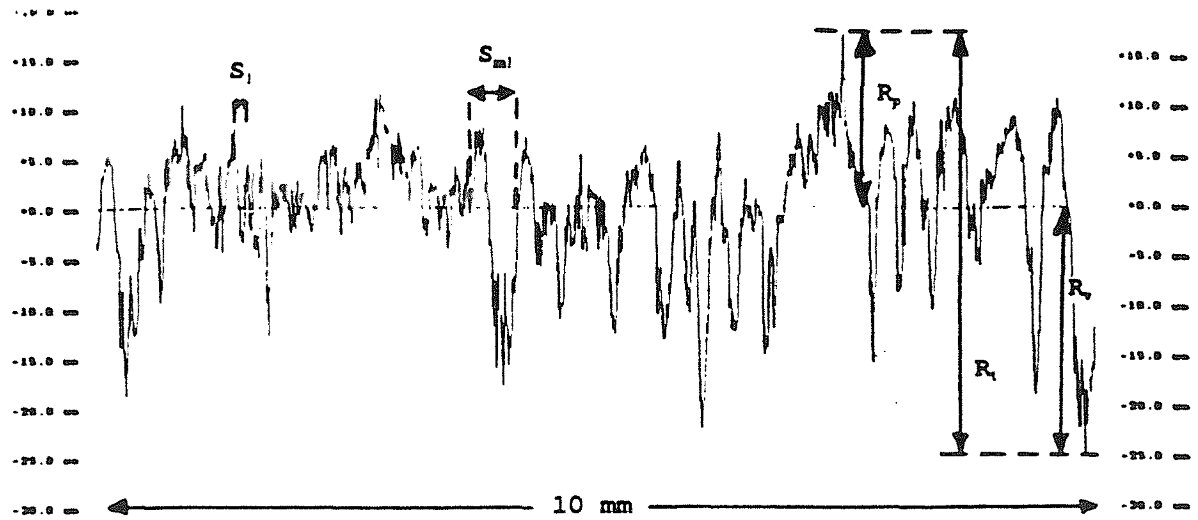

Figure VI-1 Typical profile of a stainless steel surface sample

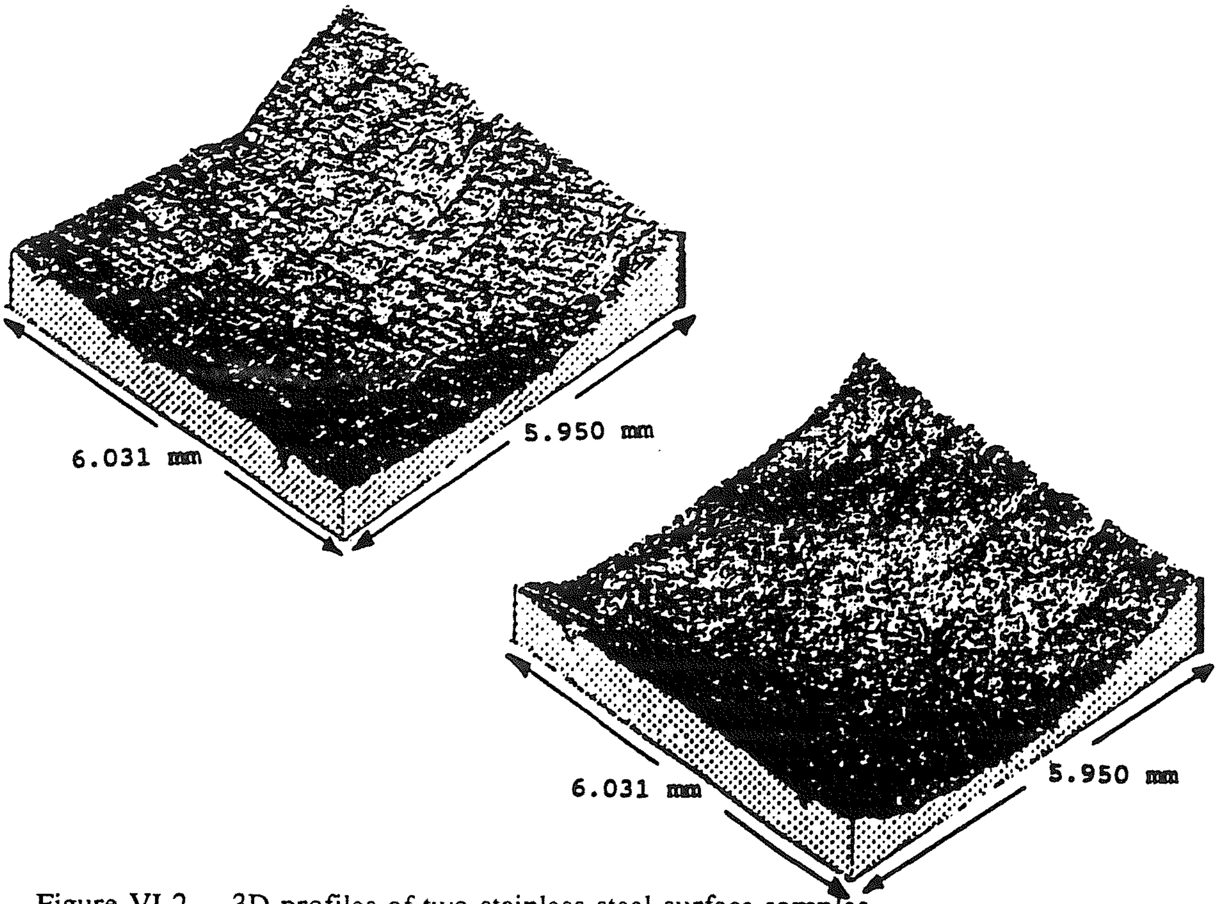

Figure VI-2 3D profiles of two stainless steel surface samples

As the piston is in moving contact with the steel walls, wear will undoubtedly occur over time, and the profile will change. It would therefore be a useful exercise to take replica samples of the piston bore after the piston has been in operation for a period of time. This would only be possible when the vessel has been dismantled, which, fortunately, was not necessary and therefore not carried out in the present programme.

VI.2 Scanning electron microscopy

The stainless steel surface was also investigated using a scanning electron microscope. Several 25 mm x 25 mm samples from the vessel bore were photographed, and can be seen in plate I. The samples, again, came from the sections cut away from the main vessel body to enable the window mountings to be inserted. The photographs, with a magnification in the range, 2000-2700 times, shows quite clearly the numerous pits and crevices in the surface. The crevices observed on the stainless steel surface measured up to a few mm in length. Analysis of the stainless steel composition was also carried out, during the scanning of the surface samples, yielding the results given in the table below.

Element	Wt %
Fe	70
Cr	18
Ni	10
Mo	2

Table VI-3 Analysis of the composition of a stainless steel sample taken from the inside vessel wall

In addition to investigating the surface of the vessel walls, scanning electron microscopy was also used to investigate the surfaces of the 5μm uni-sized silica flour particles used in the experiments to investigate the influence of insoluble nuclei on the rate of evolution. The photomicrographs can be seen in plate II.

Again, a useful exercise would be to take additional photomicrographs of the inside walls of the pressure vessel once the vessel has been in operation for a while, in order to investigate the changes in the surface texture with time, after the inside walls have been exposed to brine solutions and acidic solutions containing CO_2. This, again, can only really be done, by taking photomicrographs of cast replicas of the inside surface of the vessel walls, once the vessel has been dismantled.

REFERENCES

[1] Morris D., Fuelling Technology, Science and Public Affairs, 11, August 1991.

[2] Vekris E., Cunningham J. and Hodgkiess T, Topsides wt/space savings on offshore platforms, optimisation of process equipment and supply systems, ME-86-03, Glasgow Marine Tech Centre, 1986.

[3] Arsheim H. and Herfjord H., Separator design, simple theory, difficult theory and some reality, Proc. 9th Lecture Series on Two Phase Flow, Norwegian Inst. Tech., Trondheim, 1984.

[4] McCain W.D., "The properties of petroleum fluids", Penwell Publ. Co., 1989.

[5] Arnold K. and Stewart M., "Surface production operations, Design of oil handling systems and facilities", Vol I, Gulf Publ. Co., 1991.

[6] Bennett G.F., Removal of oil from wastewater by air flotation, CRC Critical Reviews in Environmental Control, **18**, 189, 1988.

[7] Ikink H., Retrograde gas condensation in gas pipelines now predictable, Delft Outlook, **94.4**, 20, 1994.

[8] Jones A.M., Environmental impact of North Sea oil, Sci. Prog. Oxf., **73**, 457-468, 1989.

[9] Skilbeck F. and Thew M.T., Development and application of liquid/liquid hydrocyclones for cleaning produced water, The European Seminar on offshore water and environmental management, March 1993, London.

[10] Smyth I.C.S, Evolution of gas in a hydrocyclone, University of Southampton, Internal Report, Unpublished, 1993.

[11] Skilbeck F. and Schubert M.F., Advancements in liquid hydrocyclone technology, Water management offshore, Aberdeen, 22/23 October, 1991.

[12] Schubert M.F., Advancements in liquid hydrocyclone separation systems, Paper OTC 6869, Proc. 24th OTC, Houston, May 1992.

[13] Lummis M., UK legislation relating to discharges from offshore oil and gas operations, The European Seminar on offshore water and environmental management, March 1993, London.

[14] King N.J. and Wilkinson T.G., Sources of oil contaminated discharges arising directly from North Sea operations, Proc. Seminar on the separation of oil from water for North Sea oil operations, Inst. Offshore Eng., Heriot-Watt University, 2, June 1976.

[15] Anon., Development of oil and gas resources in the UK, Dept. of Energy, Pub. HMSO, 1987.

[16] Kennedy T. and Monk D., An understanding of the legislative impact on future control of

offshore discharges, The European Seminar on offshore water and environmental management, March 1993, London.

[17] Paige R. and Ferguson M., Water injection- practical experiences and future potential, The European Seminar on offshore water and environmental management, March 1993, London.

[18] Evans R., Reservoir engineering and process design considerations for offshore produced water re-injection, The European Seminar on offshore water and environmental management, March 1993, London.

[19] Hadfield D., Produced water technology for overboard discharge and re-injection, current practices, OWTC, Inst. Chem. Eng., Oil and Natural Gas, Sept. 1993.

[20] Markham A.E. and Kobe K.A., The solubility of gases in liquids. Chem. Rev., **28**, 519, 1941.

[21] Battino R. and Clever H.L., The solubility of gases in liquids. Chem. Rev., **66**, 395, 1966.

[22] Wilhelm E., Battino R. and Wilcock R.J., Low pressure solubility of gases in liquid water, Chem. Rev., **77**, 219, 1977.

[23] Gerrard W., "Solubility of gases and liquids", Plenum Press, New York, 1976.

[24] Gerrard W., "Gas solubilities- widespread applications", Perg. Press, Oxford, 1980.

[25] Fogg P.G.T. and Gerrard W., "Solubility of gases in liquids", Wiley, 1991.

[26] Wiebe R., The binary system carbon dioxide - water under pressure, Chem. Rev., **29**, 475, 1942.

[27] Houghton G., Mclean A.M. and Ritchie P.D., Compressibility, fugacity and solubility of CO_2 in the region 0-36 atm and 0-100°C, Chem. Eng. Sci., **6**, 132, 1957.

[28] Zawisza A. and Malesinski B., Solubility of carbon dioxide in liquid water and of water in gaseous carbon dioxide in the range 2-5 MPa and at temperatures up to 473 K, J. Chem. Eng. Data, **26**, 388, 1981.

[29] Carroll J.J., Slupsky J.D. and Mather A.E., Solubility of carbon dioxide in water at low pressure, J. Phys. Chem. Ref. Data, **20**, 1201, 1991.

[30] Stewart P.B. and Munjal P., Solubility of carbon dioxide in pure water, synthetic sea water and synthetic sea water concentrates at -5°C to 25°C and 10 to 40 atm pressure, J. Chem. Eng. Data, **15**, 67, 1970.

[31] Murray C.N. and Riley J.P., The solubility of gases in distilled water and sea water, IV carbon dioxide, Deep Sea Res., **18**, 533, 1971.

[32] Malinin S.D. and Savelyeva N.I., The solubility of CO_2 in NaCl and $CaCl_2$ solutions at

25, 50 and 75°C under elevated CO_2 pressures, Geochem. Int., **5**, 410, 1972.

[33] Malinin S.D. and Kurovskaya N.A., Solubility of CO_2 in chloride solutions at elevated temperatures and CO_2 pressures, Geochem. Int., **12**, 199, 1975.

[34] Nighswander J.A., Kalogerakis N. and Mehrotra A.K., Solubility in water and 1 wt% NaCl solutions at pressures up to 10 MPa and temperatures from 80 to 200°C, J. Chem. Eng. Data, **34**, 355, 1989.

[35] Fogg P.G.T., "CO_2 in non aqueous solvents at pressures less than 200kPa, Solubility Data Series", Vol 50, Perg. Press, Oxford, 1992.

[36] Murray C.N. and Riley J.P., The solubility of gases in distilled water and seawater, III Ar, Deep Sea Res., **17**, 203, 1970.

[37] Clever H.L., "Solubility Data Series, Vol 4, Ar", Perg. Press, Oxford, 1980.

[38] Smith S.P. and Kennedy B.M., The solubility of noble gases in water and NaCl brine, Geochim. and Cosmochim. Acta, **47**, 503, 1983.

[39] Rettich T.R., Battino R. and Wilhelm E., Determination of Henry fugacities for Ar in water, 2-40°C, J. Soln. Chem., **21**, 987, 1992.

[40] Smith N.O., Kelemen S. and Nagy B., The solubility of natural gases in aqueous salt solutions- II N_2 in aqueous NaCl, $CaCl_2$, Na_2SO_4 and $MgSO_4$ at room temperatures and at pressures below 1000 psia, Geochim. and Cosmochim. Acta, **26**, 921, 1962.

[41] Battino R., "Solubility Data Series, Vol 10, N_2", Perg. Press, Oxford, 1982.

[42] Rettich T.R., Solubility of gases in liquids 16, Henrys law coefficients for N_2 in water, 5-50°C, J. Soln. Chem., **13**, 184, 1984.

[43] Bryk D.V., Makitra R.G., Pirig Y.N. and Stefanik Y.V., Influence of the physiochemical properties of solvents on the solubility of N_2, J. Appl. Chem, **63**, 281, 1990.

[44] Weiss R.F., Solubility of N_2, O_2 and Ar in water and seawater, Deep Sea Res., **17**, 721, 1970.

[45] Battino R., "Solubility Data Series, Vol 7, O_2", Perg. Press, Oxford, 1981.

[46] Clegg S.L. and Brimblecombe P., The solubility and activity coefficient of O_2 in salt solutions and brines, Geochim. and Cosmochim. Acta, **54**, 3315, 1990.

[47] Rettich T.R., Solubility of gases in liquids 13, Henrys law constants for CH_4 and C_2H_6 in water at 275-328K, J. Phys. Chem., **85**, 3230, 1981.

[48] Clever H.L. and Young C.L., "Solubility Data Series, Vol 27/28, CH_4", Perg. Press, Oxford, 1987.

[49] Cargill R.W., Solubility of gases in water-alcohol mixtures, Chem. Soc. Rev., **22**, 135, 1993.

[50] Kennan R.P. and Pollack G.L., Pressure dependence of solubility of nitrogen, argon, krypton and xenon in water. J. Chem. Phys., **93**, 2724, 1990.

[51] Uhlig H.H., The solubility of gases and surface tension, J. Phys. Chem., **41**, 1215, 1937.

[52] Eley D.D., Solubility of gases 1. The inert gases in water, 2. Comparison of organic solvents with water, Trans. Faraday Soc., **35**, 1281 and 1421, 1939.

[53] Frank H.S. and Evans M.W., Free volume and entropy in condensed systems, J. Chem. Phys., **13**, 507, 1945.

[54] Reiss H., Frisch H.L., Helfand E. and Lebowitz J.L., Aspects of the statistical thermodynamics of real fluids, J. Chem. Phys., **32**, 119, 1960.

[55] Pollack G.L., Why gases dissolve in liquids, Science, **251**, 1323, 1991.

[56] Pierotti R.A., The solubility of gases in liquids, J. Phys. Chem., **67**, 1840, 1963.

[57] Pierotti R.A., Aqueous solutions of non polar gases, J. Phys. Chem., **69**, 281, 1965.

[58] Hirschfelder J.O., Curtiss C.F., and Bird R.B., "Molecular theory of gases and liquids", Wiley & Sons, New York, 1954.

[59] Reid R.C., Prausnitz J.M. and Poling B.E., "The properties of gases and liquids", McGraw-Hill, New York, 1987.

[60] Fernandez-Prini R., Crovetto R., Japas M.L. and Laria D., Thermodynamics of dissolution of simple gases in water, Acc. Chem. Res., **18**, 207, 1985.

[61] Soave G., Equilibrium constants from a modified Redlich-Kwong equation of state, Chem. Eng. Sci., **27**, 1197, 1972.

[62] Peng D.Y. and Robinson D.B., A new two-constant equation of state, Ind. Eng. Fund., **15**, 59, 1976.

[63] Heidemann R.A., Three phase equilibria using equations of state, AICHE J., **20**, 847, 1974.

[64] Peng D.Y. and Robinson D.B., Two- and three- phase equilibrium calculations for systems containing water, Can. J. Chem. Eng., **54**, 595, 1976.

[65] Peng D.Y. and Robinson D.B., Newman S.A. Ed., Thermodynamics of aqueous systems with industrial applications, Amer. Chem. Soc. Symp. Ser., **133**, 393, 1980.

[66] Nghiem L.X. and Heidemann R.A., General acceleration procedure for multiphase flash calculation with application to oil-gas-water systems, Proc. Second Eur. Sym. on Enhanced Oil Rec., Paris Editions, Technip Paris 303, 1982.

[67] Heidemann R.A. and Prausnitz J.M., Equilibrium data for wet-air oxidation water content and thermodynamic properties of saturated combustion gases, Ind. Eng. Chem. Process Des. Dev., **16**, 375, 1977.

[68] Barta K. and Bradley D.J., Extension of the specific interaction model to include gas solubilities in high temperature brines, Geochim. Cosmochim. Acta, **49**, 195, 1986.

[69] Li Y-K. and Nghiem L.X., Phase equilibria of oil, gas and water/brine mixtures from a cubic equation of state and Henry's Law, Can. J. Chem. Eng., **64**, 486, 1986.

[70] Enick R.M. and Klara S.M., CO_2 solubility in water and brine under reservoir conditions, Chem. Eng. Comm., **90**, 23, 1990.

[71] Soreide I. and Whitson C.H., Peng-Robinson predictions for hydrocarbons, CO_2, N_2 and H_2S with pure water and NaCl brine, Fluid Phase Equil., **77**, 217, 1992.

[72] Guillot B. and Guissani Y., Temperature dependence of non polar gases in liquids, Molec. Phys., **79**, 53, 1993.

[73] Alger D.B., Effect of temperature on the solubility of gases in liquids, J. Chem. Ed., **69**, 62, 1992.

[74] Zarzyci R. and Chacuk A., "Absorption", Perg. Press, 1993.

[75] Hansen, R.S. and Deridan, J., Problems in foam origin, drainage and rupture, Proc. Symp. Soc of Chem. Ind., Coll. and Surf. Chem. Group, Brunel Univ., Sept. 1975.

[76] Clift R., Grace J.R. and Weber M.E., "Drops, bubbles and particles", Academic Press, 1978.

[77] Blake W.K., "Mechanics of flow induced sound and vibration, Vol. 1, Chapter 6, Introduction to bubble dynamics and cavitation", Academic Press Inc., 1986.

[78] Ronald-Young F., "Cavitation", McGraw Hill Book Co., 1989.

[79] Matsumoto T. and Takemura F., Influence of internal phenomena on gas bubble motion, Proc. of Inst. Mech. Eng., Cavitation, Int. Conf., 29, 1992.

[80] Morch K.A., Energy considerations on the collapse of cavity clusters, Appl. Sci. Res., **38**, 313, 1982.

[81] Arakeri V.H. and Shanmuganathan, Evidence for the effect of bubble interference on cavitation, J. Fluid Mech., **159**, 131, 1985.

[82] Takahira H., Fujikawa S. and Akamatsu T., Some analytical aspects on the dynamics of a cluster of bubbles, Proc. of Inst. Mech. Eng., Cavitation, Int. Conf., 9, 1992.

[83] Weyl W.A. and Marboe E.C., Some mechano-chemical properties of water, Research, **2**, 19, 1949.

[84] Katz J. and Acosta A., Observations of nuclei in cavitating flows, Appl. Sci. Res., **38**, 123, 1982.

[85] Yang Y.C. and Maa J.R., Microbubbles in water and boiling superheat, J. Coll. and Int. Sci., **120**, 87, 1987.

[86] Trevena D.H., "Cavitation and tension in liquids", Adam Hilger, 1987.

[87] Crum L.A., Nucleation and stabilization of microbubbles in liquids, Appl. Sci. Res., **38**, 101, 1982.

[88] Crum L.A., Tensile strength of water, Nature, **278**, **148**, 1979.

[89] Lubetkin S.D., Measurement of bubble nucleation rates by an acoustic method, J. Appl. Elec., **19**, 668, 1989.

[90] Kenning D.B.R. and Thirunavukkarasu S.K., Bubble nucleation following a sudden pressure reduction in water, Procs. 4th Int. Heat Transf. Conf., **5**, B29, 1, 1976.

[91] Morch K.A. and Song J.P., Cavitation nuclei at solid-liquid interfaces, Proc. of Inst. Mech. Eng., Cavitation, Int. Conf., 1, 1992.

[92] Song J.P, Morch K.A., Carneiro K. and Tholen A.R., STM investigations of solid surfaces in water and air, Surf. Sci., **296**, 299, 1993.

[93] Yount D., Microscopic investigation of bubble formation nuclei, J. Acoust. Soc. of Amer., **76**, 1511, 1984.

[94] Yount D., Use of bubble formation model to calculate diving tables, Aviat. Space and Env. Med., **57**, 149, 1986.

[95] Hayward A.T.J., Role of stabilized gas nuclei in hydrodynamic cavitation inception, J. Phys. D, **3**, 574, 1970.

[96] Oxtoby D.W. and Kashchiev D., General relation between nucleation work and size of nucleus in multi-component nucleation, J. Chem. Phys., **100**, 7665, 1994.

[97] Hemmingsen E.A., Supersaturation of gases in water, Science, **167**, 1493, 1970.

[98] Gorbunov B.Z., Zapadinsky E.L. and Sabelfeld K.K., Influence of inhomogeneity and fluctuations of supersaturation on heterogeneous nucleation, Chem. Phys. Lett., **215**, 31, 1993.

[99] Bernath L., Theory of bubble formation in liquids, Ind. and Eng. Chem. **44**, 1310, 1952.

[100] Skripov V.P., "Metastable states", John Wiley and Sons, 1974.

[101] Blander M. and Katz J.L., Bubble nucleation in liquids, AICHE J., **21**, 833, 1975.

[102] Lothe J. and Pound G.M., Reconsiderations of the nucleation theory, J. Chem. Phys., **36**, 2080, 1962.

[103] Reiss H., Katz J.L. and Cohen E.R., Translation-rotation paradox in the theory of nucleation, J. Chem. Phys., **48**, 5553, 1968.

[104] Zettlemoyer A.C., "Nucleation", Dekker, New York, 1969.

[105] Ruth V., Hirth J.P. and Pound G.M., On the theory of homogeneous nucleation and spinodal decomposition in condensation from the vapour phase, J. Chem. Phys., **88**, 7079,

1988.

[106] Hagen D.E. and Kassner J.L., Homogeneous nucleation rate for water, J. Chem. Phys., **81**, 1416, 1984.

[107] Miller R.C., Anderson R.J., Kassner J.L. and Hagen D.E., Homogeneous nucleation rate measurements for water over a wide range of temperature and nucleation rate, J. Chem. Phys, **78**, 3204, 1983.

[108] Viisanen Y., Strey R. and Reiss H., Homogeneous nucleation rates for water, J. Chem. Phys., **99**, 4680, 1993.

[109] Kacker A. and Heist R.H., Homogeneous nucleation rate measurements, 1. ethanol, n-propanol and i-propanol, J. Chem. Phys., **82**, 2735, 1985.

[110] Hung, C.H., Krasnopoler, M.J. and Katz, J.L., Condensation of a supersaturated vapour, VIII homogeneous nucleation of n-nonane, J. Chem. Phys., **90**, 1856, 1989.

[111] Hung C.H., Krasnopoler M.J. and Katz J.L., Condensation of a supersaturated vapour, VIII homogeneous nucleation of n-nonane, J. Chem. Phys., **92**, 7722, 1990.

[112] Strey R., Wagner P.E. and Viisanen Y., The problem of measuring homogeneous nucleation rates and the molecular contents of nuclei, J. Phys. Chem., **98**, 7748, 1994.

[113] Oxtoby D.W. and Evans R., Non classical nucleation theory for gas-liquid transition, J. Chem. Phys., **89**, 7521, 1988.

[114] Zeng X.C. and Oxtoby D.W., Binary homogeneous-nucleation theory for gas-liquid transition- non classical approach, J. Chem. Phys., **95**, 5941, 1991.

[115] Kwak H.Y. and Lee S., Homogeneous bubble nucleation predicted by a molecular interaction model, Trans. ASME, **113**, 714, 1991.

[116] Dillmann A. and Meier G.E.A., Refined approach to problem of homogeneous nucleation from vapour phase, J. Chem. Phys., **94**, 3872, 1991.

[117] Kalikmanov V.I. and van Dongen M.E.H., Cluster approach to the theory of homogeneous nucleation, Europhys. Lett., **21**, 645, 1993.

[118] Zhukhovitskii D.I., Size corrected theory of homogeneous nucleation, J. Chem. Phys., **101**, 5076, 1994.

[119] Deligiannis P. and Cleaver J.W., Influence of surrounding bubbles on rate of nucleation, Int. J. Heat and Mass Trans., **36**, 3697, 1993.

[120] Heist R.H., Janjia M. and Ahmed J., Effects of background gases on the homogeneous nucleation of vapours, J. Phys. Chem., **98**, 4443, 1994.

[121] Wegener P.P. and Mirabel P., Homogeneous nucleation in supersaturated vapours, Naturwissenschaften, **74**, 111, 1987.

[122] Katz J.L., Homogeneous nucleation, theory and experiment, Pure and Appl. Chem., **64**, 1661, 1992.

[123] Oxtoby D.W., Homogeneous nucleation, theory and experiment, J. Phys. Cond. Matter, **4**, 7627, 1992.

[124] Weinberg M.C., Multiple nucleation sites, J. Chem. Phys., **92**, 7515, 1990.

[125] Fletcher N.H., Size effect in heterogeneous nucleation, J. Chem. Phys., **29**, 572, 1958.

[126] Ward C.A., Johnson R.D., Ho S., Forest T.W. and Fraser W.D., Heterogeneous bubble nucleation and conditions for growth in a liquid-gas system of constant mass and volume, J. Appl. Phys., **54**, 1833, 1983.

[127] Ward C.A., Tikuisis P. and Venter R.D., Stability of bubbles in a closed volume of liquid-gas solution, J. Appl. Phys., **53**, 6076, 1982.

[128] Lutrus C.K., Hagen D.E and Salk S.H., Temperature and supersaturation dependence of nucleation rates of hot water by molecular cluster calculations, J. Chem. Phys., **99**, 9962, 1993.

[129] Deligiannis P. and Cleaver J.W., Determination of the heterogeneous nucleation factor during a transient-liquid expansion, Int. J. Mult. Flow, **18**, 273, 1992.

[130] Deligiannis P. and Cleaver J.W., The influence of critical bubble swarms on the rate of nucleation, Chem. Eng. Sci., **47**, 3142, 1992.

[131] Alamgir M.D. and Leinhard J.H., Correlation of pressure undershoot during hot water depressurization, ASME J. Heat Trans., **103**, 52, 1981.

[132] Alamgir M.D., Kan C.Y. and Leinhard J.H., Experimental study of rapid depression of hot water, ASME J. Heat Trans., **102**, 433, 1980.

[133] Forest T.W. and Ward C.A., Effect of dissolved gas on the homogeneous nucleation pressure of a liquid, J. Chem. Phys., **66**, 2322, 1977.

[134] Forest T.W. and Ward C.A., Homogeneous nucleation of bubbles in solutions at pressures above the vapour pressure of the pure liquid, J. Chem. Phys., **69**, 2221, 1978.

[135] Mori Y., Hijikata K. and Nagatani T., Effect of dissolved gas on bubble nucleation, Int. J. Heat Mass Trans., **19**, 1153, 1976.

[136] Hemmingsen E.A., Cavitation in gas supersaturated solutions, J. Appl. Phys., **46**, 213, 1975.

[137] Hemmingsen E.A., Spontaneous formation of bubbles in gas-supersaturated water, Nature, **267**, 141, 1977.

[138] Kwak H.Y. and Panton R.L., Gas bubble formation in non equilibrium water-gas solutions, J. Chem. Phys., **78**, 5795, 1983.

[139] Finkelstein A. and Tamir A., Formation of gas bubbles in supersaturated solutions of gases in water, AICHE J., **31**, 1409, 1985.

[140] Chirkov Y.G. and Pshenichnikov A.G., Estimate of probability of spontaneous gas bubble nucleation in supersaturated solutions, Sov. Elec., **21**, 114, 1985.

[141] Chirkov Y.G., Rostokin V.I. and Pshenichnikov A.G., Gas bubble nucleation in supersaturated solutions, Sov. Elec., **22**, 493, 1986.

[142] Rubin M.R. and Noyes R.M., Thresholds for nucleation of bubbles of N_2 in various solvents, J. Phys. Chem., **96**, 993, 1992.

[143] Wilt P.M., Nucleation rates and bubble stability in water and CO_2 solutions, J. Coll. and Int. Sci., **112**, 530, 1986.

[144] Fidi N., Jeelani S.A.K., May K. and Hartland S., Use of submerged jets in gas desorption from supersaturated solutions, Chem. Eng. Sci., **48**, 1833, 1993.

[145] Danckwerts P.V., "Gas-liquid reactions", McGraw Hill Co., 1970.

[146] Weiland R.H., Thuy L.T. and Liveris A.N., Transition from bubbling to quiescent desorption of dissolved gases, Ind. Eng. Chem. Fundam., **16**, 332, 1977.

[147] Thuy L.T. and Weiland R.H., Mechanism of gas desorption from aqueous solutions, Ind. Eng. Chem. Fund., **15**, 286, 1976.

[148] Hikita H. and Konishi Y., Desorption of CO_2 from supersaturated water in an agitated vessel, AICHE J., **30**, 945, 1984.

[149] Hikita H. and Konishi Y., Desorption of CO_2 from aqueous electrolyte solutions supersaturated CO_2 in an agitated vessel, AICHE J., **31**, 697, 1985.

[150] Detsch R. and Harris I., Dissolution and rise velocity of small air bubbles in water and salt water, Oceans, part 1, 286, 1989.

[151] Guthrie R.I.L. and Bradshaw A.V., Spherical capped bubbles rising in aqueous media, Chem. Eng. Sci, **28**, 191, 1973.

[152] Brankovic A., Currie I.G. and Martin W.W., Laser doppler measurements of bubble dynamics, Phys. of Fluids, **27**, 348, 1984.

[153] Ishikawa H., Miki T., Okamoto M. and Hikita H., Gas desorption from liquids: mass transfer and drag coefficients for single bubbles in free rise through newtonian liquids, Chem. Eng. Sci., **41**, 2309, 1986.

[154] Chang M.Y. and Morsi B.I., Mass transfer characteristics of gases in aqueous and organic liquids at elevated pressures and temperatures in agitated reactors, Chem. Eng. Sci., **46**, 2639, 1991.

[155] Wilke C.R. and Chang P., Correlations of diffusion coefficients in dilute solution, AICHE

J., **1**, 264, 1955.

[156] Leinhard J.H., Alamgir M.D and Treta M., Early response of hot water to sudden release from high pressure, J. Heat Trans., **100**, 473, 1978.

[157] Bartak J., Study of rapid depression of hot water and dynamics of vapour bubble generation, Int. J. Mult. Flow, **16**, 789, 1990.

[158] Weisman J., Bussell G., Jashnani I.L. and Hsieh T., The initiation of boiling during pressure transients, ASME paper n°73-WA/HT-25, 1973.

[159] Kendoush A., Delay time during depression of saturated water, ASME J. Heat Mass Trans., **32**, 2149, 1989.

[160] Wang Z. and Bankoff S.G., Bubble growth on a solid wall, Int. J. Mult. Flow, **17**, 425, 1991.

[161] Wang Z. and Bankoff S.G., Effective rapid nucleation rates on a solid wall in a rapidly depressurizing liquid pool, ASME, Thermal Eng. Proc. **2**, 229, 1991.

[162] Haque M.A., Richardson S.M., Saville G. and Chamberlin G., Rapid depressurization of pressure vessels, J. of Loss Prev. in Process Ind., **3**, 4, 1990.

[163] Eggers R. and Green V., Pressure discharge from a pressure vessel filled with CO_2, J. Loss Prev. Process Ind., **3**, 59, 1990.

[164] Xia J.L., Smith B.L. and Yadigaroglu G., Simplified model for depressurization of gas filled vessels, Int. Comm. Heat and Mass Trans., **20**, 653, 1993.

[165] Haque M.A., Richardson S.M. and Saville G., Blowdown of pressure vessels, Trans. IChemE, **70**, 3, 1992.

[166] Snoeyink V.L. and Jenkins D., "Water Chemistry", Wiley and Sons, 1980.

[167] Garrels R.M. and Christ C.L., "Solutions, minerals and equilibria", Harper Row Inc., 1965.

[168] Harvey E.N., McElroy W.D. and Whitely A.H., Cavity formation in water, J. Appl. Phys., **18**, 162, 1947.

[169] Lide D.R., "Handbook of Chemistry and Physics", 75th Ed., CRC Press, 1994.

[170] Riley J.P. and Skirrow G., "Chemical Oceanography", Vol 2, Academic Press, 1975.

[171] Unterberg W., Thermophysical properties of aqueous sodium chloride solutions, Report N° 64-21, University of California, 1964.

[172] Cengel Y.A. and Boles M.A., "An engineering approach to thermodynamics", 2nd Ed., McGraw-Hill Inc., 1994.

[173] Usdowski E., Reactions and equilibria in the systems CO_2-H_2O and $CaCO_3$-CO_2-H_2O, 0-50°C, N. Jb. Miner. Abh., **144**, 148, 1982.

[174] Atkins P.W, "Physical Chemistry", 3rd Ed., Ox. Univ. Press, 1986.

[175] Eng Sci Data, Properties of ice, water, steam, heavy water and sea water, Item 77024, 1979.

[176] Garrels R.M. and Christ C.L., "Solutions, minerals and equilibria", Harper Row Inc., 1965.

[177] Stumm W. and Morgan J.J., "Aquatic chemistry", Wiley Interscience, 1970.

[178] Bernill D.L, Hartman K.O. and Hisatsune I.C., Infra red spectra of isotopic bicarbonate monomer ions, J. Chem. Phys., 42, 3553, 1965.

[179] Dagnall H., "Exploring surface texture", Rank Taylor Hobson, 1980.

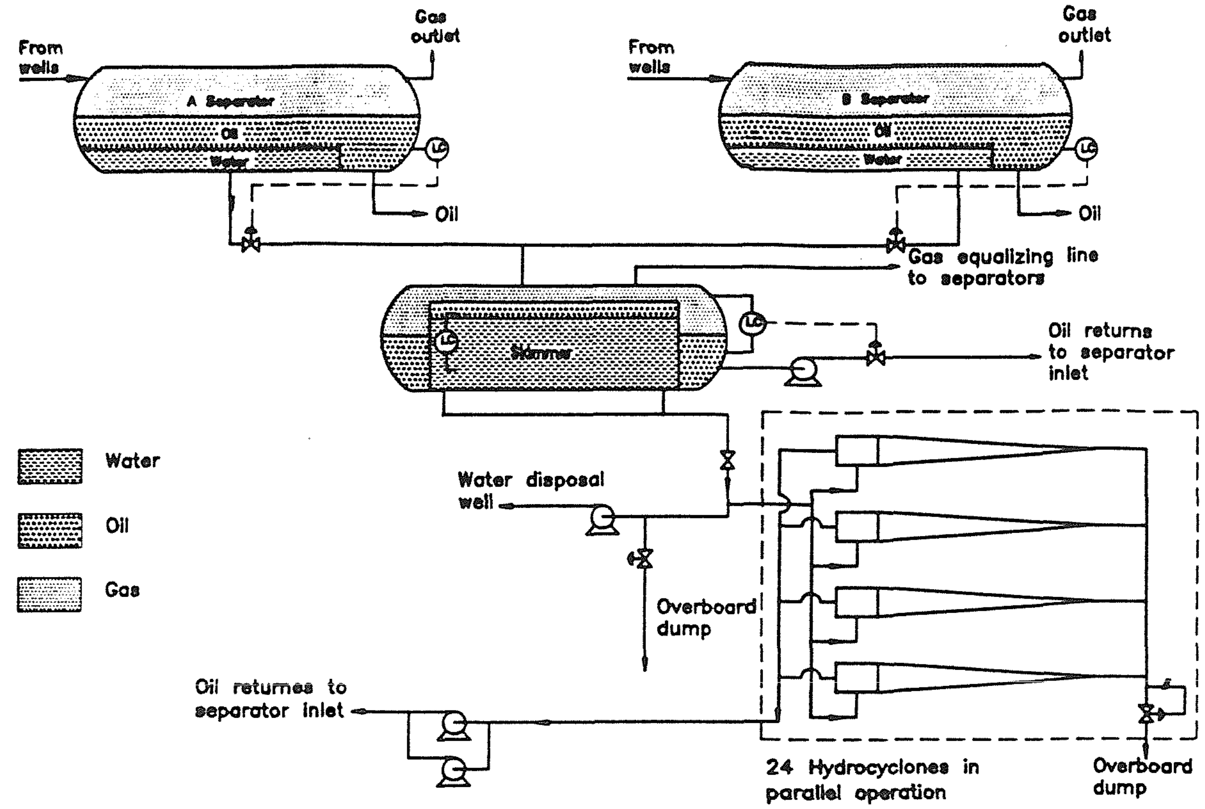

Figure 2.1 Typical offshore stage separation processing layout
[McErlean B.J., Use of hydrocyclones for oil/water separation in the Piper and Claymore oil fields, Inst. Mech. Eng. Seminar, 22 Mar. 1988]

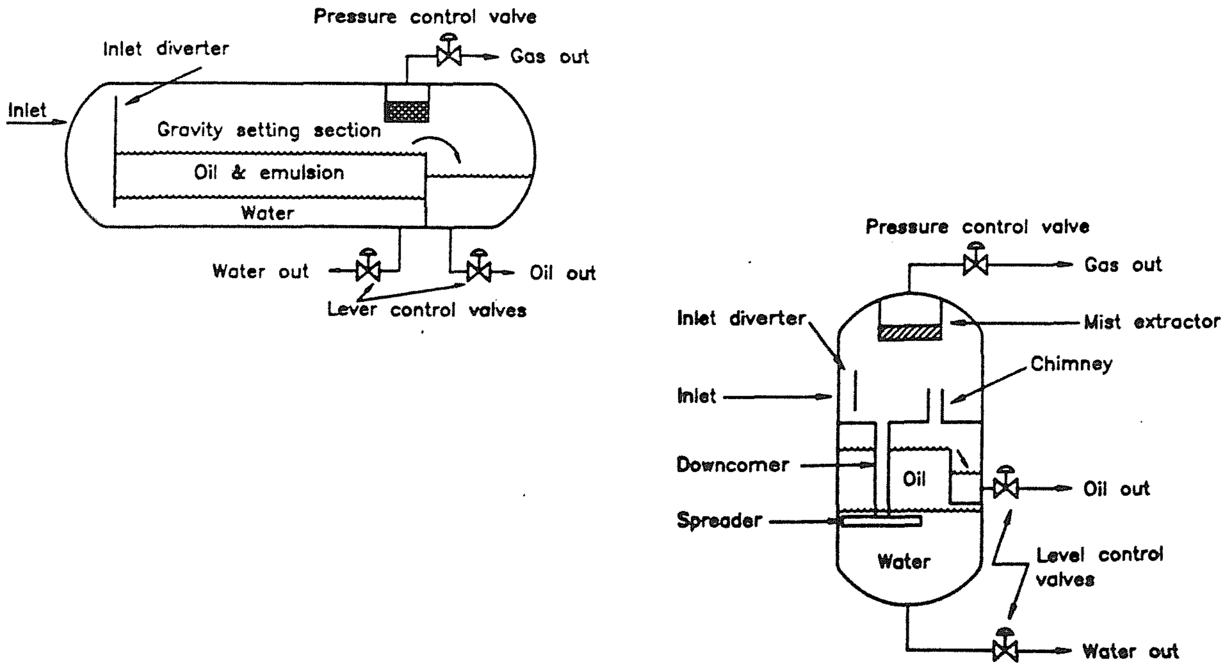

Figure 2.2 Three phase separators, a) horizontal, b) vertical
[Arnold K. and Stewart M., "Surface Production Operations", Vol I, Gulf Publishing Co., 1991]

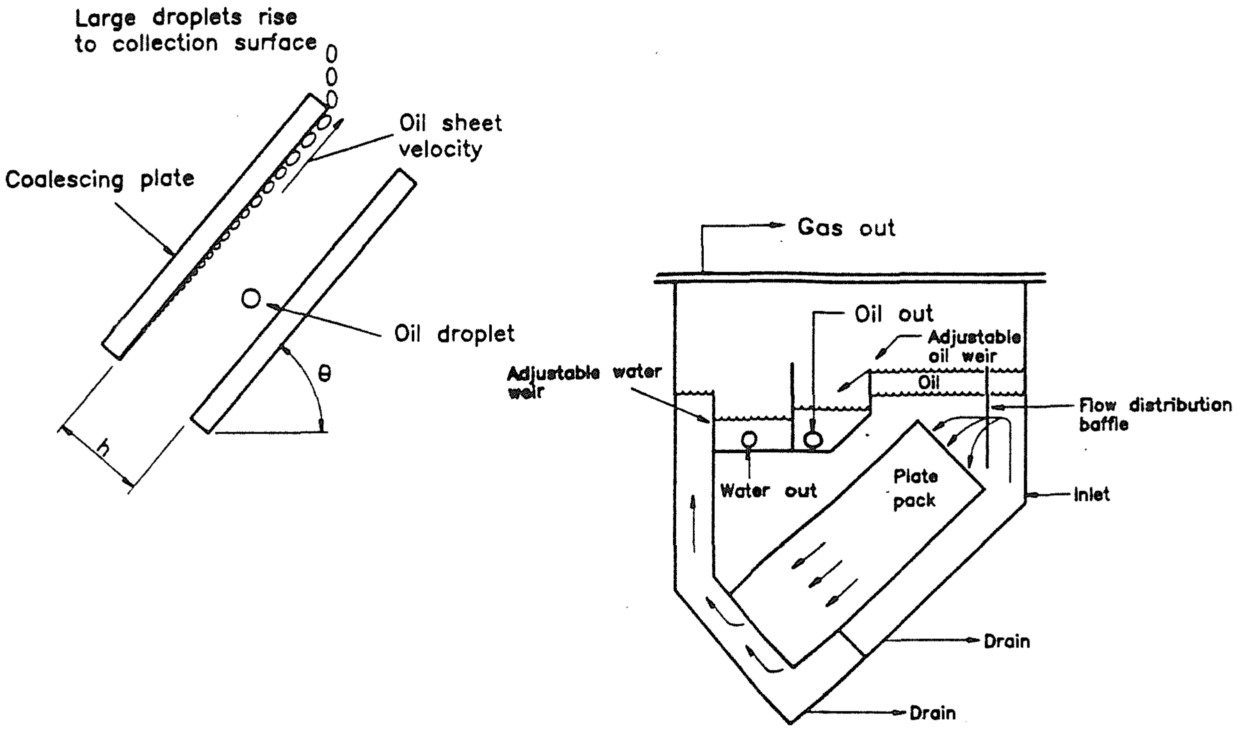

Figure 2.3 Tilted plate interceptor, a) plate coalescer, b) packing arrangement [Arnold K. and Stewart M., "Surface Production Operations", Vol I, Gulf Publishing Co., 1991]

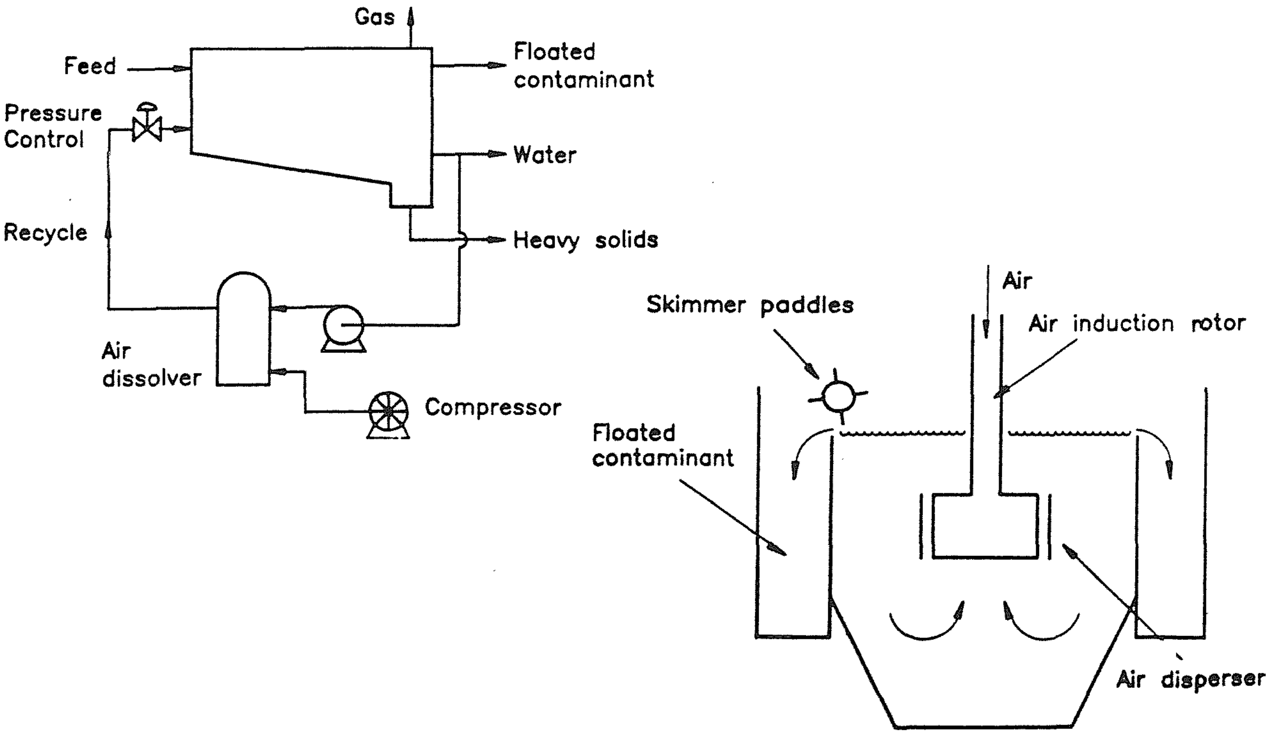

Figure 2.4 Gas flotation units, a) dissolved gas, b) induced air [Miller J.H., Offshore separation processes, Report prepared for LUT, Dept. of Chem. Eng., 1992]

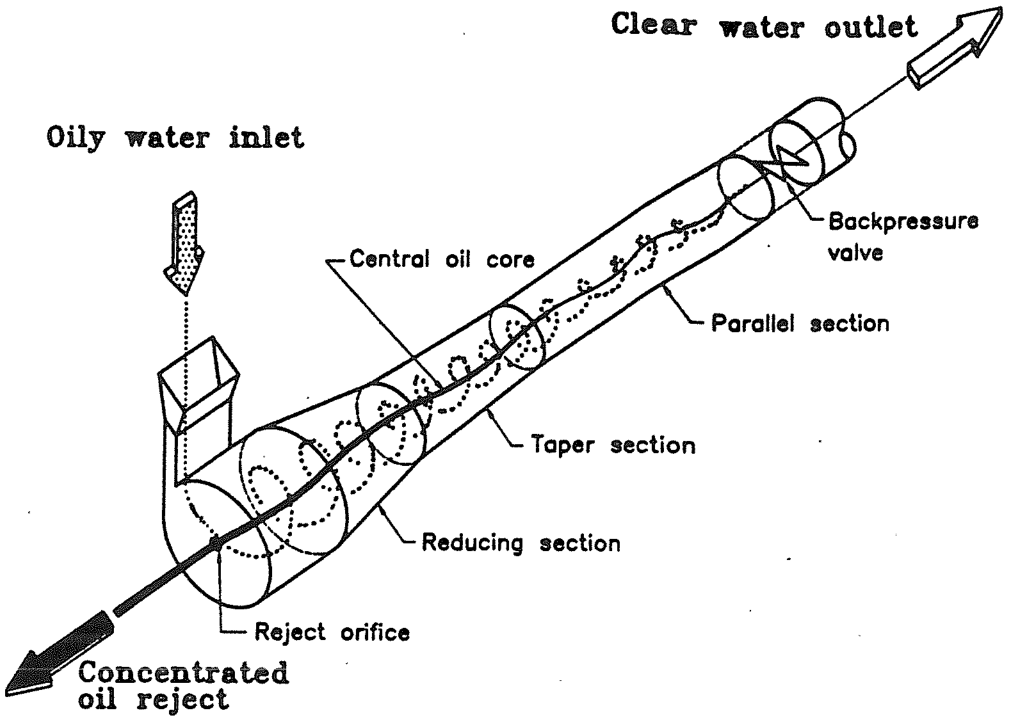

Figure 2.5 Schematic of a hydrocyclone unit [Vortoil Separation Systems technical manual, 1991]

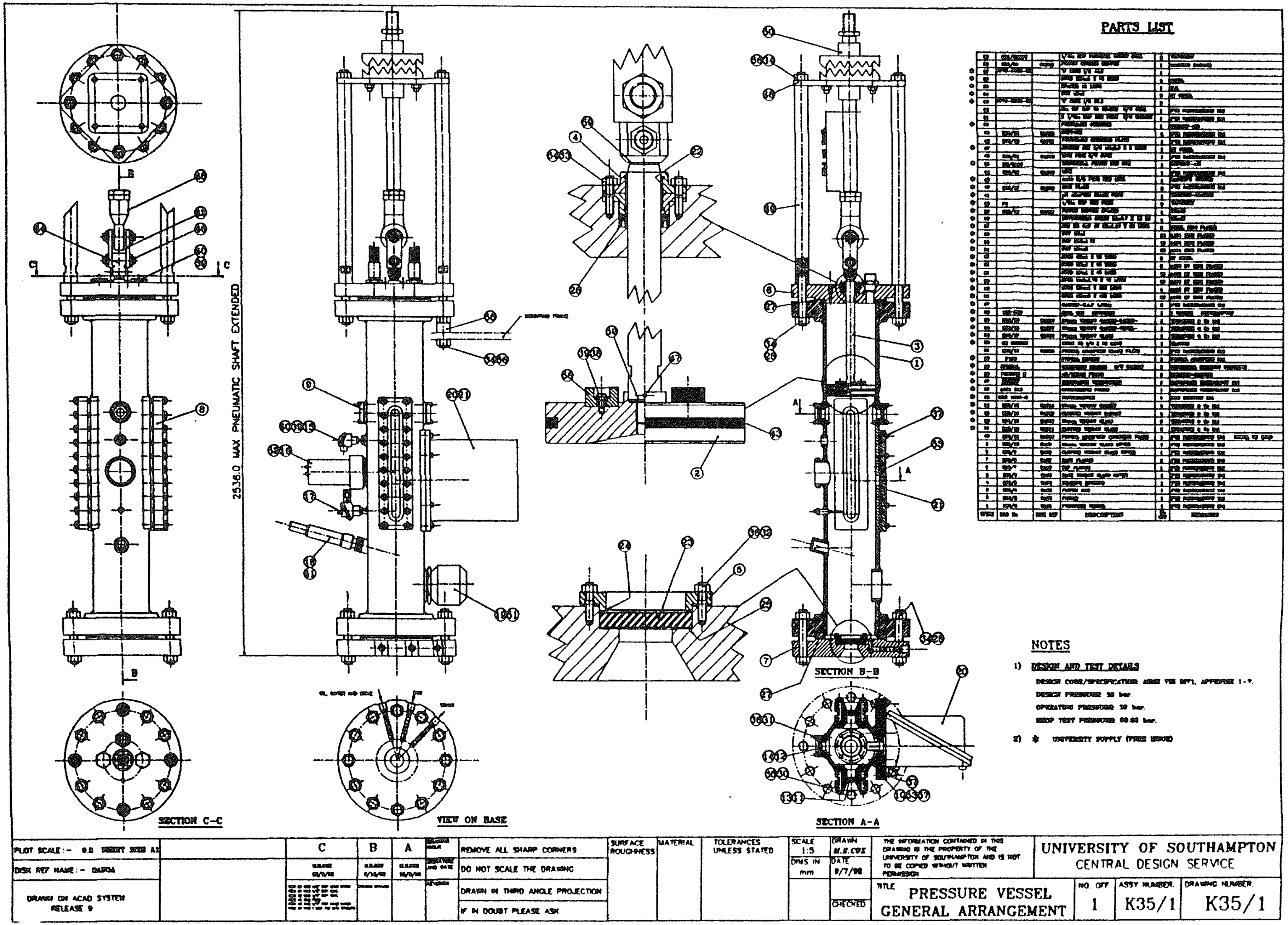

Figure 4.1 General arrangement of the pressure vessel

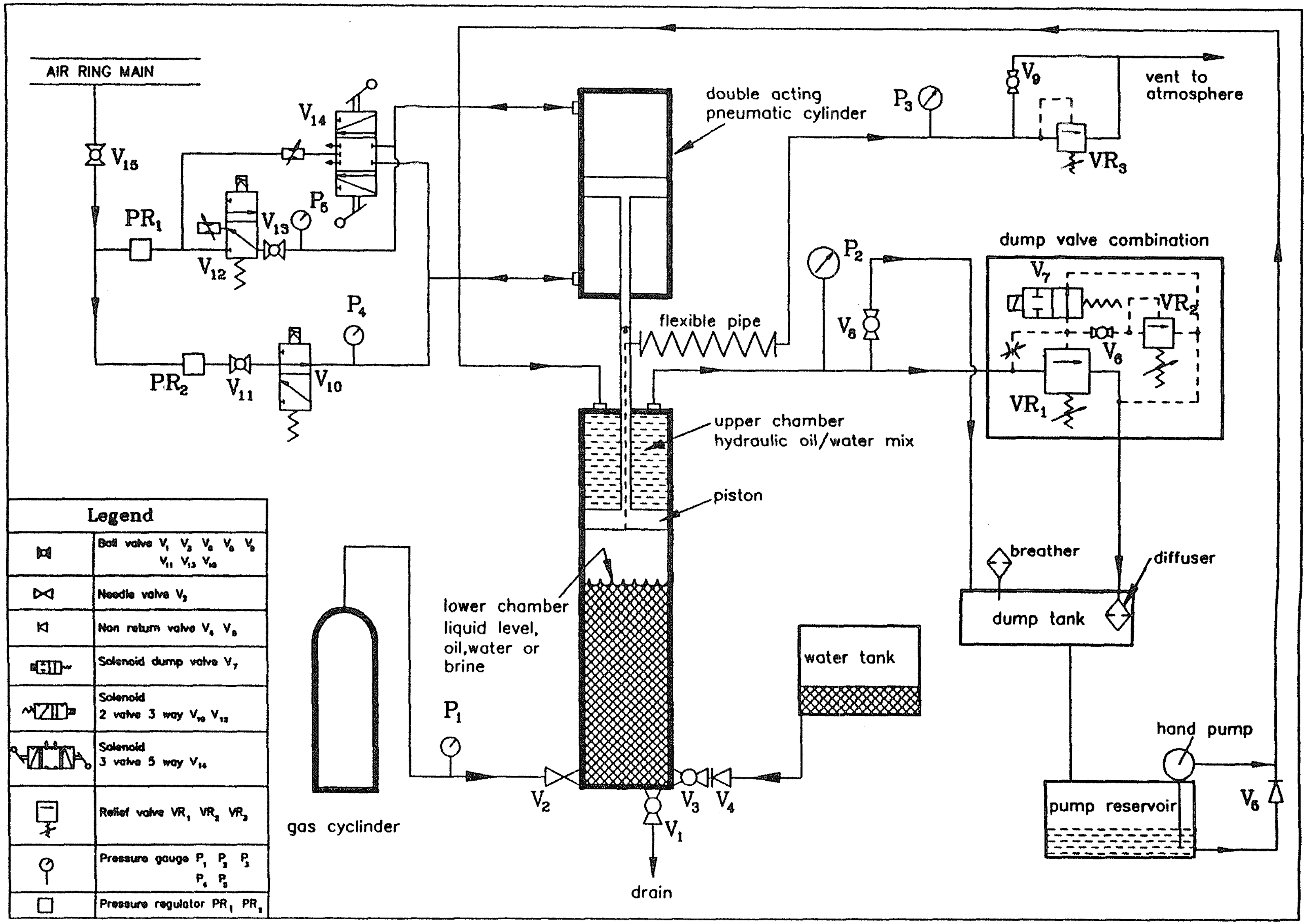

Figure 4.2 Systems set up of the rig facility

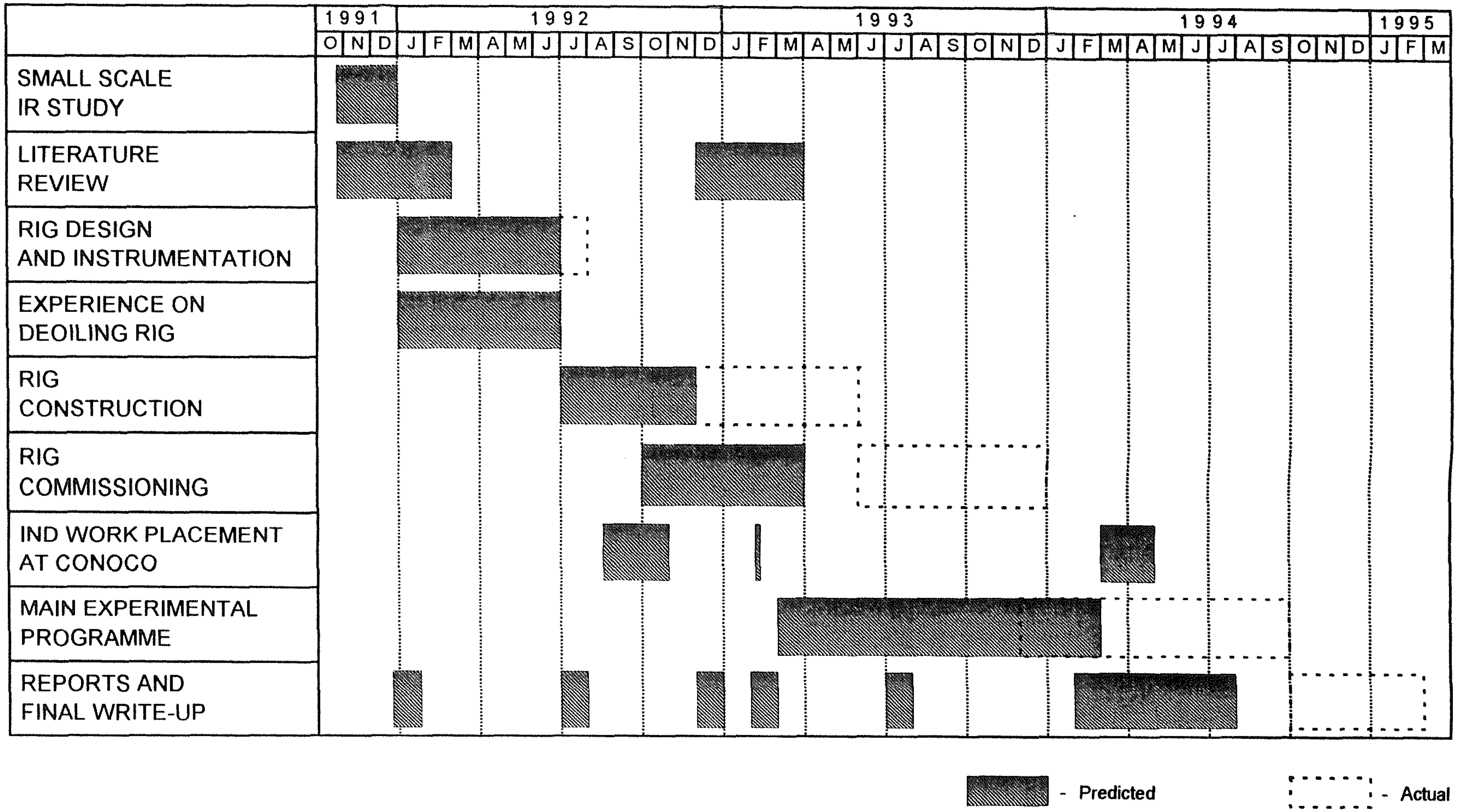

Figure 4.3 Bar chart representing the intended and actual schedule of the programme

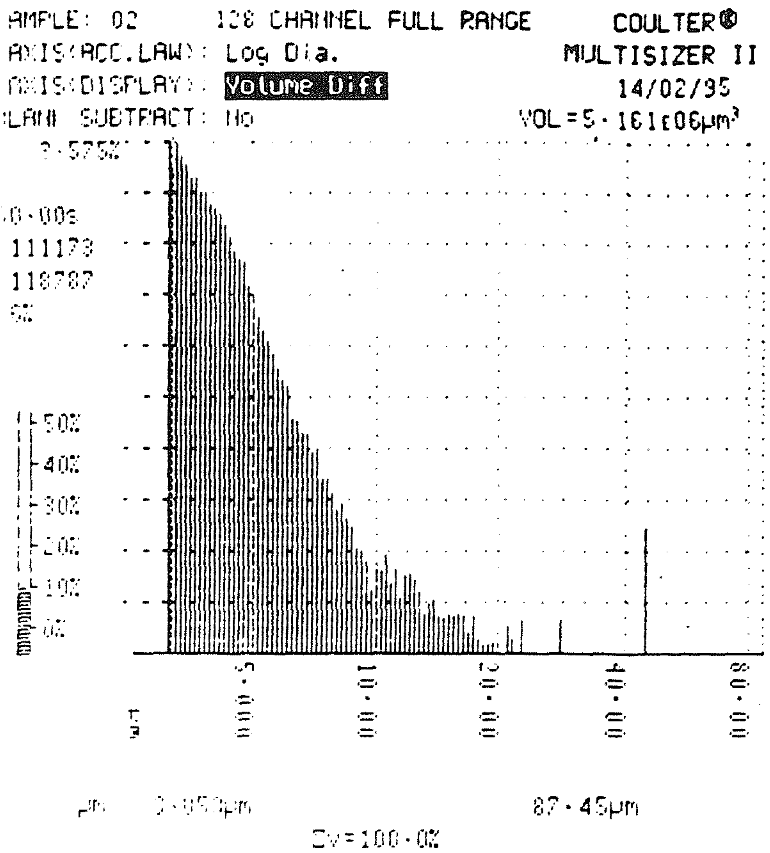

Figure 5.1 Coulter counter size distribution spectrum for 5μm uni-sized silica flour particles

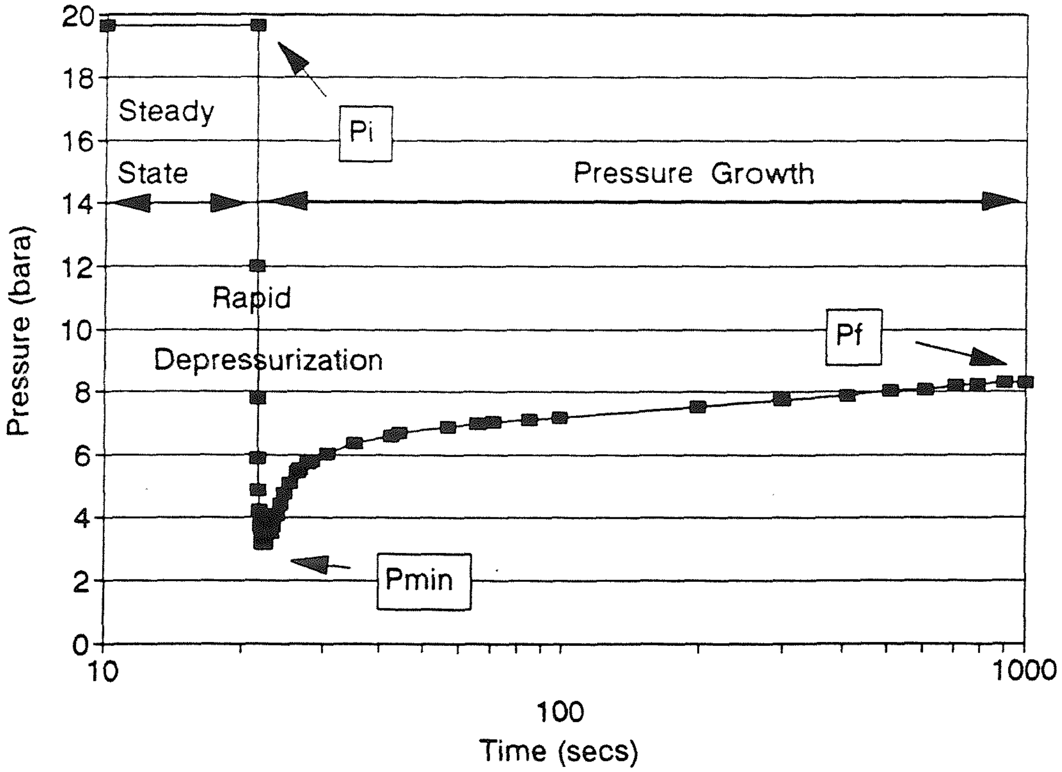

Figure 5.2 Typical pressure-time history obtained for the depressurization and pressure recovery process for a CO_2 in water system, 100 l/min, 30 mins, 20.6°C, initial saturation pressure, 20 bara

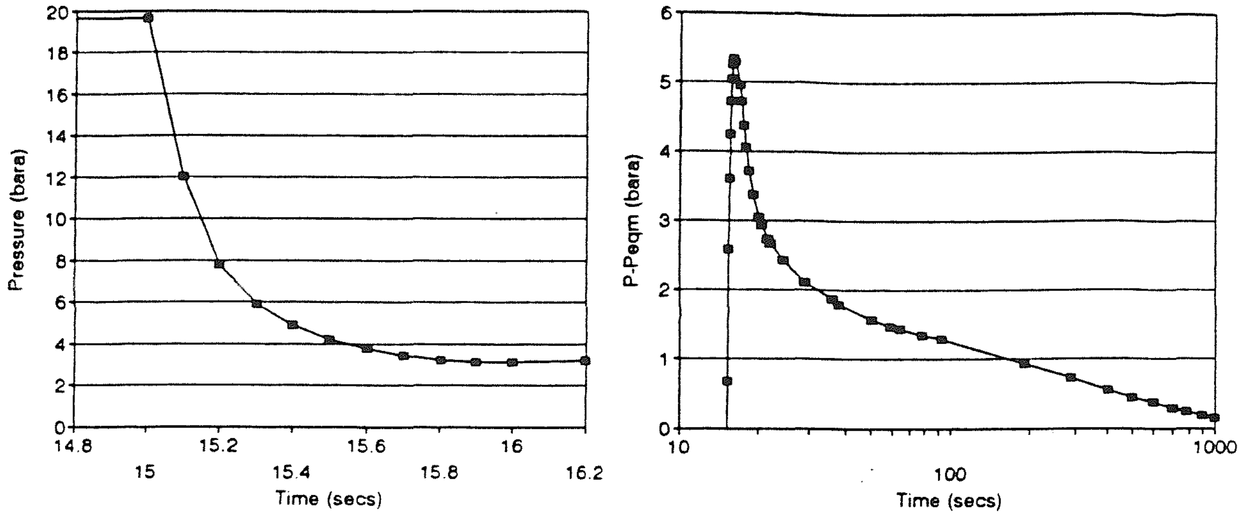

Figure 5.3 Typical a) pressure time history of the rapid depressurization process and b) p-p_{eqm} versus time plot during the approach to equilibrium for a CO_2 in water system, 100 l/min, 30 mins, 20.6°C, initial saturation pressure, 20 bara

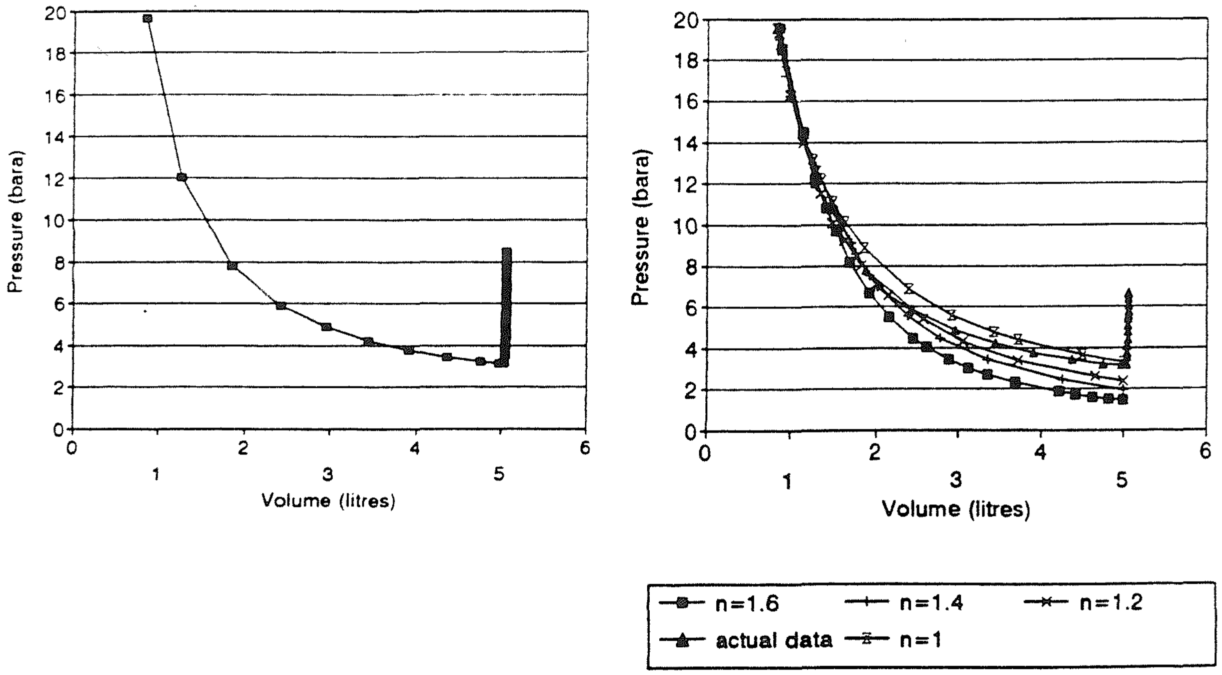

Figure 5.4 Typical a) pressure-volume plot obtained for the rapid depressurization process and b) pressure-volume plots for various values of the index, n, for a CO_2 in water system, 100 l/min, 30 mins, 20.6°C, initial saturation pressure, 20 bara

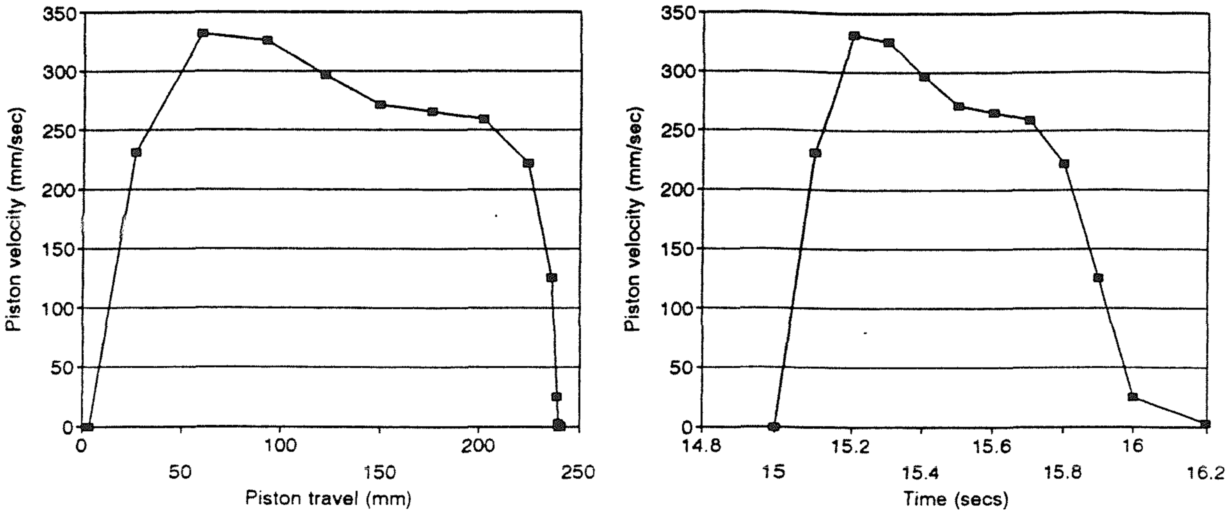

Figure 5.5 Typical a) piston velocity-distance plot and b) piston velocity-time plot obtained during rapid depressurization of a CO_2 in water system, 100 l/min, 30 mins, 20.6°C, initial saturation pressure, 20 bara

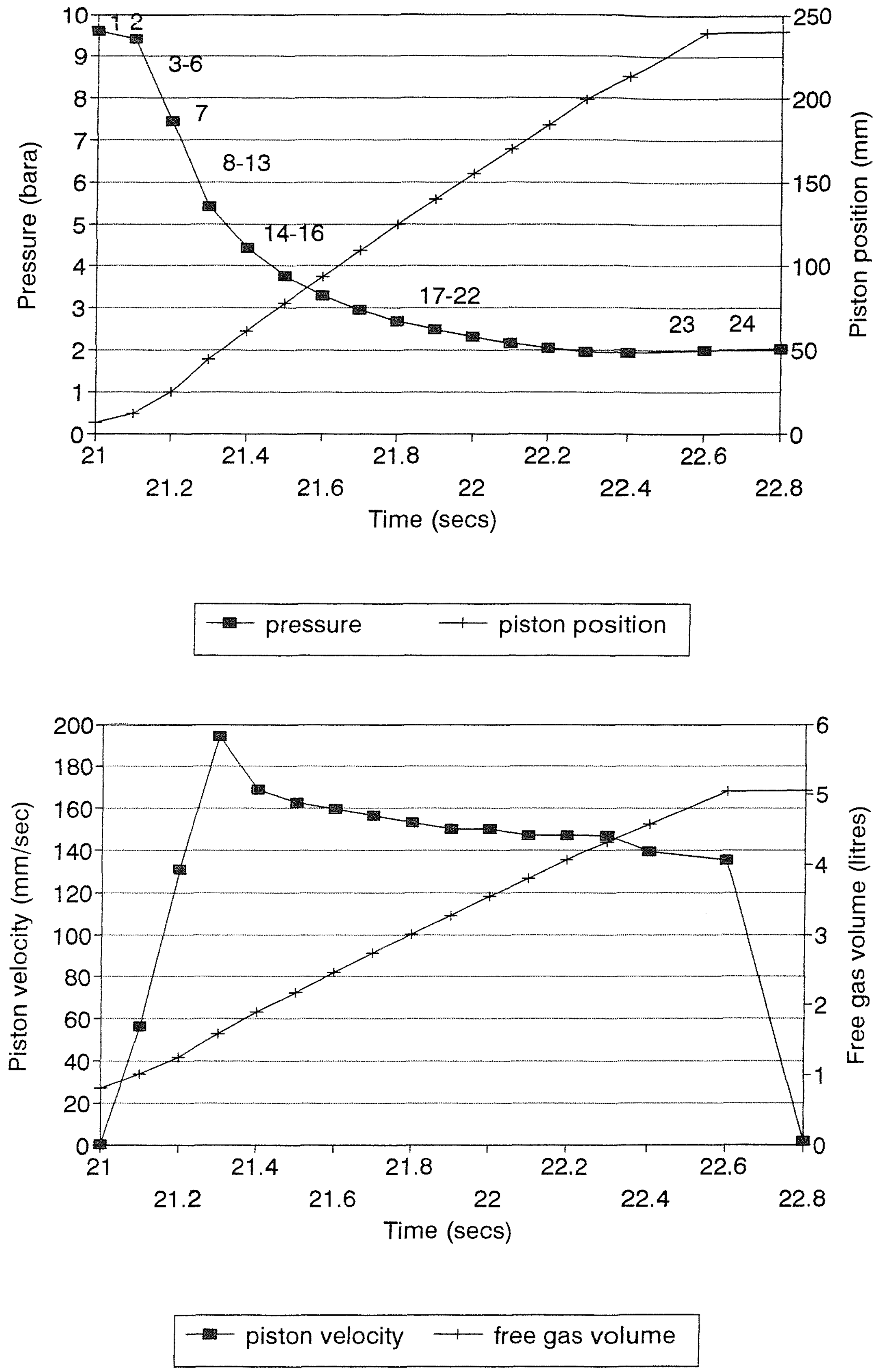

Figure 6.1 Rapid depressurization of a CO_2 in water system, 100 l/min, 15 mins, 18.6°C, a) pressure-piston position-time plot, b) piston velocity-free gas volume-time plot

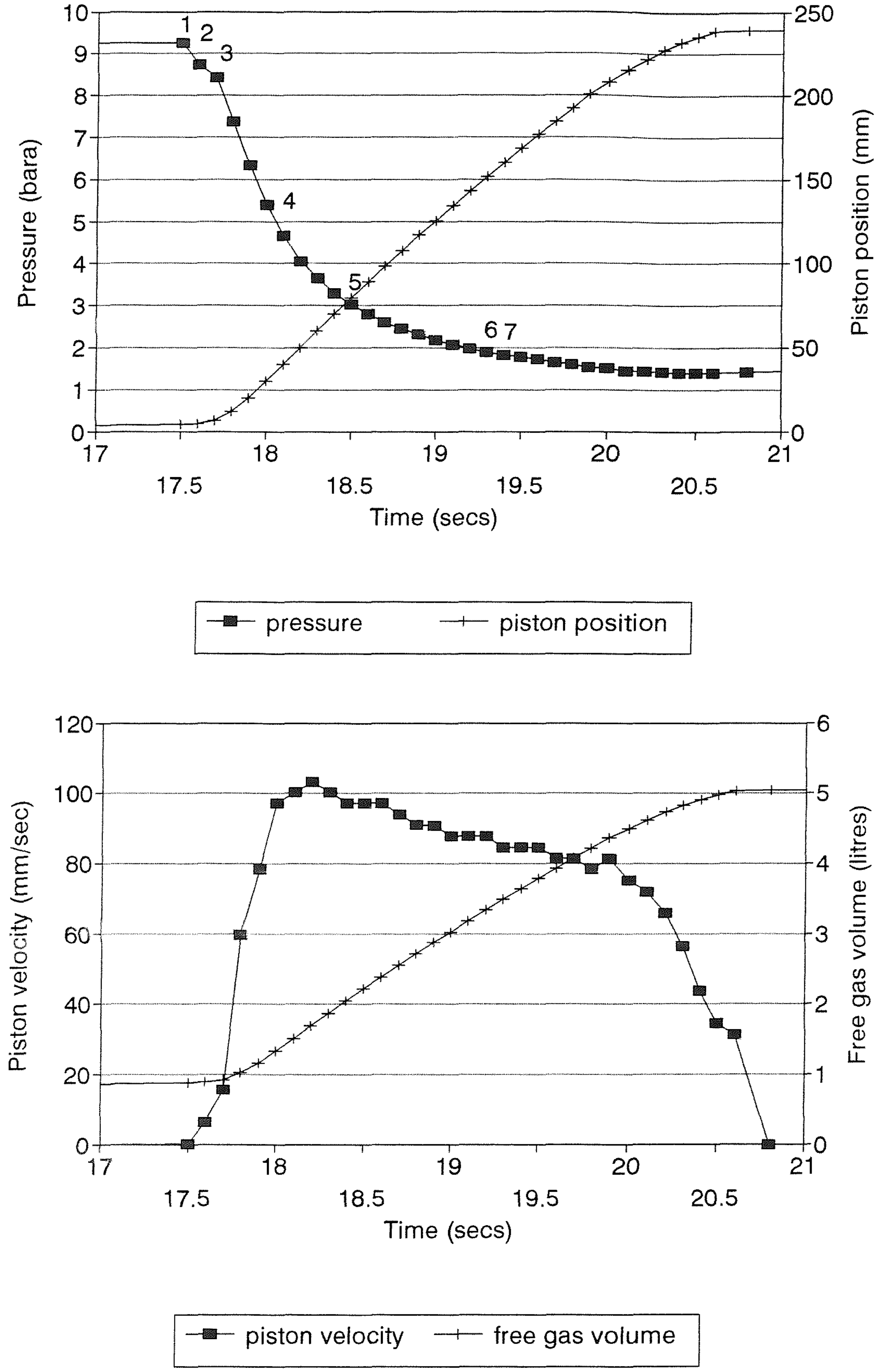

Figure 6.2 Rapid depressurization of a N_2 in water system, 100 l/min, 15 mins, 17.8°C, a) pressure-piston position-time plot, b) piston velocity-free gas volume-time plot

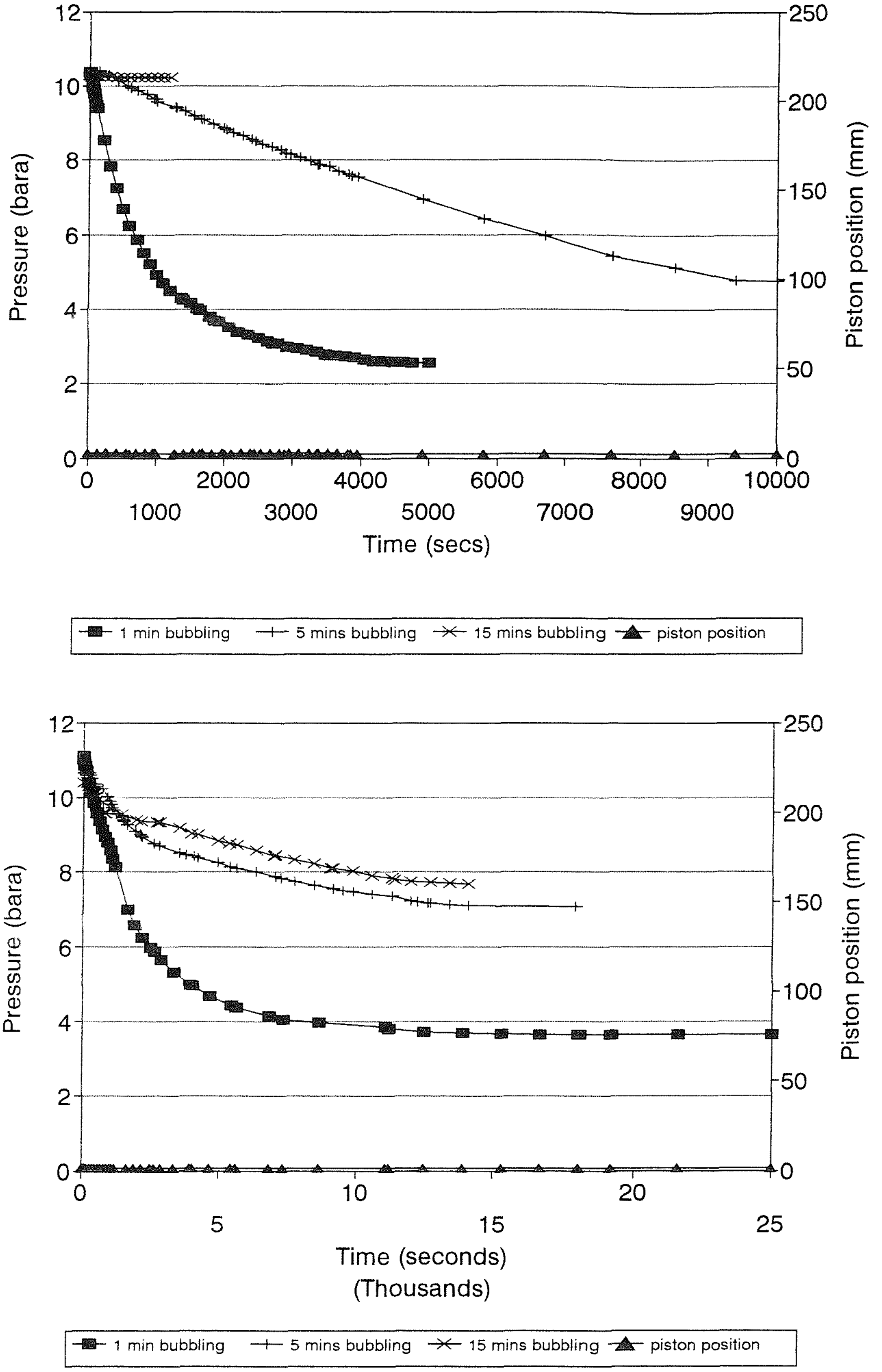

Figure 6.3 Pressure-time histories recorded for partly saturated systems during isolation; no depressurization, 100 l/min, 15 mins, 17°C ±2°, a) Ar in water, b) CO_2 in water

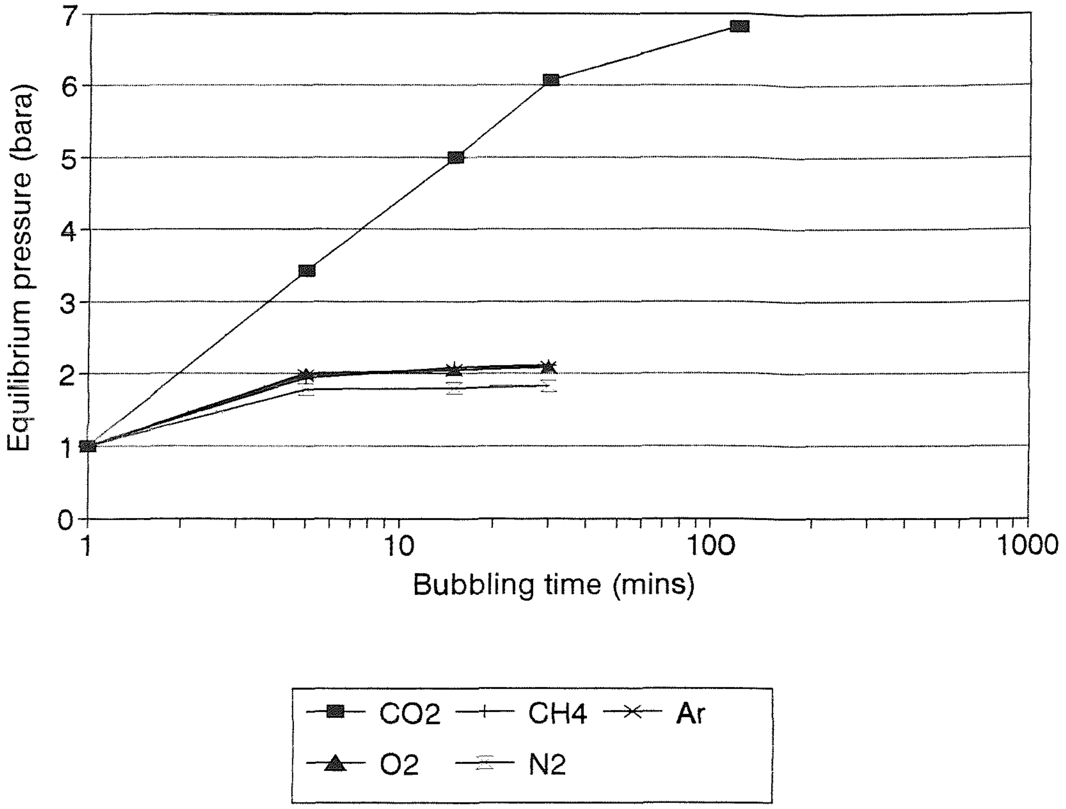

Figure 6.4 Final equilibrium pressures obtained after depressurization, as a function of bubbling time for several gases in water, 100 l/min, 15 mins, 17°C ±2°

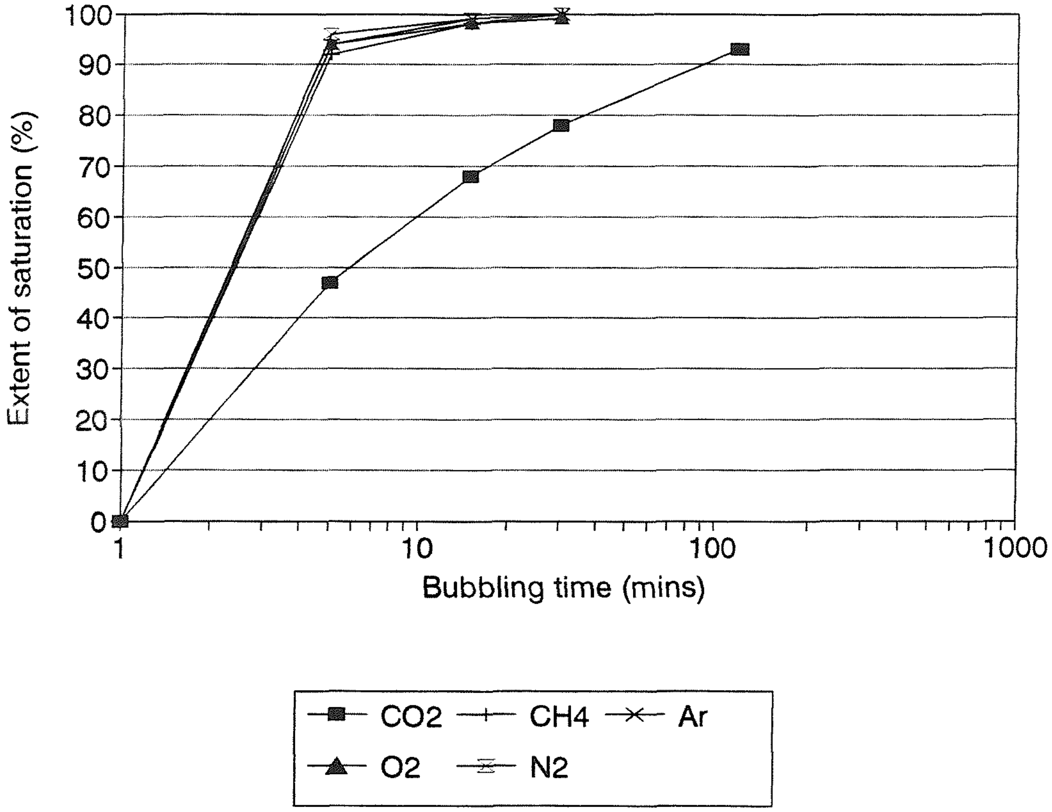

Figure 6.5 Predicted degree of saturation as a function of bubbling time for several gases in water, 100 l/min, 15 mins, 17°C ±2°

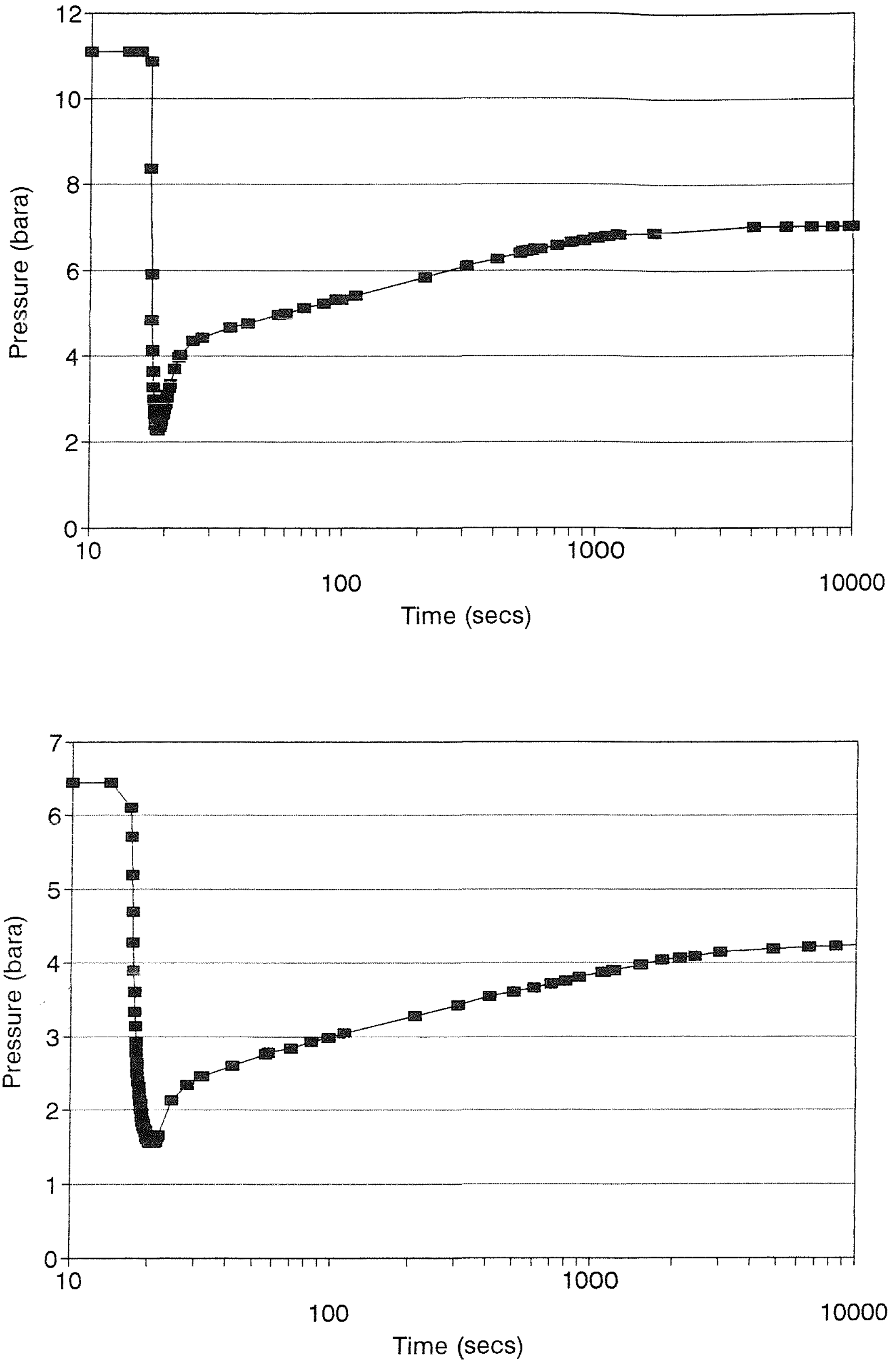

Figure 6.6 Pressure recovery-time plots for a CO_2 in water system, a) 100 l/min, 120 mins, 18.3°C, b) 100 l/min, 60 mins, 17.8°C, initial saturation pressure, 5 barg

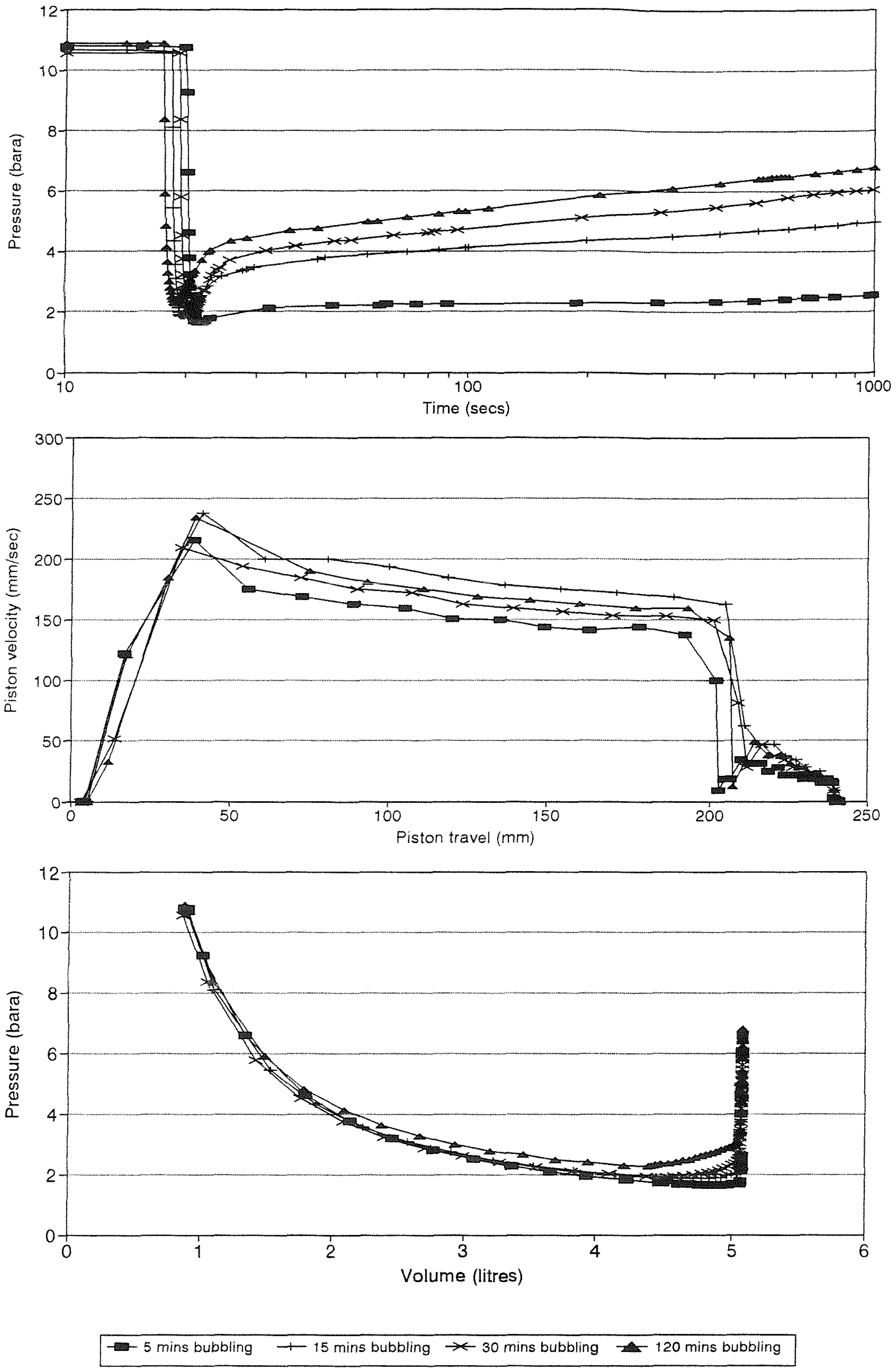

Figure 6.7 Effect of increasing the bubbling time for a CO_2 in water system, 100 l/min, 15 mins, 20°C ±1°, a) pressure-time plot, b) piston velocity-travel plot, c) pressure-volume plot

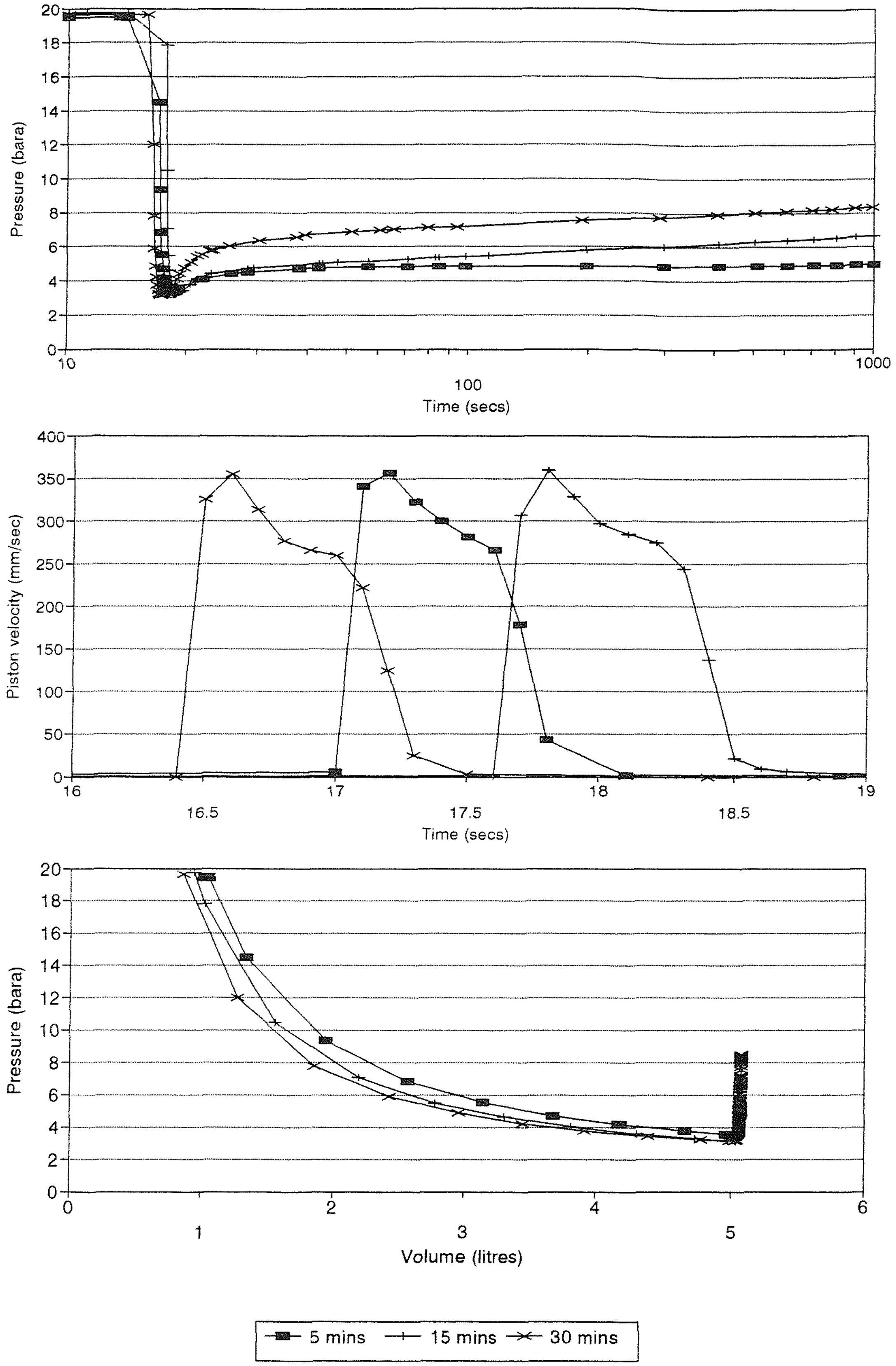

Figure 6.8 Effect of increasing the bubbling time for a CO_2 in water system, 100 l/min, 15 mins, 20.8°C ±0.2°, initial saturation pressure 20 bara, a) pressure-time plot, b) piston velocity-time plot, c) pressure-volume plot

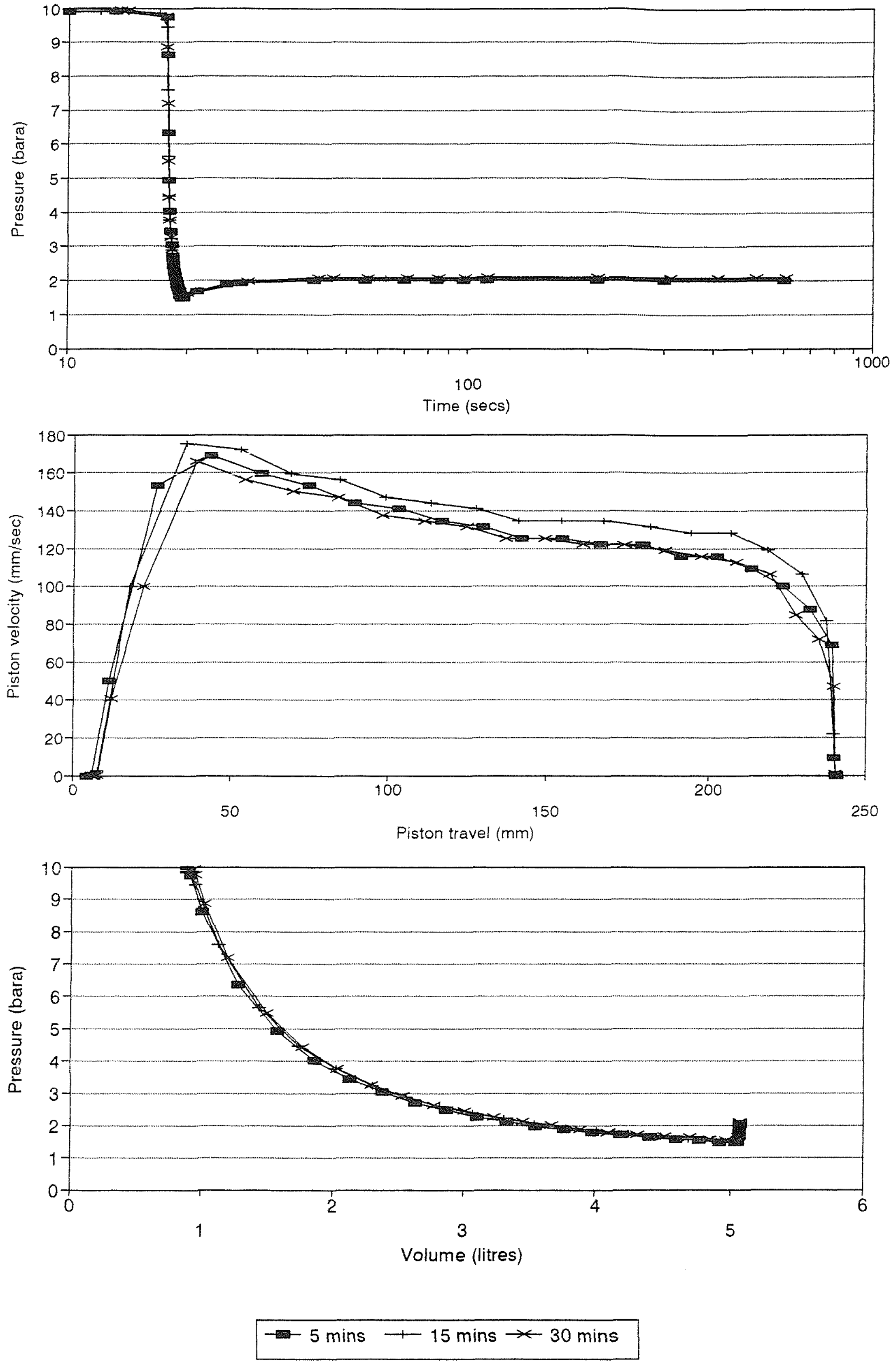

Figure 6.9 Effect of increasing the bubbling time for an O_2 in water system, 100 l/min, 15 mins, 22.7°C ±0.3°, a) pressure-time plot, b) piston velocity-travel plot, c) pressure-volume plot

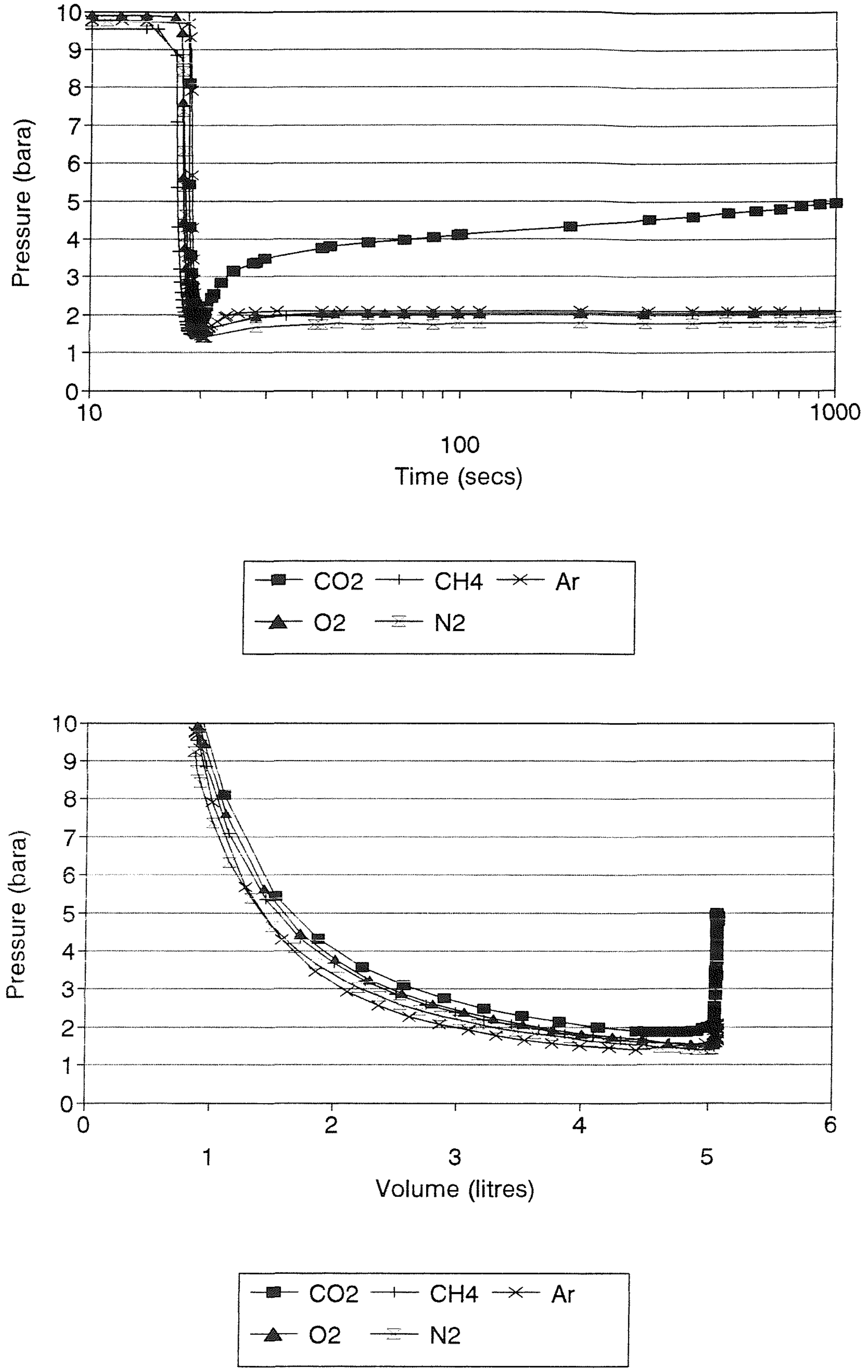

Figure 6.10 Comparison of gases in water, 100 l/min, 15 mins, 18°C ±2°, a) pressure-time plot, b) pressure-volume plot

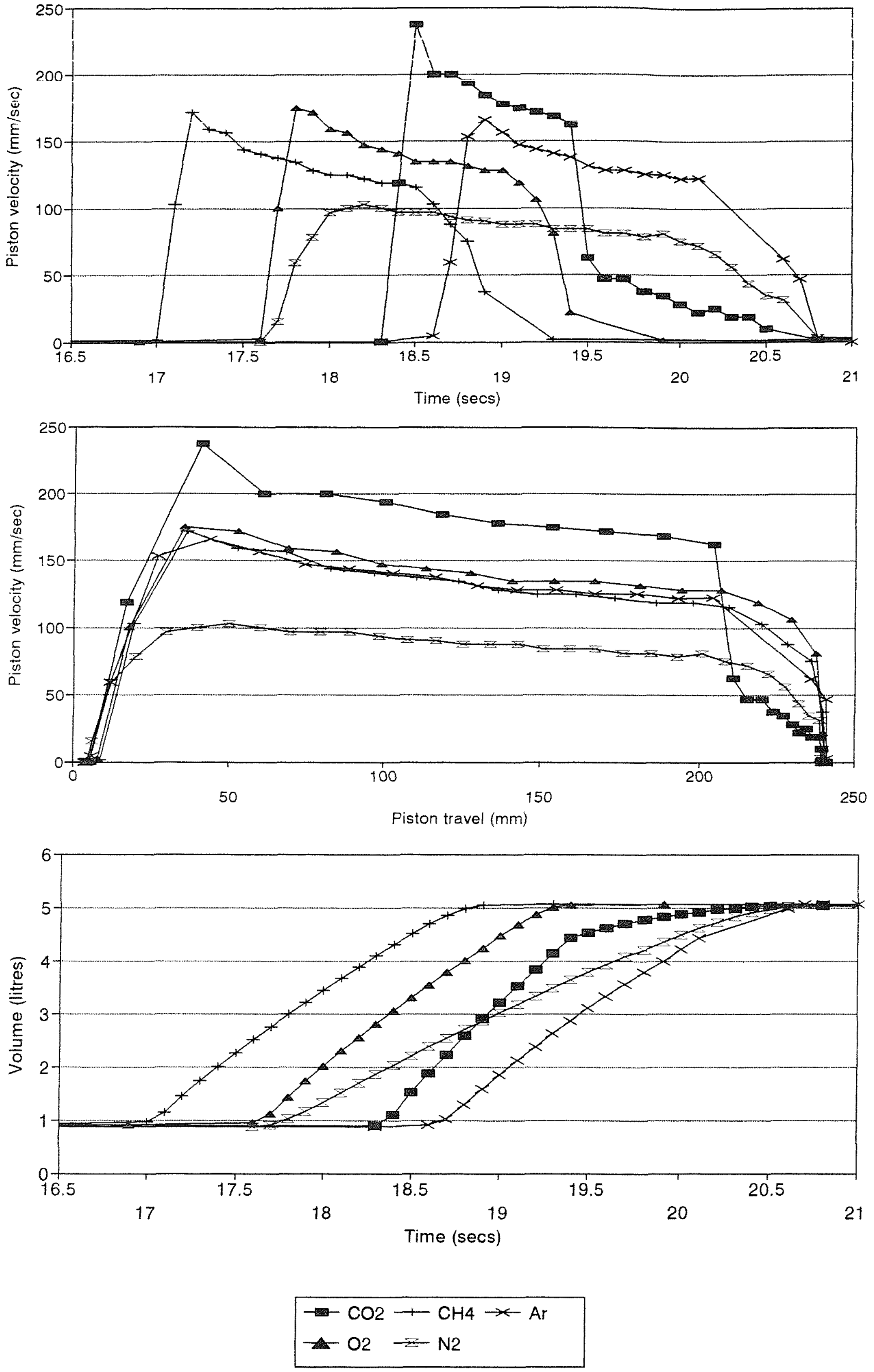

Figure 6.10 cont.. c) piston velocity-time plot, d) piston velocity-travel plot, e) volume-time plot

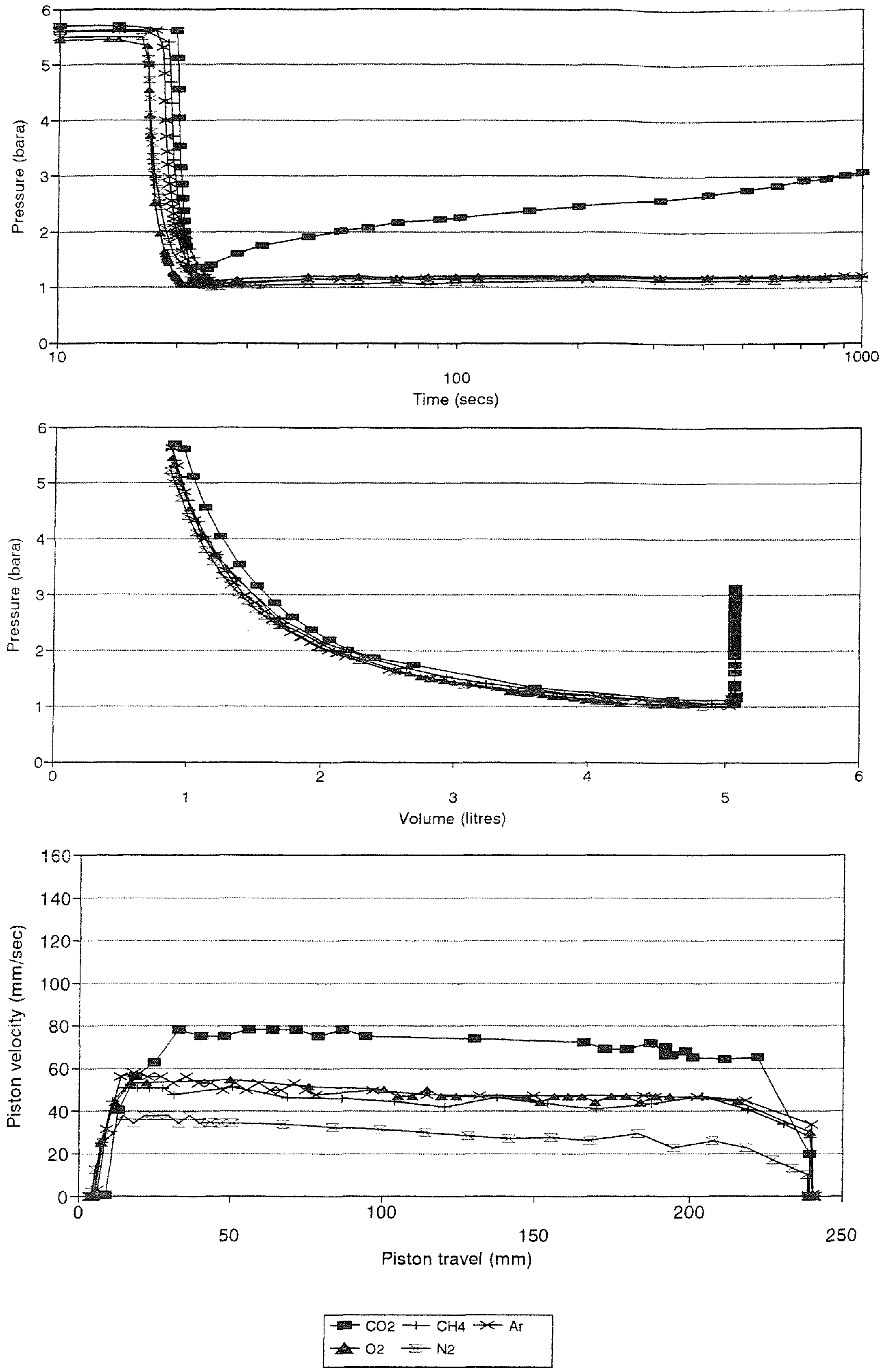

Figure 6.11 Comparison of gases in water, 100 l/min, 15 mins, 19°C ±2°, initial saturation pressure 5 bara, a) pressure-time plot, b) pressure-volume plot, c) piston velocity-travel plot

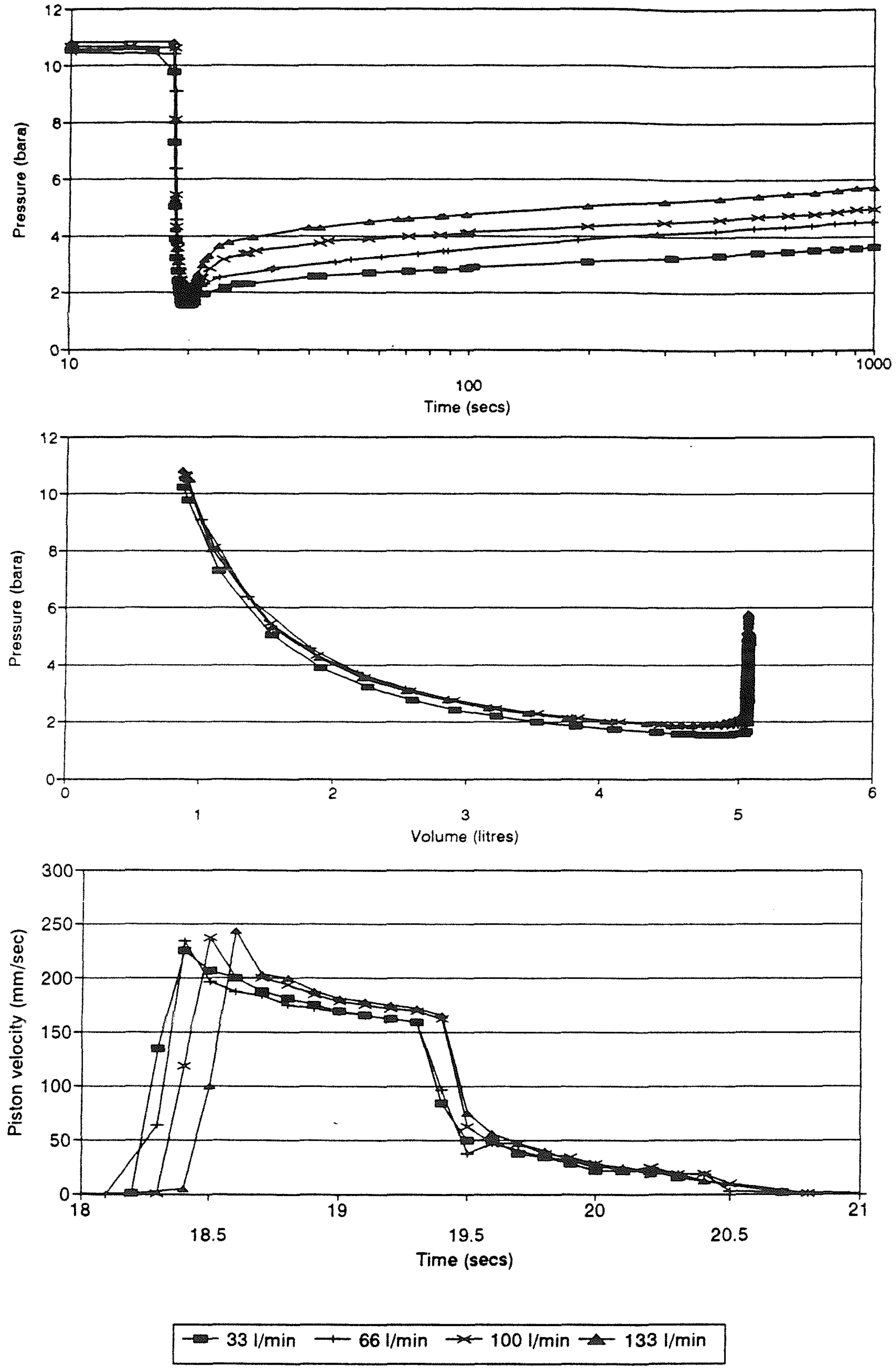

Figure 6.12 Effect of gas flow rate during saturation of water using CO_2, 15 mins, 16.4°C ±0.4°, a) pressure-time plot, b) pressure-volume plot, c) piston velocity-time plot

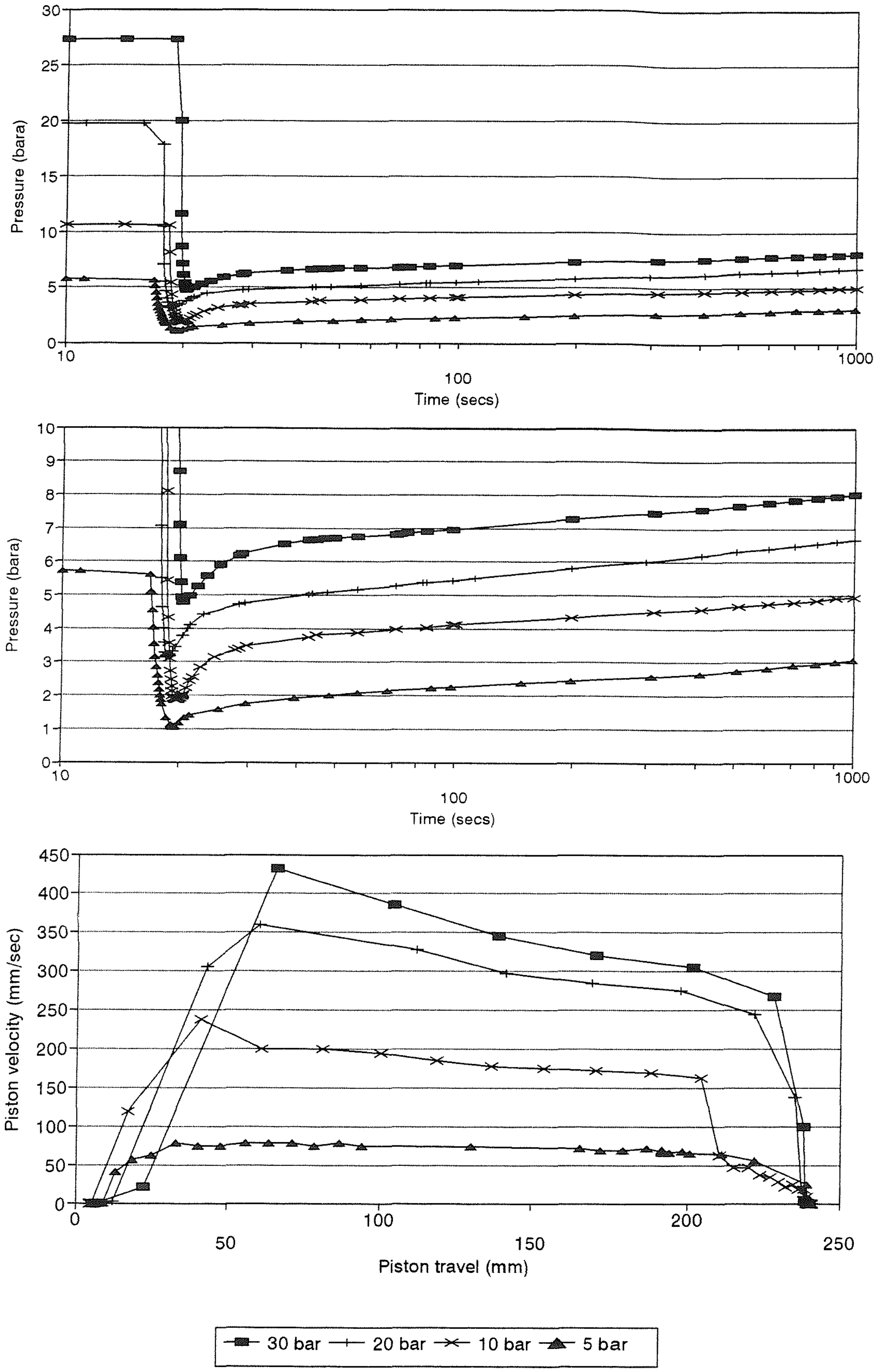

Figure 6.13 Effect of initial saturation pressure on the CO_2/water system, 100 l/min, 15 mins, 18°C ±2°, a and b) pressure-time plot, c) piston velocity-travel plot

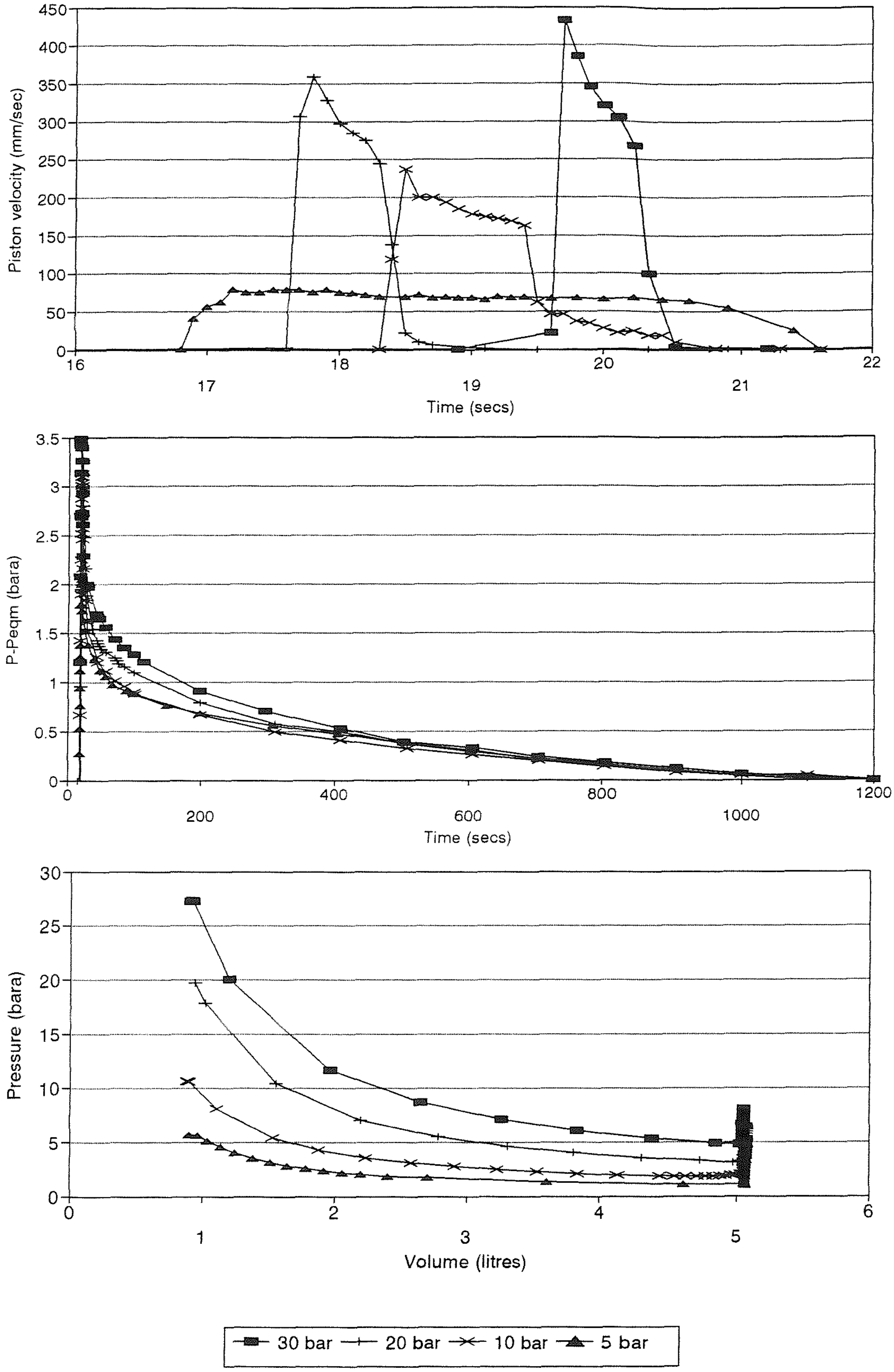

Figure 6.13 cont.. d) piston velocity-time plot, e) p-p_{eqm}-time plot, f) pressure-volume plot

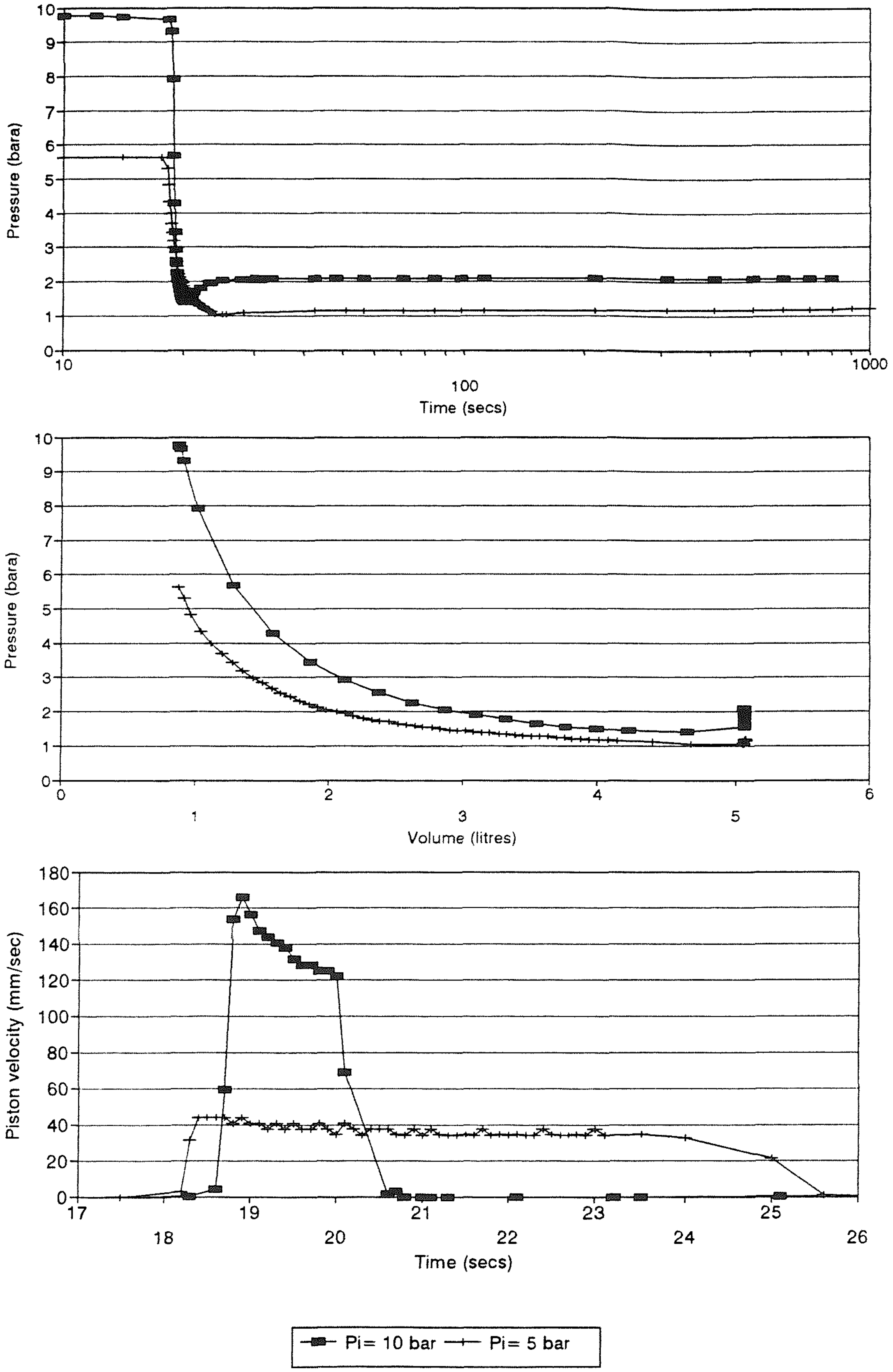

Figure 6.14 Effect of initial saturation pressure on the Ar/water system, 100 l/min, 15 mins, 22.7°C, a) pressure-time plot, b) pressure-volume plot, c) velocity-time plot

See Figures 6.10 and 6.11 for comparable CH_4 data

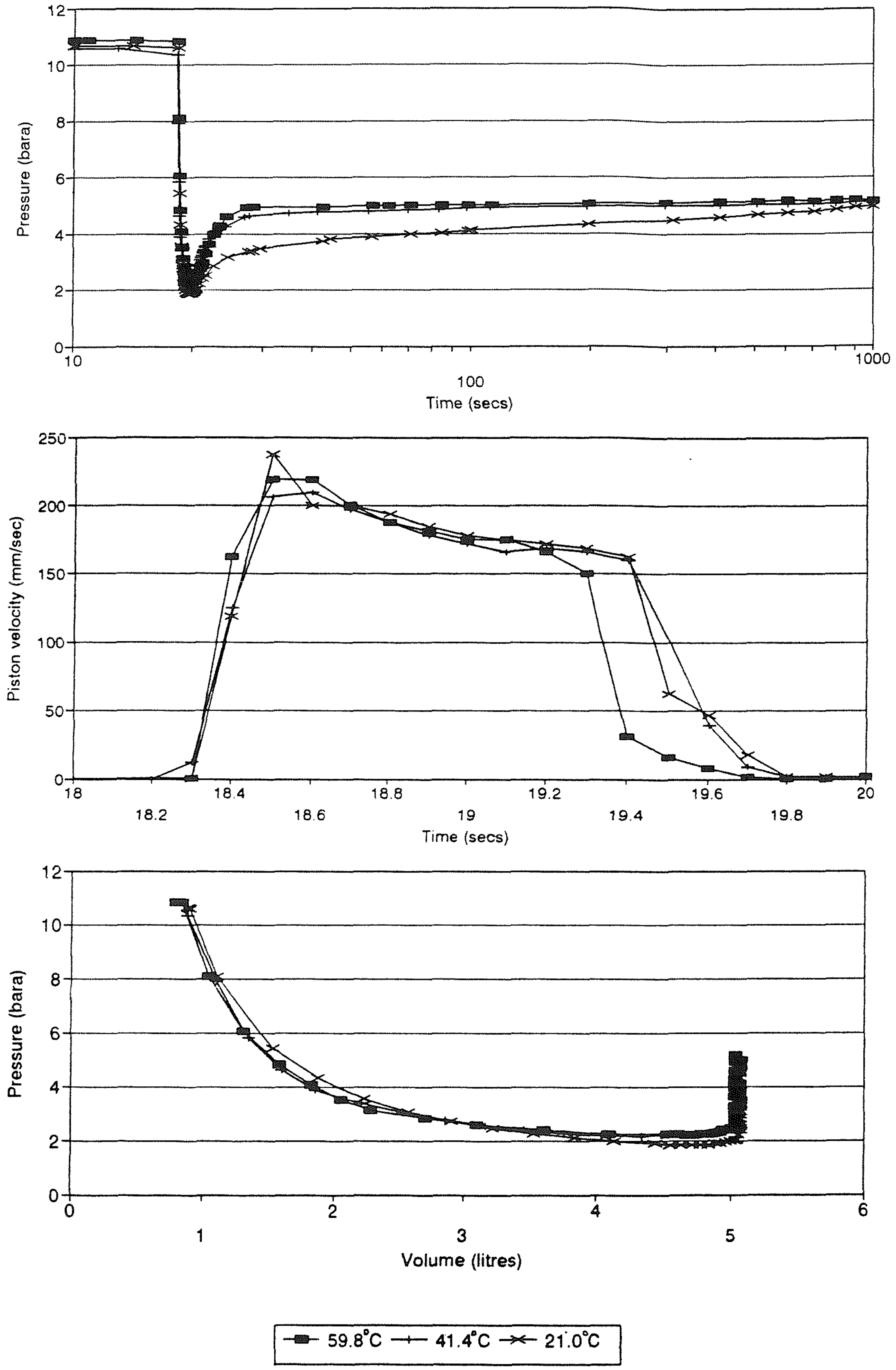

Figure 6.15 Effect of initial temperature on the rate of gas evolution in a CO_2/water system, 100 l/min, 15 mins, a) pressure-time plot, b) velocity-time plot, c) pressure-volume plot

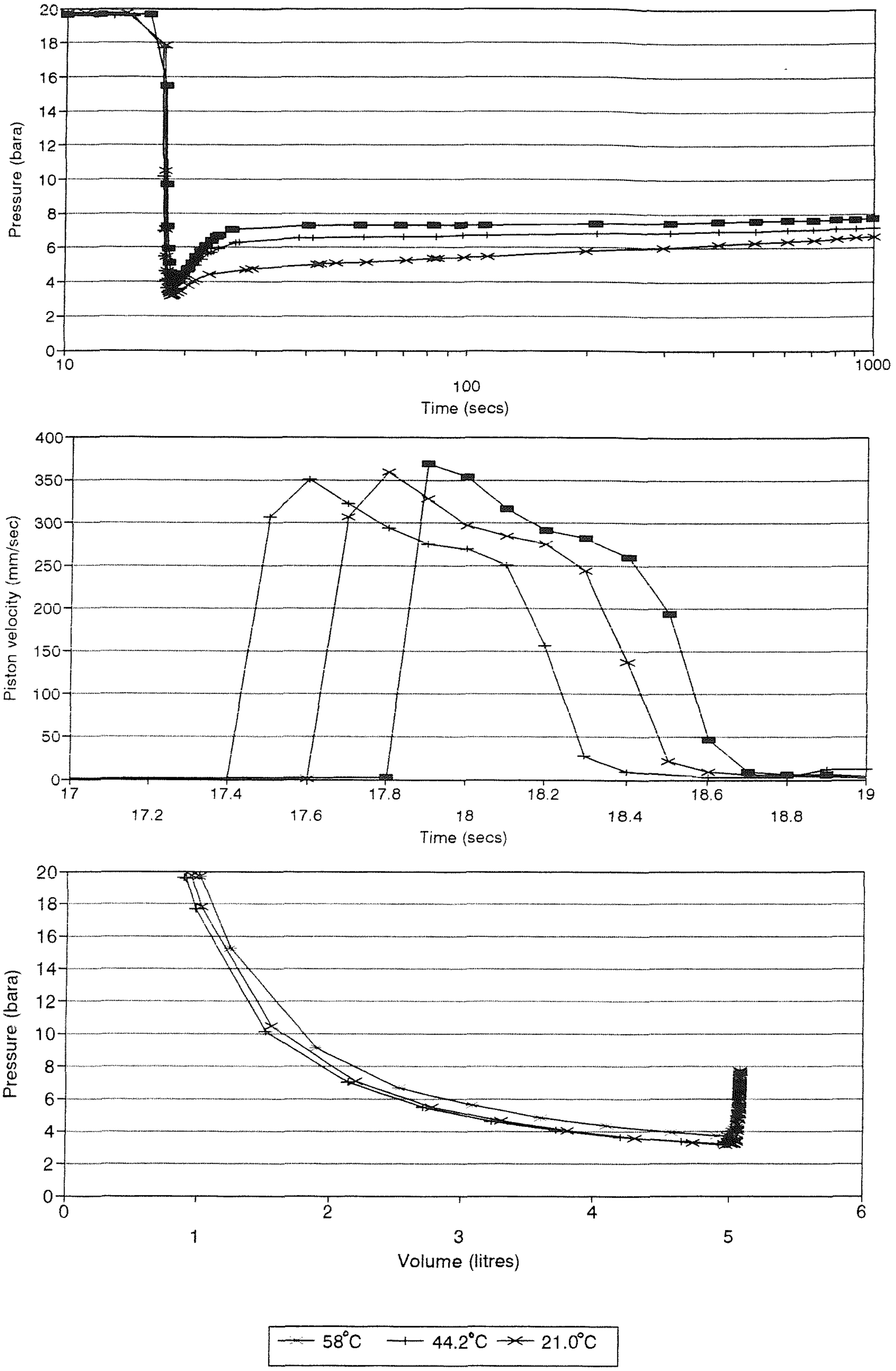

Figure 6.16 Effect of initial temperature on the rate of gas evolution in a CO_2/water system, 100 l/min, 15 mins, initial saturation pressure 20 bara, a) pressure-time plot, b) velocity-time plot, c) pressure-volume plot

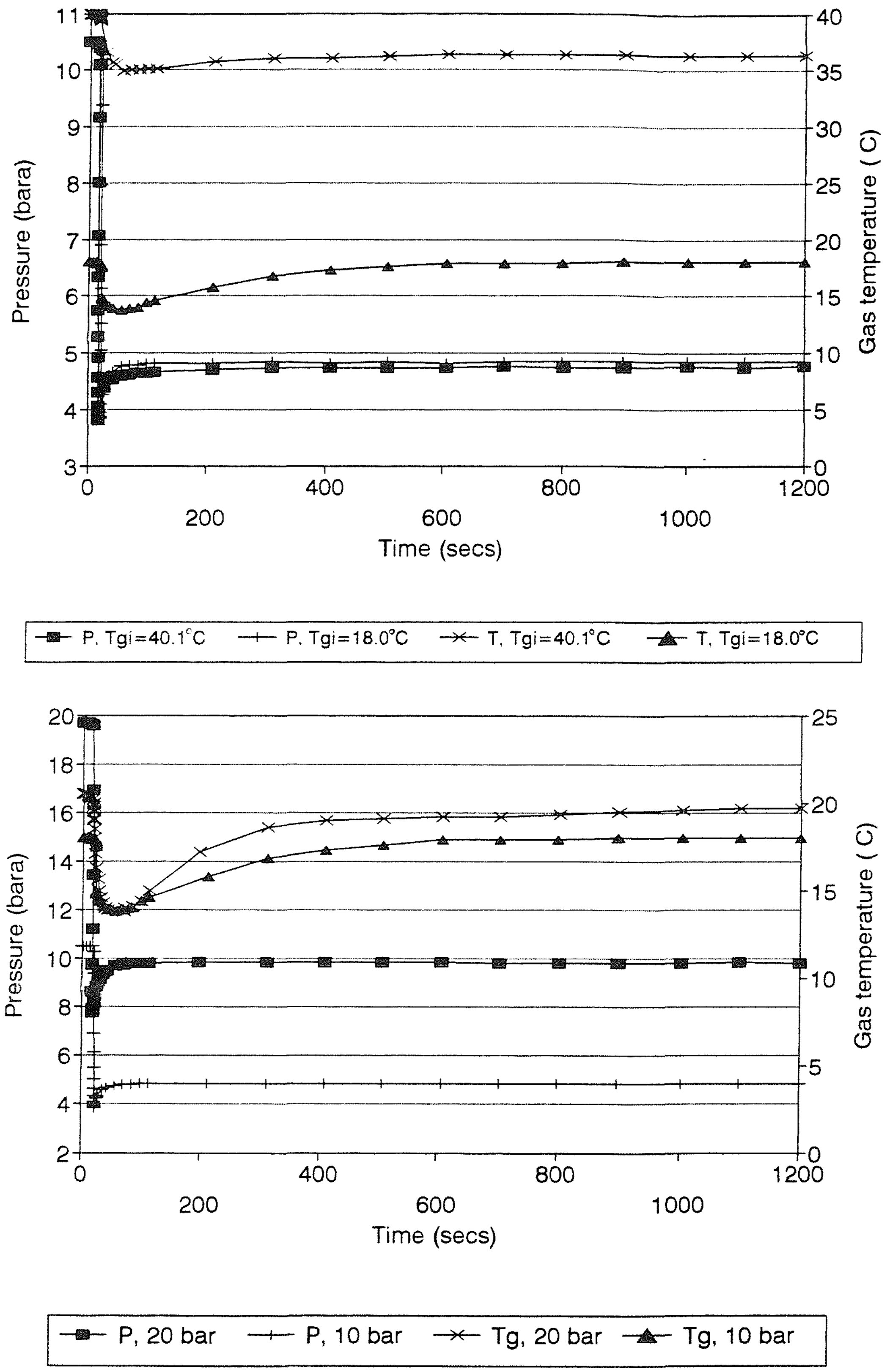

Figure 6.17 Pressure-temperature-time plots displaying the gas phase temperature recovery during and after depressurization in a CO_2 in water system, 100 l/min, 15 mins, from a) initial gas temperatures of 18° and 40°C, V_{gi} 3.6l, b) initial saturation pressures of 10 and 20 bara, V_{gi} 3.6l, T_{gi} 19°C ±1°

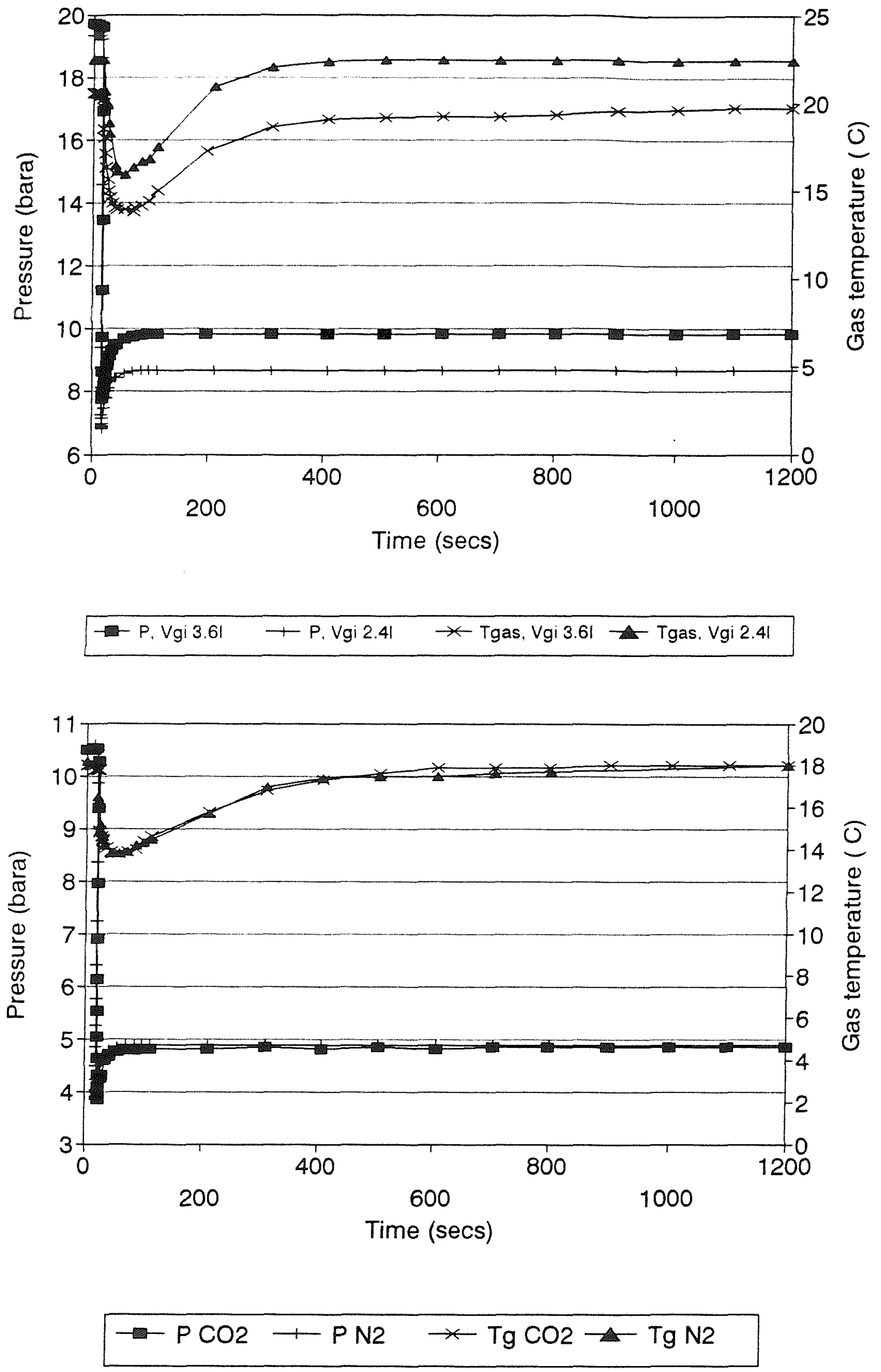

Figure 6.17 cont.. c) initial free gas volumes of 2.4 and 3.6 litres, T_{gi} 21.5°C ±1°, d) from a CO_2 and N_2 system, V_{gi} 3.6l, T_{gi} 18.1°C ±0.1°

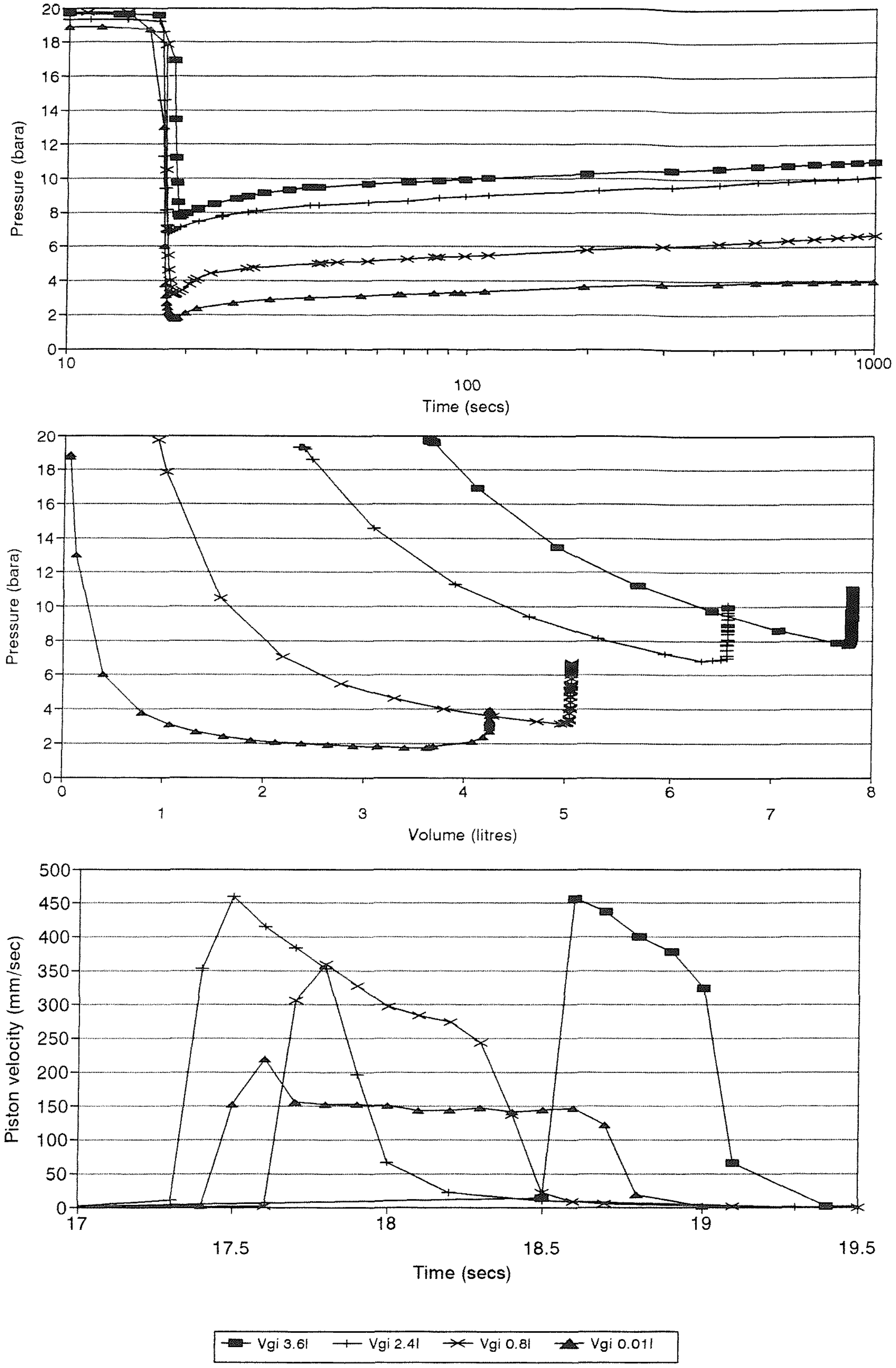

Figure 6.18 Effect of initial free gas volume on a CO_2/water system, 100 l/min, 15 mins, 21.5°C ±1°, initial saturation pressure 20 bara, a) pressure-time, b) pressure-volume plot, c) velocity-time plot

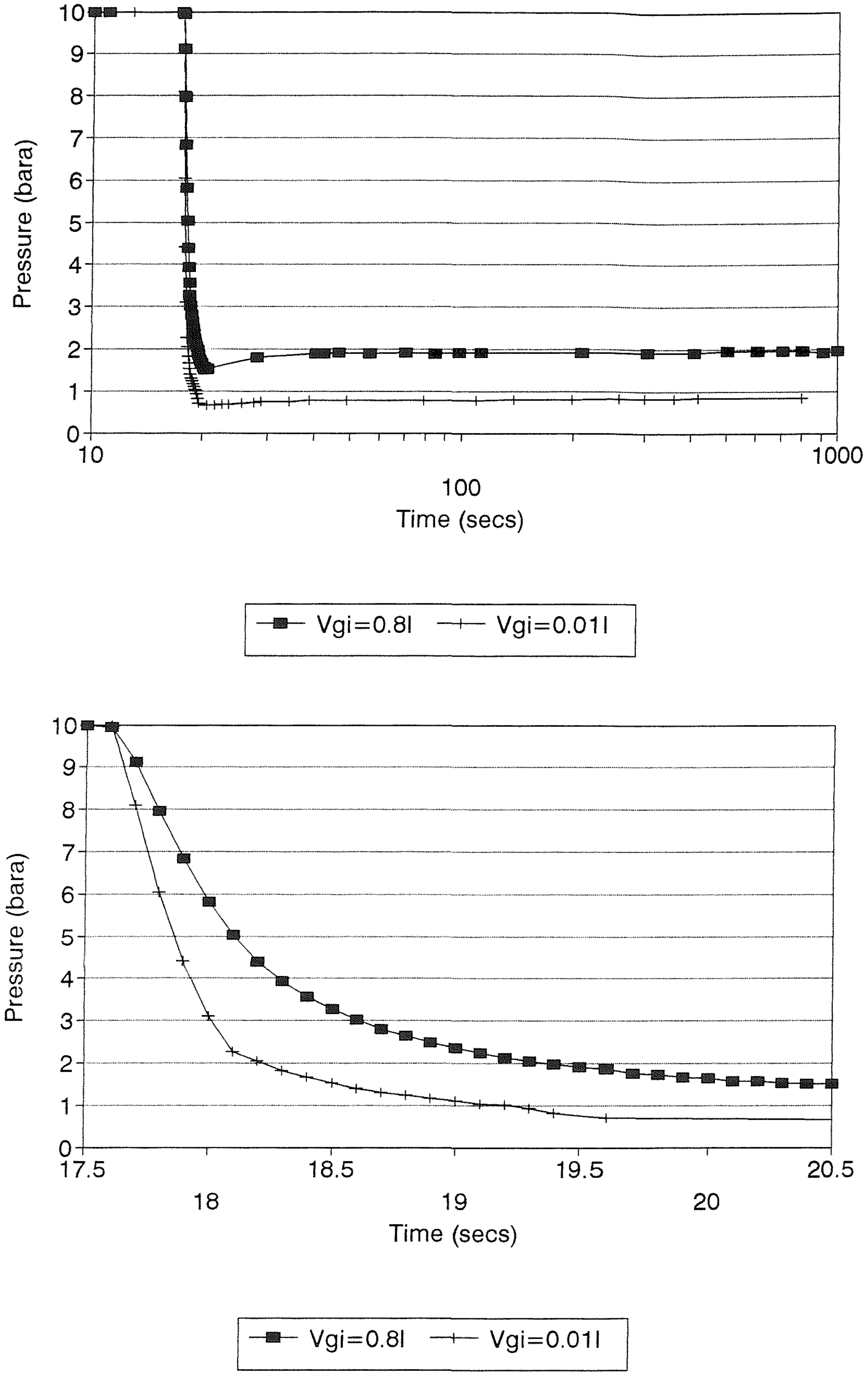

Figure 6.19 Effect of initial free gas volume on a N_2/water system, 100 l/min, 15 mins, 6.8°C ±0.4°, a and b) pressure-time

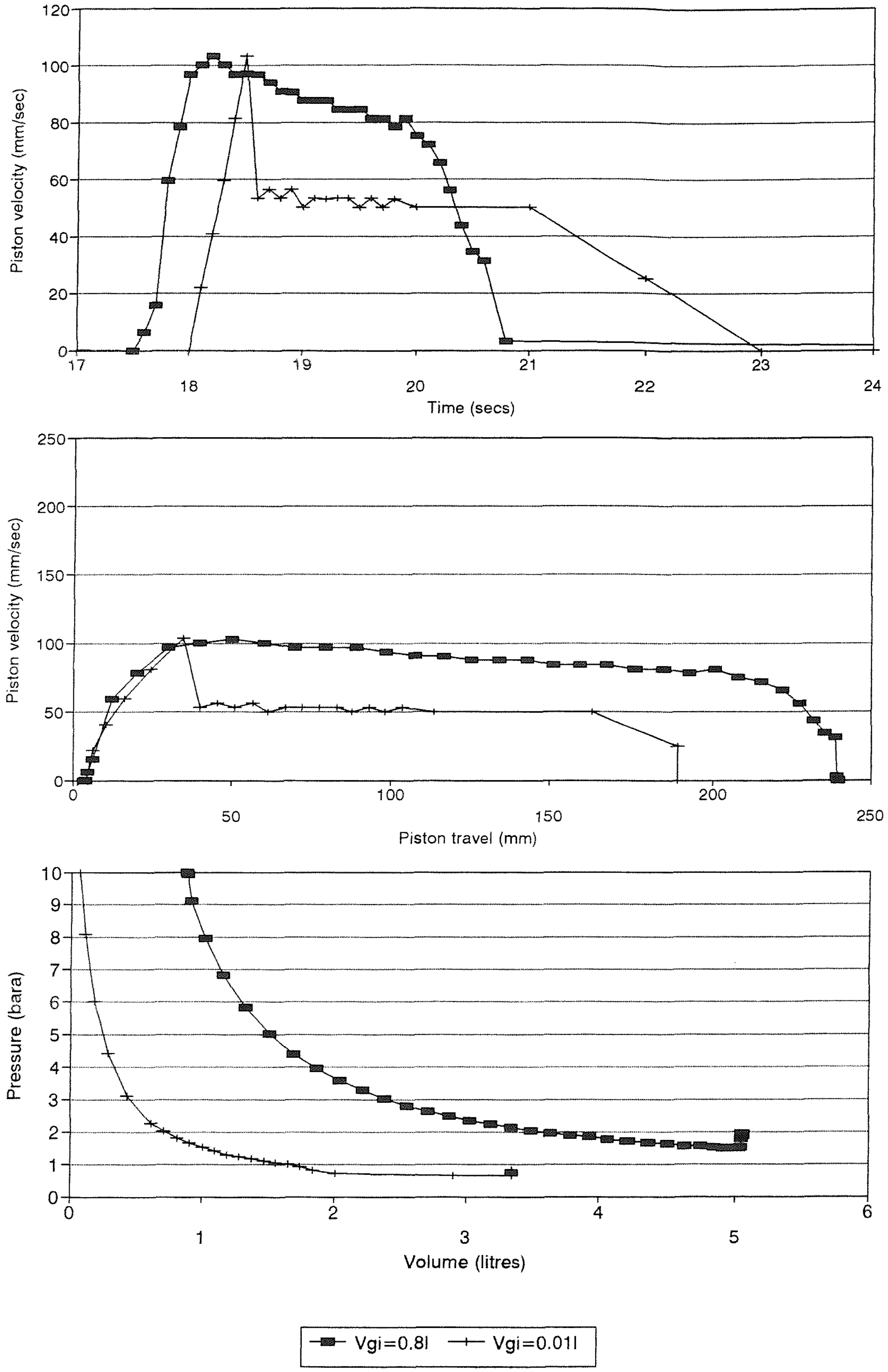

Figure 6.19 cont.. c) velocity-time plot, d) velocity-travel plot, e) pressure-volume plot

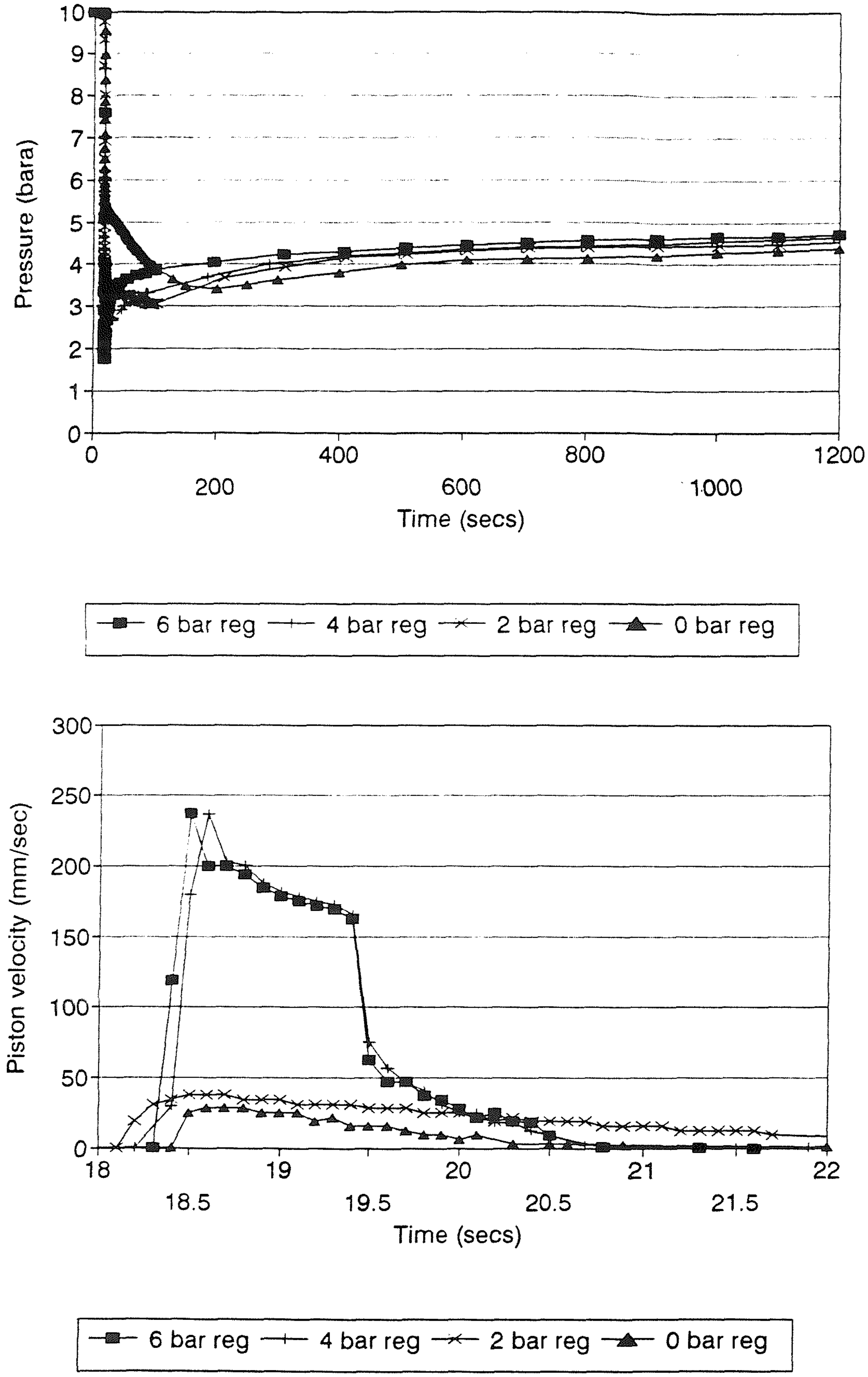

Figure 6.20 Effect of piston velocity on the rate of gas evolution from a CO_2/water system, 100 l/min, 15 mins, 17.6°C ±2°, a) pressure-time plot, b) piston velocity-time plot

Note: legend refers to pressure of actuator air cylinder

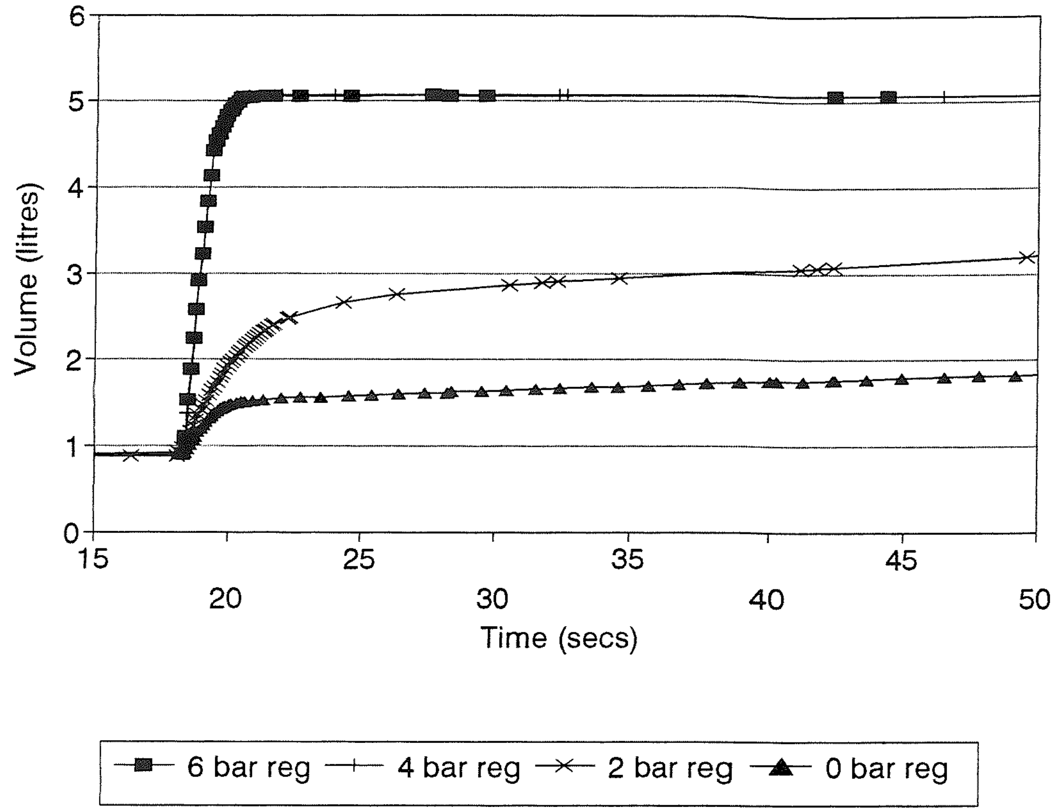

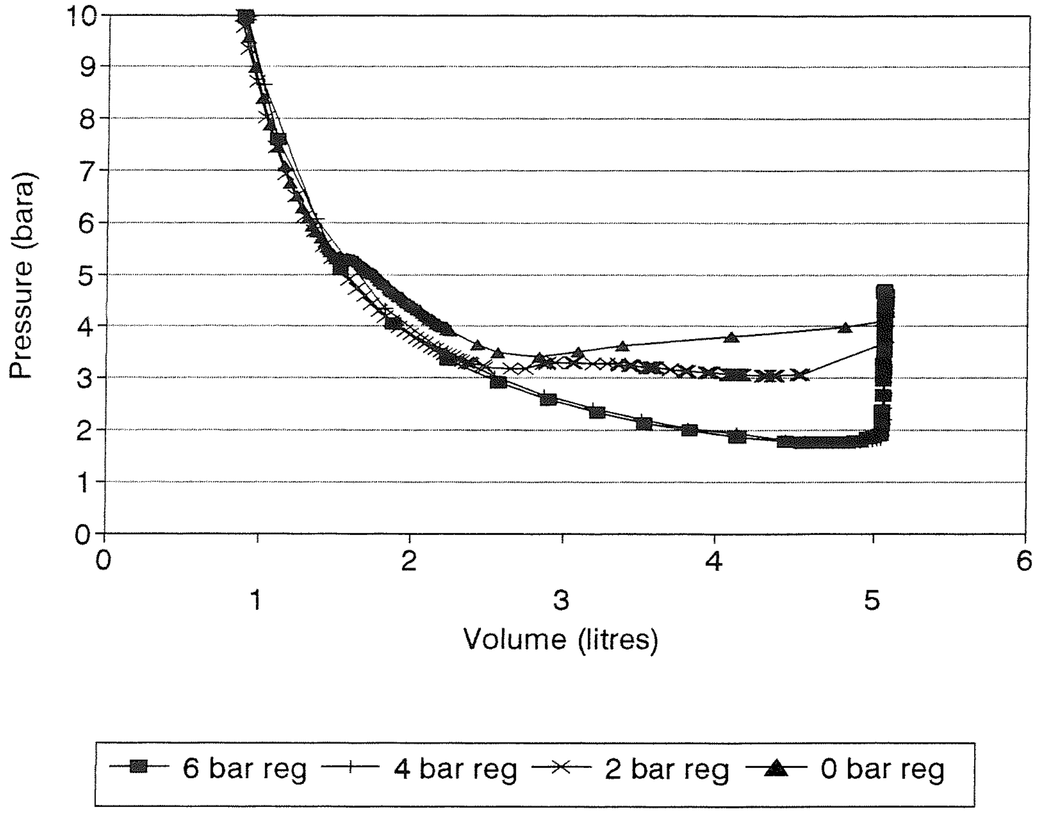

Figure 6.20 cont.. c) volume-time plot, d) pressure-volume plot

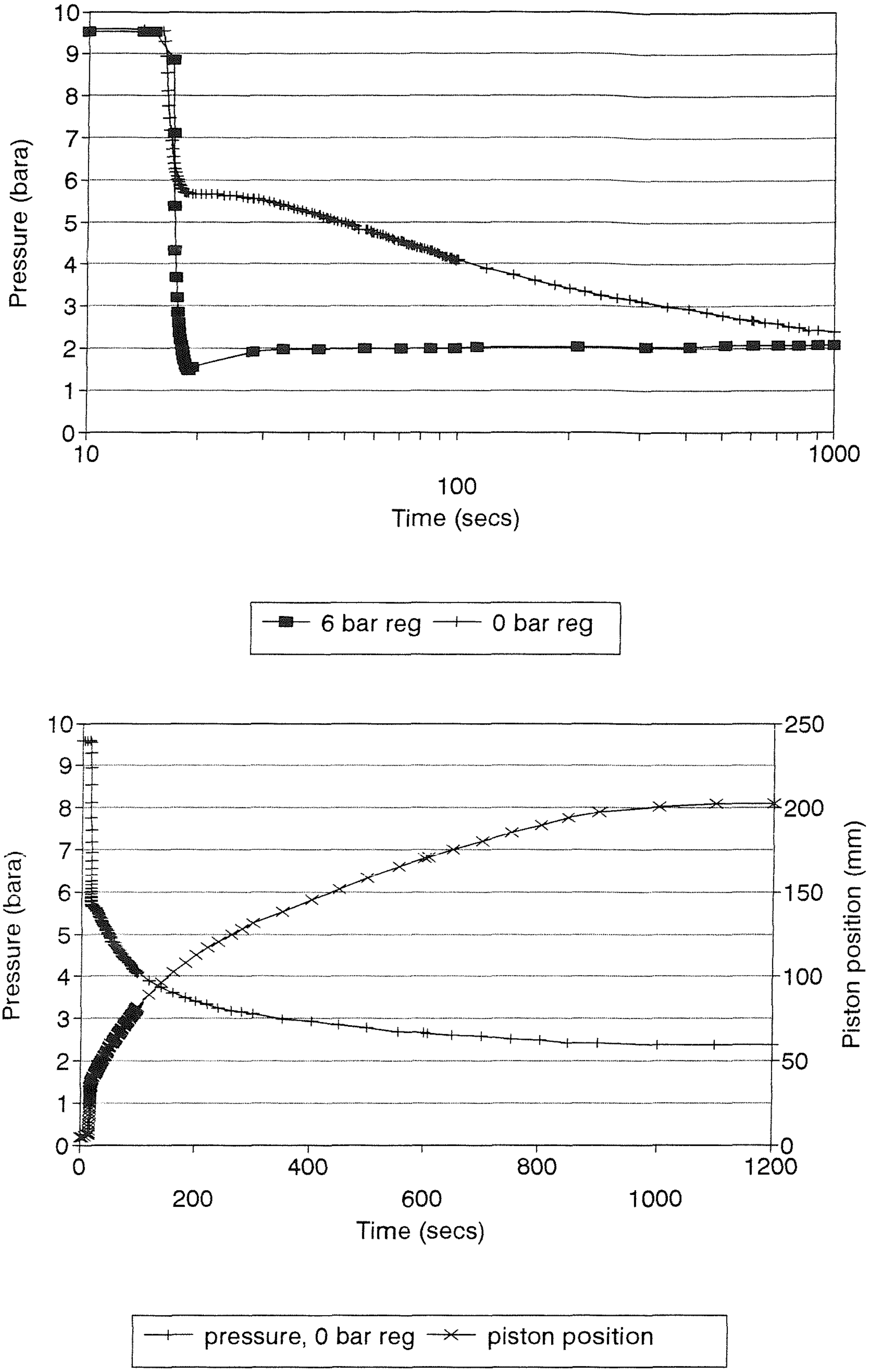

Figure 6.21 Effect of piston velocity on the rate of gas evolution from a CH_4/water system, 100 l/min, 15 mins, 21.1°C ±0.1°, a) pressure-time plot, b) pressure-piston position-time plot

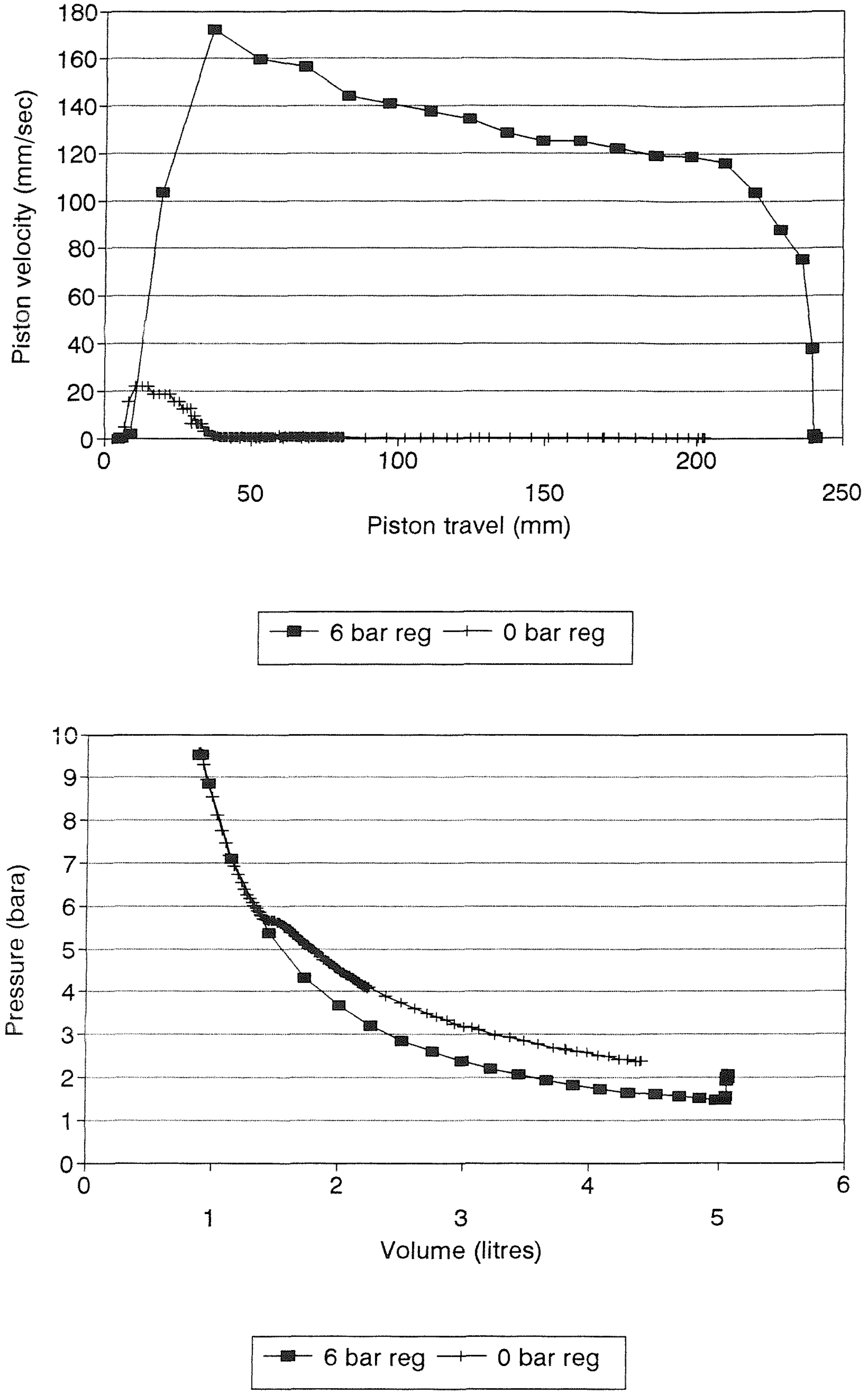

Figure 6.21 cont.. c) velocity-travel plot, d) pressure-volume plot

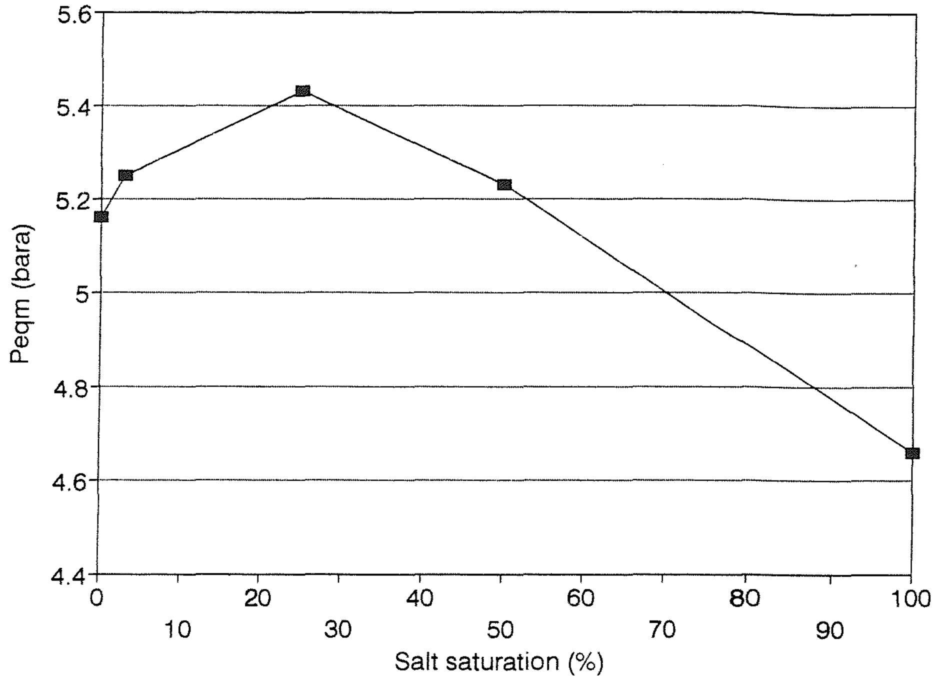

Figure 6.22 Effect of salinity on the final pressures obtained after depressurization, for a CO_2 in water system, 100 l/min, 15 mins, 18°C ±1°

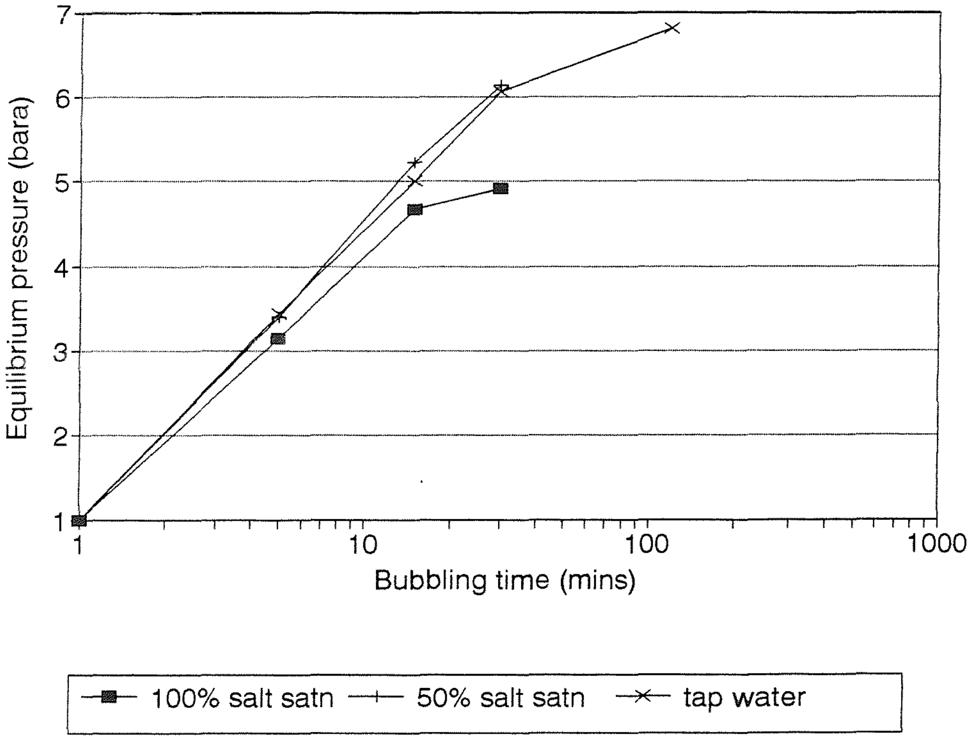

Figure 6.23 Final equilibrium pressures obtained after depressurization, as a function of bubbling time for concentrated salt solutions, 100 l/min, 15 mins, 18°C ±1°

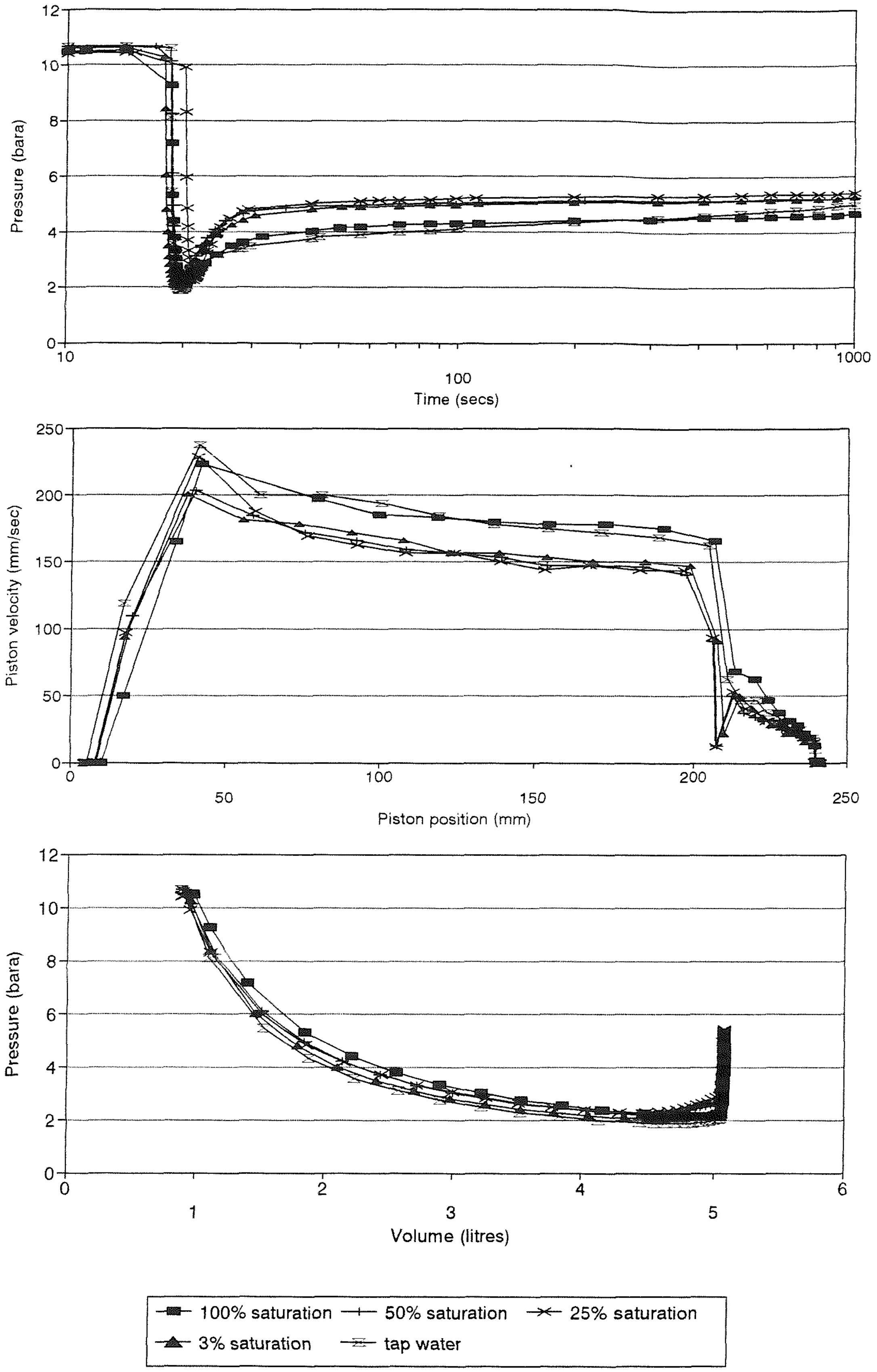

Figure 6.24 Effect of salinity on gas evolution from a CO_2 in water system, 100 l/min, 15 mins, 18°C ±1°, a) pressure-time plot, b) velocity-travel plot, c) pressure-volume plot

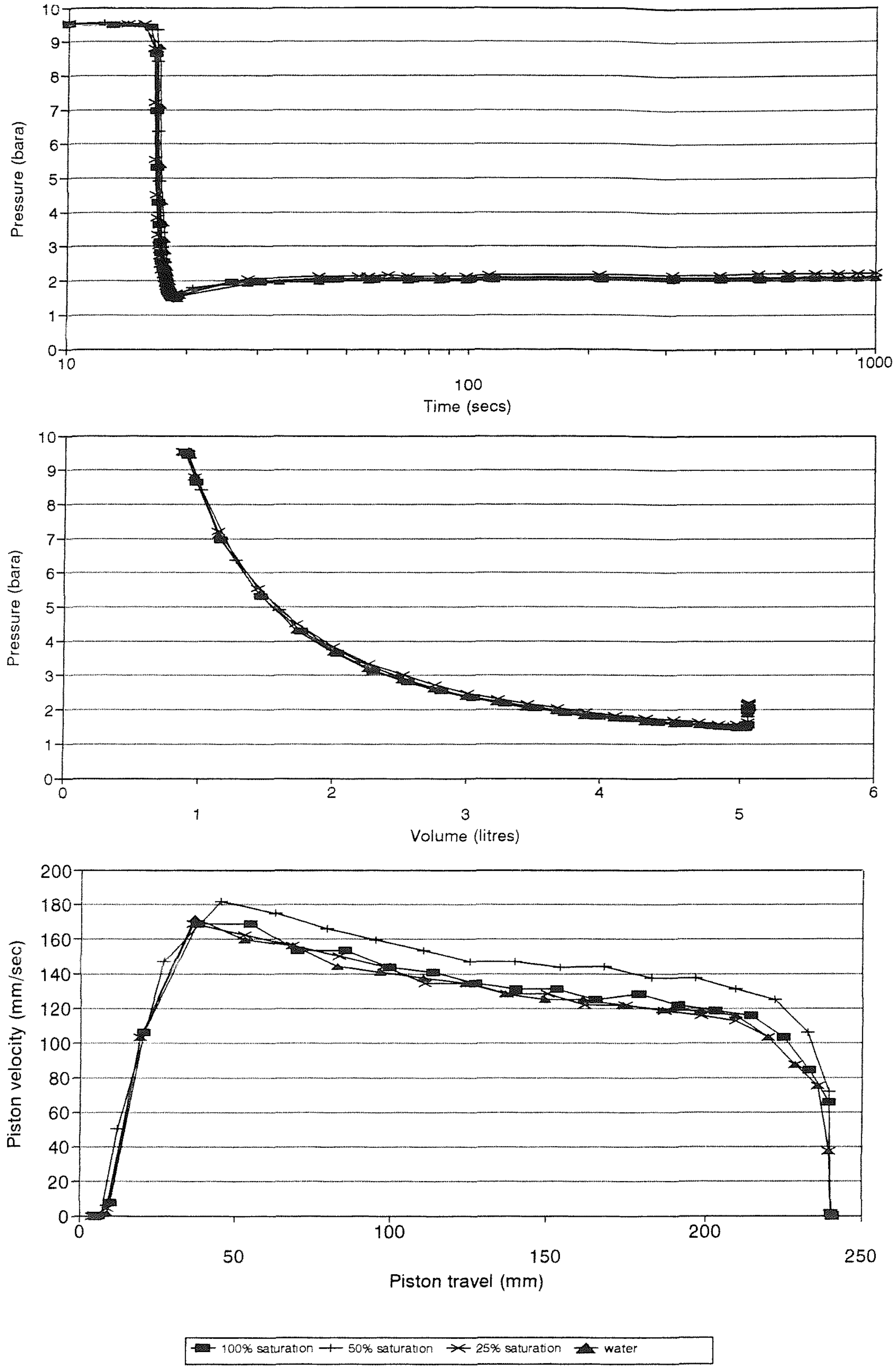

Figure 6.25 Effect of salinity on gas evolution from a CH_4 in water system, 100 l/min, 15 mins, 20.6°C ±0.5°, a) pressure-time plot, b) pressure-volume plot, c) piston velocity-travel plot

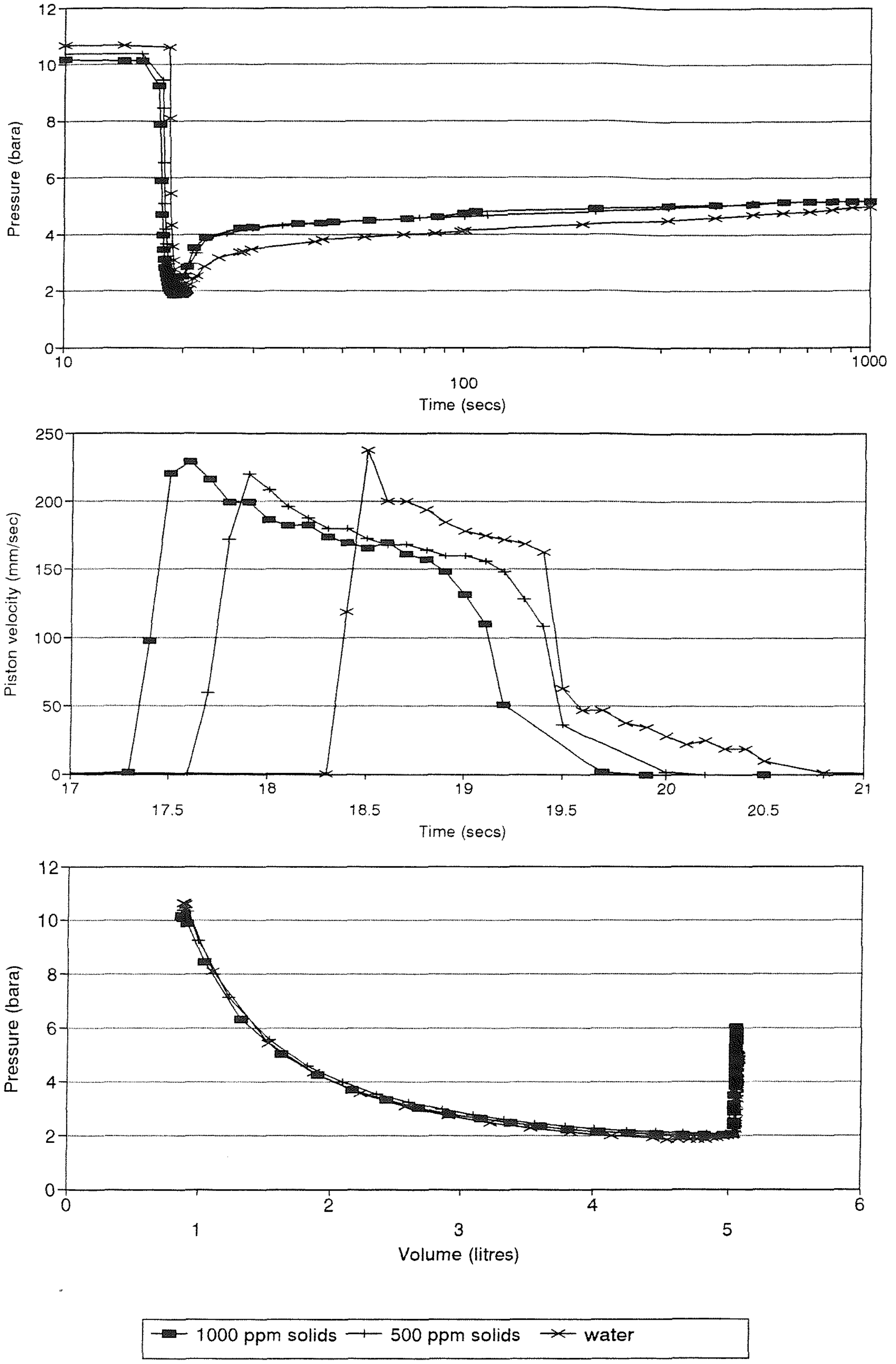

Figure 6.26 Effect of 500 ppm silica flour on the rate of gas evolution from a CO_2/water system, 100 l/min, 15 mins, 19°C ±1°, a) pressure-time plot, b) piston velocity-time plot, c) pressure-volume plot

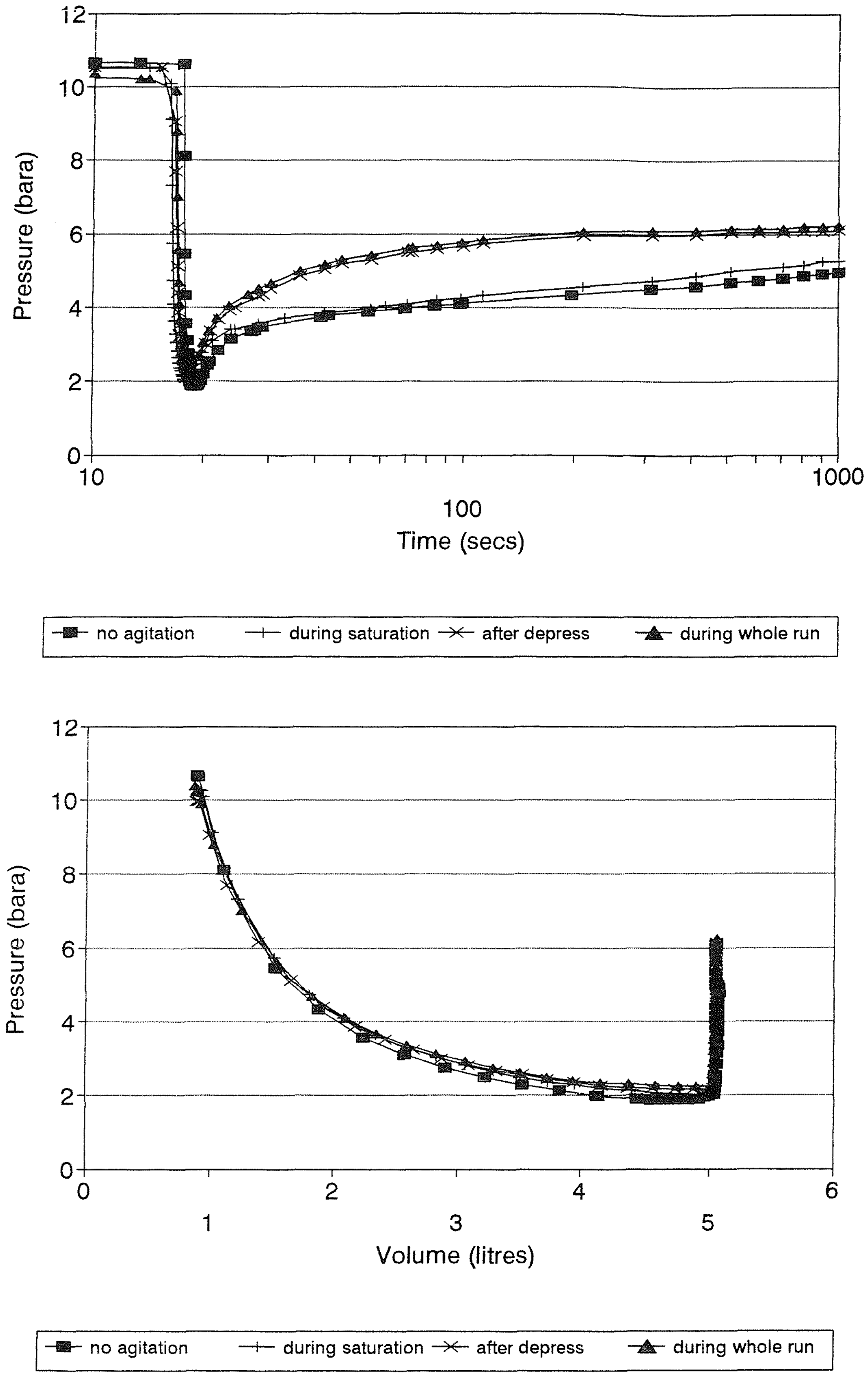

Figure 6.27 Effect of fluid agitation on the rate of gas evolution from a CO_2/water system, 100 l/min, 15 mins, 19.6°C ±0.2°, a) pressure-time plot, b) pressure-volume plot

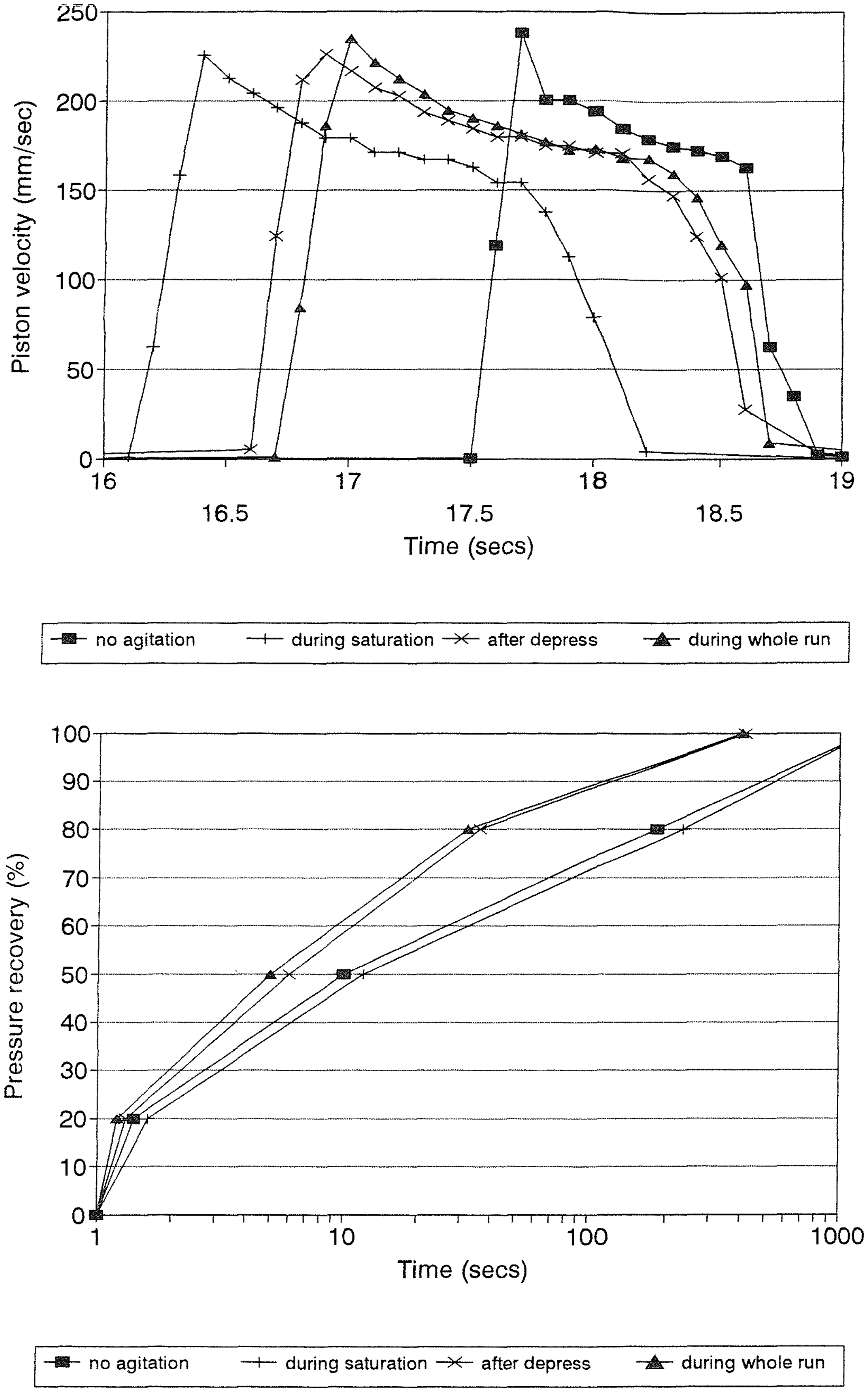

Figure 6.27 cont.. c) piston velocity-time plot, d) pressure recovery-time plot

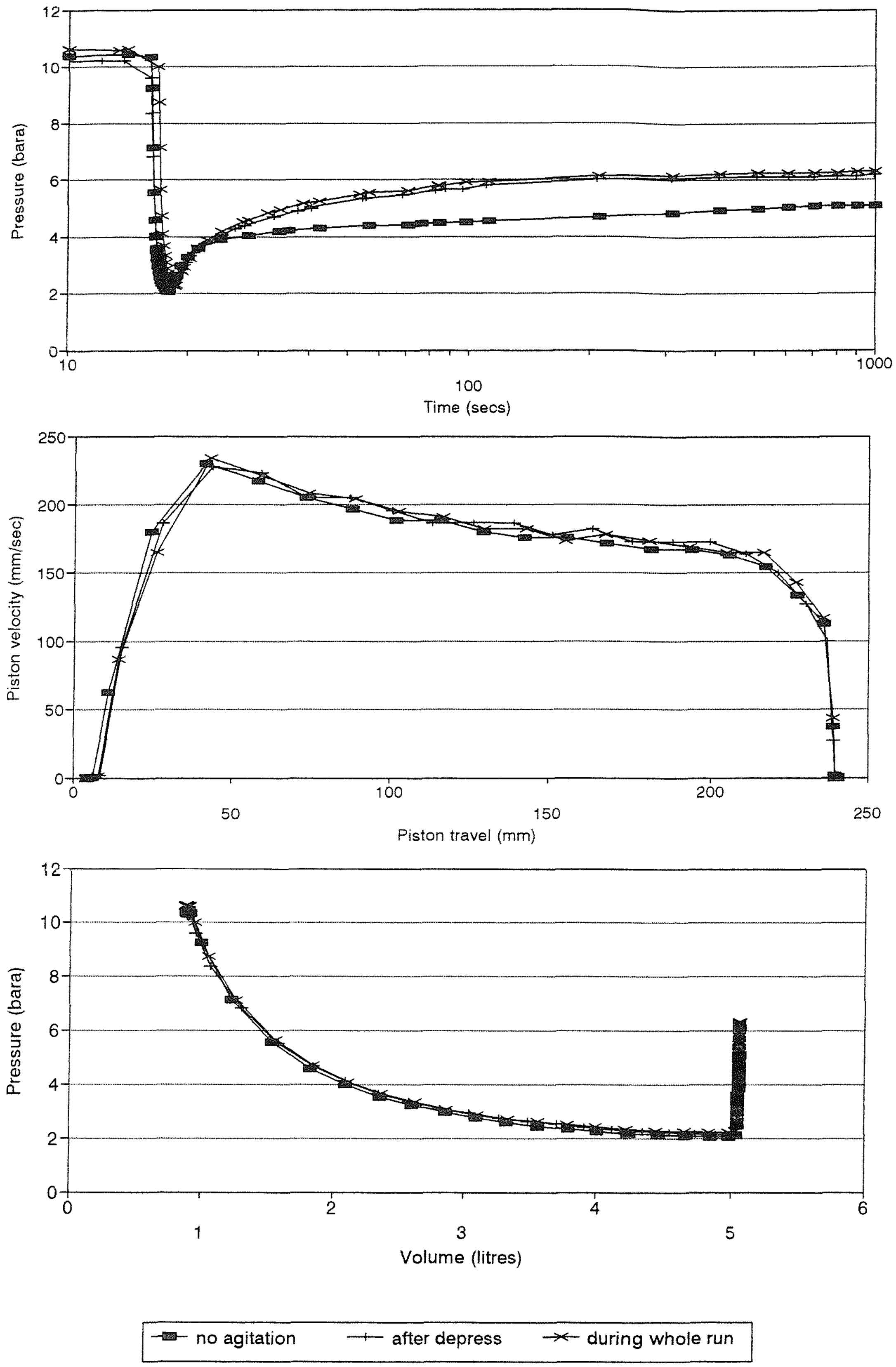

Figure 6.28 Effect of fluid agitation on the rate of gas evolution from a CO_2/water system, containing 500 ppm silica flour, 100 l/min, 15 mins, 20.3°C ±0.5°, a) pressure-time plot, b) piston velocity-travel plot, c) pressure-volume plot

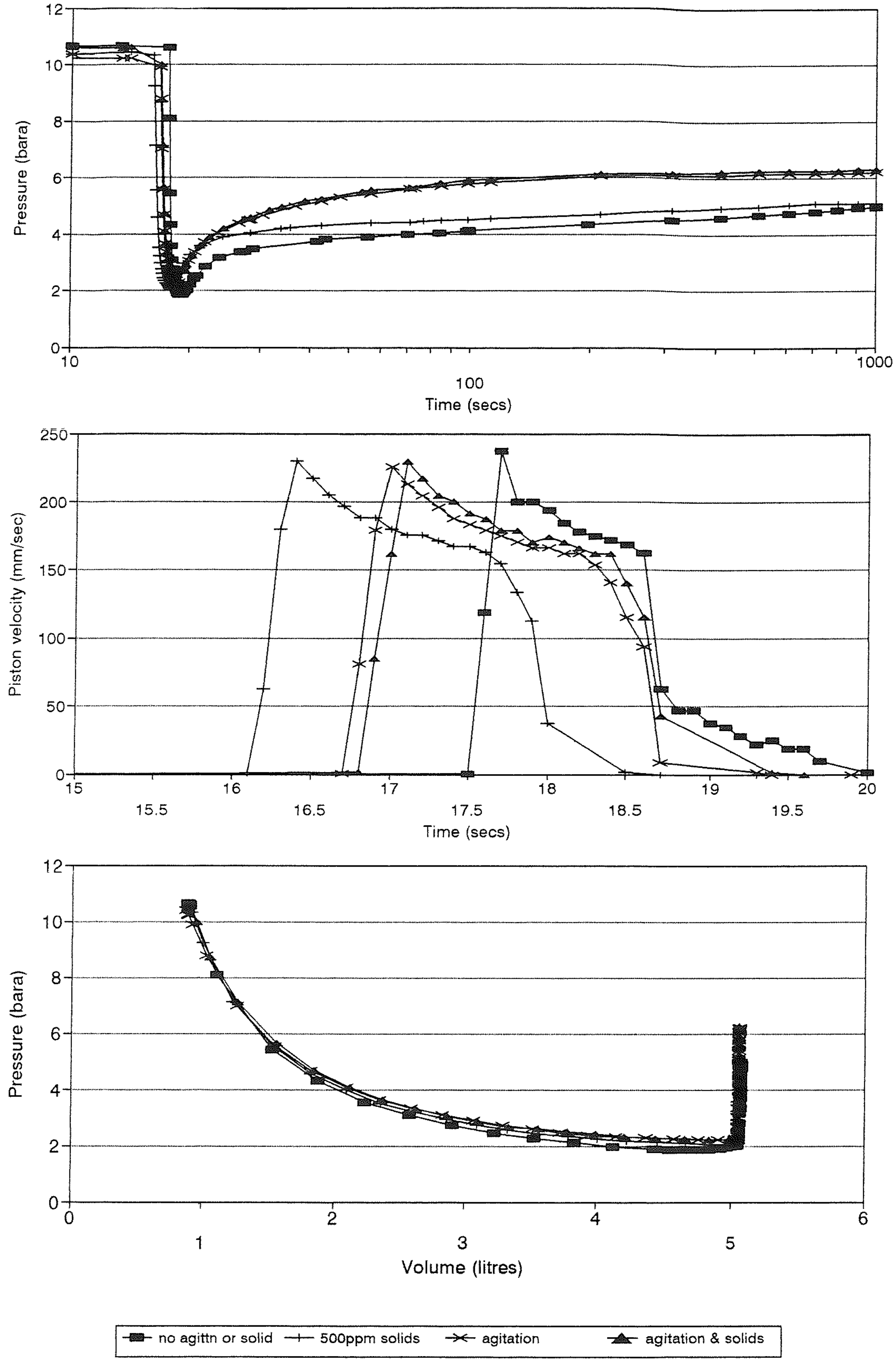

Figure 6.29 Effect of fluid agitation and 500 ppm silica flour on the rate of gas evolution from a CO_2/water system, 100 l/min, 15 mins, 20.3°C ±0.8°, a) pressure-time plot, b) piston velocity-time plot, c) pressure-volume plot

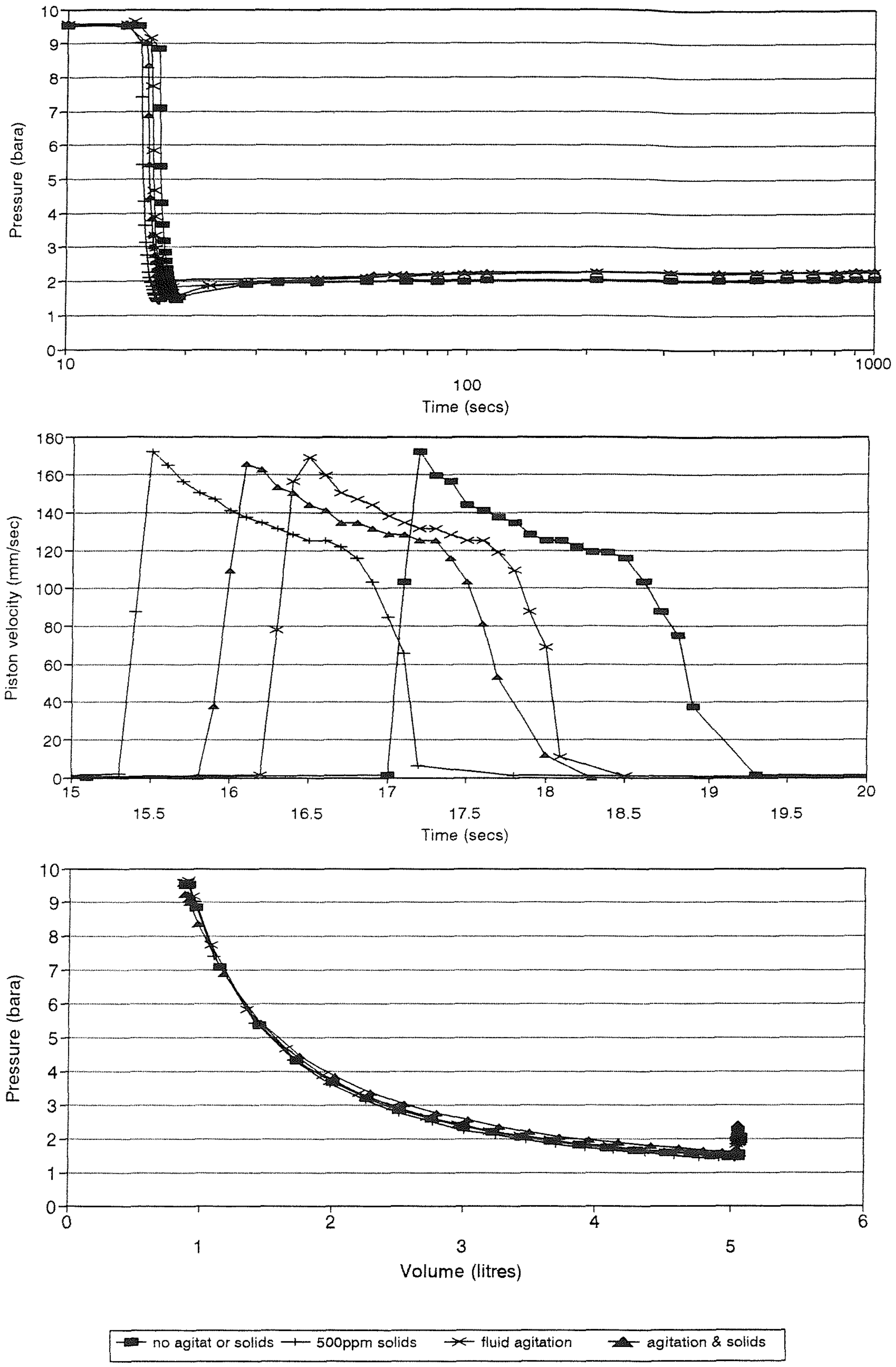

Figure 6.30 Effect of fluid agitation and 500 ppm silica flour on the rate of gas evolution from a CH_4/water system, 100 l/min, 15 mins, 16.4°C ±0.2°, a) pressure-time plot, b) piston velocity-time plot, c) pressure-volume plot

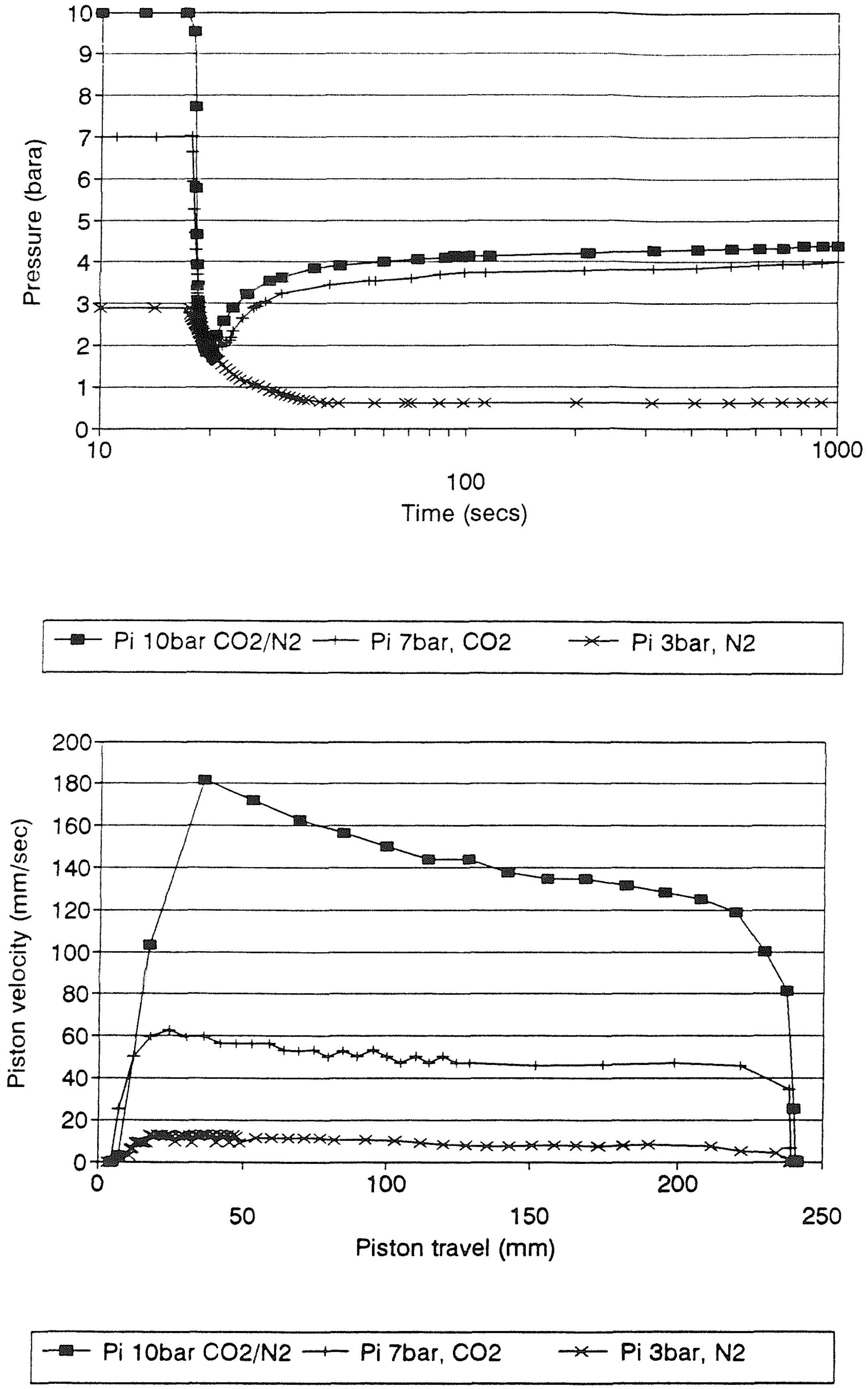

Figure 6.31 Effect of mixed gas composition CO_2 70%/N_2 30% on the rate of gas evolution, 100 l/min, 30 mins, 20°C ±0.5°, a) pressure-time plot, b) velocity-travel plot

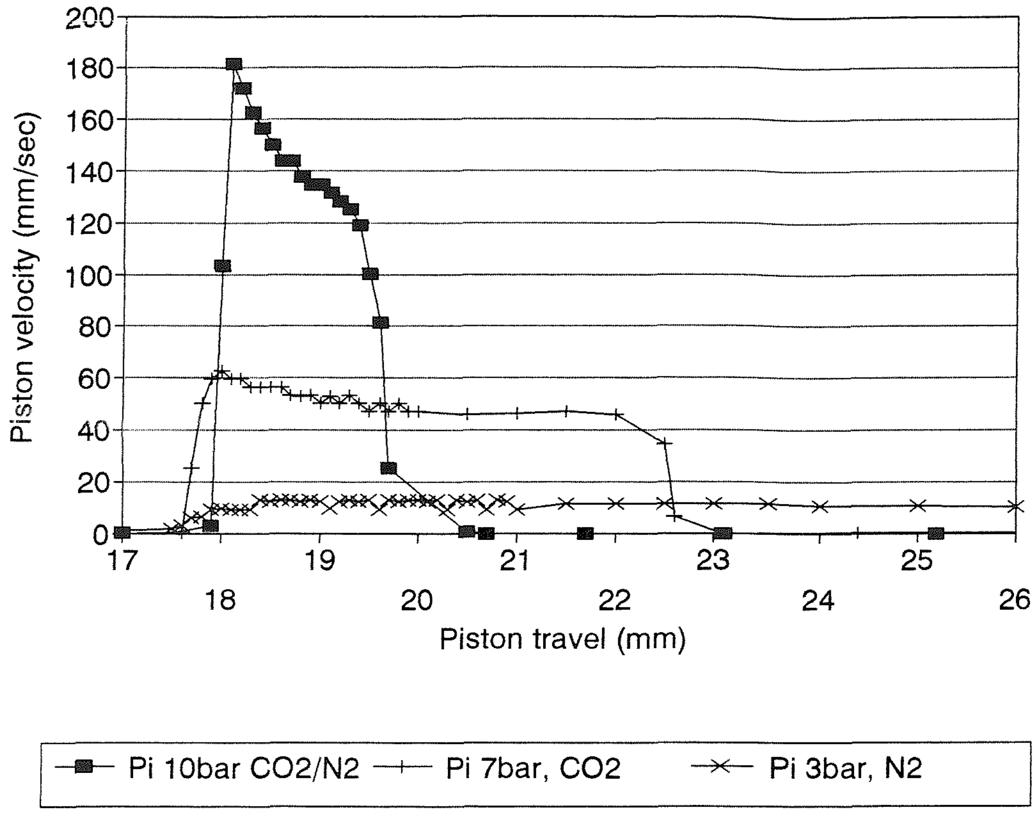

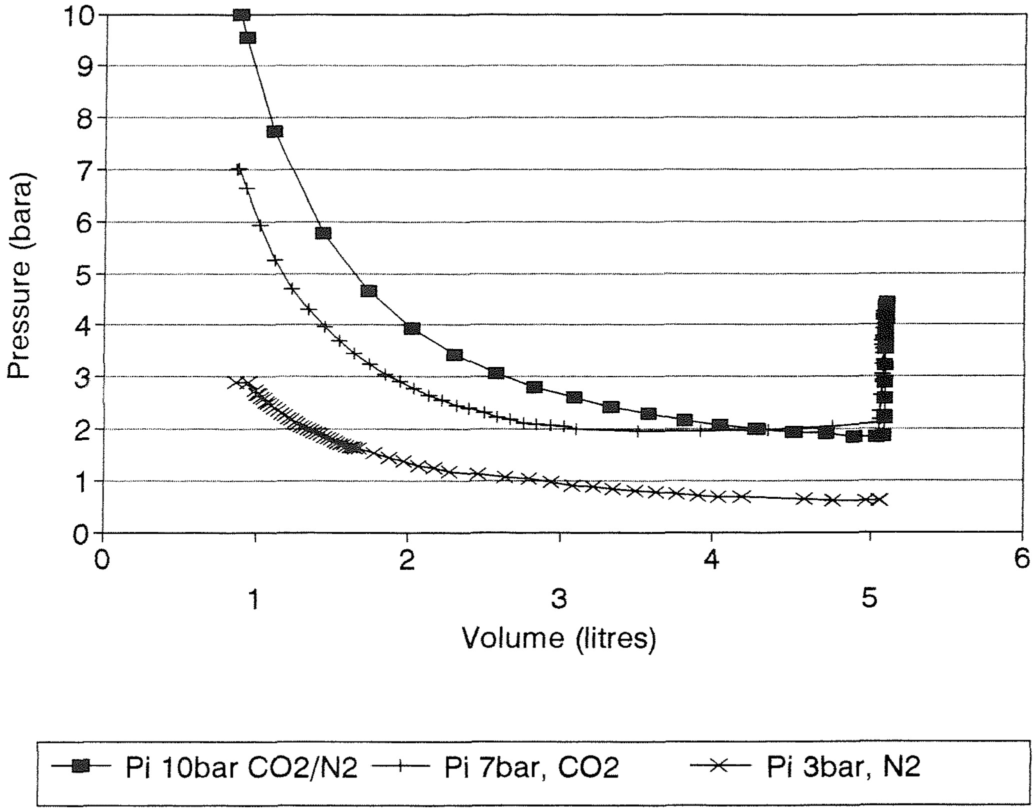

Figure 6.31 cont.. c) velocity-time plot, d) pressure-volume plot

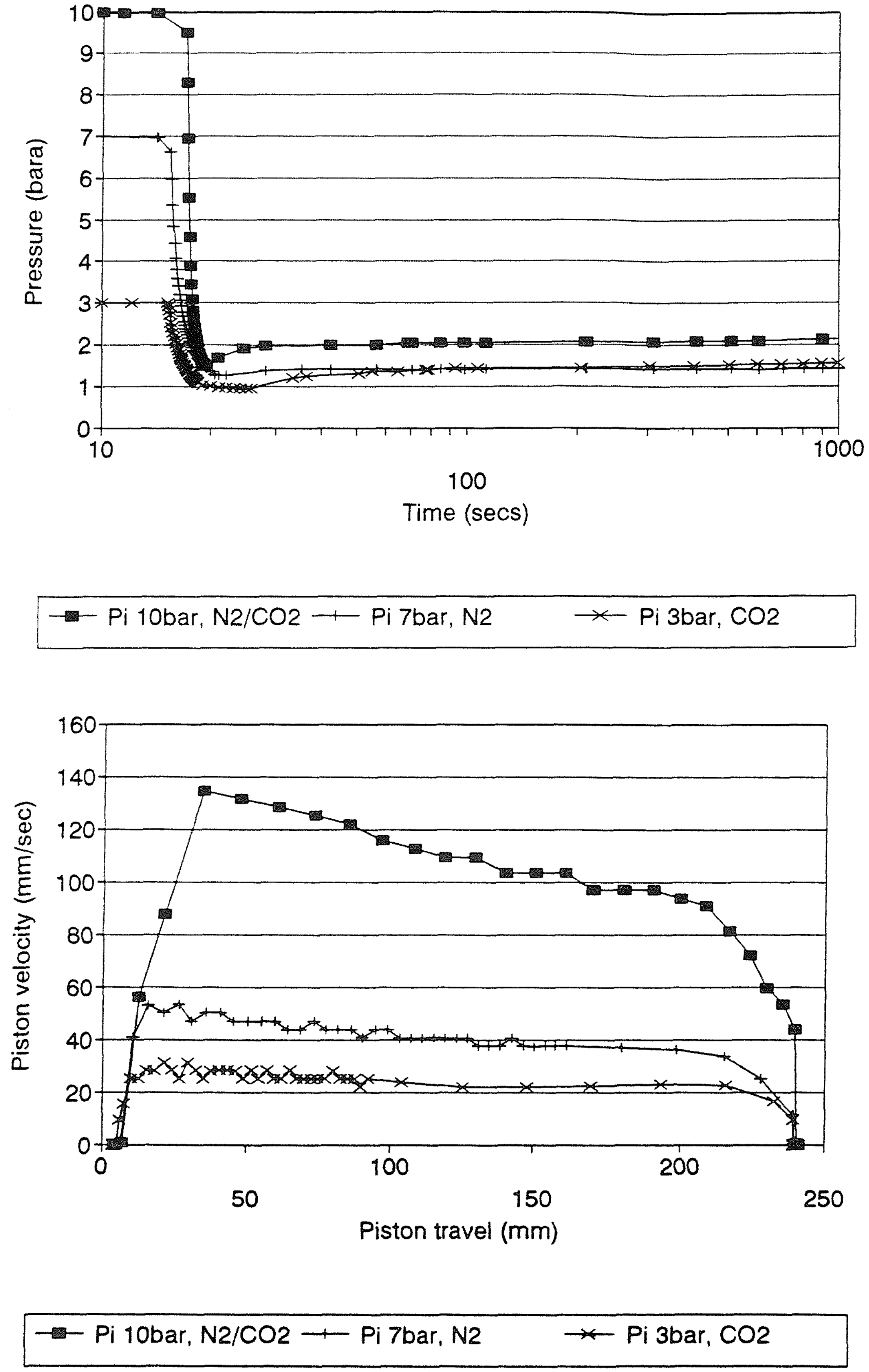

Figure 6.32 Effect of mixed gas composition N_2 70%/CO_2 30% on the rate of gas evolution, 100 l/min, 30 mins, 21.1°C ±1°, a) pressure-time plot, b) velocity-travel plot

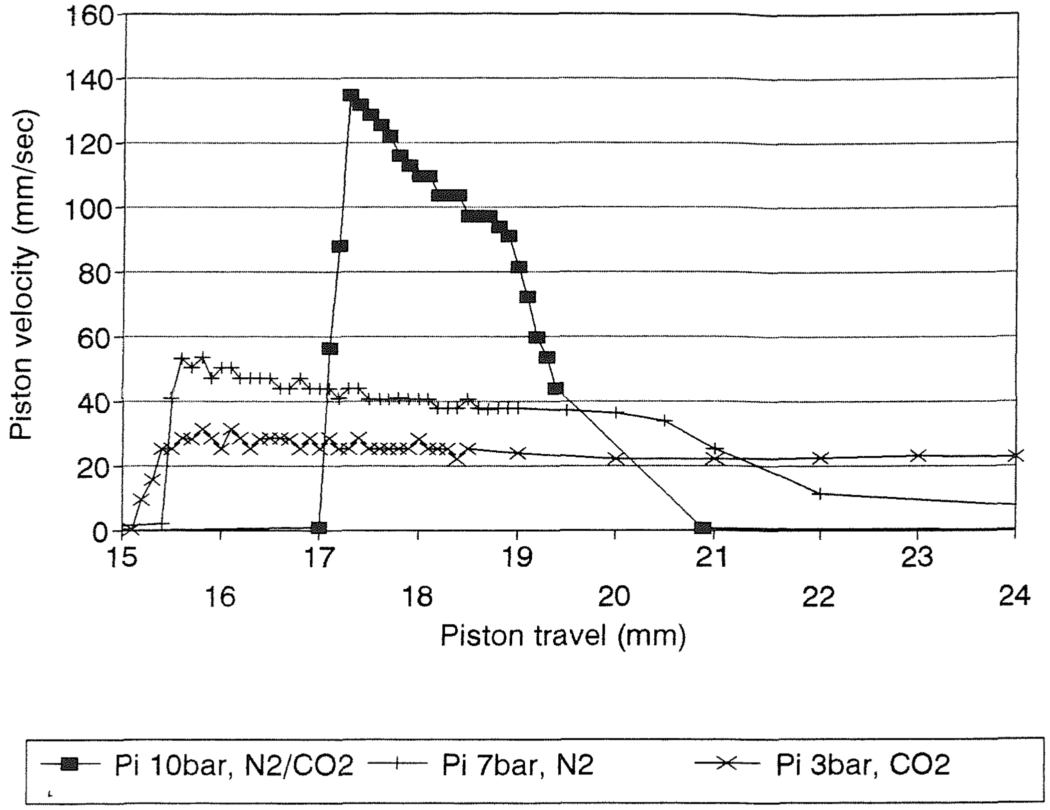

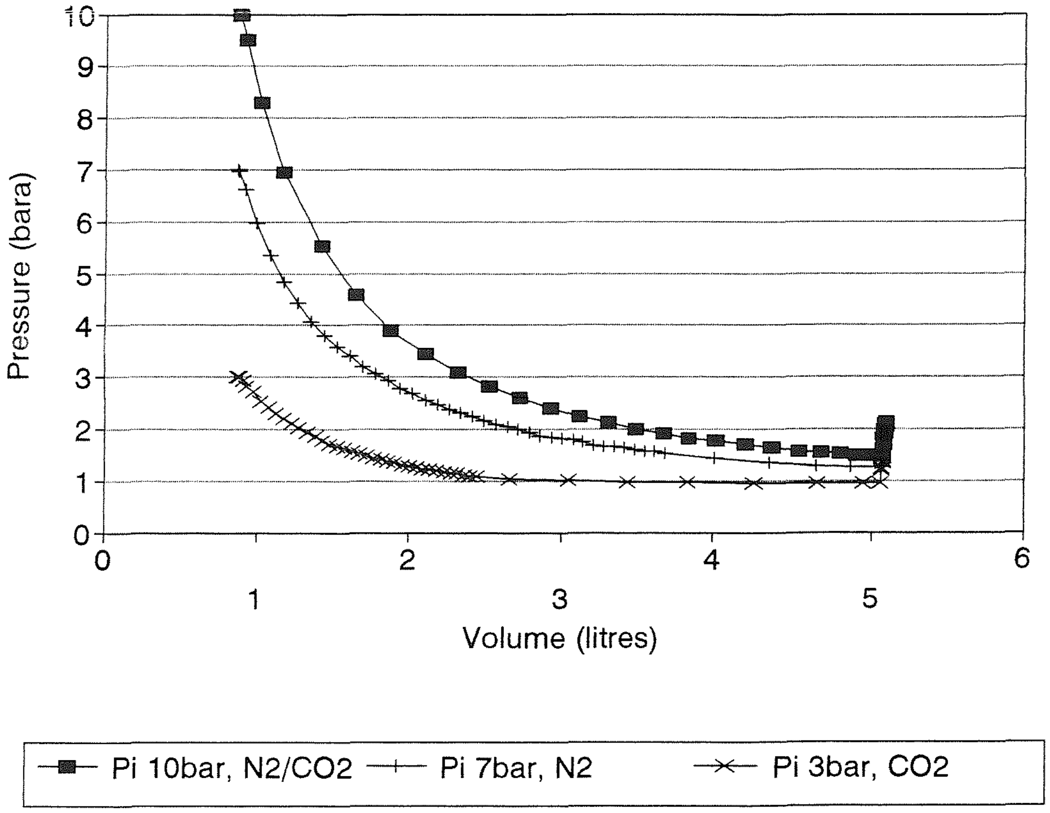

Figure 6.32 cont.. c) piston velocity-time plot, d) pressure-volume plot

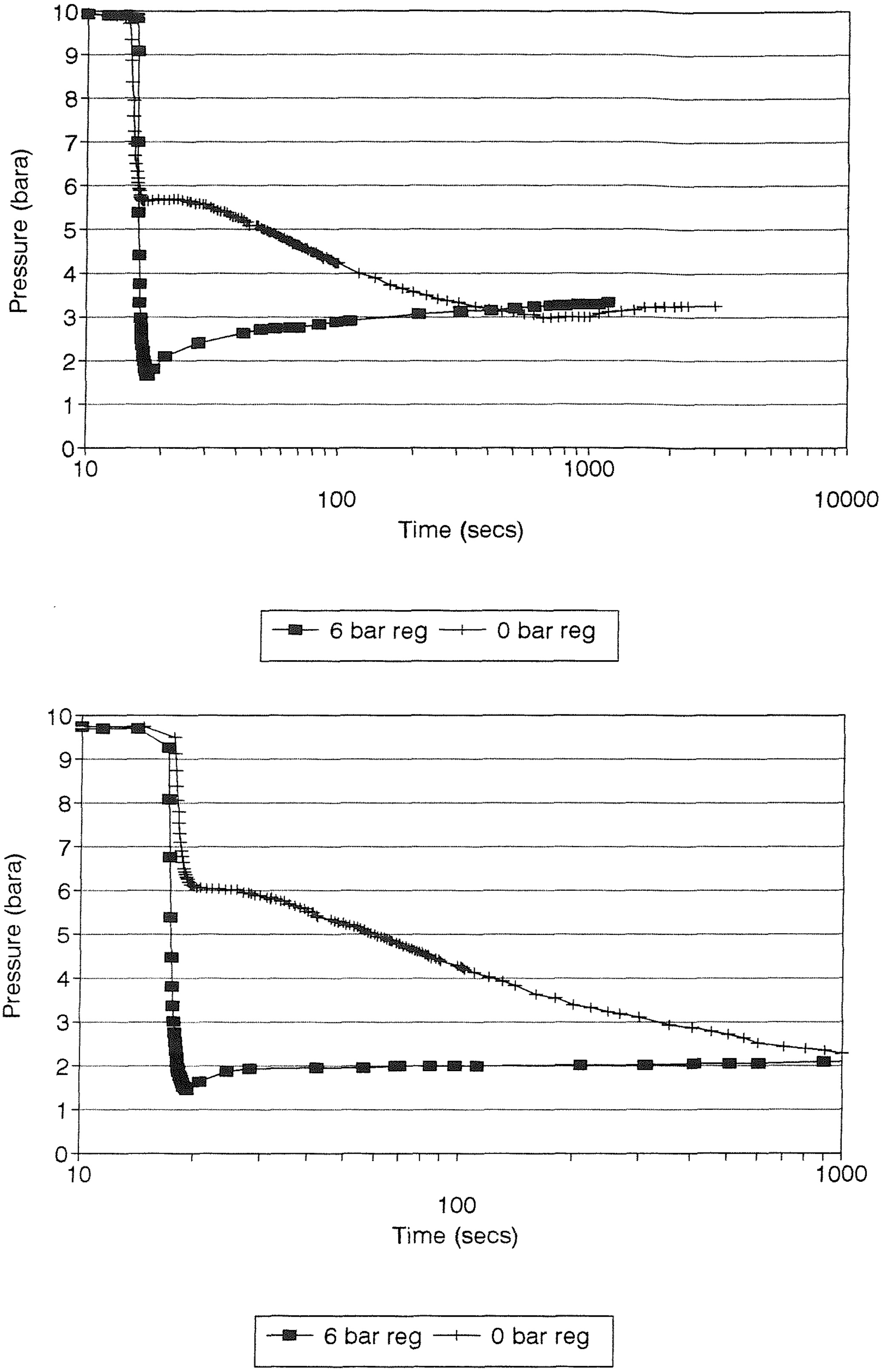

Figure 6.33 Effect of piston velocity on the rate of gas evolution from a mixed gas composition 100 l/min, 15 mins, 22.8°C ±1°, a) pressure-time plot, CO_2 70%/N_2 30% /water system, b) pressure-time plot, N_2 70%/CO_2 30% /water system

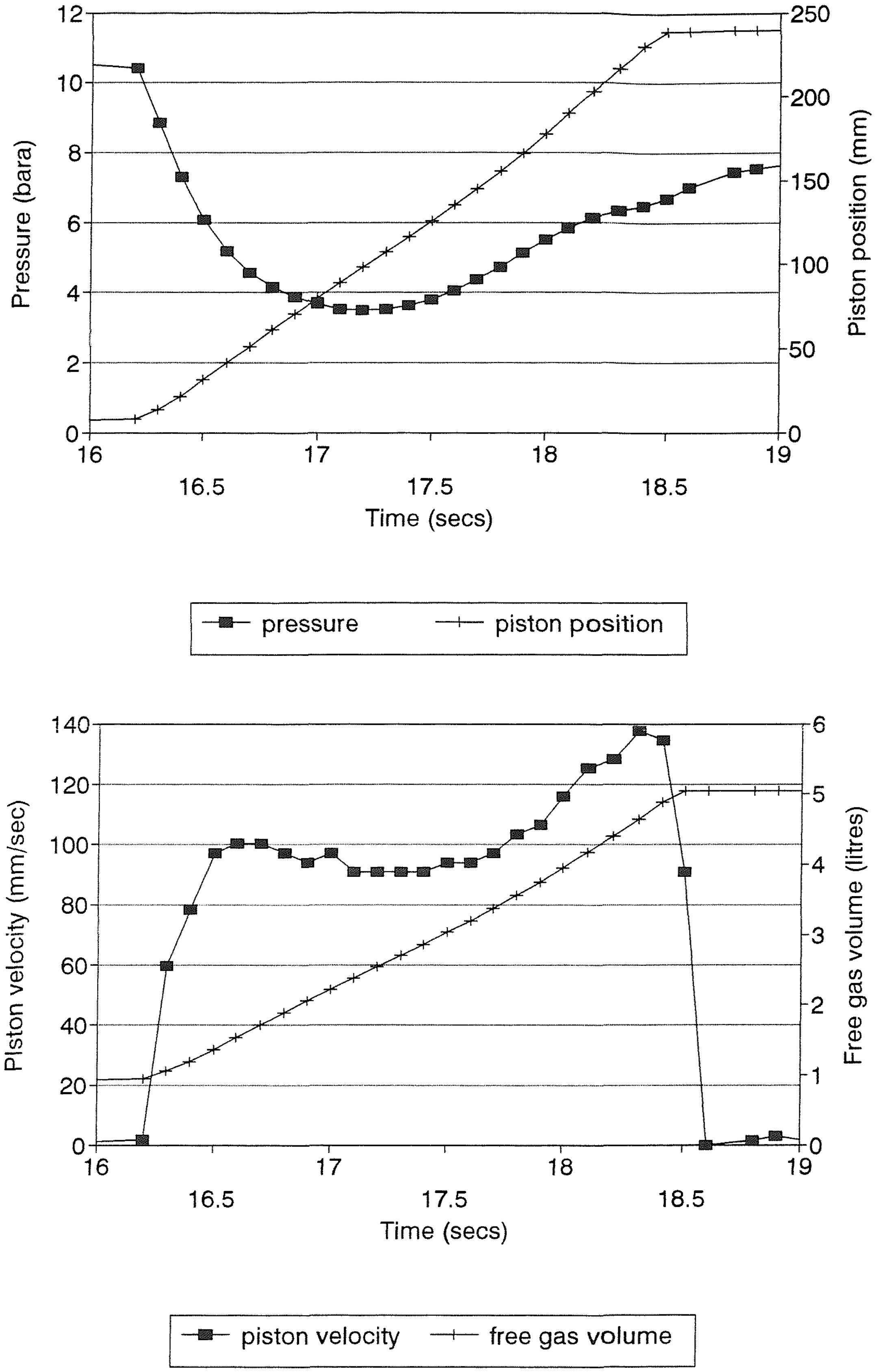

Figure 6.34 Rapid depressurization of a CO_2 in kerosene system, 100 l/min, 15 mins, 22.2°C, a) pressure-piston position-time plot, b) piston velocity-free gas volume-time plot

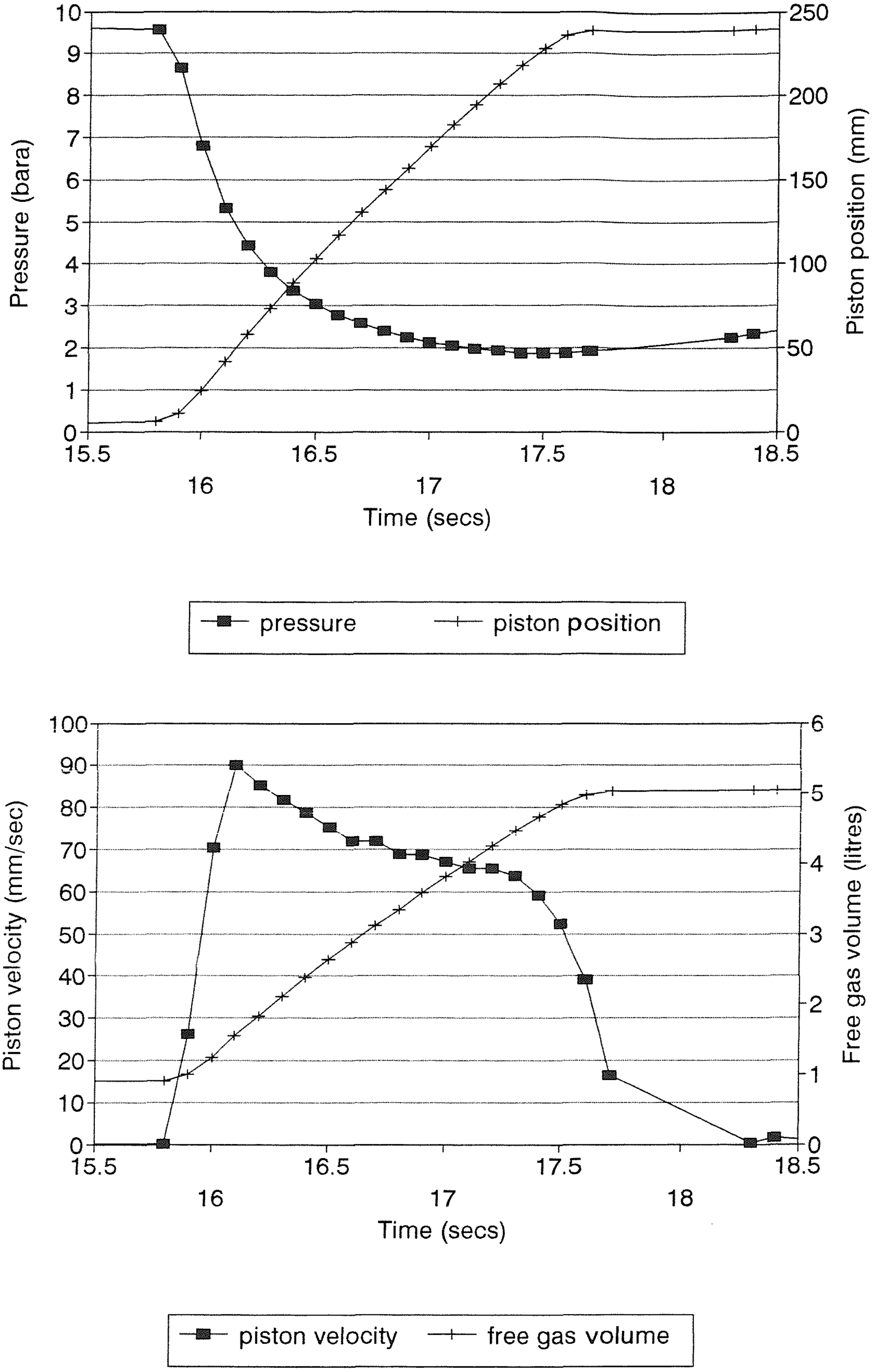

Figure 6.35 Rapid depressurization of a N_2 in kerosene system, 100 l/min, 15 mins, 21.9°C, a) pressure-piston position-time plot, b) piston velocity-free gas volume-time plot

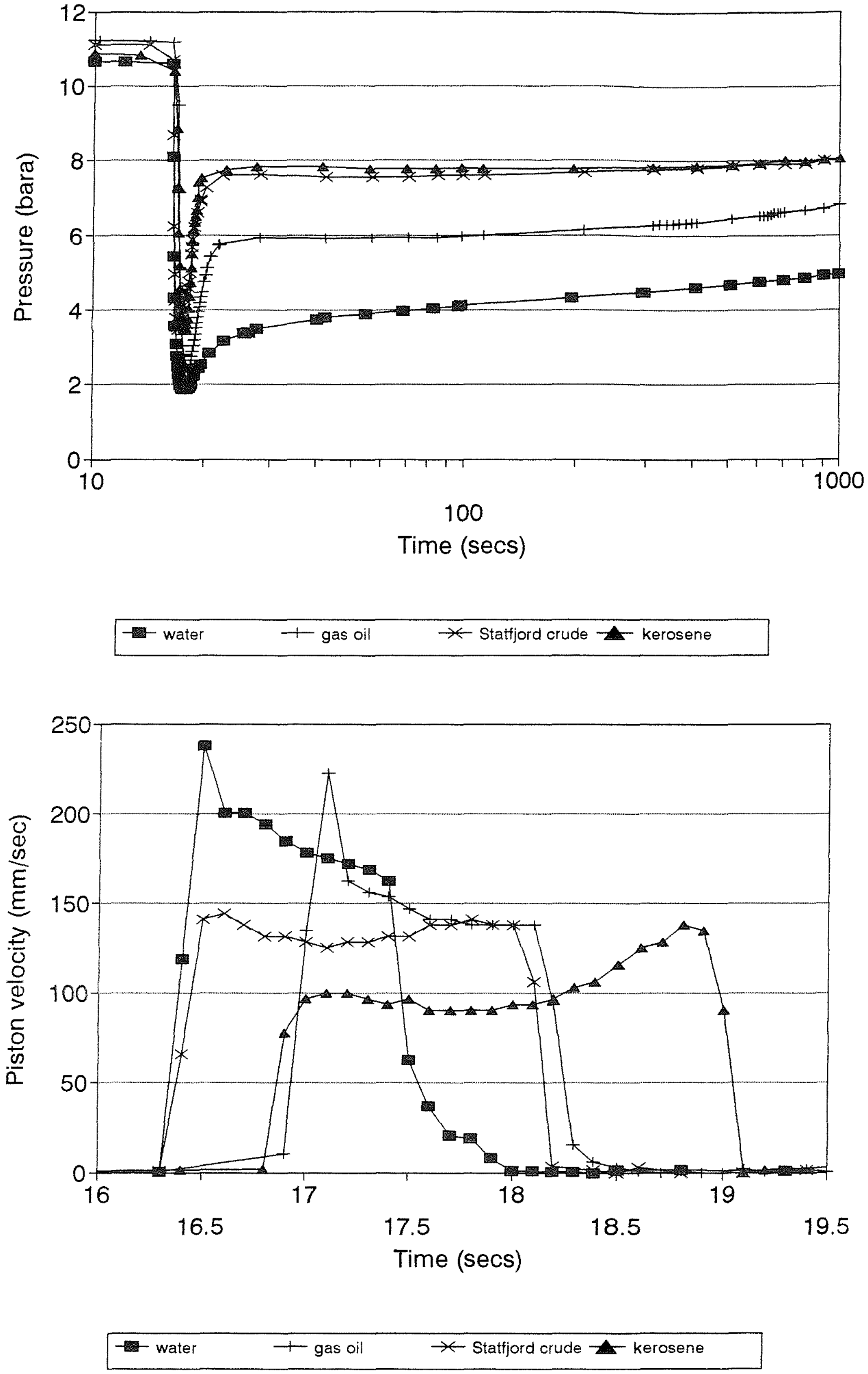

Figure 6.36 Comparison of CO_2 evolution in water and hydrocarbons, 100 l/min, 15 mins, 22°C ±2°, a) pressure-time plot, b) piston velocity-time plot

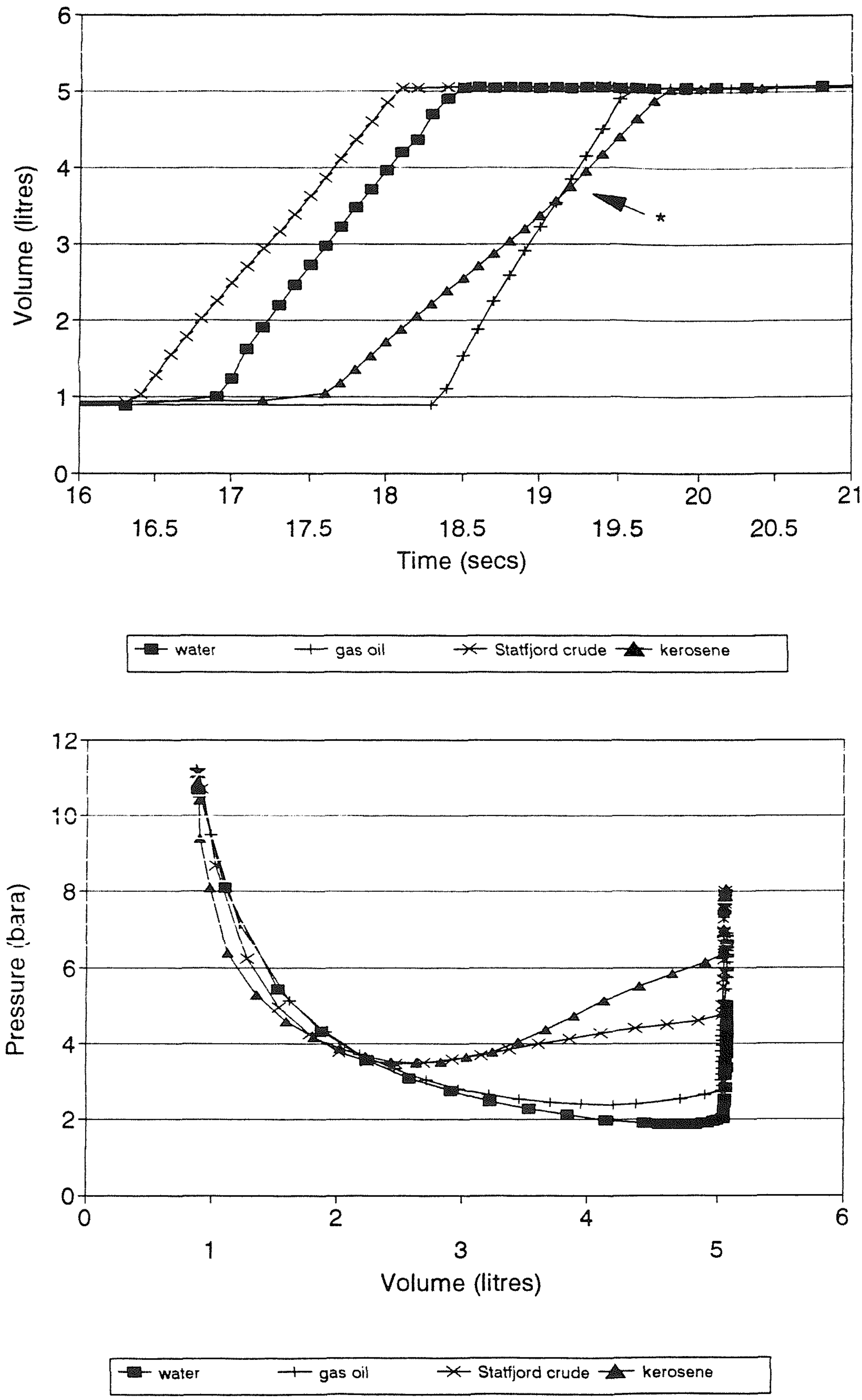

* change of gradient (see chapter 6.19)

Figure 6.36 cont.. c) volume-time plot, d) pressure-volume plot

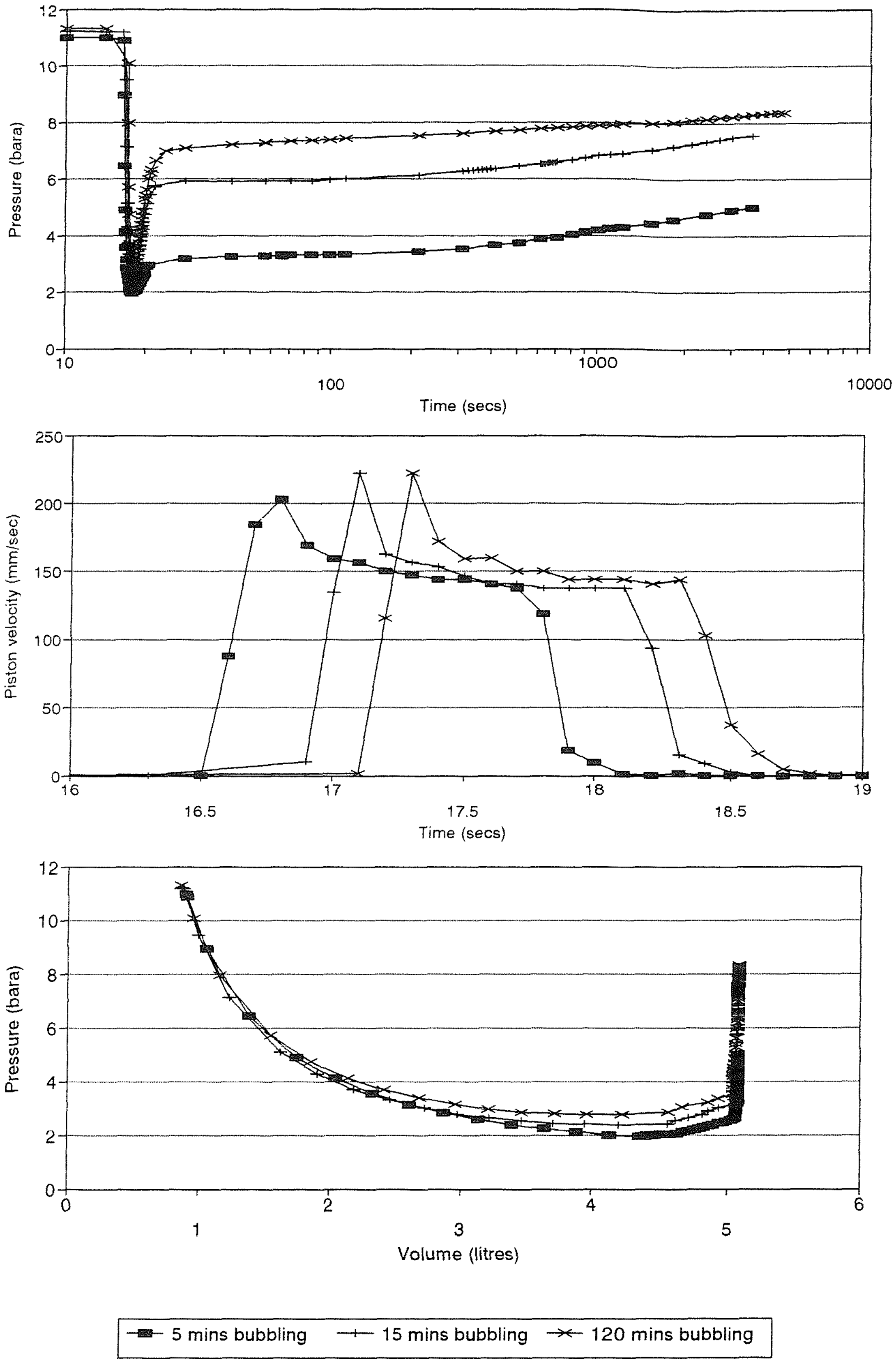

Figure 6.37 Effect of increasing the bubbling time for a CO_2 in gas oil system, 100 l/min, 15 mins, 18.6°C ±0.5°, a) pressure-time plot, b) piston velocity-time plot, c) pressure-volume plot

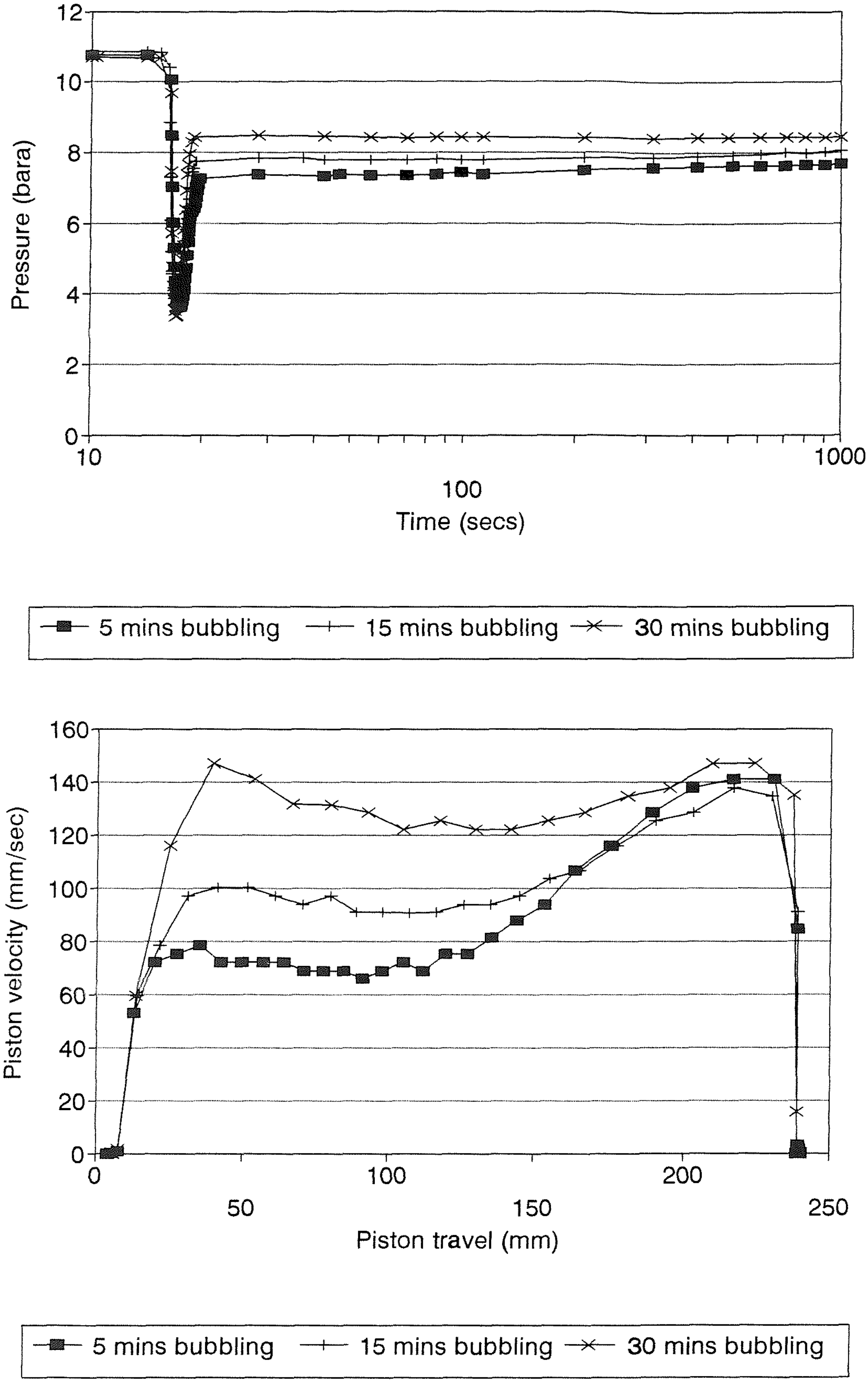

Figure 6.38 Effect of increasing the bubbling time for a CO_2 in kerosene system, 100 l/min, 15 mins, 18.7°C ±0.2°, a) pressure-time plot, b) piston velocity-travel plot

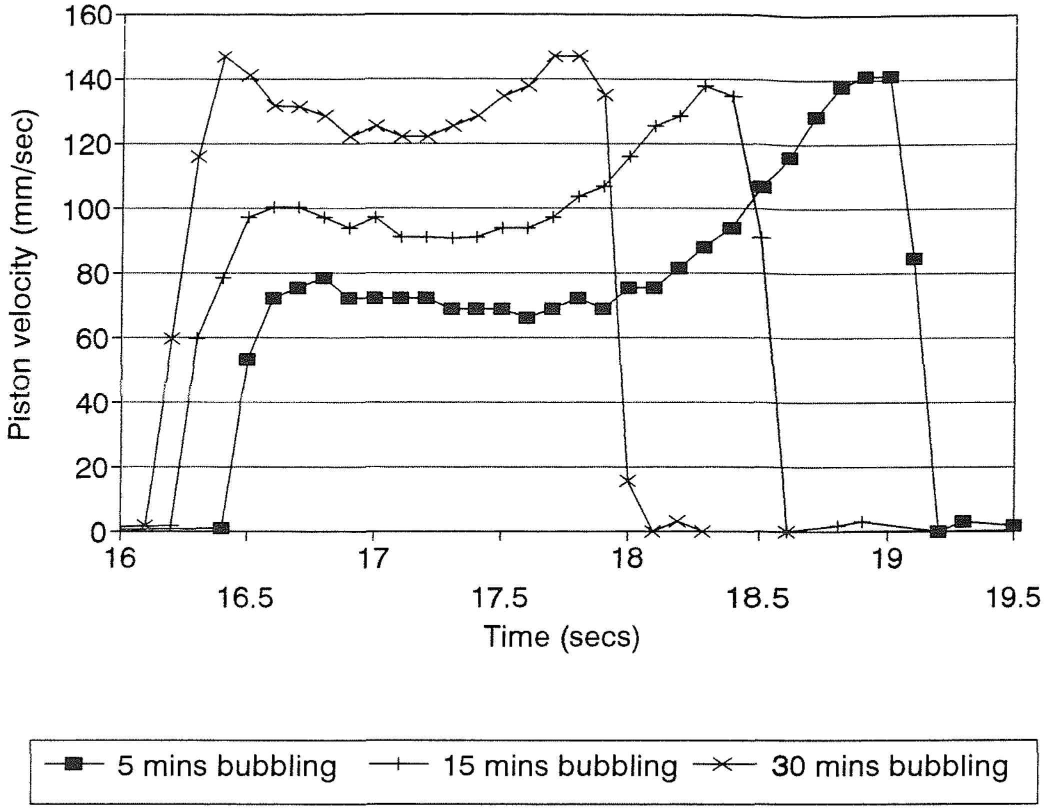

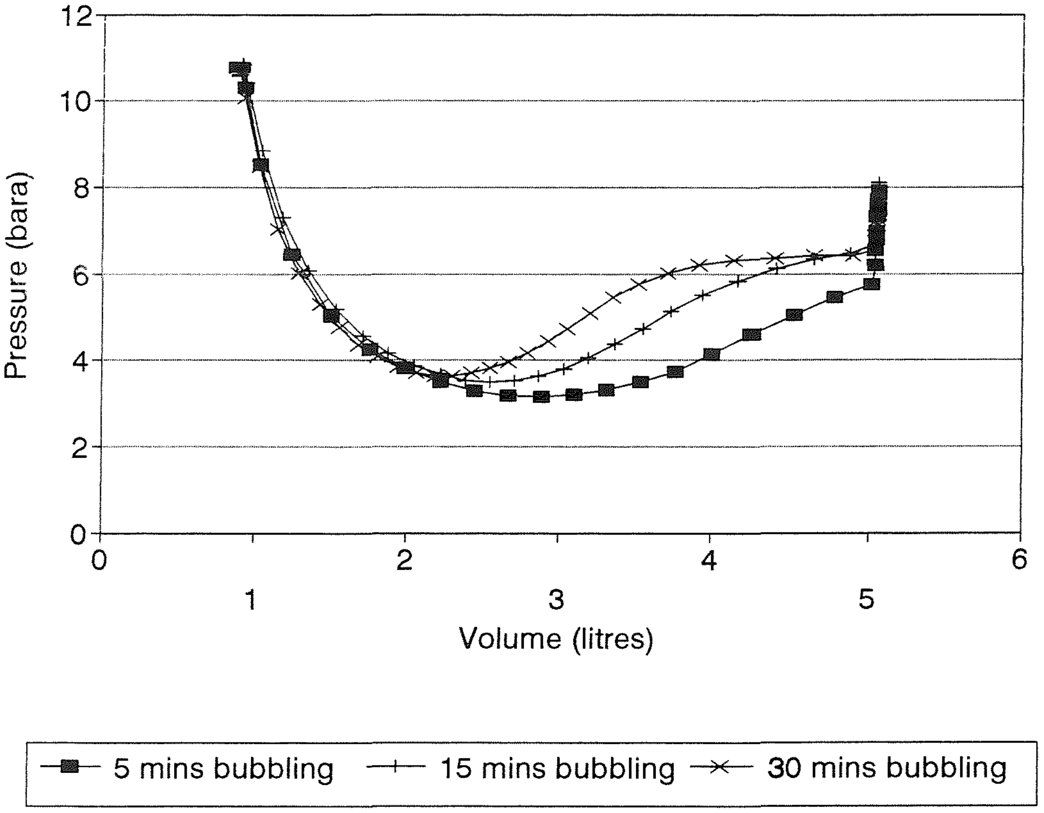

Figure 6.38 cont.. c) piston velocity-time plot, d) pressure-volume plot

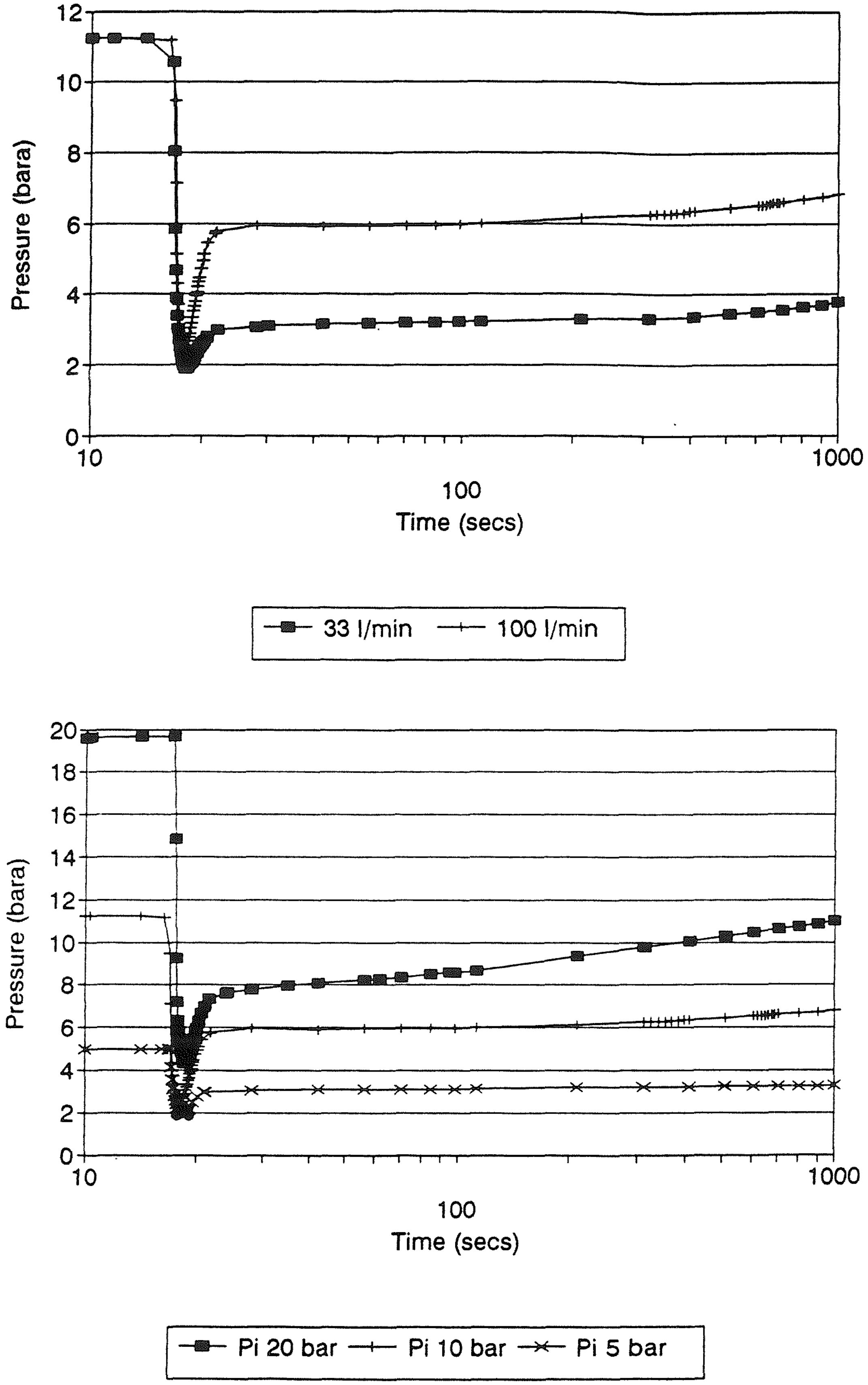

Figure 6.39 Effect of initial gas flow rate, saturation pressure and initial temperature of a CO_2 in gas oil system, 15 mins, a) gas flow rate, 18.8°C ±0.2°, b) saturation pressure, 100 l/min, 19.2°C ±0.6°

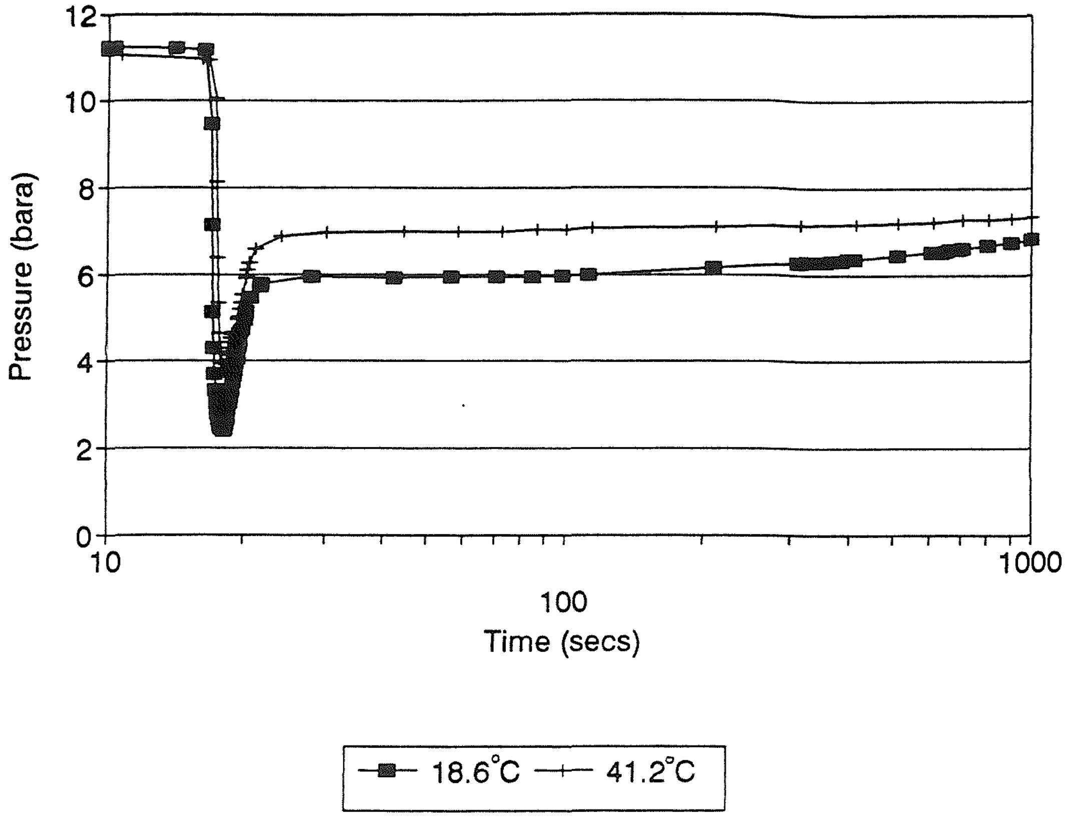

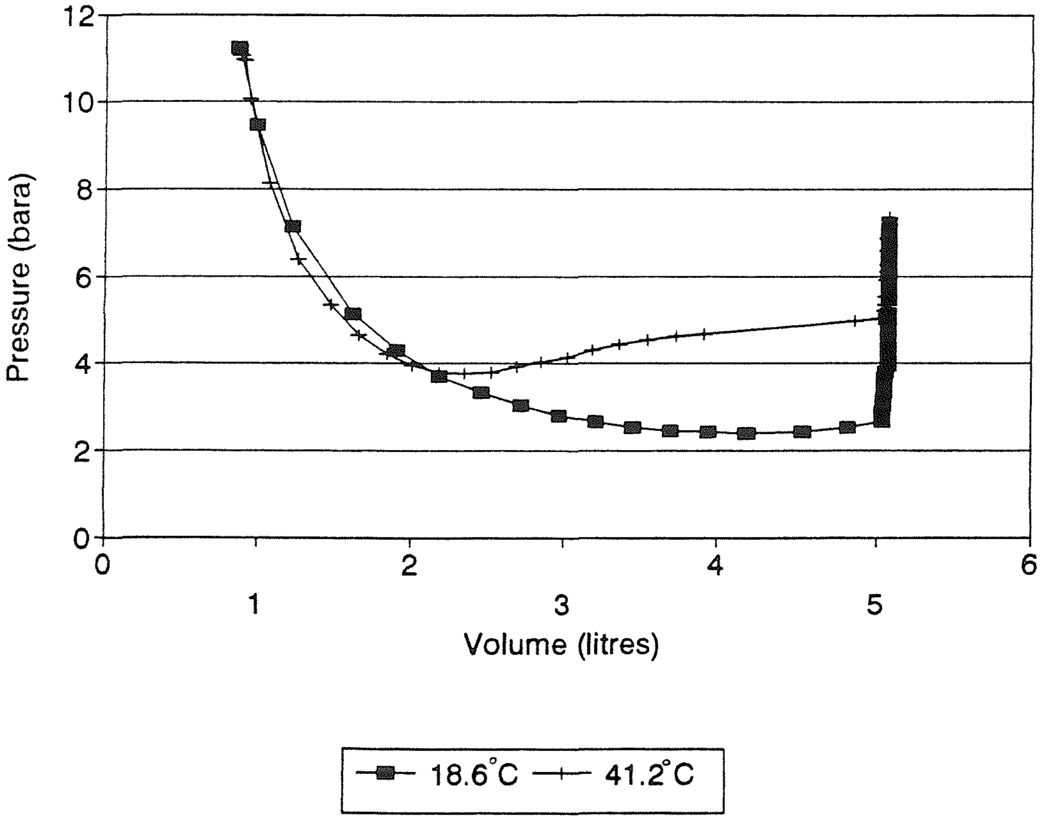

Figure 6.39 cont.. c) initial temperature, 100 l/min i) pressure-time plot, ii) pressure-volume plot

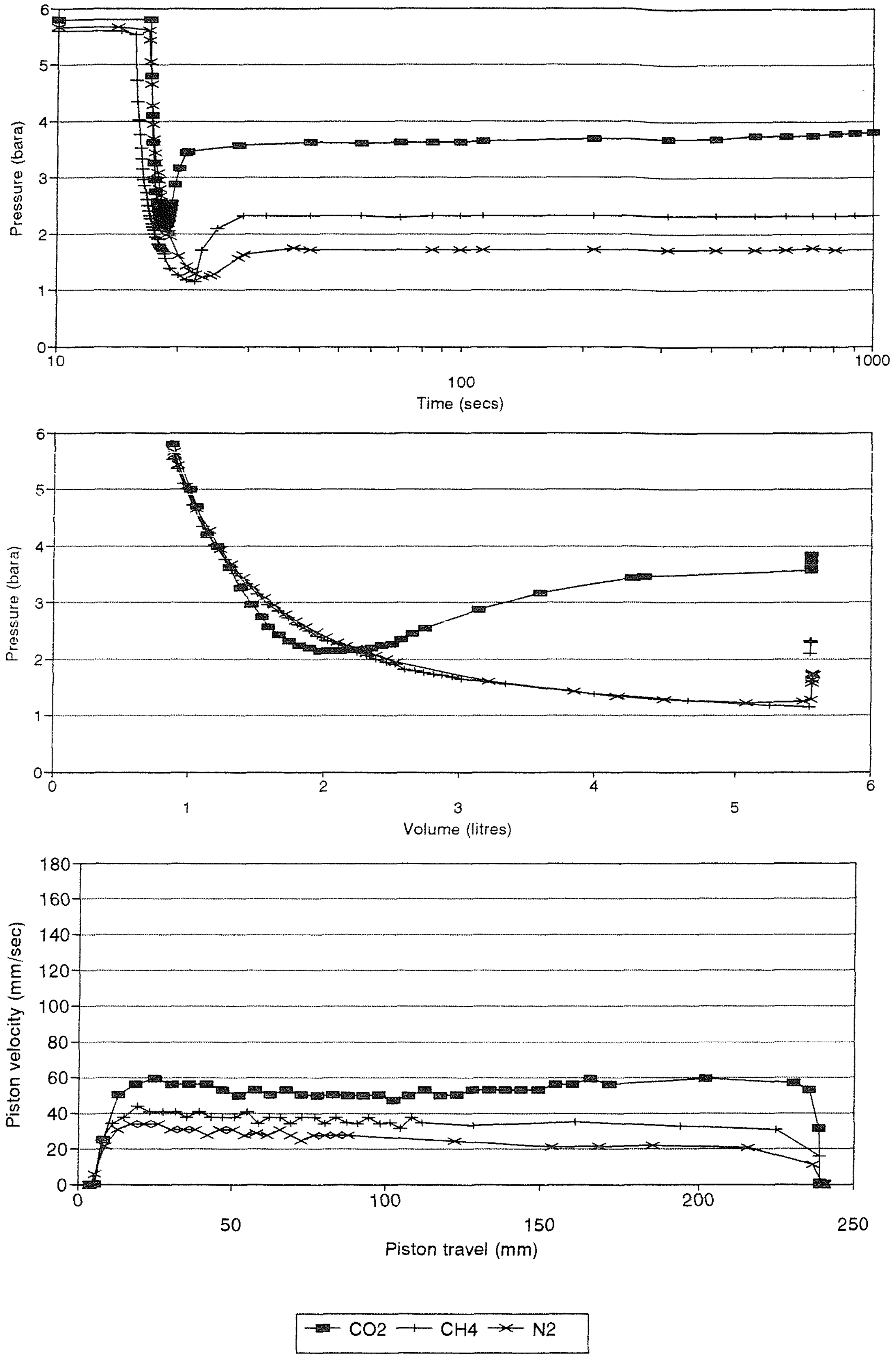

Figure 6.40 Comparison of gases in kerosene system, 100 l/min, 15 mins, 18°C ±0.2°, initial saturation pressure 5 bara, a) pressure-time plot, b) pressure-volume plot, c) piston velocity-travel plot

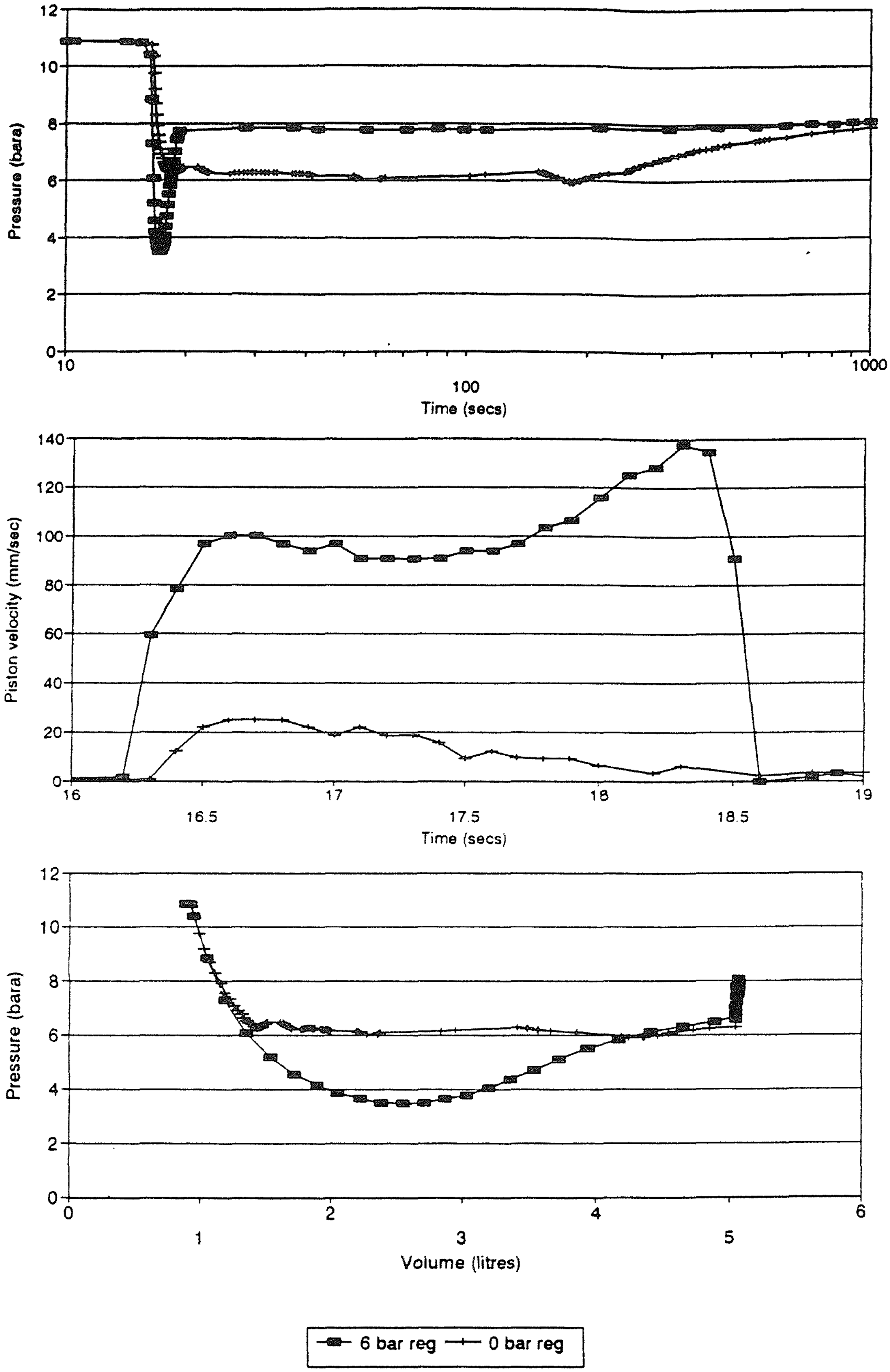

Figure 6.41 Effect of piston velocity on the rate of gas evolution from a CO_2/kerosene system, 100 l/min, 15 mins, 18.9°C ±0.2°, a) pressure-time plot, b) piston velocity-time plot, c) pressure-volume plot

Note: legend refers to pressure of actuator air cylinder

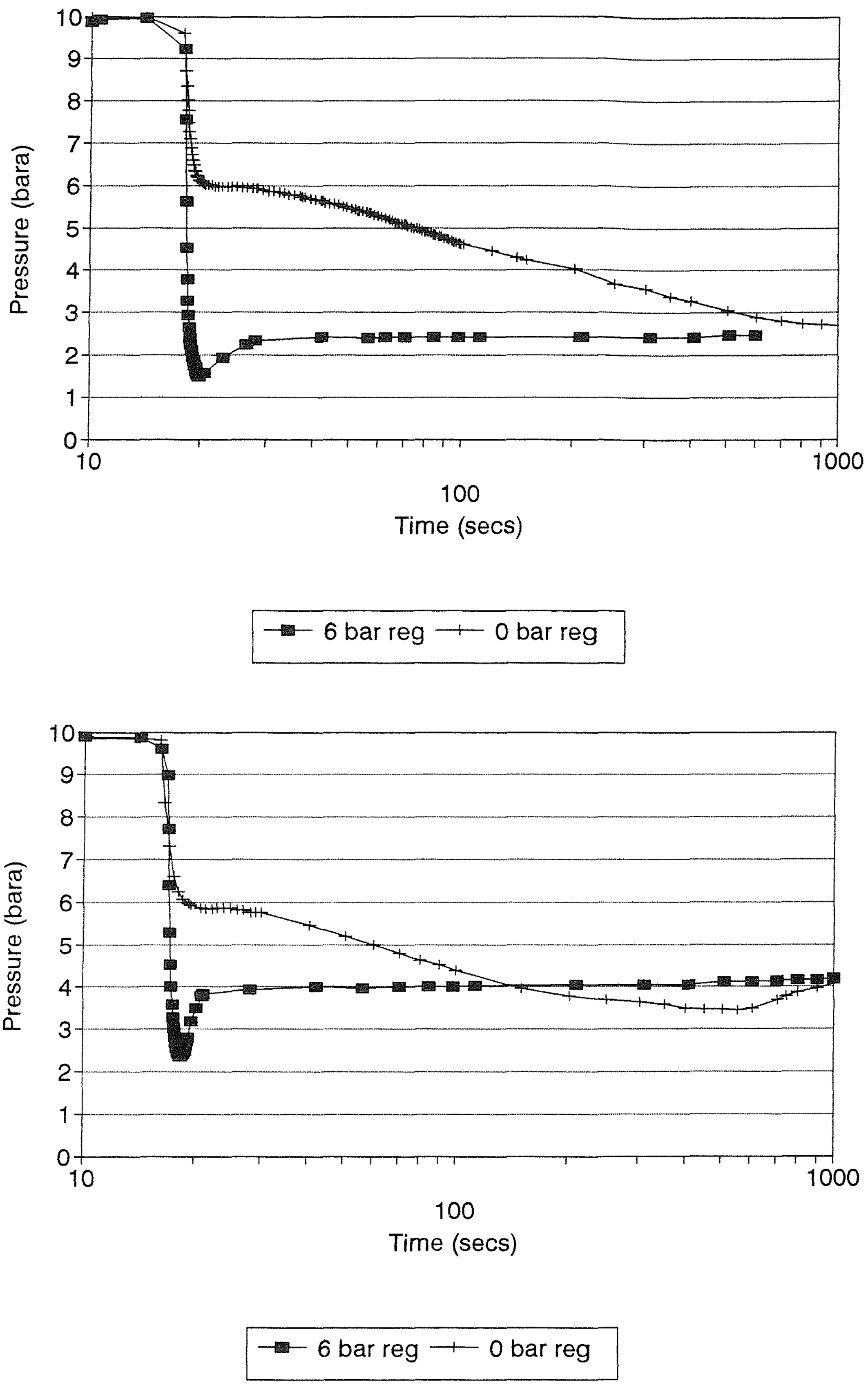

Figure 6.42 Effect of piston velocity on the rate of gas evolution from a) a N_2/gas oil system, 100 l/min, 15 mins, 21.1°C ±0.1°, b) a CH_4/kerosene system, 100 l/min, 15 mins, 18.3°C ±0.3°

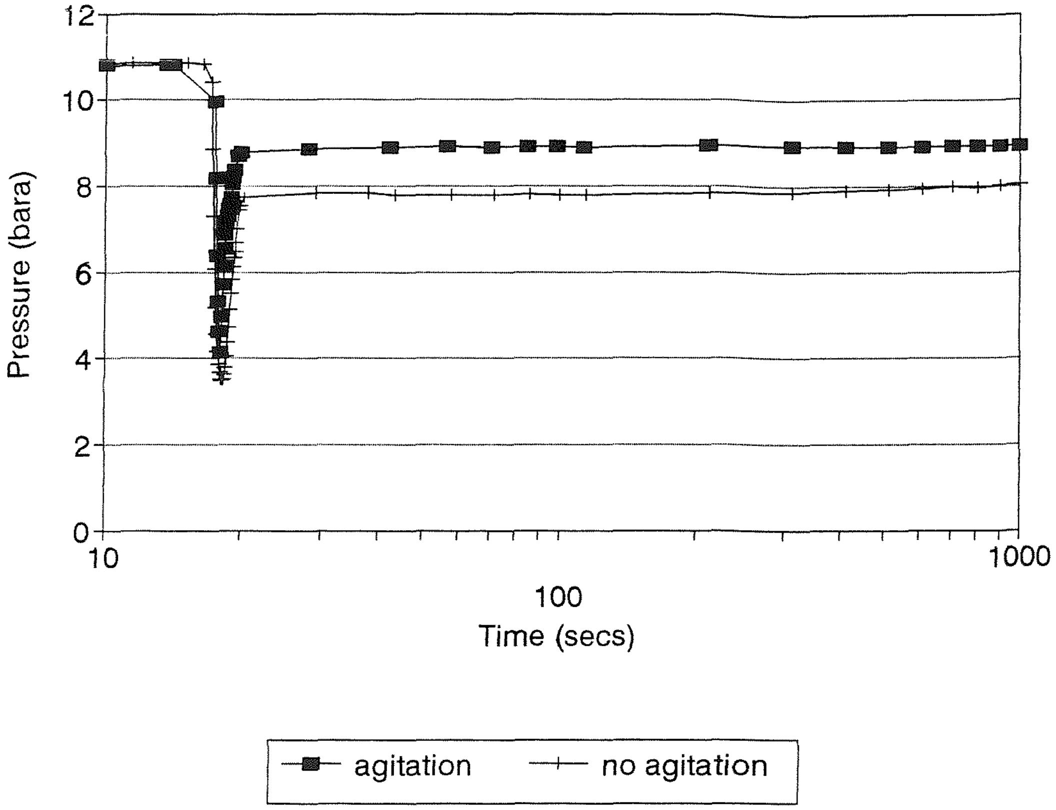

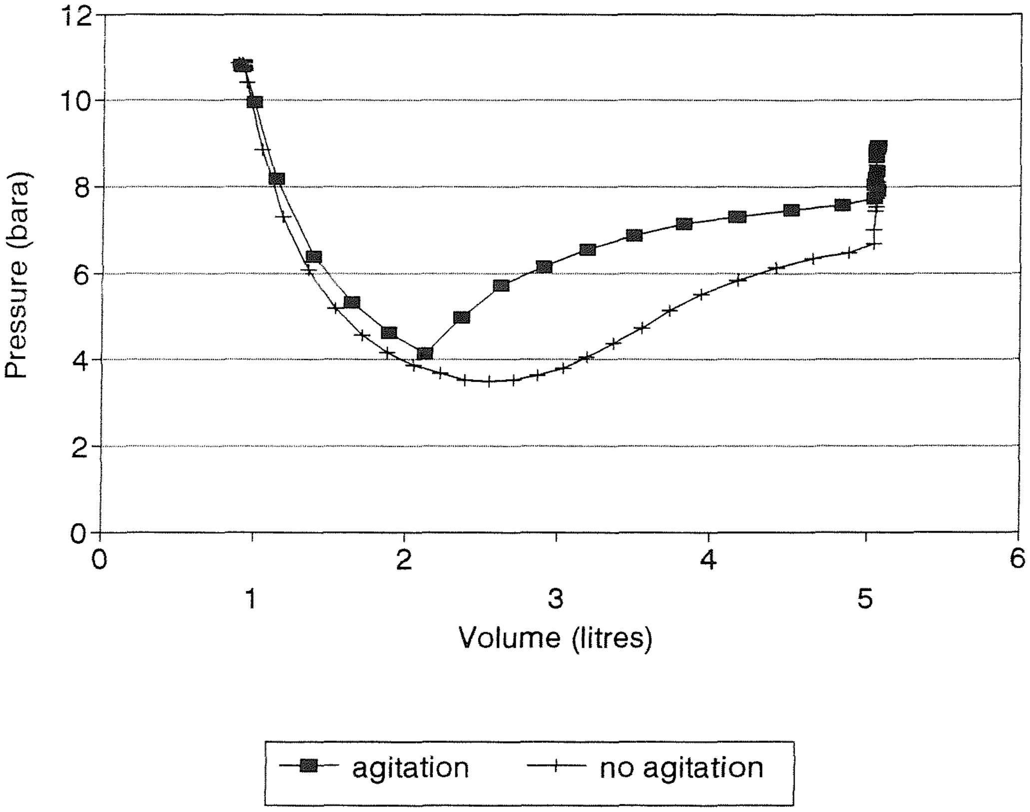

Figure 6.43 Effect of fluid agitation on the rate of gas evolution from a CO_2/kerosene system, 100 l/min, 15 mins, 18.7°C ±0.1°, a) pressure-time plot, b) pressure-volume plot

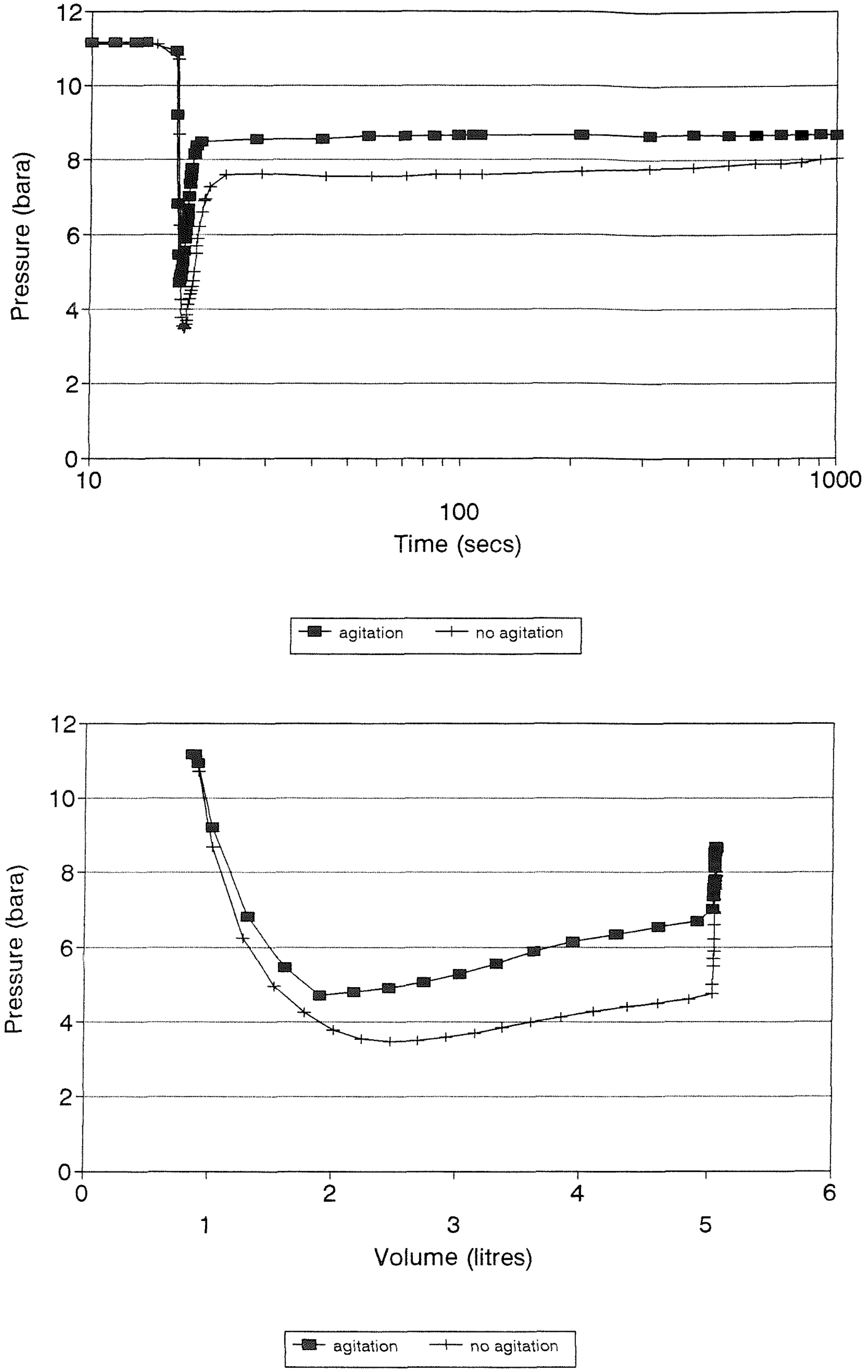

Figure 6.44 Effect of fluid agitation on the rate of gas evolution from a CO_2/Statfjord crude system, 100 l/min, 15 mins, 18.2°C ±0.2°, a) pressure-time plot, b) pressure-volume plot

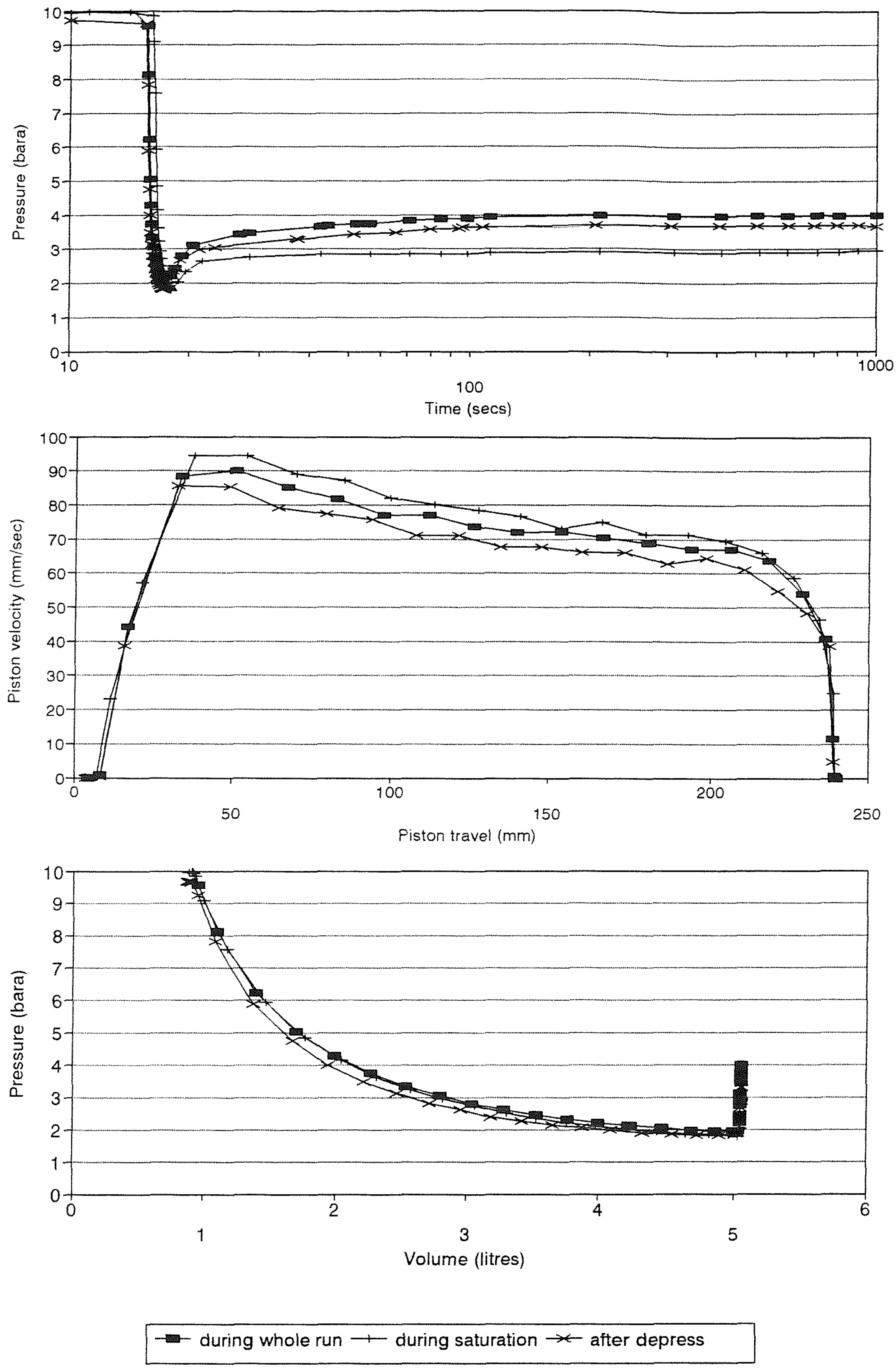

Figure 6.45 Effect of fluid agitation on the rate of gas evolution in a N_2/kerosene system, 100 l/min, 15 mins, 16.6°C ±0.6°, a) pressure-time plot, b) piston velocity-travel plot, c) pressure-volume plot

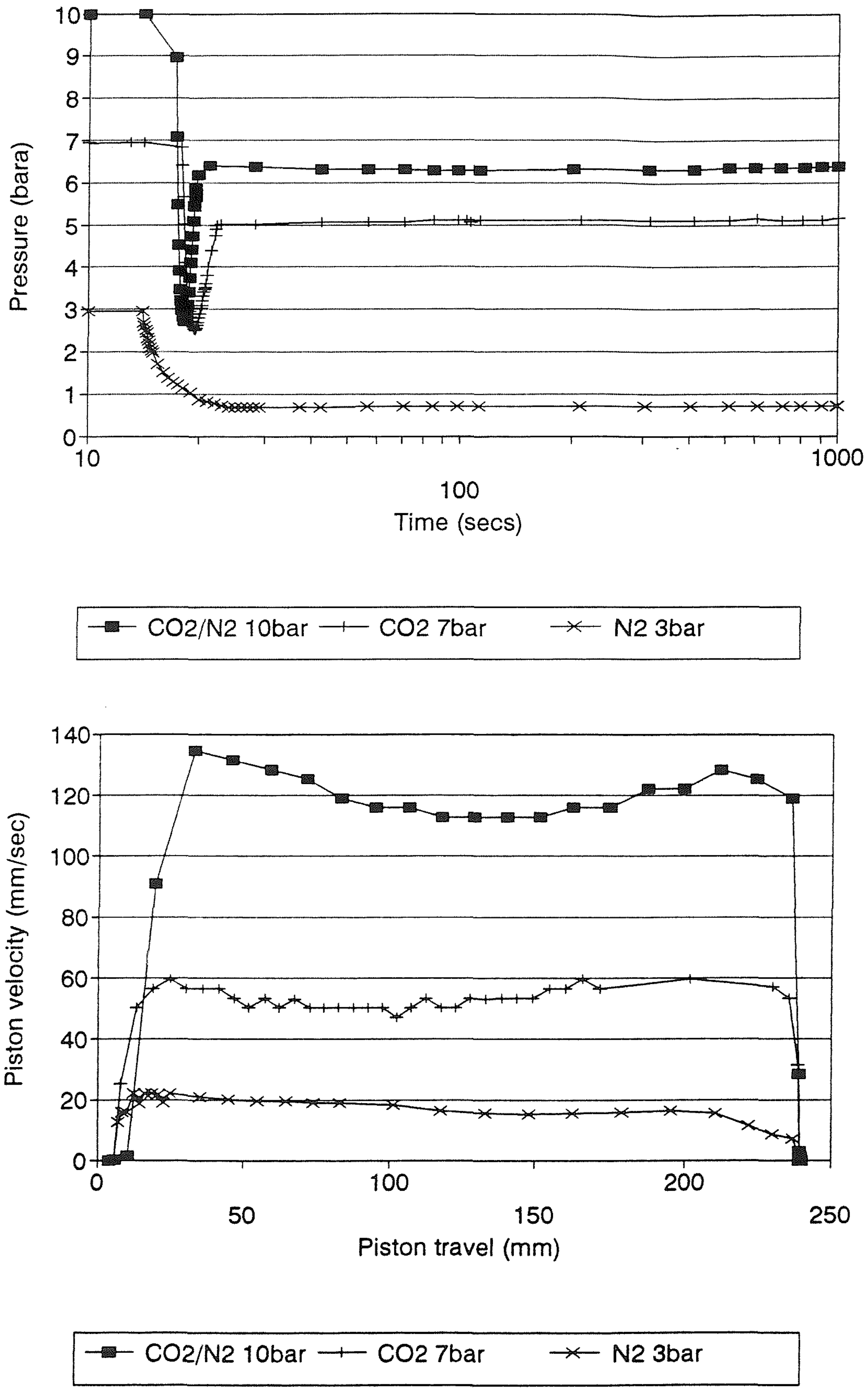

Figure 6.46 Effect of mixed gas composition CO_2 70%/N_2 30% on the rate of gas evolution from kerosene, 100 l/min, 30 mins, 20°C ±0.5°, a) pressure-time plot, b) piston velocity-travel plot

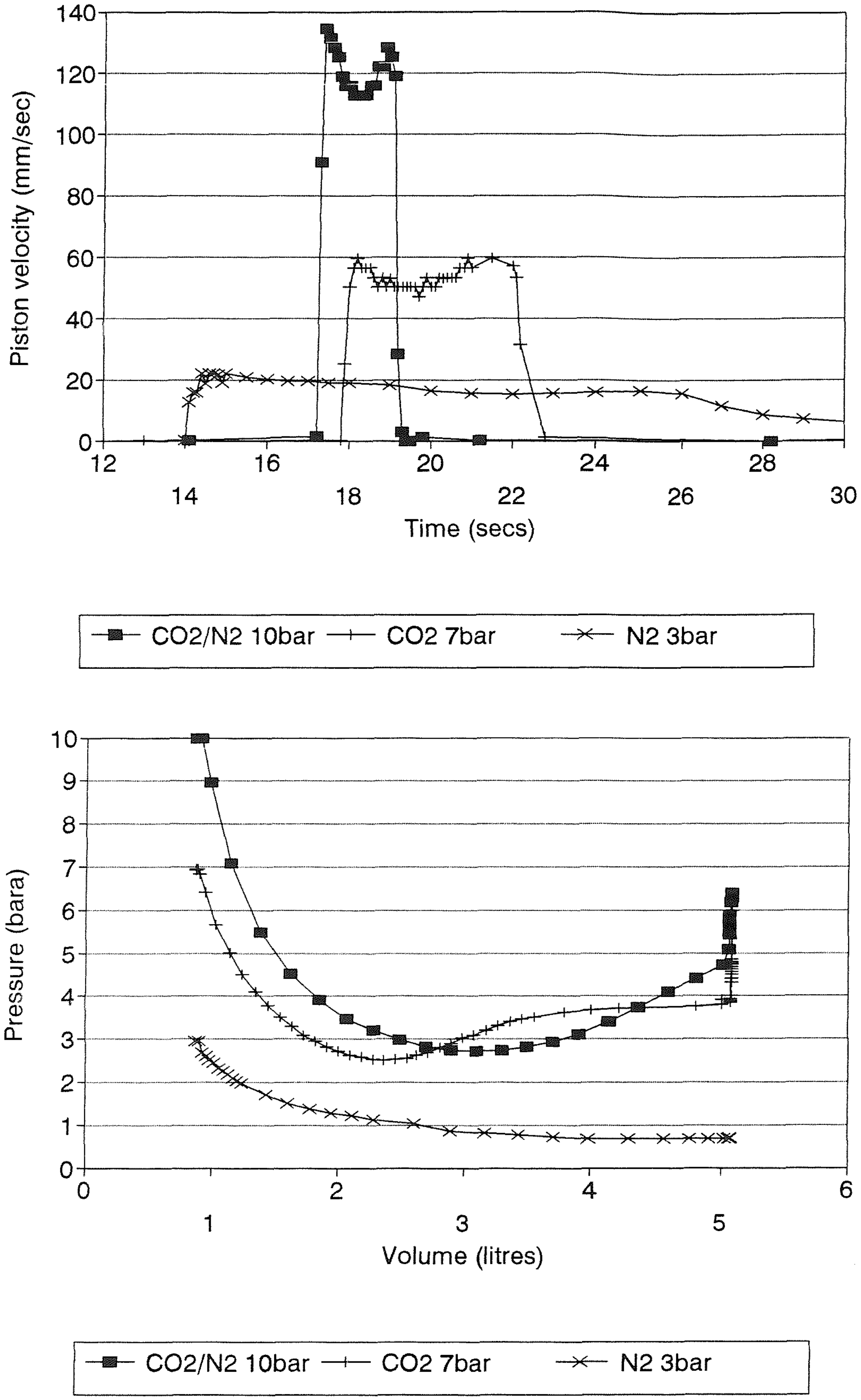

Figure 6.46 cont.. c) piston velocity-time plot, d) pressure-volume plot

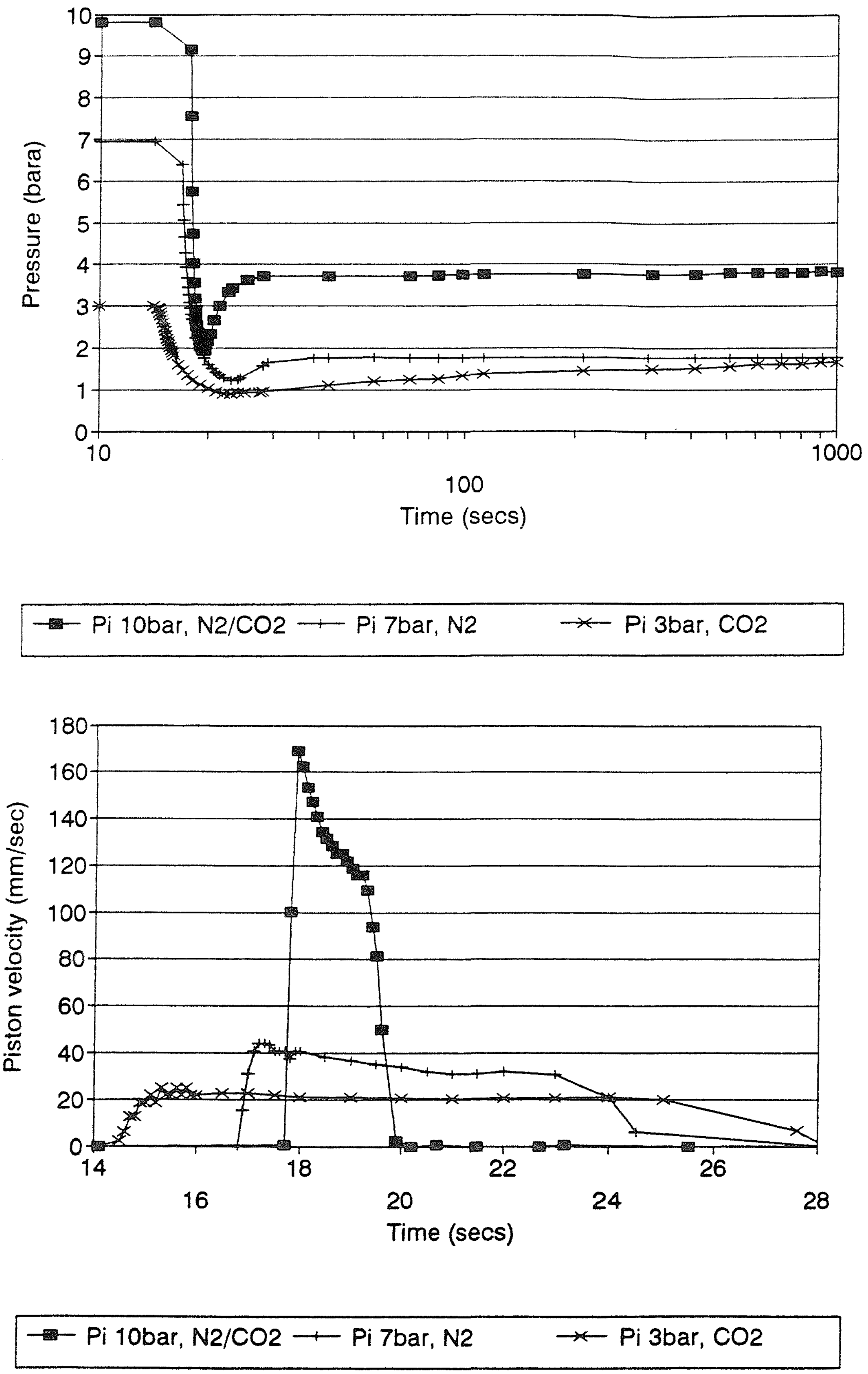

Figure 6.47 Effect of mixed gas composition N_2 70%/CO_2 30% on the rate of gas evolution from gas oil, 100 l/min, 30 mins, 21.1°C ±1°, a) pressure-time plot, b) piston velocity-travel plot

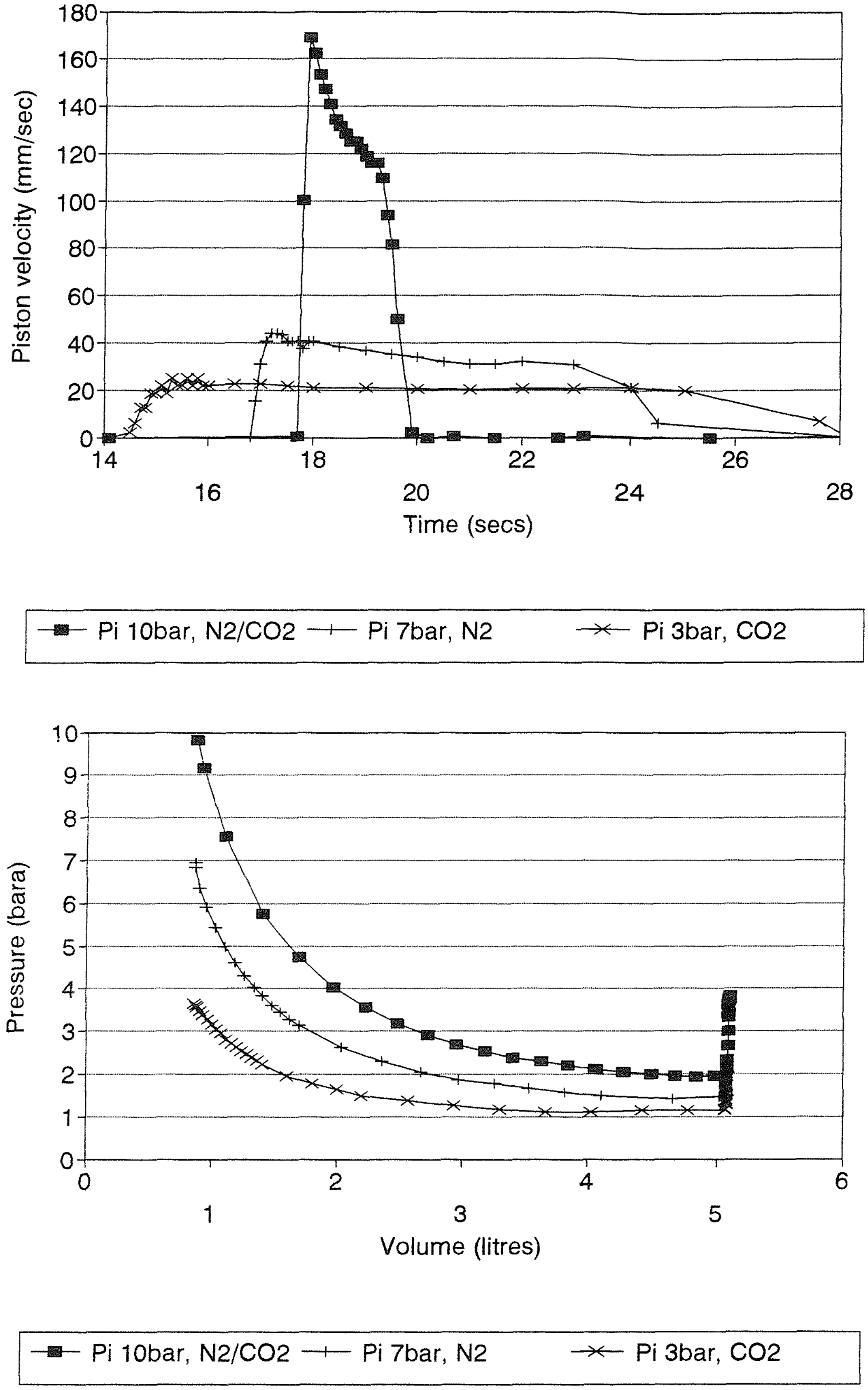

Figure 6.47 cont.. c) piston velocity-time plot, d) pressure-volume plot

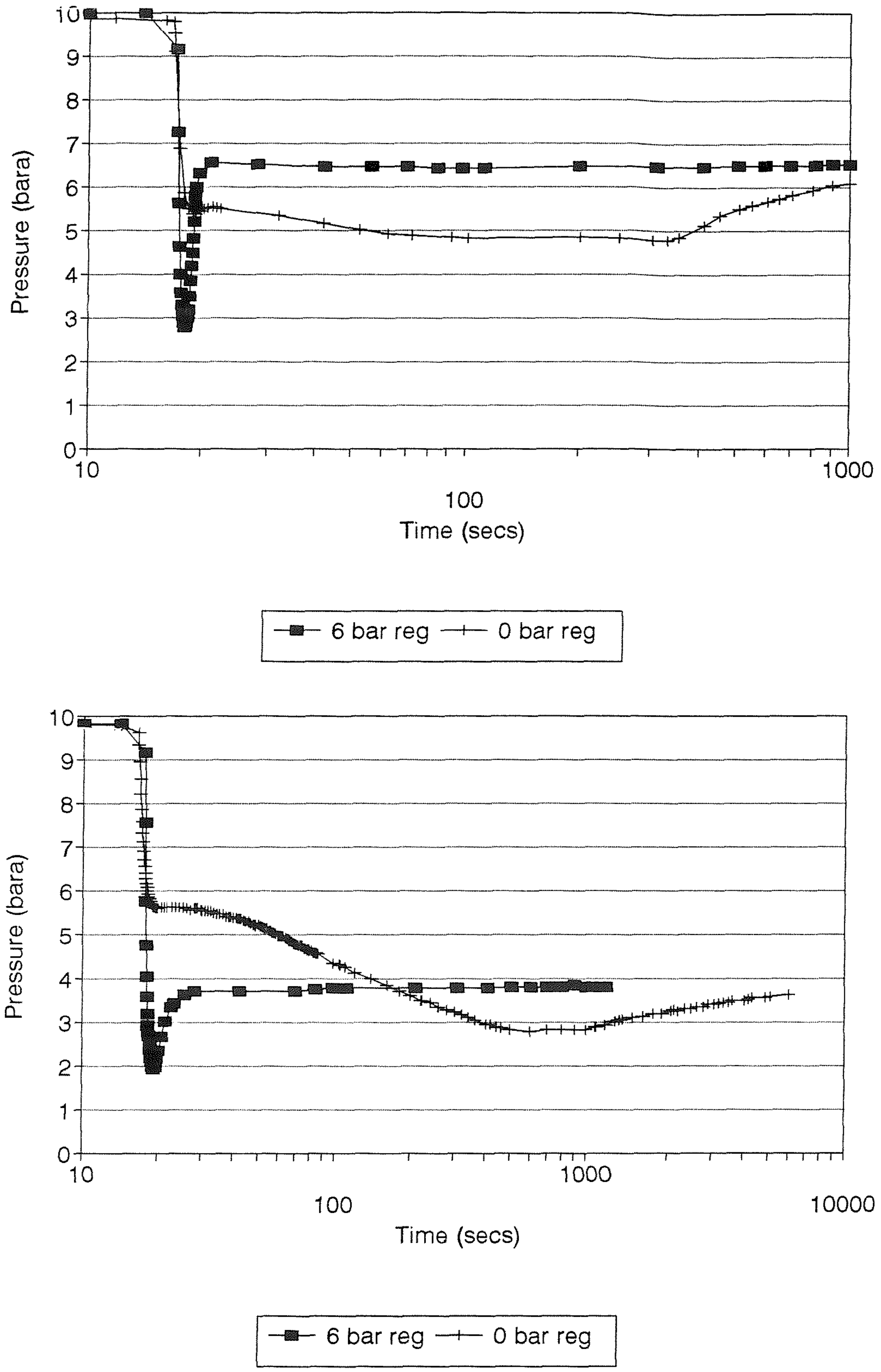

Figure 6.48 Effect of piston velocity on the rate of gas evolution from a mixed gas composition 100 l/min, 15 mins, 21°C ±2°, a) pressure-time plot, CO_2 70%/N_2 30% /kerosene system, b) pressure-time plot, N_2 70%/CO_2 30% /gas oil system

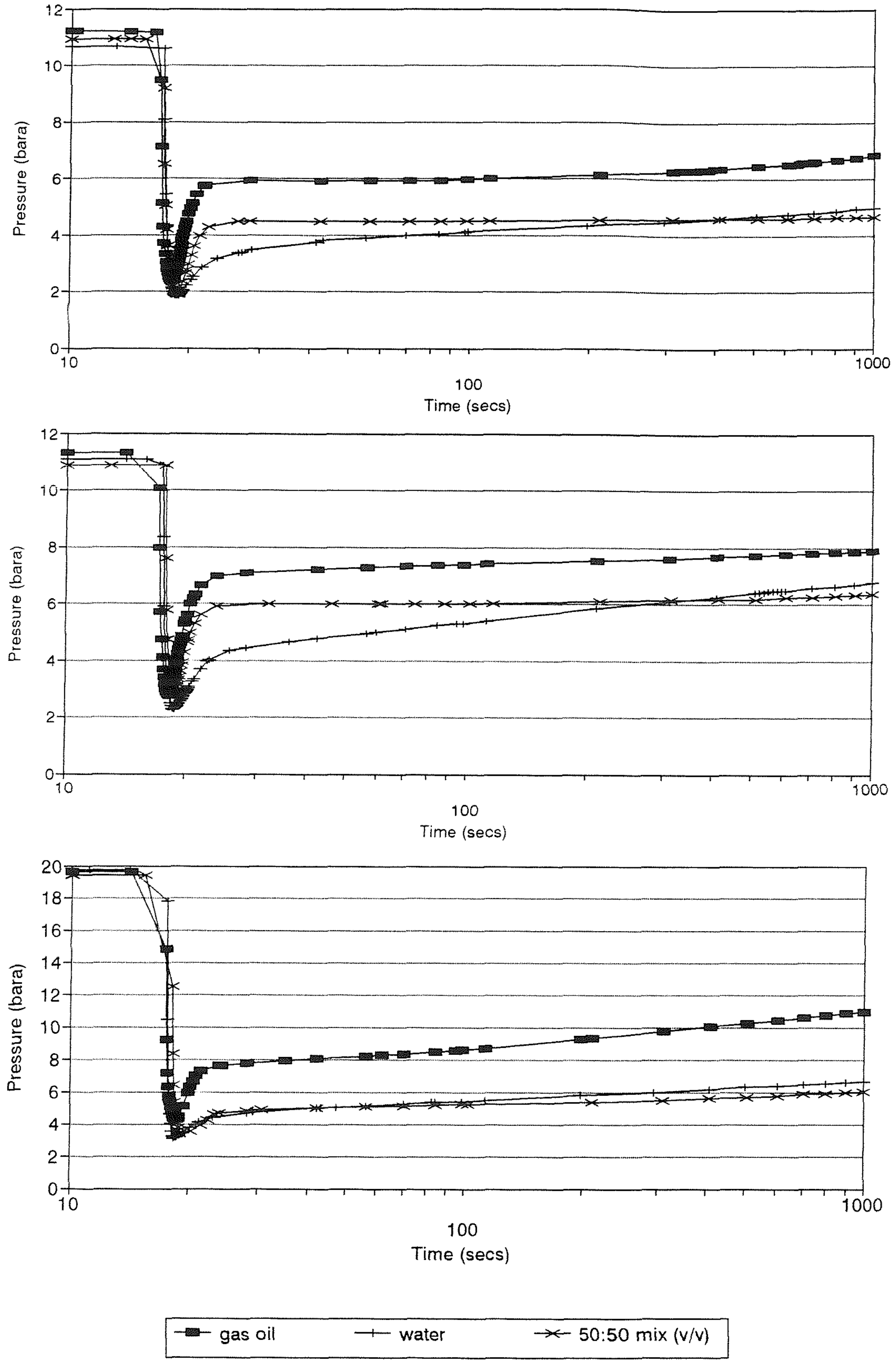

Figure 6.49 Effect of a gas oil/water mix, 50:50 v/v, on the rate of evolution of CO_2, a) 100 l/min, 15 mins, 22.2°C, b) 100 l/min, 120 mins 19.4°C ±0.6°, c) 100 l/min, 15 mins 20°C ±1°, initial saturation pressure 20 bara

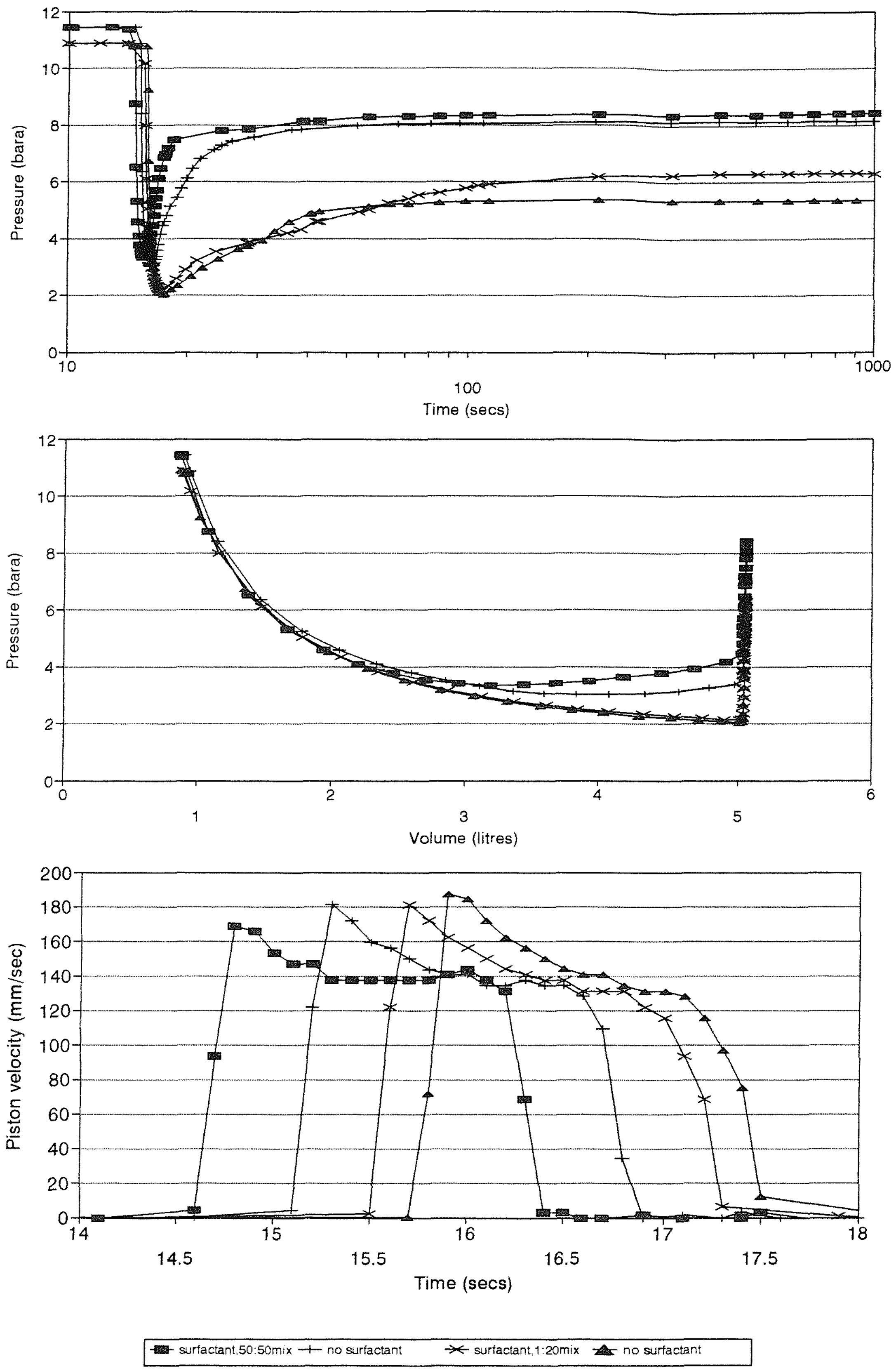

Figure 6.50 Effect of the surfactant, Span 80, on the rate of evolution of CO_2 from a kerosene/water mix, 50:50 v/v, and a kerosene/water mix, 1:20 v/v, 100 l/min, 15 mins, 18°C ±0.6°, a) pressure-time plot, b) pressure-volume plot, c) piston velocity-time plot

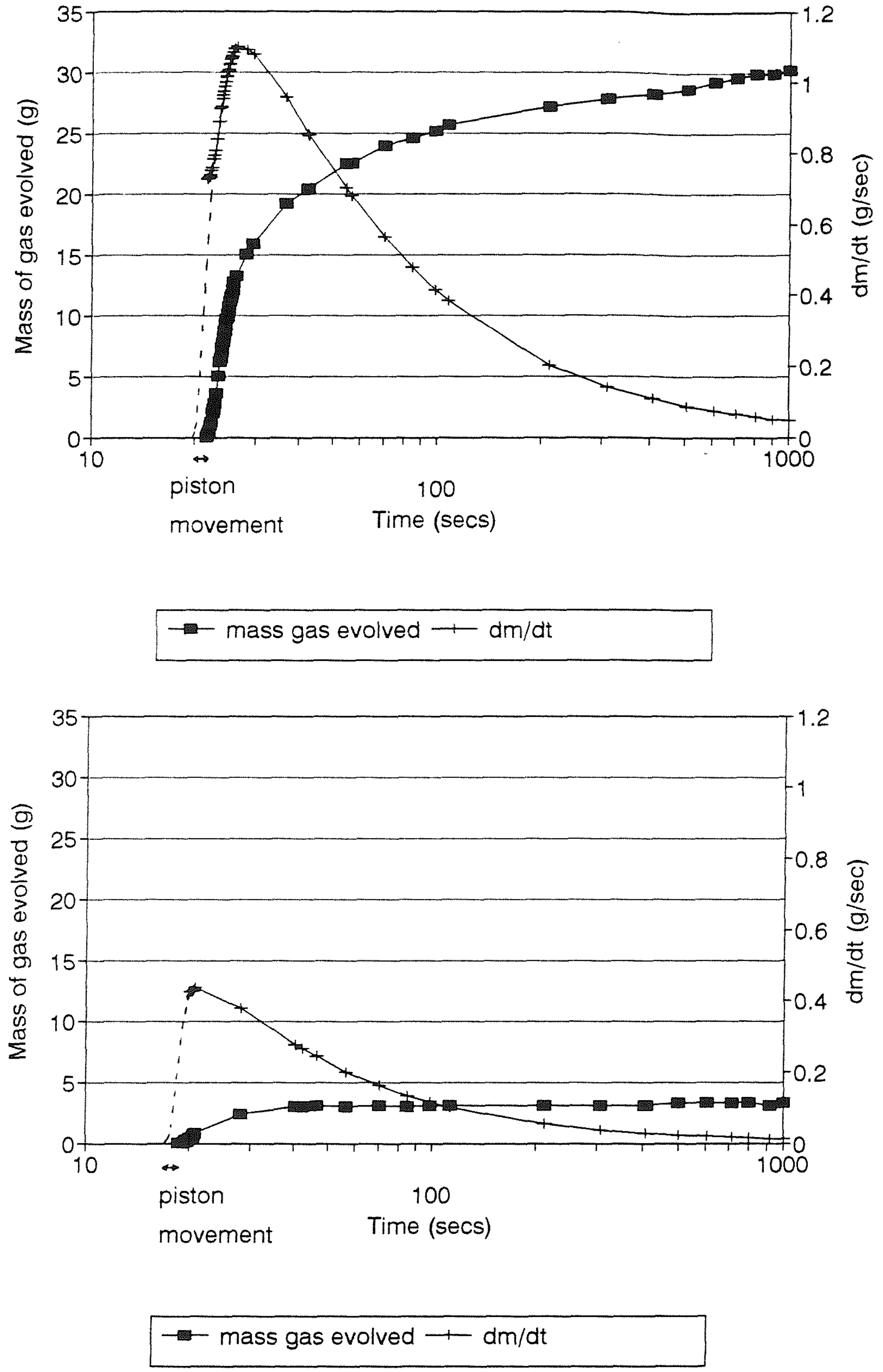

Figure 7.1 Mass of gas evolved and the rate of gas evolved following the rapid depressurization of a) a CO_2 in water system, 100 l/min, 15 mins, 18.6°C and b) a N_2 in water system, 100 l/min, 15 mins, 17.8°C

Note: CO_2 and N_2 plots correspond to plates V avd VI, respectively

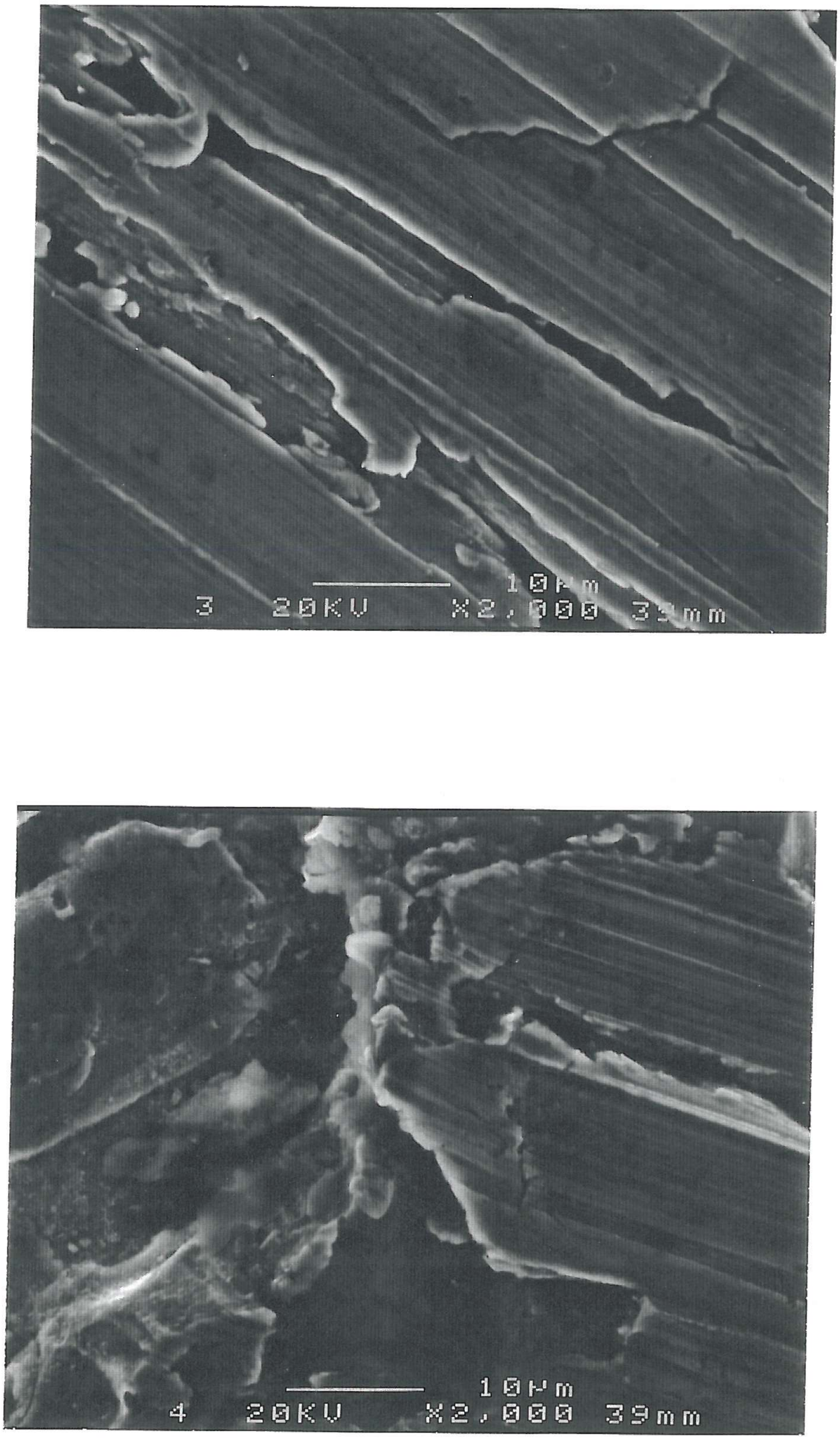

Plate I Photomicrographs taken from samples of the inside walls of the stainless steel pressure vessel

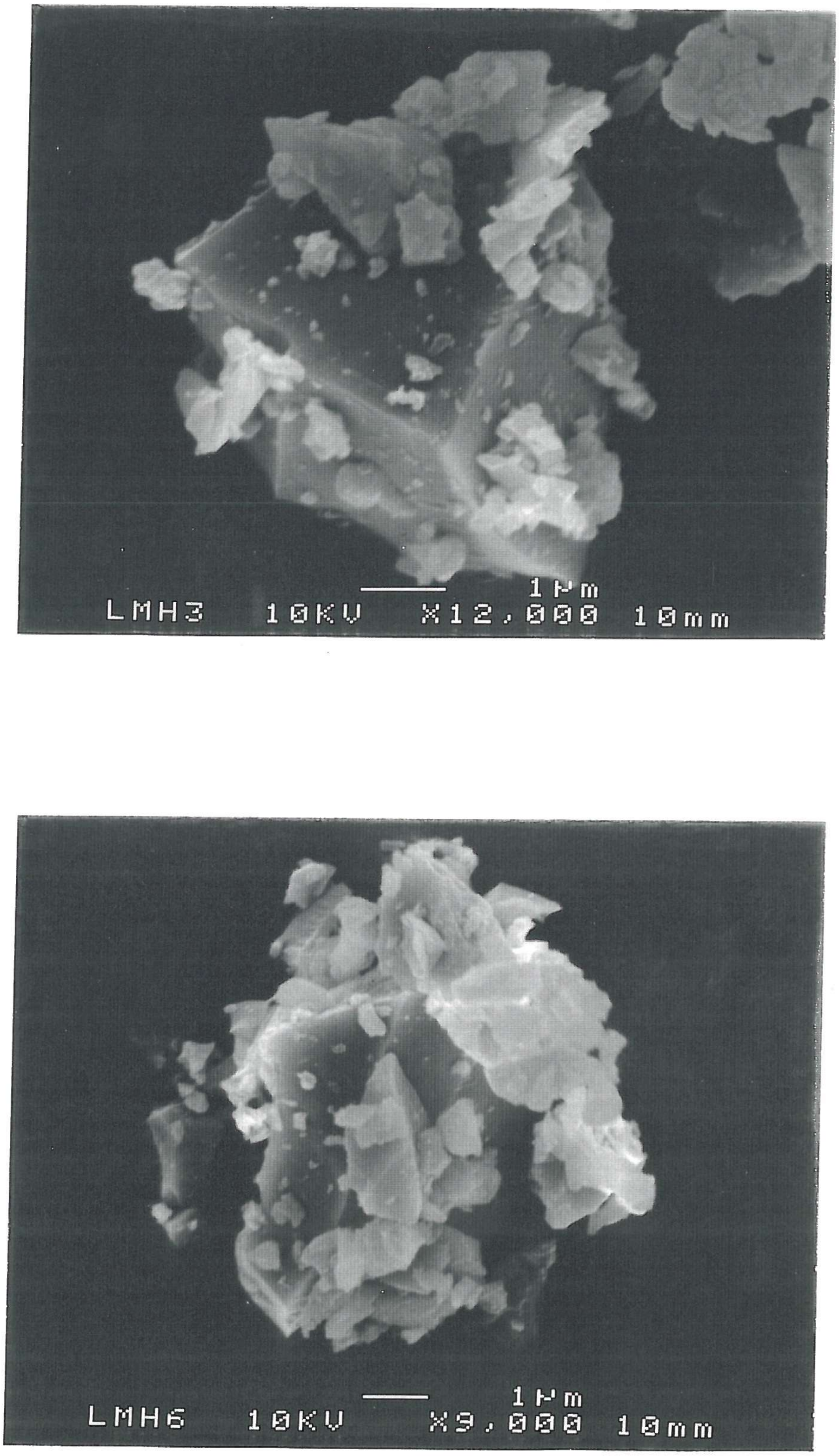

Plate II Photomicrographs of 5μ silica flour particles

Plate III Pressure vessel fabrication stages, i) stock materials and components

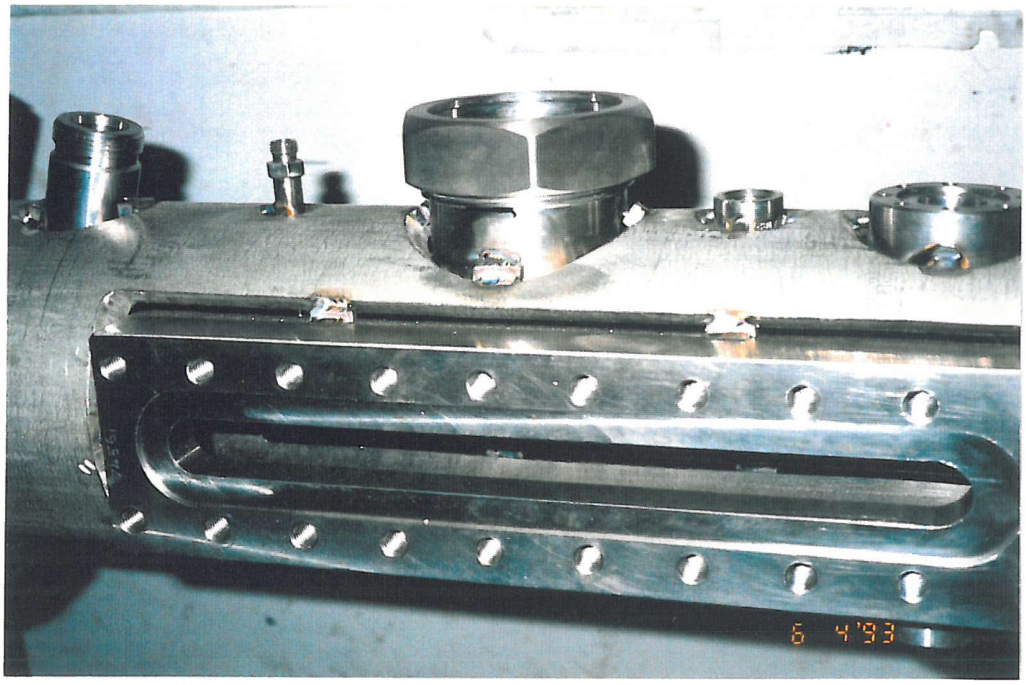

Plate III cont.. ii) tack up and welding

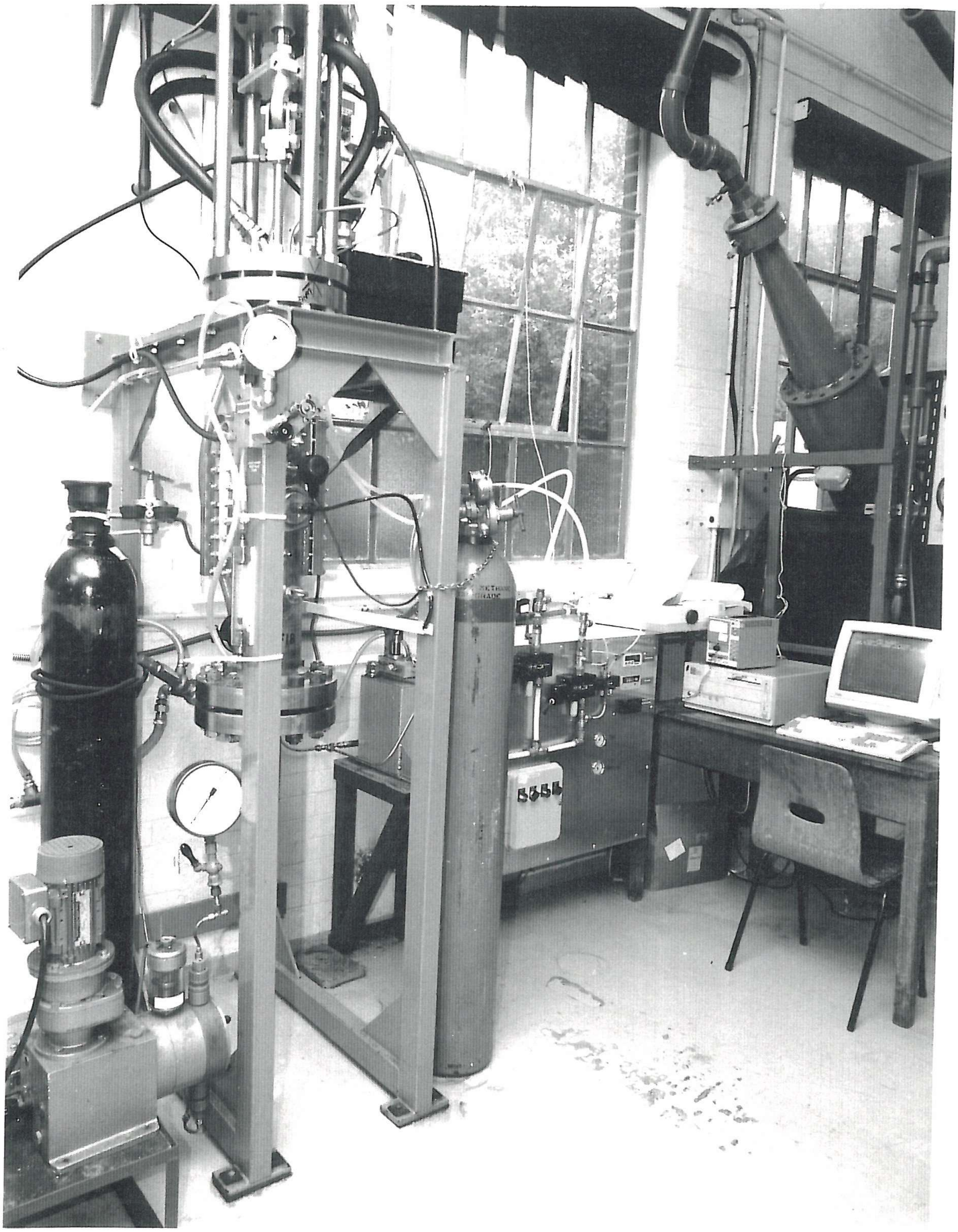

Plate IV	Experimental facility, i) complete rig

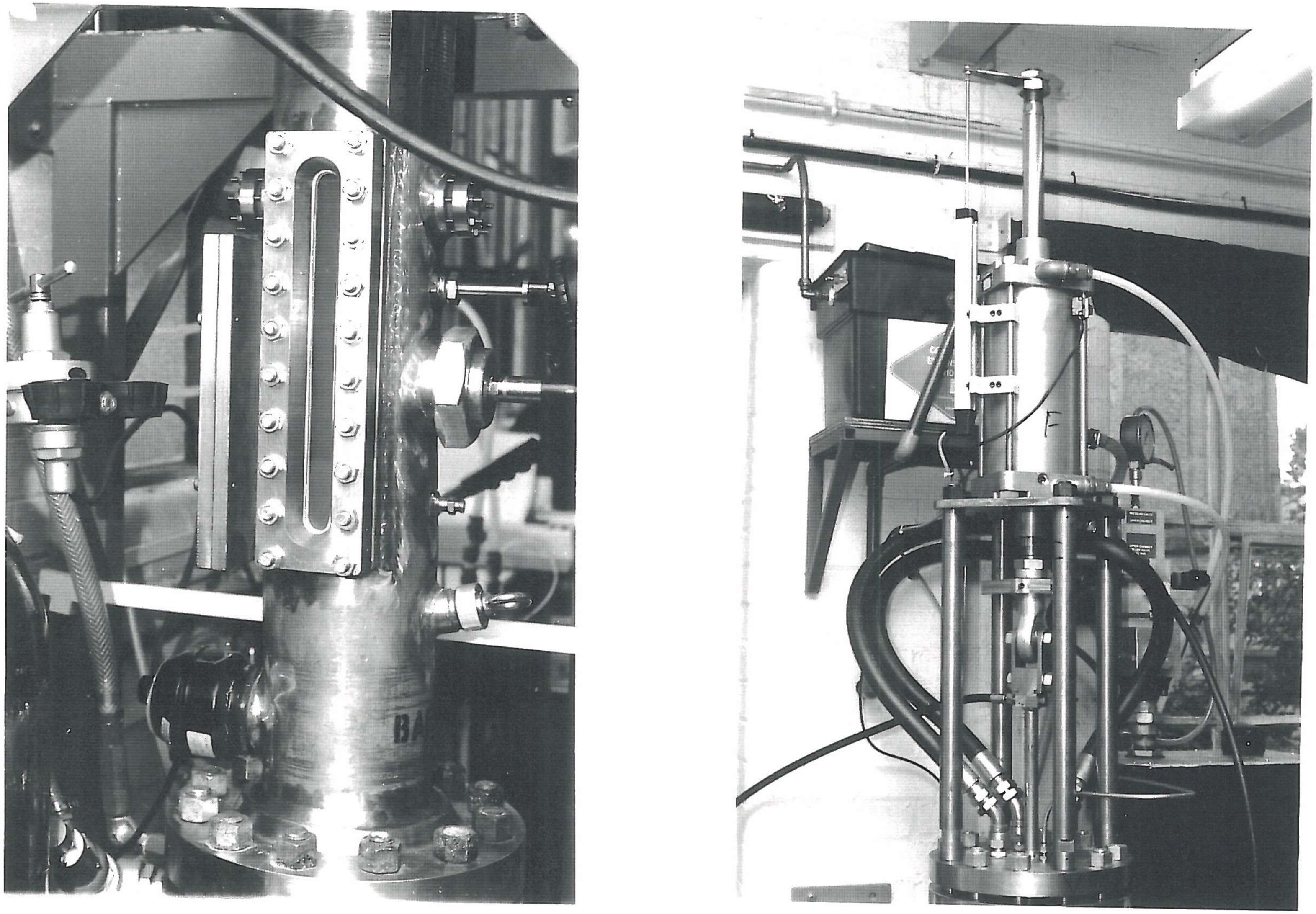

Plate IV cont..   ii) main body, iii) pneumatics system

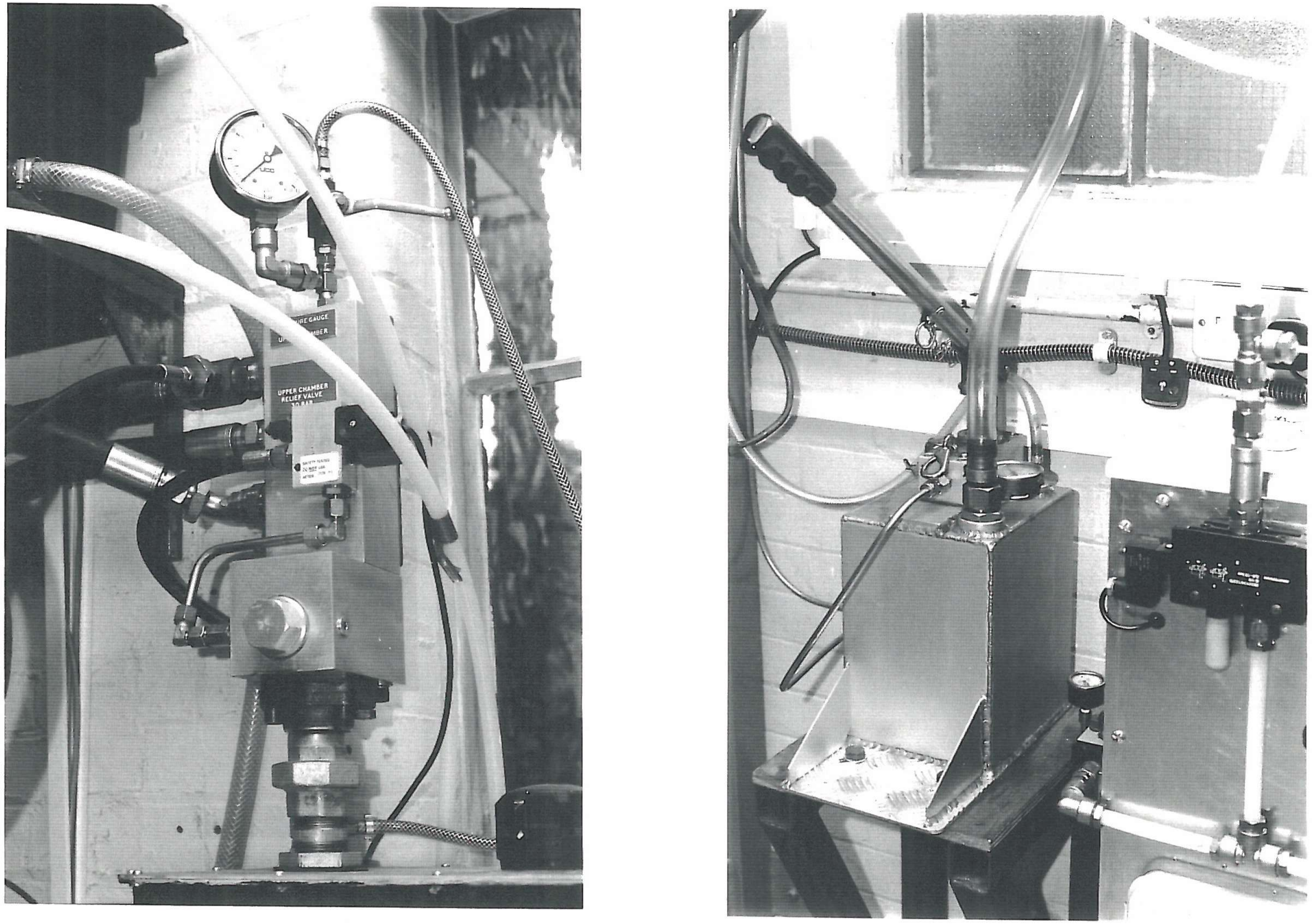

Plate IV cont.. iv) valve combination manifold, v) hand pump and reservoir

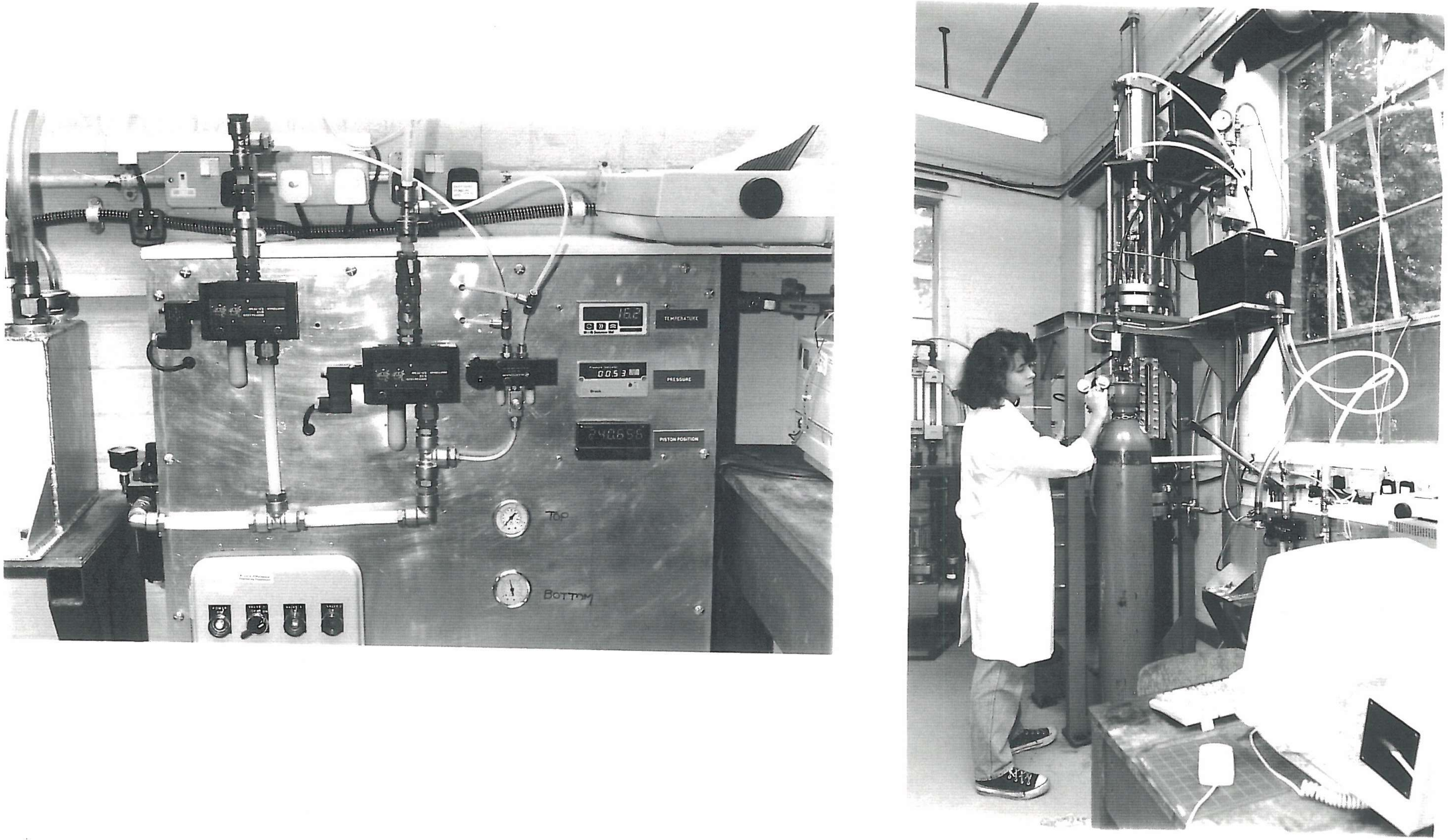

Plate IV cont.. vi) control panel, vii) laboratory set up

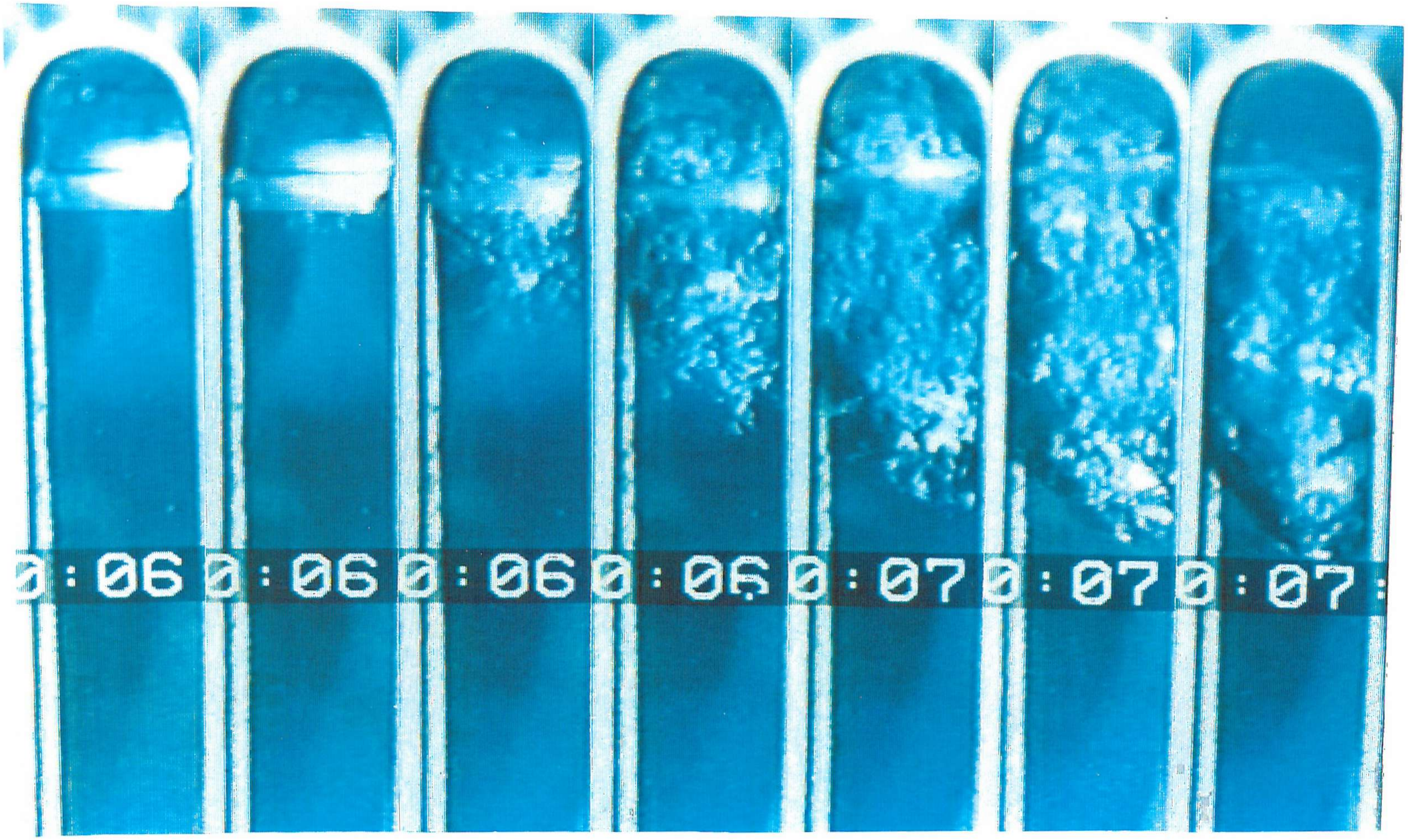

Photograph No	1	2	3	4	5	6	7
Time (secs)	0:00	0:02	0:04	0:06	0:08	0:10	0:12

Plate V Sequence of events captured during the depressurization of a CO_2 in water system, from an initial pressure of 10 bara, ambient temperature and gas flow rate of 100 l/min

Magnification ~ x 1.5

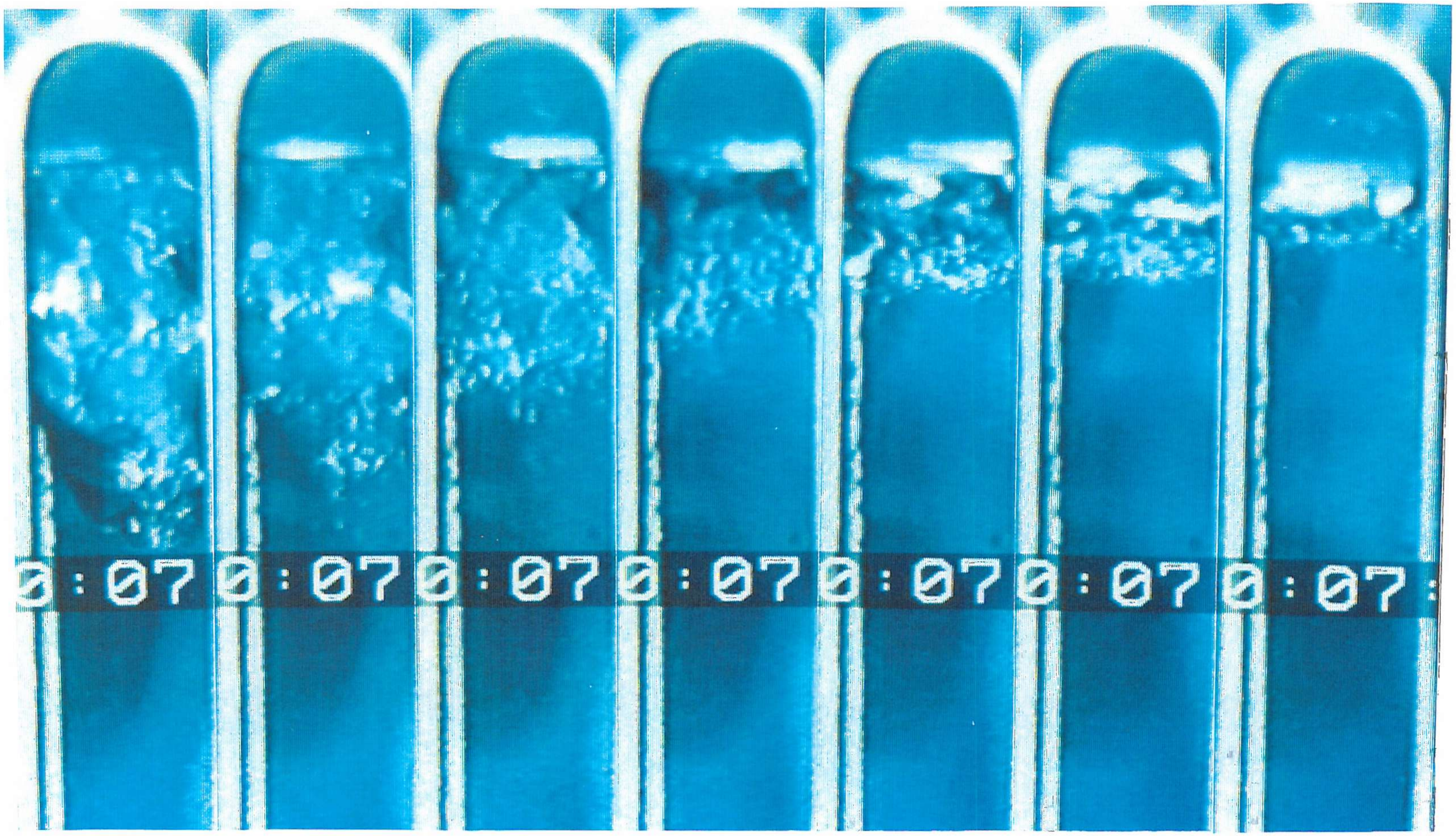

Photograph No	8	9	10	11	12	13	14
Time (secs)	0:14	0:16	0:18	0:20	0:22	0:24	0:26

Plate V cont.. Sequence of events captured during the depressurization of a CO_2 in water system, from an initial pressure of 10 bara, ambient temperature and gas flow rate of 100 1/min

Magnification ~ x 1.5

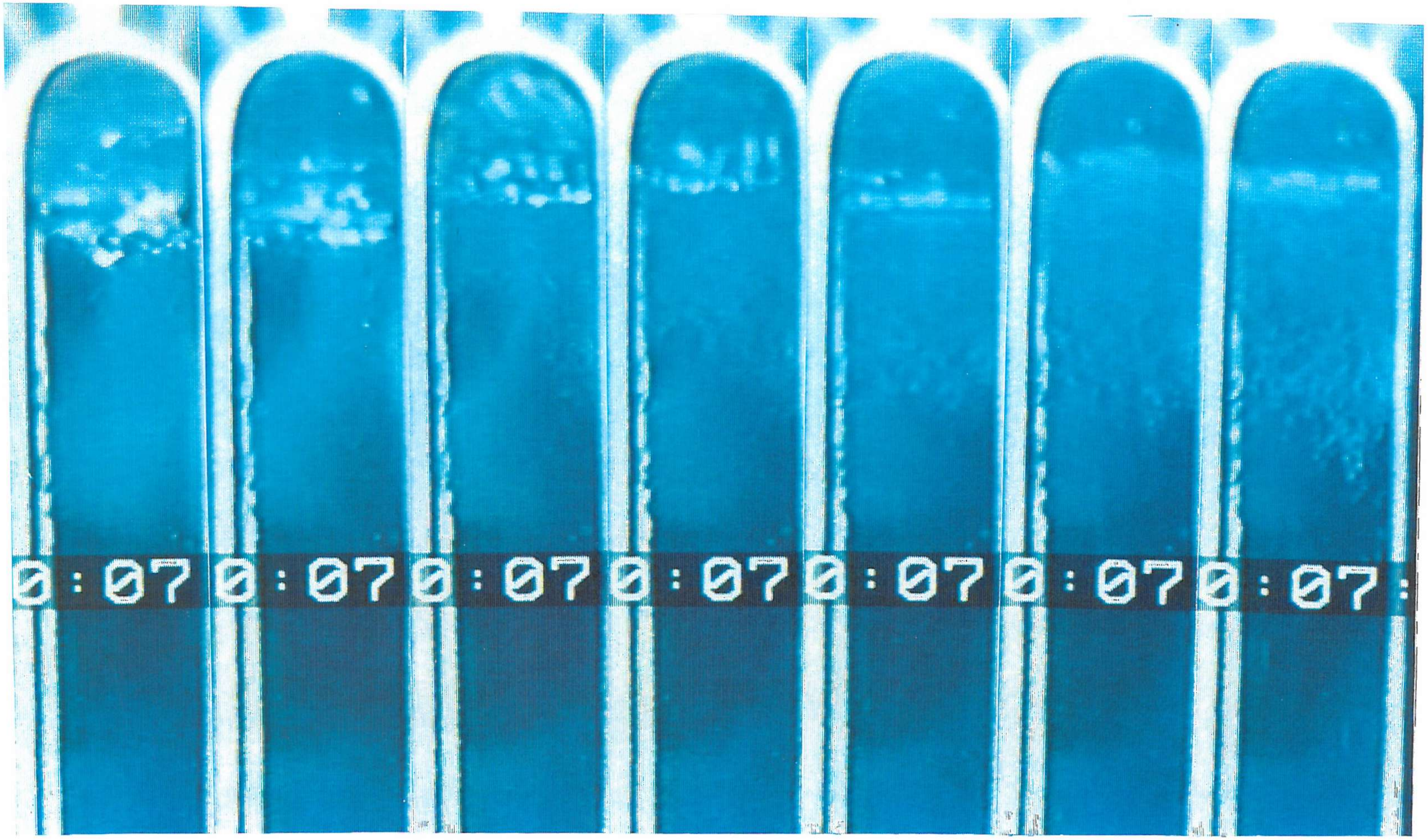

Photograph No	15	16	17	18	19	20	21
Time (secs)	0:32	0:40	0:48	0:56	0:64	0:72	0:96

Plate V cont.. Sequence of events captured during the depressurization of a CO_2 in water system, from an initial pressure of 10 bara, ambient temperature and gas flow rate of 100 1/min

Note: Photographs are not consecutive frames

Magnification ~ x 1.5

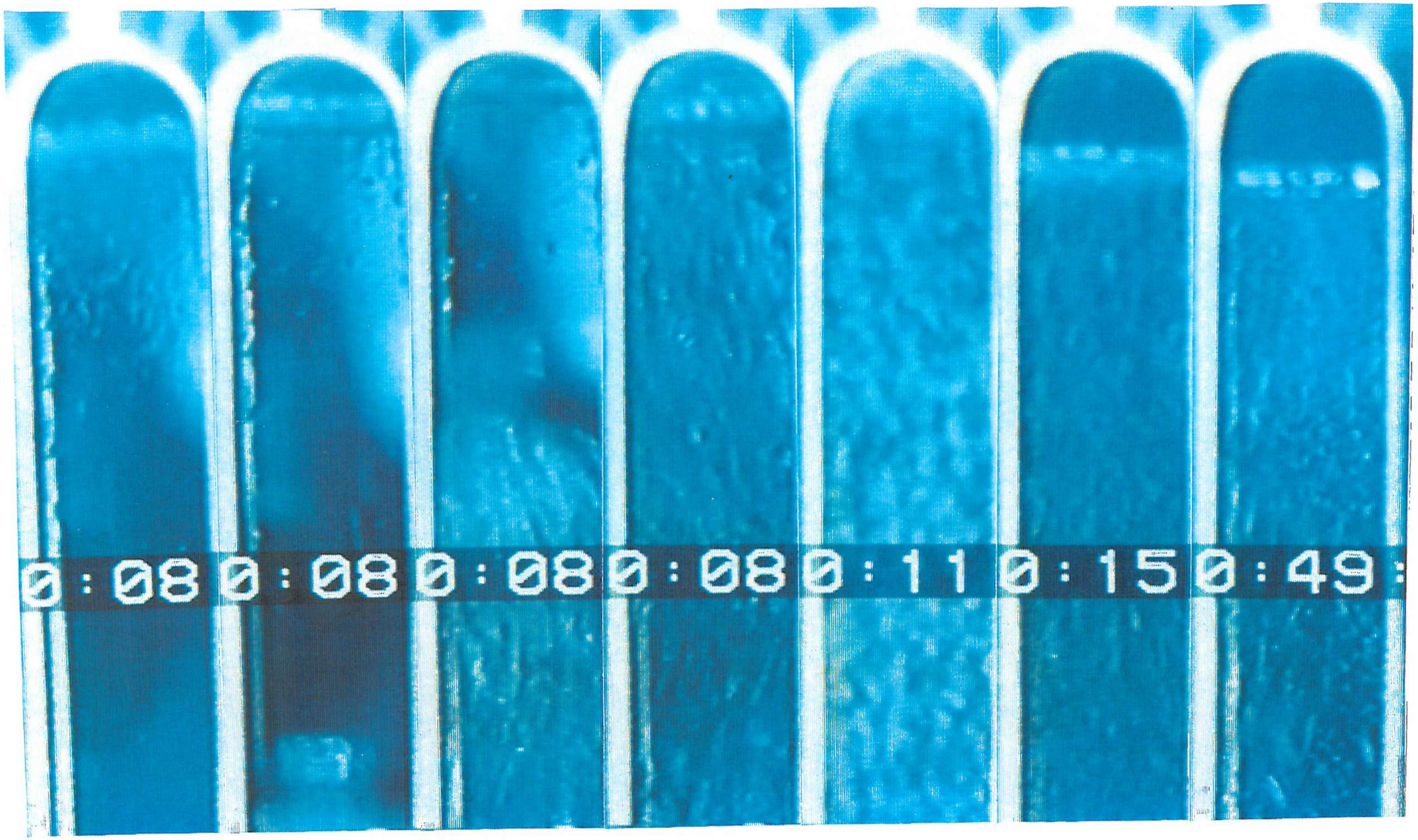

Photograph No	22	23	24	25	26	27	28
Time (secs)	1:32	1:56	1:72	1:84	4:68	9:00	43:00

Plate V cont.. Sequence of events captured during the depressurization of a CO_2 in water system, from an initial pressure of 10 bara, ambient temperature and gas flow rate of 100 1/min

Note: Photographs are not consecutive frames

Magnification ~ x 1.5

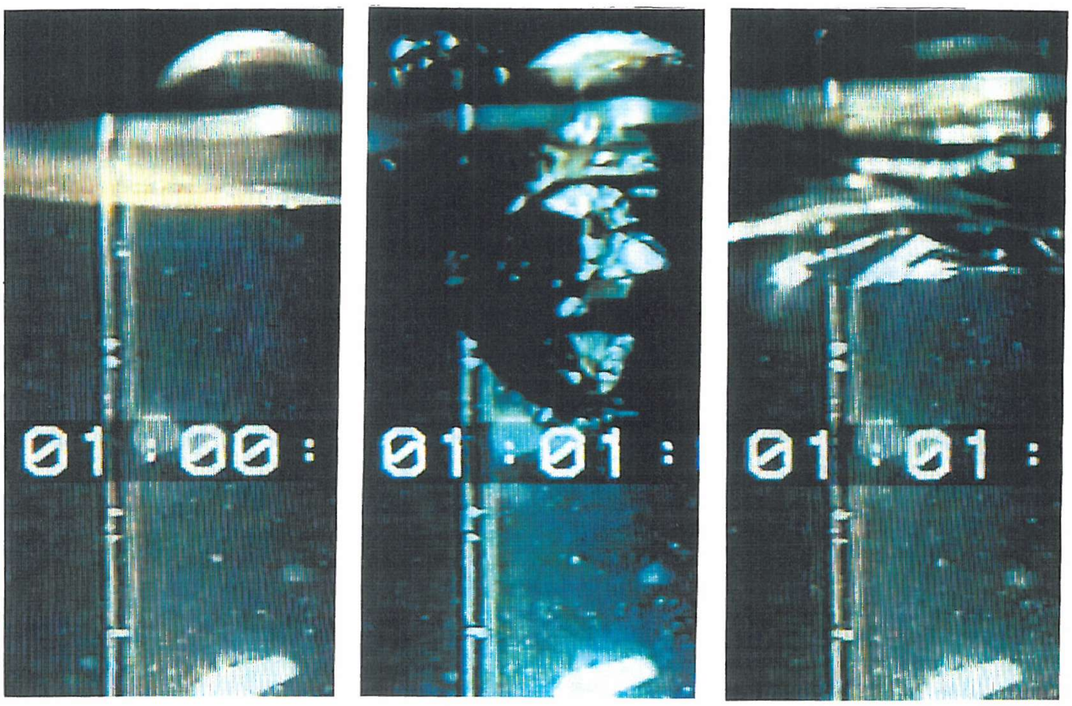

Photograph No	1	2	3
Time (secs)	0:00	0:06	0:16

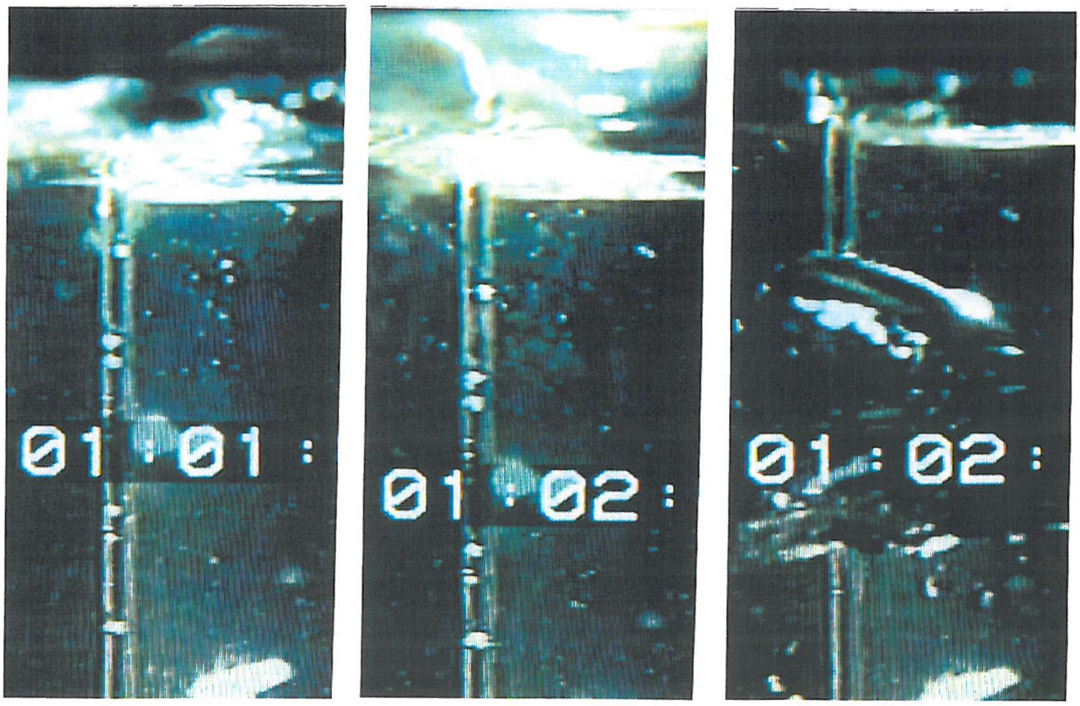

hotograph No	4	5	6
Time (secs)	0:40	1:04	1:76

Plate VI Sequence of events captured during the depressurization of a N_2 in water system, from an initial pressure of 10 bara, ambient temperature and gas flow rate of 100 l/min

Note: Photographs are not consecutive forms Magnification ~ x 2

Photograph No	7	8	9
Time (secs)	1:90	5:32	8:56

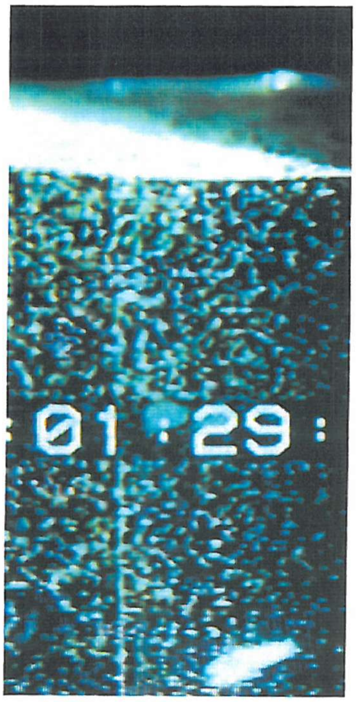

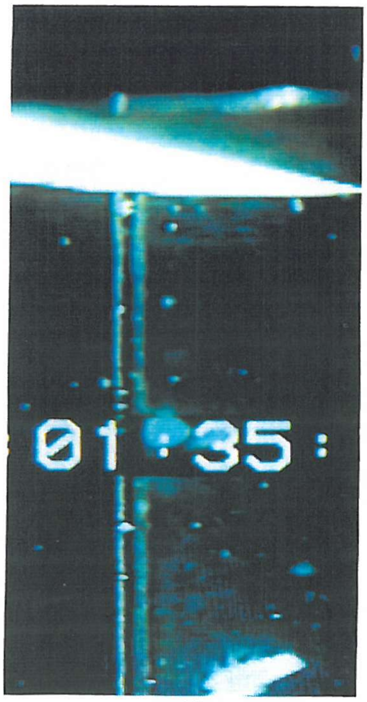

Photograph No	10	11	12
Time (secs)	28:08	31:04	34:72

Plate VI cont.. Sequence of events captured during the depressurization of a N_2 in water system, from an initial pressure of 10 bara, ambient temperature and gas flow rate of 100 l/min

Note: Photograpns are not consecutive frames - Magnification ~x 2

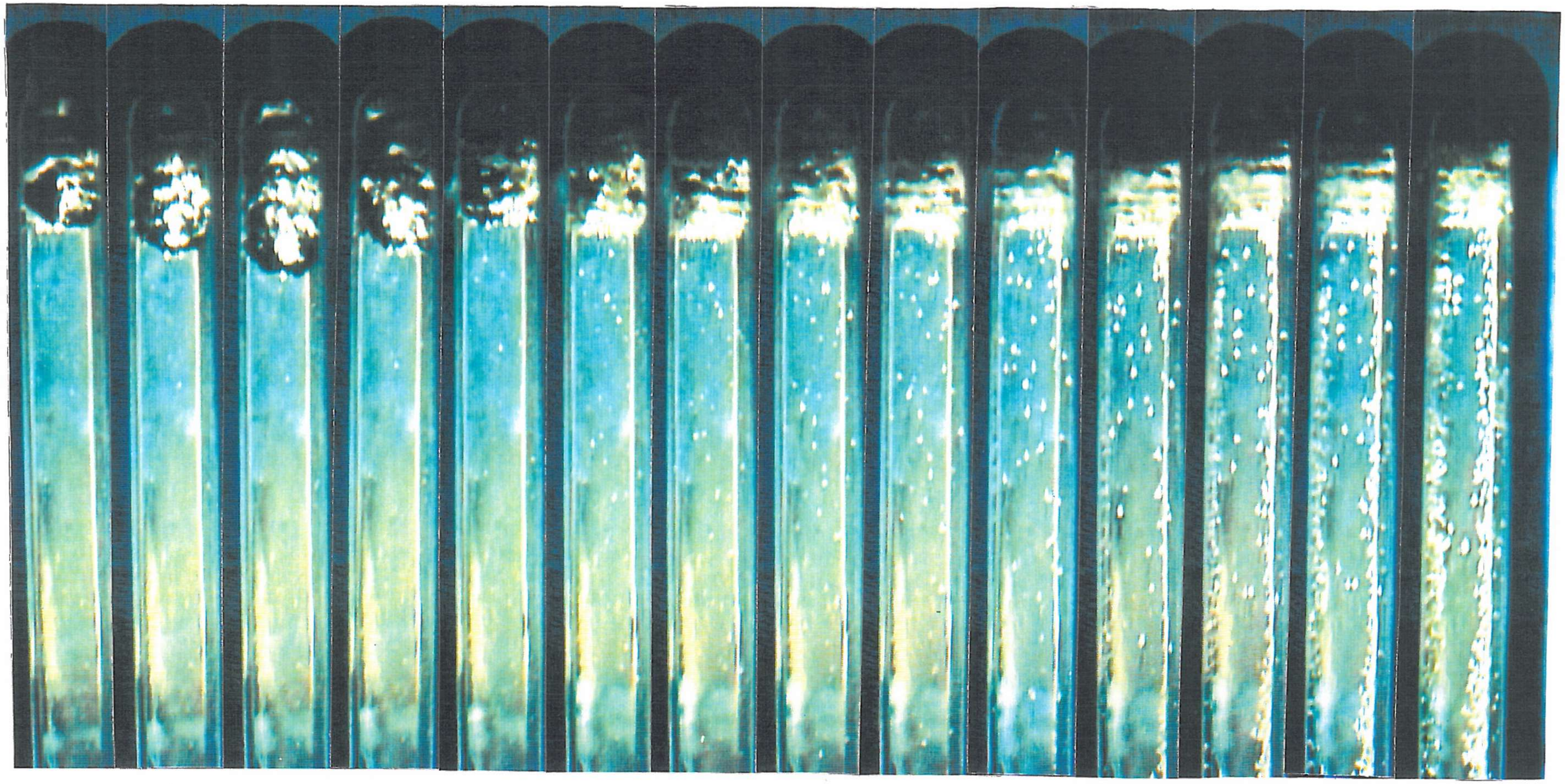

Photograph No	1	2	3	4	5	6	7	8	9	10	11	12	13	14
Time from t=0 (secs)	0:04	0:08	0:12	0:16	0:20	0:32	0:36	0:40	0:44	0:52	0:60	0:64	0:68	0:72

Plate VII Sequence of events captured during the depressurization of a CO_2 in kerosene system, from an initial pressure of 10 bara, ambient temperature and gas flow rate of 100 l/min

Note: Photographs are not consecutive frames and are ~ half full size

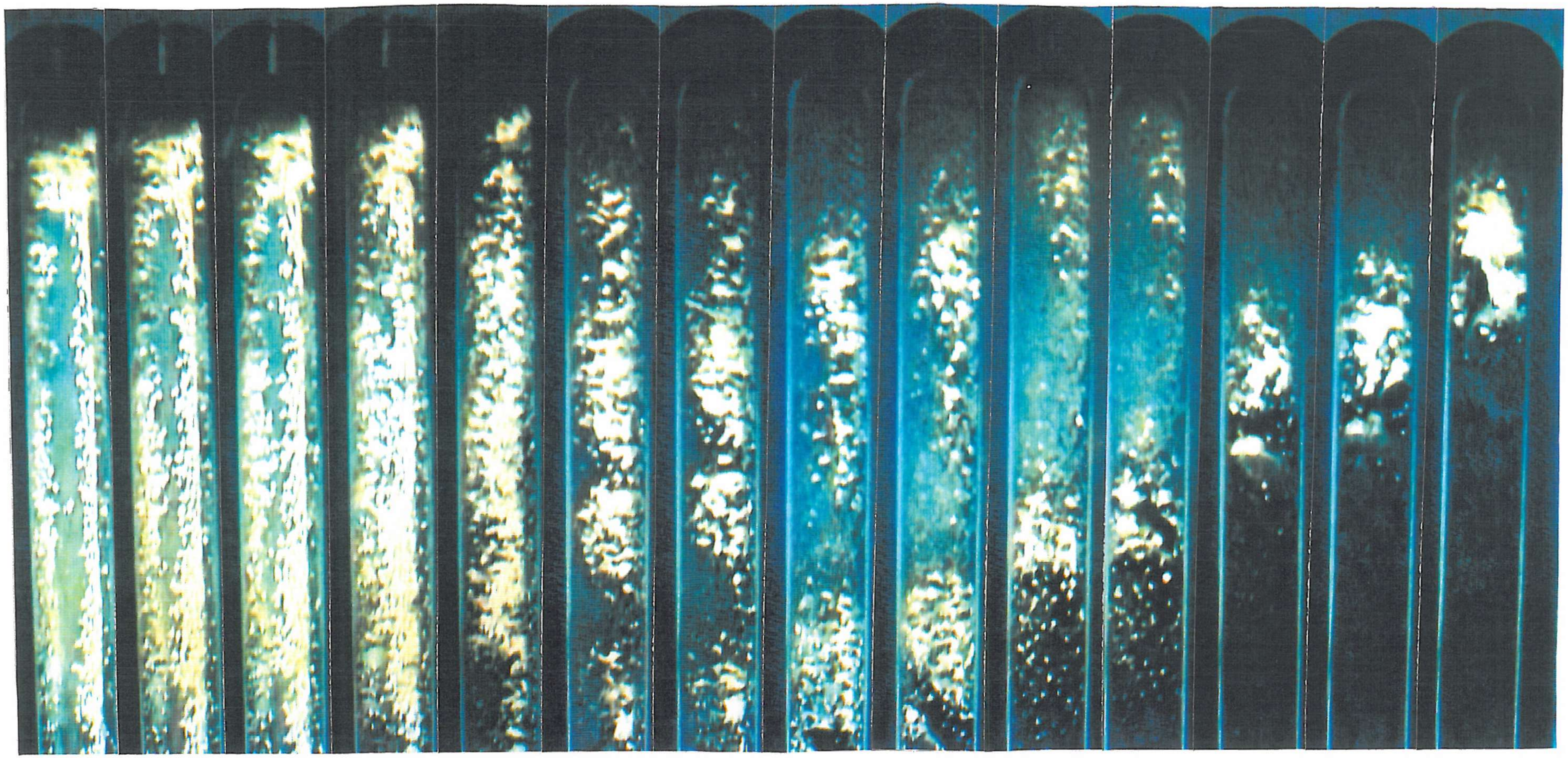

hotograph No 15 16 17 18 19 20 21 22 23 24 25 26 27 28
Time (secs) 0:76 0:80 0:84 0:88 0:96 1:04 1:08 1:12 1:16 1:20 1:24 1:28 1:32 1:36

Plate VII cont.. Sequence of events captured during the depressurization of a CO_2 in kerosene system, from an initial pressure of 10 bara, ambient temperature and gas flow rate of 100 l/min

Note: Photographs are not consecutive frames and are ~ half full size

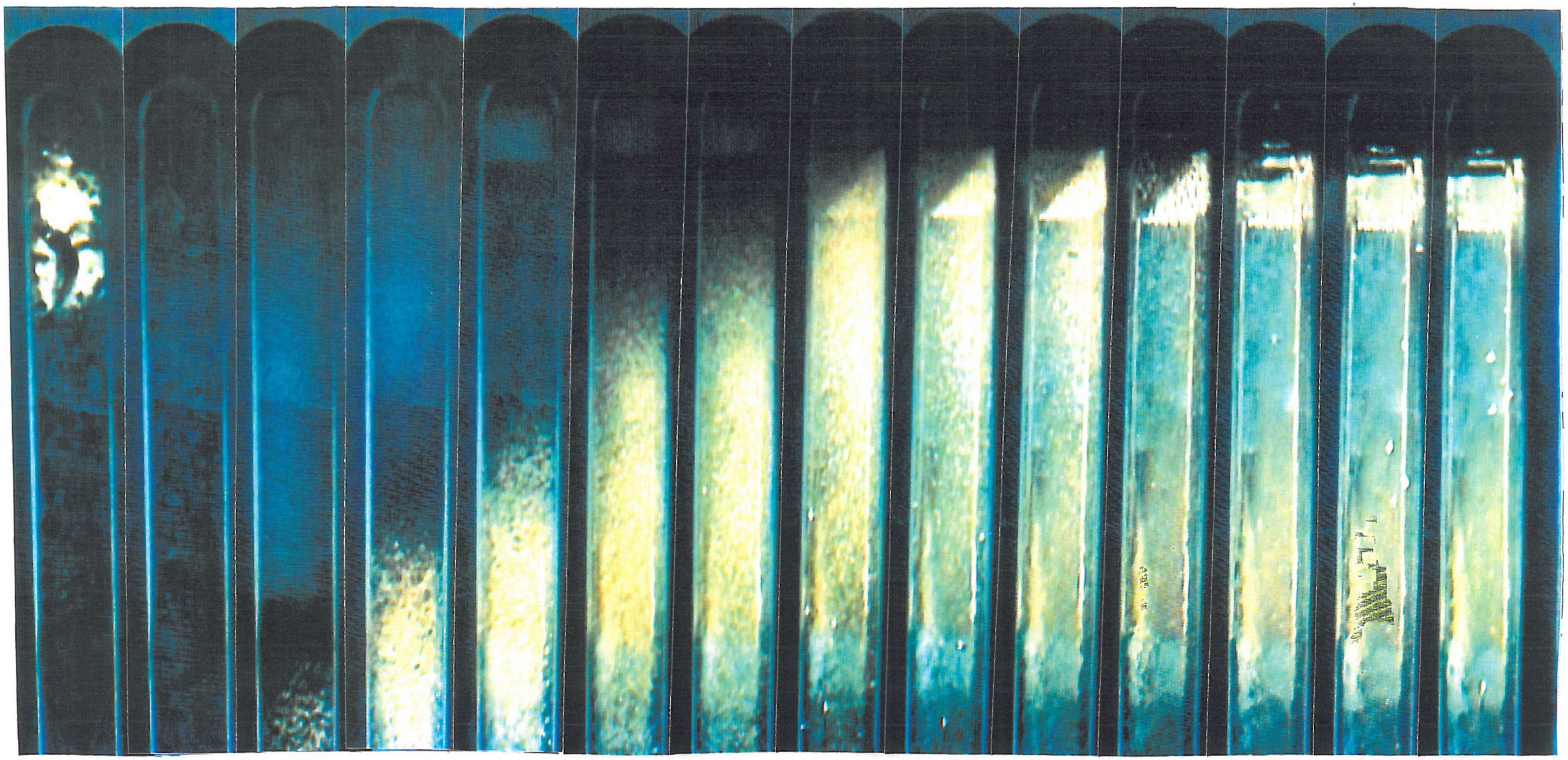

hotograph No	29	30	31	32	33	34	35	36	37	38	39	40	41	42
Time (secs)	1:40	1:48	4:76	5:76	6:76	7:76	8:28	10:28	12:28	14:28	19:28	27:28	34:68	34:84

Plate VII cont.. Sequence of events captured during the depressurization of a CO_2 in kerosene system, from an initial pressure of 10 bara, ambient temperature and gas flow rate of 100 l/min

Note: Photographs are not consecutive frames and are ~ half full size

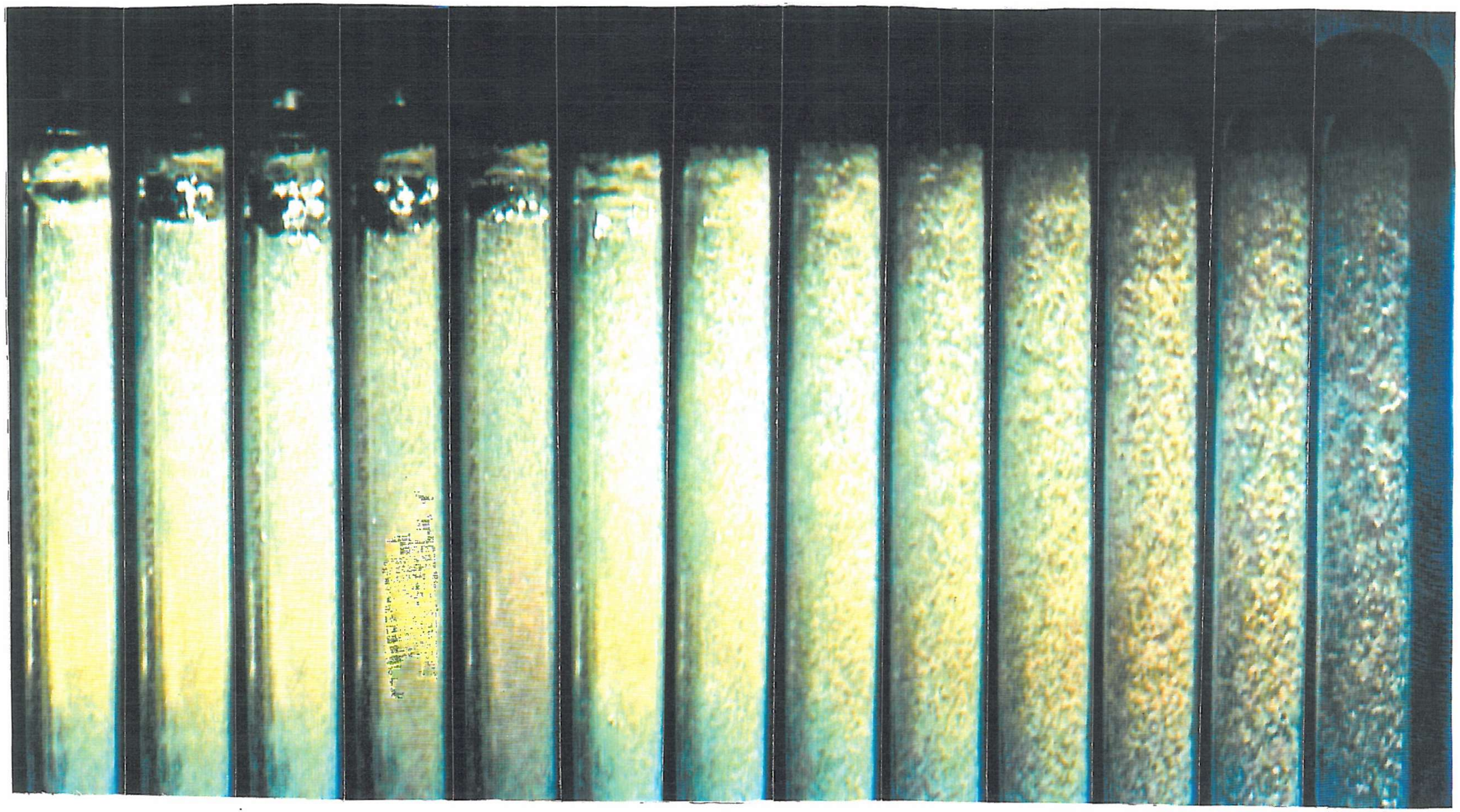

Photograph No	1	2	3	4	5	6	7	8	9	10	11	12	13
Time (secs)	0:00	0:08	0:12	0:16	0:20	0:36	0:60	0:76	0:84	0:92	1:00	1:08	1:16

Plate VIII Sequence of events captured during the depressurization of a N_2 in kerosene system, from an initial pressure of 10 bara, ambient temperature and gas flow rate of 100 l/min

note: Photographs are not consecutive frames and are ~ half full size

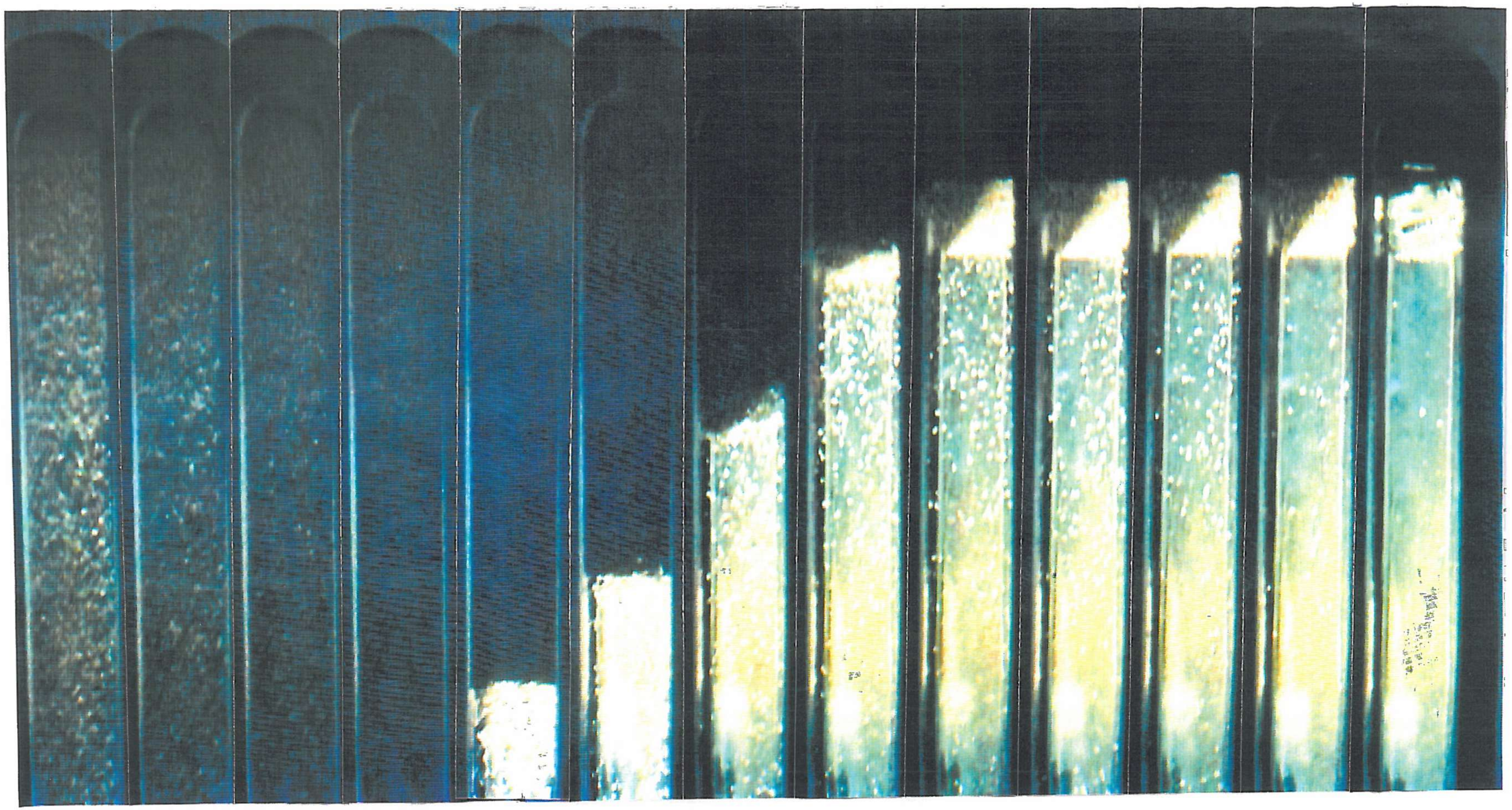

Photograph No	14	15	16	17	18	19	20	21	22	23	24	25	26
Time (secs)	1:24	1:32	1:40	1:52	5:76	6:12	6:60	7:12	7:36	7 60	8:12	11:12	18:36

Plate VIII cont.. Sequence of events captured during the depressurisation of a N_2 in kerosene system, from an initial pressure of 10 bara, ambient temperature and gas flow rate of 100 l/min

Note: Photographs are not consecutive frames and are ~ half full size